UNIVERSITY OF SOUTHAMPTON

FACULTY OF ENGINEERING AND THE ENVIRONMENT

Engineering Sciences

Evaluation of Polyetheretherketone as a Candidate Material for Cemented Total Knee Replacement

by

Kathryn E. Rankin

Thesis for the degree of Doctor of Philosophy

January 22nd, 2016

UNIVERSITY OF SOUTHAMPTON

ABSTRACT

FACULTY OF ENGINEERING AND THE ENVIRONMENT
Engineering Sciences

Doctor of Philosophy

EVALUATION OF POLYETHERETHERKETONE AS A CANDIDATE MATERIAL FOR CEMENTED TOTAL KNEE REPLACEMENT

by Kathryn E. Rankin

Total knee replacement (TKR) is an increasingly prevalent procedure for the treatment of knee joint degeneration. Aseptic implant loosening remains a predominant cause of revision surgery. Traditional metallic implants can cause stress shielding of the surrounding tissues *in-vivo*, which may lead to compromised implant support. The success rate of contemporary TKR has plateaued; alternative bearing materials may be an effective research focus to address the shortcomings of metallic TKR.

Poly-ether-ether-ketone (PEEK) is bioinert, with promising wear resistance and mechanical properties for implant applications, principally, an elastic modulus similar to that of bone. A novel cemented PEEK femoral component is currently in development as part of an all-polymer TKR. The fixation for such a concept is critical in determining its success *in-vivo*, but this may be compromised should the increased structural compliance cause higher interfacial stress. This is the first study to assess PEEK femoral fixation using bone cement and was carried out as part of a consortium project, led by Invibio Ltd.

PEEK-cement interface strength tests were performed under adverse shear loading conditions. The results showed that the interface strength is governed by the mechanical interlock alone; a hierarchical surface texture on PEEK achieved the highest interfacial shear strength with cement. This is also the first study to show that surface activation of PEEK by oxygen plasma treatment significantly improves the cement adhesion strength. Evidence of bending at the PEEK-cement lap-shear interface demonstrated the concern that increased compliance could lead to higher interfacial strains and compromise fixation, compared to metal-cement interfaces.

Digital Image Correlation (DIC) was employed to measure periprosthetic bone strains. CoCr implants produced low strains in the central metaphyseal region of the lateral bone surface compared to the intact case, indicative of stress shielding. The PEEK implant induced a strain distribution closer to that on the intact bone surface, suggesting that PEEK could promote the strains required for bone maintenance. This study demonstrates the need for rigorous DIC protocol in the biomechanics community and is presented to guide future studies for valid comparison of results.

Finally, Digital Volume Correlation (DVC) was used to demonstrate the concept of strain measurement at the bone cement fixation region of the PEEK TKR construct. With optimal μCT scan setup and DVC parameter selection, measurements may be obtained which characterise full-field cement strain with sufficient resolution, accuracy and precision. The work presented in this thesis, extended according to the suggested further work, should support future polymer orthopaedic implant developments by ensuring more robust pre-clinical analysis, with a closer representation of the unique response to the experienced *in vivo* conditions.

Contents

List of Figures

List of Tables

Glossary

Abduction Movement away from the midline of the body (coronal plane).

Acrylic bone cement PMMA based fixation medium for orthopaedic implants.

Adduction Movement towards the midline of the body (coronal plane).

Aliasing Image feature distortion or artefacts from signal reconstruction.

Anterior Front.

AP Anterio-posterior direction.

Arthroplasty Joint surgery.

BW Bodyweight.

CFR-PEEK Carbon fibre reinforced polyetheretherketone.

CoCr Cobalt-chromium metal alloy for medical use (typically ASTM F75 for TKR).

Coronal (or Frontal) Plane of the body running from side to side that divides the body into anterior and posterior portions.

CT x-ray computed tomography.

CT Artefact Any discrepancy between the CT numbers in the reconstructed image and the true attenuation coefficients of the specimen.

Cytotoxicity Toxic towards cells.

DIC Digital Image Correlation.

Distal Away from or furthest from the midline of the body or point of origin of a part.

DVC Digital Volume Correlation.

$\boldsymbol{E}$ Young's modulus.

Extension Bending moment around a joint that increases the angle between the two joint axes.

$\mathbf{E_{xx}}$ Strain in the x-direction.

$\mathbf{E_{yy}}$ Strain in the y-direction.

$\mathbf{E_{zz}}$ Strain in the z-direction.

FEA Finite element analysis.

Flexion Bending moment around a joint that decreases the angle between the two joint axes.

HA Hydroxyapatite.

Inferior Away from the head end of the body.

In vitro Within an laboratory experiment environment rather than within a living organism.

In vivo Within a living organism.

Lateral Away from the midline of the body.

μ**CT** Micro-focus x-ray computed tomography.

Medial Towards the midline of the body.

Micromotion Small movements between the prothesis and bone.

microstrain Unit of strain measurement (relative deformation), $\mu\epsilon$, which equates to 1 x 10^{-6} strain: 10,000 microstrain = 1% strain.

Migration Gradual micromotion over time leading to the prosthesis detaching from its original position to a new resting position.

ML Medio-lateral direction.

Mutagenicity Induces genetic mutations.

Osteolysis Resorption of bone tissue.

PEEK polyetheretherketone.

PMMA Polymethylmethacrylate.

Posterior Back.

Proximal Toward or nearest the midline of the body or point of origin of a part.

$\mathbf{R_a}$ Arithmetic mean of the surface roughness line profile.

Resonance stabilised Delocalised electrons within a molecular structure are drawn between functional groups with high polarity, lowering the potential energy of the substance and making it more stable than any of the contributing structures.

ROI Region of interest.

R_q Root-Mean-Square roughness of the line profile.

R_{sk} Skewness of the roughness line profile.

R_z Mean peak to valley height of the surface roughness line profile.

S_a Arithmetic mean of the areal surface texture.

Sagittal Plane of the body running from front to back, dividing parts of the body into right and left sides.

SEM Scanning electron microscopy.

S_q Root-Mean-Square roughness of the areal surface texture.

S_{sk} Skewness of the areal surface texture.

Stress shielding A decrease in stress generated in bone surrounding an implant due to its stiffness, which may result in bone resorption.

Superior Towards the head end of the body.

S_z Mean peak to valley height of the areal surface texture.

THR Total hip replacement.

TKR Total knee replacement.

TKR construct The complete femoral implant-cement-bone structure.

Transverse (or Horizontal) Plane of the body running crosswise, dividing it into superior and inferior parts.

UHMWPE ultra-high-molecular-weight-polyethylene.

Valgus A deformity involving displacement away from the midline of the body, twisted outward.

Varus A deformity involving displacement towards the midline of the body, twisted inward.

Declaration of Authorship

I, Kathryn E. Rankin, declare that the thesis entitled '*Evaluation of Polyetheretherketone as a Candidate Material for Cemented Total Knee Replacement*' and the work presented in the thesis are both my own, and have been generated by me as the result of my own original research. I confirm that:

- this work was done wholly or mainly while in candidature for a research degree at this University;
- where any part of this thesis has previously been submitted for a degree or any other qualification at this University or any other institution, this has been clearly stated;
- where I have consulted the published work of others, this is always clearly attributed;
- where I have quoted from the work of others, the source is always given. With the exception of such quotations, this thesis is entirely my own work;
- I have acknowledged all main sources of help;
- where the thesis is based on work done by myself jointly with others, I have made clear exactly what was done by others and what I have contributed myself;
- none of this work has been published before submission
- parts of this work have been published as shown in the List of Publications

Signed:..

Date:..

List of Publications and Conferences

K. Rankin, A. S. Dickinson, A. Briscoe, M. Browne. Evaluation of a novel polyetheretherketone femoral component with improved bone remodelling stimulus for total knee replacement. *Bone Joint J*, 98-B(SUPP 3), 132, 2016. *Orthopaedic proceedings from a podium presentation at the 16st Congress of the International Society for Technology in Arthroplasty*, Kyoto, Japan, September 24th-27th 2014

K. Rankin, A. S. Dickinson, M. Browne. Influence of implant material on femoral periprosthetic bone strain following total knee replacement: A Digital Image Correlation study. *Manuscript conditionally accepted to a PEEK symposium in Clinical Orthopaedics and Related Research*

K. Rankin, A. Dickinson, M. Browne. Femoral bone strain assessment following total knee replacement presented using Digital Image Correlation. *podium presentation at the 21st Congress of the European Society of Biomechanics*, Prague, Czech Republic, July 5th-8th 2015

K. Rankin, A. S. Dickinson, A. Briscoe, M. Browne. Improved bone remodelling stimulus with a novel PEEK implant for total knee replacement. *in proceedings of the 2nd International PEEK Meeting*, Washington, DC, USA, April 23rd-24th 2015

K. Rankin, A. S. Dickinson, A. Briscoe, M. Browne. A novel PEEK total knee replacement for long term bone preservation: Evaluation of femoral bone strains using Digital Image Correlation and Numerical Modelling. *poster presented at the 7th World Congress of Biomechanics*, Boston, MA, USA, July 6th-11th 2014

K. Rankin, A. S. Dickinson, A. Briscoe, M. Browne. Evaluation of the influence of implant material on femoral bone strains in total knee replacement. *in proceedings of the 16st International Conference on Experimental Mechanics*, Cambridge, UK, July 7th-11th 2014

K. Rankin, M. T. Bah, A. S. Dickinson, A. Briscoe, I. Sinclair, M. Browne. Characterisation of the fixation of a novel polyetheretherketone implant for total knee replacement. *in proceedings of the 1st International PEEK Meeting*, Philadelphia, PA, USA, April 25rd-26th 2013

Acknowledgements

This project was co-funded by Invibio Ltd (Technology Centre, Hillhouse International, Thornton Cleveleys, Lancashire, FY5 4QD, UK) and the EPSRC, through the University of Southampton Engineering Sciences PhD scholarship programme.

The greatest thanks must go to my supervisor Prof. Martin Browne, who has supported me through this project from start to finish. I am very lucky to have him as my Boss, and my time in the Bioengineering group certainly would not have been as enjoyable without him. I really appreciate the teaching opportunities that I have had, as well as the chance to present at multiple conferences. Not only was this great experience, but I also really enjoyed myself. Thanks also go to my second supervisor, Prof. Ian Sinclair, for his valuable, critical, yet constructive input for the first two years of this project, and to my third supervisor, Prof. Fabrice Pierron, for his advice in the DIC and DVC study.

I am really grateful for the industrial link that I have had with Invibio Ltd, who provided me with the focus of a real-world TKR application, and insight into the commercial orthopaedic implant approval process. More specifically, I would like to thank Dr Adam Briscoe for his valuable input in this project, securing samples for us, and making the very long journey from Lancashire to Southampton to give his support at our meetings.

In no particular order, thanks go to Dr Alex Dickinson, for his involvement in the DIC study, Dr Mark Mavrogordato from the μ-VIS centre, for his valuable help with CT scanning and manufacture of the cementing mould, Dr Liam Goodes, for his help with the Alicona, Dr Philip King from the Centre for Hybrid Biodevices, for his help with the plasma treatment, and Prof. Philipp Thurner, for kindly letting me use the distal section of cadaver bones procured for Thomas Jenkins' PhD project. I would also like to thank Prof. David Barrett for letting me observe him perform TKR surgery, which greatly helped me appreciate the complexity of the implantation process. Additional thanks go to all the support staff at the University, particularly the lab technicians, admin staff and finance team, who were available to help whenever you needed it. Plus thanks to all the PhD students and post-docs, for great tea breaks and christmas decorating competitions, and to my family for the weekend escapes to Devon.

Finally, a very special thanks must go to Alex, who has been my loyal supporter through all the ups and downs. For all the hours of proof reading, sandwich-making, and generally giving me the confidence to keep going, I am forever grateful.

Chapter 1

Introduction

1.1 Background and Motivations

Total knee replacement (TKR) is an increasingly common surgical procedure in today's ageing population. 86,067 primary TKRs were recorded in 2011 alone in the National Joint Registry for England, Wales and Northern Ireland. With a 40% increase since 2006 (Figure 1.1), this makes total knee arthroplasty the most common joint replacement procedure (National Joint Registry for England and Wales, 2011). TKR can provide relief from pain and restoration of function in the majority of patients suffering from degeneration of the articular surfaces of the knee joint, as a result of osteoarthritis, rheumatoid arthritis, congenital disorders and trauma (Bellemans et al., 2005; Ethgen et al., 2004).

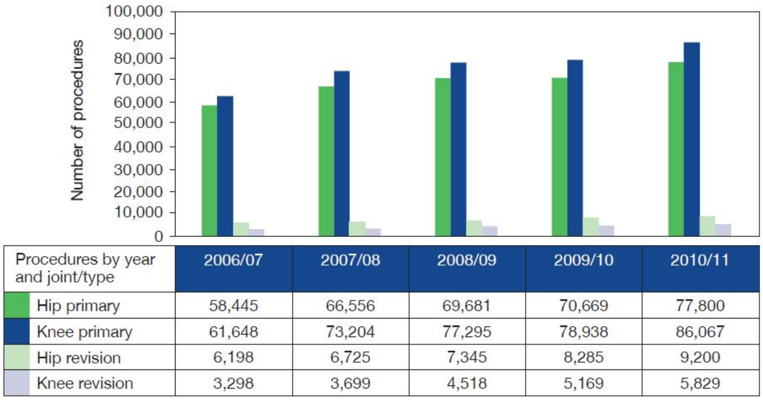

Procedures by year and joint/type	2006/07	2007/08	2008/09	2009/10	2010/11
🟩 Hip primary	58,445	66,556	69,681	70,669	77,800
🟦 Knee primary	61,648	73,204	77,295	78,938	86,067
🟩 Hip revision	6,198	6,725	7,345	8,285	9,200
🟪 Knee revision	3,298	3,699	4,518	5,169	5,829

Figure 1.1: Hip and knee joint replacement procedures recorded in the UK's National Joint Registry from 2006/07 to 2010/11 (National Joint Registry for England and Wales, 2011)

The anatomy of the healthy knee joint is illustrated in Figure 1.2. Together, the femur (thigh bone), tibia (shin bone) and the patella (kneecap) form the tibio-femoral joint. It is the largest synovial joint in the human body, which acts like a hinge during flexion and extension of the leg, as the distal femoral condyles slide and roll over the proximal tibial condyles and the anterior groove of the distal femur articulates with the patella (kneecap). This complex motion also involves internal-external rotation due to the curved profile of the femoral condyles and the flattened condyles of the tibia.

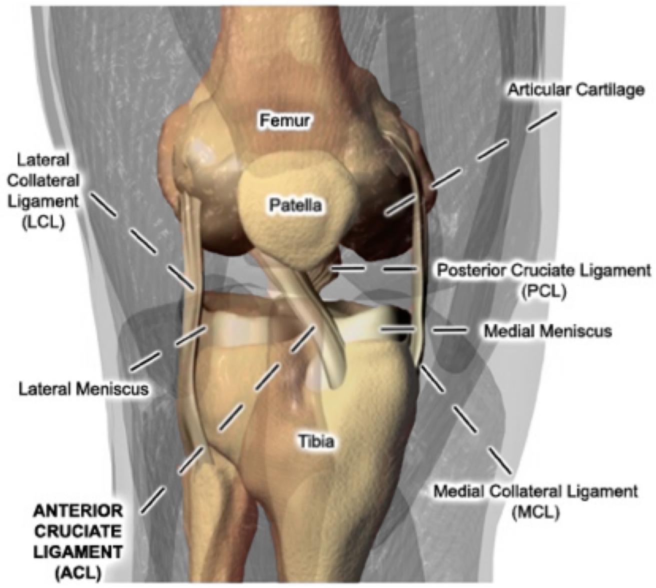

Figure 1.2: Healthy knee anatomy (modified from (Lowe, 2012))

The medial and lateral menisci, crescent-shaped fibrous cartilaginous plates, act as a cushion between the bones. Two ligaments cross the centre of the knee joint, the anterior and posterior cruciate ligaments, which stabilise the movement of the knee, along with the medial and lateral collateral ligaments that extend from the sides of the femur (Van Wynsberghe et al., 1995).

For a knee joint to function normally, the smooth articular cartilage layer plays a key role. With age, the cartilage in joints becomes thinner and there is often a reduction in volume of synovial fluid, which contributes to the effects of arthritis. When the articular surfaces become degenerated enough, such that pain and loss of mobility significantly affects day-to-day activities and alternatives such as drug treatment, complementary therapies and debridement (smoothing of the articular surfaces) are no longer viable options, total knee arthroplasty may be performed with the aim to restore the natural kinematics of the knee joint and reduce pain. Uni-condylar knee replacement may also be performed in a complex surgical procedure where only one of the condyles is resurfaced, when the other remains sufficiently functionable (Arthritis Research UK Ltd, 2012; Van Wynsberghe et al., 1995).

Prosthesis design and surgical technique have evolved over the years, but there is still much controversy in the optimal design of total knee replacement. Traditionally the femoral component is manufactured from a metal, a cobalt chromium alloy (CoCr), and the tibial component is manufactured from a polymer, ultra high molecular weight polyethylene (UHMWPE), often with a metal backing (Figure 1.3a) (Bellemans et al., 2005; Walker and Sathasivam, 2000). Different types of TKR designs are implanted in the bone with or without acrylic cement, with a mobile or fixed polymer bearing insert and the posterior cruciate ligament is either retained or resected. Often, the patella is also resurfaced.

During knee arthroplasty, the articular surfaces of the tibia and the femur are resected and cavities are drilled using bony landmarks as reference points. This exposes the cancellous bone beneath the cortical bone, into which bone cement is packed, creating an interdigitated layer. Thus a macro-interlock between the implant and bone enables the cement to fix the prosthesis in place. In the case of cementless TKR, an interference fit between the bone and prosthesis is used to achieve the primary implant stability. Secondary fixation is then achieved through osseointegration (bone ingrowth) to a bioactive coating. Correct medio-lateral soft tissue balance must be maintained to avoid joint instability or loss of motion, and this is influenced by the position and accuracy of the surgical cuts, and choice of bearing thickness (Bellemans et al., 2005). Figure 1.3b illustrates the implanted state of a typical total knee replacement.

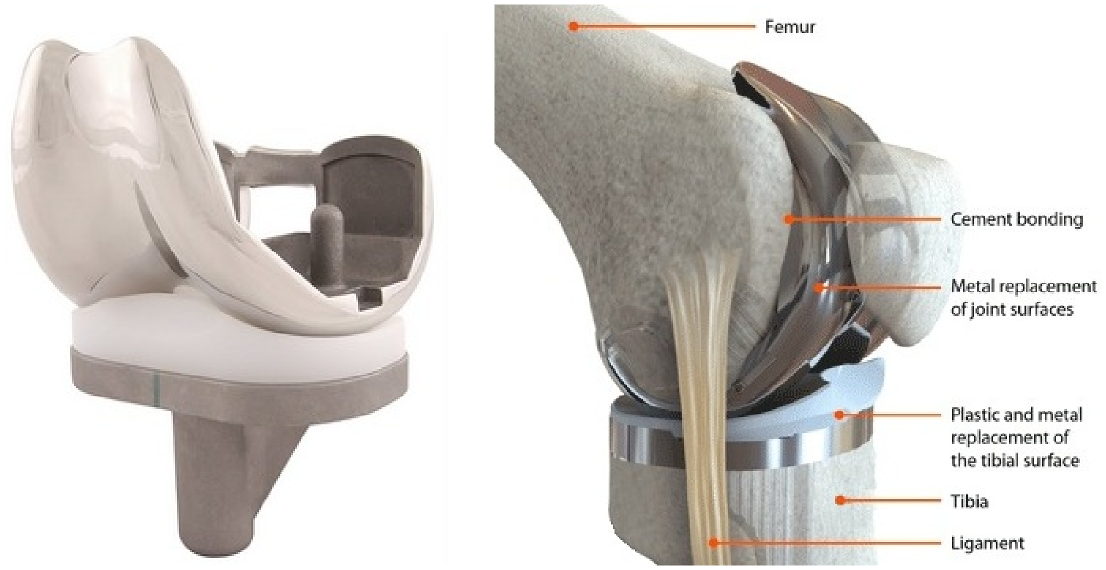

(a) Freedom Knee® posterior stabilised TKR prosthesis (Maxx Orthopaedics Inc., PA, USA)

(b) A typical total knee replacement (modified from (Arthritis Research UK Ltd, 2012))

Figure 1.3

The survivorship of total knee replacement has plateaued and a revision rate of around 4% remains at 7 years, depending on the prosthesis type. As the number of primary procedures increases, the number of revisions required also increases at a great cost to the healthcare provider. Careful patient selection for different types of prostheses plays an important role in the success of TKR. The estimated revision rates for primary knee replacements by prosthesis type from the National Joint Registry's 8th annual report (2011) is shown in Figure 1.4.

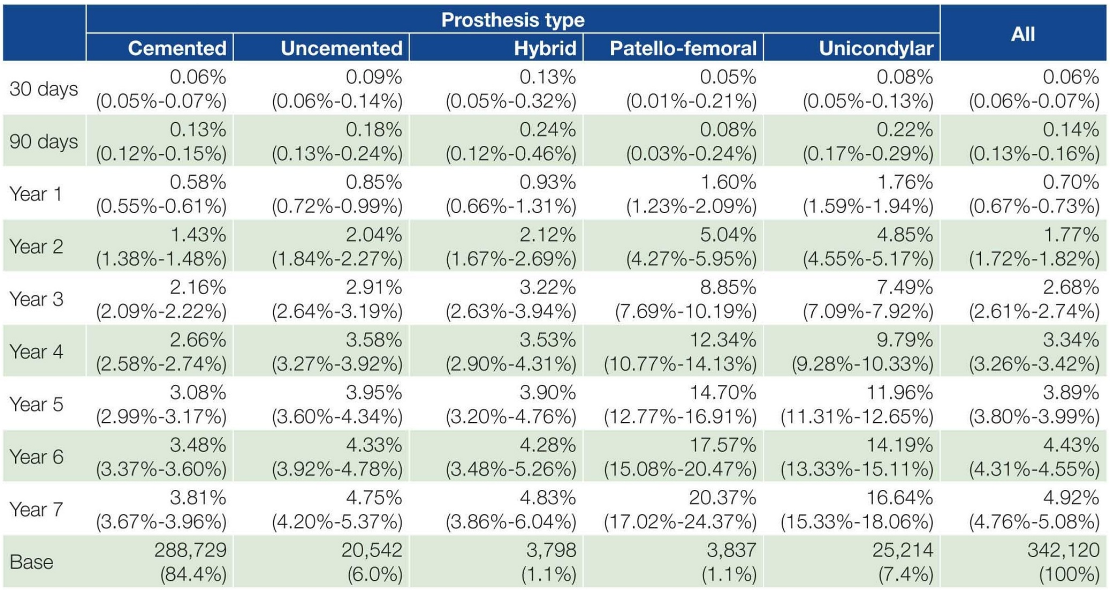

	Prosthesis type					All
	Cemented	Uncemented	Hybrid	Patello-femoral	Unicondylar	
30 days	0.06% (0.05%-0.07%)	0.09% (0.06%-0.14%)	0.13% (0.05%-0.32%)	0.05% (0.01%-0.21%)	0.08% (0.05%-0.13%)	0.06% (0.06%-0.07%)
90 days	0.13% (0.12%-0.15%)	0.18% (0.13%-0.24%)	0.24% (0.12%-0.46%)	0.08% (0.03%-0.24%)	0.22% (0.17%-0.29%)	0.14% (0.13%-0.16%)
Year 1	0.58% (0.55%-0.61%)	0.85% (0.72%-0.99%)	0.93% (0.66%-1.31%)	1.60% (1.23%-2.09%)	1.76% (1.59%-1.94%)	0.70% (0.67%-0.73%)
Year 2	1.43% (1.38%-1.48%)	2.04% (1.84%-2.27%)	2.12% (1.67%-2.69%)	5.04% (4.27%-5.95%)	4.85% (4.55%-5.17%)	1.77% (1.72%-1.82%)
Year 3	2.16% (2.09%-2.22%)	2.91% (2.64%-3.19%)	3.22% (2.63%-3.94%)	8.85% (7.69%-10.19%)	7.49% (7.09%-7.92%)	2.68% (2.61%-2.74%)
Year 4	2.66% (2.58%-2.74%)	3.58% (3.27%-3.92%)	3.53% (2.90%-4.31%)	12.34% (10.77%-14.13%)	9.79% (9.28%-10.33%)	3.34% (3.26%-3.42%)
Year 5	3.08% (2.99%-3.17%)	3.95% (3.60%-4.34%)	3.90% (3.20%-4.76%)	14.70% (12.77%-16.91%)	11.96% (11.31%-12.65%)	3.89% (3.80%-3.99%)
Year 6	3.48% (3.37%-3.60%)	4.33% (3.92%-4.78%)	4.28% (3.48%-5.26%)	17.57% (15.08%-20.47%)	14.19% (13.33%-15.11%)	4.43% (4.31%-4.55%)
Year 7	3.81% (3.67%-3.96%)	4.75% (4.20%-5.37%)	4.83% (3.86%-6.04%)	20.37% (17.02%-24.37%)	16.64% (15.33%-18.06%)	4.92% (4.76%-5.08%)
Base	288,729 (84.4%)	20,542 (6.0%)	3,798 (1.1%)	3,837 (1.1%)	25,214 (7.4%)	342,120 (100%)

Figure 1.4: Estimated revision rates of primary knee replacement by prosthesis type from the 2011 UK National Joint Registry (with 95% confidence intervals) (National Joint Registry for England and Wales, 2011).

Aseptic implant loosening and pain remain a predominant cause of revision surgery (National Joint Registry for England, Wales and Northern Ireland, 2013). A traditional high modulus metallic implant can cause stress shielding of the surrounding tissues *in vivo*, which may lead to loss of bone mass, leaving the supporting bone weak and porotic; this can cause implant loosening and further complicate revision surgery. In addition, concerns over metal ion release (leading to bone deterioration, inflammation and loosening), difficulty in medical imaging and patient discomfort remain problems with metallic TKR.

Alternative bearing combinations have previously been investigated in the literature. An all-polymer knee replacement was previously developed and manufactured from polyacetal articulating on polyethylene when a shortage of CoCr for medical implants became apparent (Scholes and Unsworth, 2010). It was discovered that the wear rate of the UHMWPE tibial component was 60% less when articulating with a polyacetal femoral component compared to articulation against metal. An advantage of this system was that any concerns over metal ion release over long time periods were also eliminated. Nonetheless, 20% of these knees replacements failed and were revised over a minimum follow-up period of 10 years, but this was found to be due to the use of an inadequate fixation technique and poor packaging after sterilisation (McKellop et al., 1993; Moore et al., 1998).

Polyetheretherketone (PEEK) is a high performance thermoplastic polymer manufactured as a biomaterial by Invibio Ltd (Thornton Cleveleys, UK). PEEK was originally used in the orthopaedic industry for spinal implants and is widely accepted as a radiolucent alternative to metallic implants. It is bioinert, resistant to sterilisation and shows promising wear performance in various bearing material combinations (Scholes and Unsworth, 2007, 2009, 2010; Wang et al., 1998, 1999). Above all, PEEK has an elastic modulus of 4 GPa, significantly lower than that of a metal such as cobalt chromium with a modulus of 220 GPa and within the range of that of bone (1 - 20 GPa (An and Draughn, 2000)). Hence, PEEK has the potential to promote a more physiological load transfer and reduce the stress shielding effects experienced with metallic components (Godara et al., 2007; Kurtz and Devine, 2007).

The concept of an all-polymer total knee replacement with a femoral component manufactured from PEEK, articulating on a UHMWPE tibial component is under development by a technical consortium, led by Invibio Ltd. By changing the material of an established TKR design whilst maintaining the same geometry, the number of independent variables is limited, which allows fairer comparisons of experimental results between PEEK and CoCr implants. The Freedom Total Knee® System (Freedom Knee, Figure 1.3a) is a high flexion device which was designed specifically for the Asian demographic by Maxx Medical Pvt Ltd, manufactured by Maxx Orthopedics Inc (PA, USA). The design facilitates the deep knee bending required by daily activities in Asian individuals and provides a more anthropometric fit. With a component geometry which allows reduced bone resection compared to other designs on the market, the Freedom Knee offers both cruciate retaining and posterior stabilised designs and a fixed all polymer tibial component option (Maxx Medical Pvt Ltd, 2013).

In modular TKR, backside wear and osteolysis is associated with metal backed tibial trays and polyethylene inserts so a fixed all-polymer tibial component has the potential of eliminating this problem at a lower cost, along with any concerns over metal ion release (Gioe and Maheshwari, 2010; Ranawat et al., 2005). The all-polymer total knee replacement aims to be a more cost effective method of joint replacement, prolonging the lifetime of the component *in vivo* and reducing the demand for revision surgery by reducing bone loss through stress shielding, whilst eliminating risk of metal sensitivity. However, as a novel biomaterial in TKR, the PEEK femoral component requires rigorous preclinical testing to ensure it is efficacious and safe.

From reviewing the literature, the success of the total joint replacement can be broadly determined by 5 key areas:

(i) The implant, cement and bone material properties

(ii) The bone and structural implant properties

(iii) The external loading modes it is subjected to

(iv) The interfacial properties (implant-cement and cement-bone interfacial strengths, as well as the femoral-tibial interface)

(v) The surgical technique used for implantation

Acrylic bone cement was chosen as the most suitable fixation medium for a PEEK femoral component *in vivo*. Although cementless fixation aims to preserve bone stock, if combined with an implant with increased compliance, excessive micromotions may result, leading to interface failure and revision surgery (Beckmann et al., 2011). Loss of implant-cement-bone interface integrity is a major cause of failure, necessitating revision surgery (An and Draughn, 2000). Therefore the fixation of PEEK with acrylic bone cement must be characterised as part of the implant development process, to ensure that a femoral component with increased compliance can withstand the *in vivo* loading conditions.

The work of this thesis focuses on the PEEK femoral fixation as part of the larger consortium project, where the implant structural integrity and wear properties are being investigated at Radboud University Medical Centre, NL, and University of Leeds, UK, respectively. A review of the literature in Chapter 2 first establishes the PEEK, cement and bone material properties before assessing the biomechanical environment at the knee joint, and the forces that the implant-cement-bone interface will have to endure. A review of adhesion properties and mechanical testing of interfacial properties then follows to determine how the PEEK-cement-bone interface strength could be enhanced and assessed. Methods for assessment of strain are then reviewed for application to the implanted TKR and the interface, to assess bone remodelling stimulus and interfacial cement strain, respectively.

Chapter 3 describes a study of the fixation strength of PEEK with cement and Chapter 4 describes a study where a method for evaluation of femoral strains induced by different TKR materials were evaluated using an analogue bone model. In Chapter 5, the method is applied to cadaver bones, to measure strain in a more representative model. Chapter 6 then describes a feasibility study for measurement of strain within the implanted TKR and at the cement interface in three dimensions. The findings are summarised with the conclusions in Chapter 7 and recommendations for further work are outlined.

1.2 Aims and Objectives

The overall aim for this project was to characterise the biomechanical response to a new generation all polymer Total Knee Replacement. The primary aim was to assess the integrity of cemented fixation in this novel implant system, incorporating a PEEK component, with a view to optimising it for long term fixation. Following that, the aim was to characterise the strain response of the surrounding bone construct, to verify its long term survivorship. The individual objectives can be outlined as:

- To characterise the adhesion properties between PEEK and cement through shear strength tests at the coupon level using different PEEK surface topographies,
- To compare the PEEK-cement interfacial shear strength to that of contemporary metallic implant materials,
- To evaluate selected methods to enhance the adhesion strength between PEEK and cement,
- To measure the bone strain distribution induced by a PEEK implant, compared to that with a CoCr implant to assess the stress shielding effects, and
- To develop a method for the measurement of volumetric interfacial strain *in situ*

Chapter 2

Literature Review

The literature survey first focuses on the properties of polyetheretherketone (PEEK) and acrylic bone cement which are proposed for use in an all-polymer total knee replacement (TKR). The structural properties of bone are also covered, as the femoral bone will be interacting directly with the PEEK and the cement *in vivo*; together they form the TKR construct. The biomechanical environment at the knee joint is considered to assess the nature of the forces that the TKR construct will need to endure, together with the interface and bulk stresses they generate, and outline potential areas of weakness. A review of adhesion follows with the aim to understand how the PEEK-cement interface will behave and how the interface strength could be enhanced. Finally, mechanical testing techniques for interfacial-strength and strain within the construct are assessed. This would aid the determination of suitable pre-clinical testing methods for sufficient validation that the PEEK femoral component will have adequate fixation integrity *in vivo*.

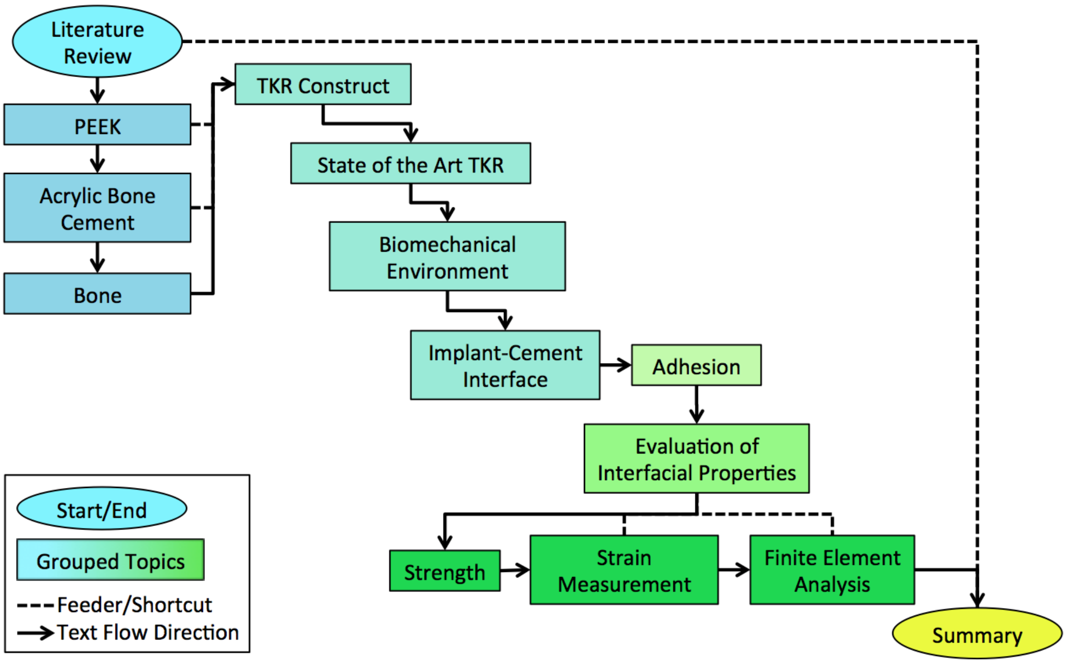

Figure 2.1: Flow chart of the literature review

2.1 Polyaryletherketones

Polyaryletherketone, PAEK, is the name given to the family of high temperature thermoplastic polymers which have an aromatic backbone molecular chain containing ketone and ether functional group connections. These molecules exhibit high strength to weight ratios, chemical stability at temperatures exceeding 300°C, compatibility with reinforcing agents such as carbon fibres, and resistance to chemical and radiation damage, making them desirable in many engineering applications.
Polyetheretherketone, PEEK, emerged as a suitable candidate for orthopaedic implants in the late 1990s which could replace the metal implant components in orthopaedics and trauma (Kurtz, 2011). The following section reviews the properties of PEEK with regard to orthopaedic applications.

2.1.1 PEEK - Structure, Polymerisation and Manufacture

PEEK is a semi-crystalline member of the high temperature thermoplastic PAEK family whose material stiffness arises from covalent bonds between adjacent aromatic ring structures in the polymer chain. The bridging ketone group and two ether linkages, highlighted on the PEEK monomer unit in Figure 2.2, further limit the flexibility of the polymer structure (Boinard et al., 2000).

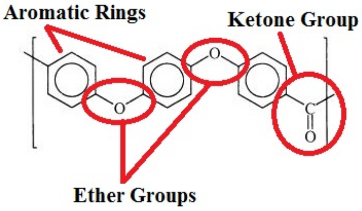

Figure 2.2: PEEK monomer unit

PEEK pellets are produced commercially by a nucleophilic displacement reaction route, also known as step growth polymerisation, which involves the displacement of a carbonyl activated fluoride (difluorobenzophenone) by phenoxide anions with the use of a high temperature solvent, diphenylsulphone. Generally, a phenate is produced *in situ* by reaction of the bisphenol (hydroquinone) with alkali metal carbonates, usually sodium or potassium carbonate (Figure 2.3). ‘Ar’ is the ketone-activated aromatic ring and ’M’ is the alkali metal (Kemmish et al., 2011; Walton and Lorimer, 2000). The overall reaction is shown in Figure 2.4.

PEEK pellets can be formed into various shape components by injection moulding, compression moulding and extrusion. The manufacture method requires temperatures

$$\mathrm{FArF + HOAr'OH + M_2CO_3 \longrightarrow 2MF + CO_2 + H_2O + \text{-}Ar\text{-}O\text{-}\,Ar'\text{-}}$$

Figure 2.3: Production of phenate by reaction of bisphenol with alkali metal carbonates (Ar = ketone-activated aromatic ring, M = sodium or potassium) (Kemmish et al., 2011)

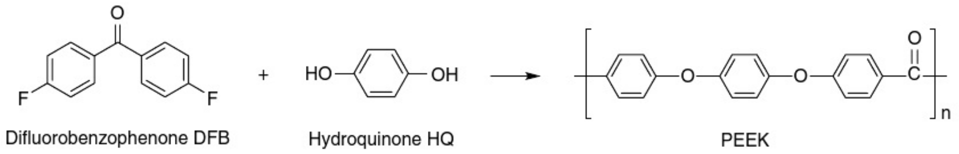

Figure 2.4: Preparation of PEEK via a nucleophilic displacement reaction (Kemmish et al., 2011)

in excess of 300°C, as PEEK has a high crystalline melt temperature (335-441°C) and a glass transition temperature (T_g) of around 143°C, leaving it in the glassy state at room temperature (Kurtz, 2011). The degree of crystallinity of a PEEK component can greatly affect its mechanical properties, but this is controlled for medical grade injection moulded PEEK components, at 30 to 35% crystallinity (Nieminen et al., 2008).

Carbon fibre reinforced PEEK composites (CFR-PEEK) can be prepared by including varying lengths and orientations of carbon fibre with PEEK during manufacture by composite flow moulding. This allows the material properties to be tailored to the application, as discussed in section 2.1.3.

2.1.2 Chemical Stability of PEEK-Based Materials

PEEK is a relatively unreactive polymer and has a degree of chemical resistance due to the delocalisation of higher orbital electrons along the entire polymer chain. This results from the location of the ketone and ether groups at opposite ends of the aryl rings, which provide a resonance stabilised effect. Hence, PEEK can withstand repeated sterilisation and long-term exposure to high temperatures (120°C, below the glass transition temperature of 143°C) with no significant impact on the mechanical properties (Godara et al., 2007; Kurtz, 2011; Kurtz and Devine, 2007).

Strong polar groups, such as the ketone group within a PEEK polymer chain, favour the bonding of water molecules and act as potential proton acceptors to form hydrogen complexes (Baschek et al., 1999). However, PEEK is reported to have low moisture absorption (quoted to be approximately 0.5wt% at equilibrium and is known to be highly resistant to many chemicals (Bismarck et al., 2007; Boinard et al., 2000). The formation of hydrogen bonds may be restricted by neighbouring atoms in the molecular chain. In the case of PEEK, an oxygen atom on either side of a ketone group is considered to hinder the formation of hydrogen bonds (Baschek et al., 1999).

Water absorption occurs via a type I Fickian diffusion process in PEEK and CFR-PEEK composites, but has been reported to have no significant effect on the compressive modulus, tensile strength, compressive strength or Poisson's ratio of the material in multiple studies (Rankin, 2011; Williams et al., 1987; Zhang et al., 1996). Water absorption in CFR-PEEK is noted in the literature as a possible concern due to the space between the matrix and the fibres. Both the carbon fibre reinforcement and PEEK matrix in CFR-PEEK composites have relatively good resistance to moisture absorption and ageing, so the material component most likely to degrade in the physiological environment is considered to be the fibre-matrix interface (Zhang et al., 1996). Nevertheless, Zhang (1998) showed that the fibre/matrix interface was unaffected even after 8000 hours of immersion in 90°C water. Scanning electron photomicrographs indicated that interfacial debonding did not occur to a significant degree in the CFR-PEEK following environmental conditioning in physiological saline at 37, 65 and 95°C (Zhang, 1998).

2.1.3 Material Properties of PEEK-Based Materials

The typical physical material properties of PEEK and CFR-PEEK are displayed in Table 2.1, as summarised in a review by Kurtz and Devine (2007). These are shown for specific grades of PEEK biomaterials provided by Invibio Ltd. The addition of short, chopped carbon fibres to PEEK allows the flexural modulus to be tailored more closely to that of cortical bone and can greatly enhance the structural material properties, as well as fatigue life and toughness (Godara et al., 2007; Kurtz and Devine, 2007).

The properties of PEEK are insensitive to temperature at the working conditions *in vivo*; however, it was advised that impact loading during implantation and frictional contact, which may generate heat in a joint replacement scenario, require more detailed consideration (Kurtz and Devine, 2007). PEEK is a viscoelastic material, so can exhibit rate-dependent deformation, creep, which must be accounted for in the implant design process.

Property (ISO)	**OPTIMA, LT1** [1]	**LT1CA30** [2]	**Endolign** [3]	**UHMWPE**	**PMMA**
Polymer type	Semi-crystalline	Semi-crystalline	Semi-crystalline	Semi-crystalline	Amorphous
Molecular Weight	0.08-0.12	0.08-0.12	0.08-0.12	2-6	0.1-0.8
Poisson's ratio	0.36	0.40	0.38	0.46	0.35
Specific gravity	1.3	1.4	1.6	0.932-0.945	1.180-1.246
Flexural modulus (GPa)	4	20	135	0.8-1.6	1.5-4.1
Tensile strength (MPa)	93	170	< 2000	39-48	24-49
Tensile elongation (%)	30-40	1-2	1	350-525	1-2
Degree of crystallinity (%)	30-35	30-35	30-35	39-75	Non-crystalline

[1] Unfilled PEEK
[2] 30% (w/w) chopped carbon fibre reinforced PEEK
[3] 68% (v/v) continuous carbon fibre reinforced PEEK

Table 2.1: Summary of typical material properties of selected PEEK and CFR-PEEK biomaterials compared with UHMWPE and PMMA at 23°C (Kurtz and Devine, 2007).

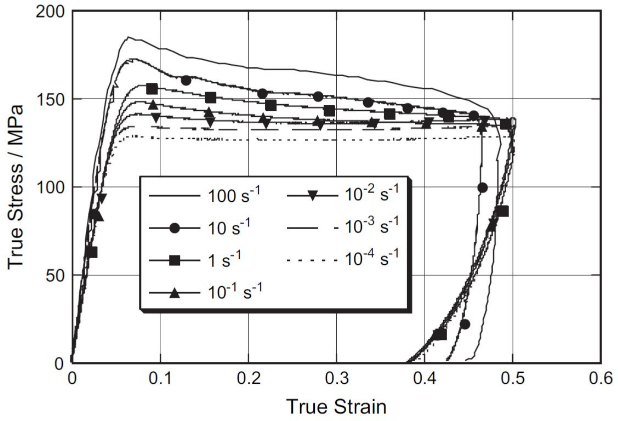

Figure 2.5: Effect of strain rate on the compressive properties of PEEK at 23°C (Rae et al., 2007)

Rae et al. (2007) showed that the mechanical response of PEEK is a function of the strain rate, (Figure 2.5), and also testing temperature, (Figure 2.6). However, the loading modulus is largely unaffected by either strain rate or temperature below the glass transition temperature (T_g). Below T_g the viscoelastic behaviour of PEEK has been shown to be strongly dependent on the thermal treatment of the material (physical ageing) during manufacture, which must be accounted for by using dynamic tests at multiple stress levels to check for linearity before applying a classical linear viscoelastic approach in the study of creep and stress relaxation behaviour (D'Amore et al., 1991).

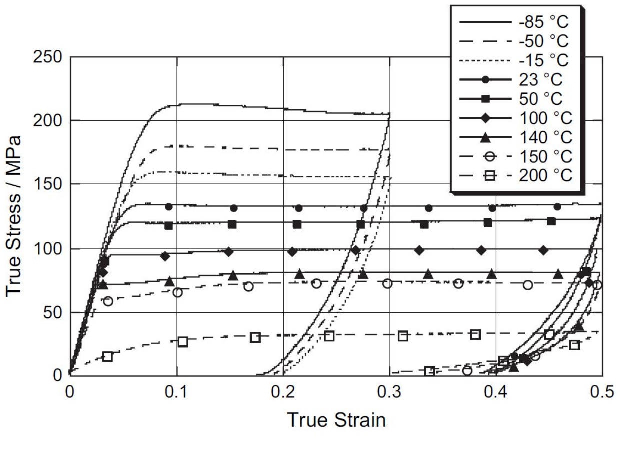

Figure 2.6: Effect of temperature on the compressive properties of PEEK at a strain rate of 1 x 10^{-3} s^{-1} (Rae et al., 2007)

The fracture toughness of a material, and a material interface, is an important consideration in implant design as a measure of the implant's resistance to crack propagation from a flaw within the material, ultimately leading to implant failure (An and Draughn, 2000). PEEK is relatively tough as an unfilled polymer. Rae et al.

(2007) quote a fracture toughness value of the crack driving force G_{Ic} (critical energy release rate) between 8 and 12 kJm^{-2} for PEEK, from studies at moderate loading rates using linear elastic fracture mechanics (LEFM), which corresponds to a K_{Ic} (critical stress intensity factor) of approximately 2 $\text{MPa}\sqrt{\text{m}}$, similar to that of UHMWPE (Teoh, 2000). This is significantly lower than that of current TKR cobalt chromium alloys, which have a K_{Ic} value of approximately 100 $\text{MPa}\sqrt{\text{m}}$, making them much tougher (Davis, 2003). Therefore, PEEK may be more notch sensitive for a TKR femoral component application with greater susceptibility to fatigue fracture under tensile loading conditions (Sobieraj et al., 2010).

The stiffness of an implant is a critical design variable because it largely determines how the applied loads are transferred to the bone (see section 2.3.3) (Huiskes et al., 1989). The modulus of trabecular bone ranges from 1 to 8 GPa, whereas the modulus of cortical bone is of the order of 20 GPa (An and Draughn, 2000). PEEK is considered an ‘isoelastic’ material as it has a modulus of 4 GPa, which lies between that of cancellous and cortical bone (Kurtz and Devine, 2007).

The fatigue performance of a material is also an important consideration in the design of an implant due to the nature of the variable cyclic load patterns it sustains *in vivo* (Carr and Goswami, 2009). Even though the crack growth behaviour and fracture properties of materials such as PEEK can be studied from a fracture mechanics perspective, often bulk material fatigue, impaction and wear measurements have limited application for decisions in implant design as they result from a combination of the material properties and structural design. Hence, these test methods are used to rank materials in terms of their suitability (Benham et al., 1987). Functional fatigue and wear testing must be conducted for each specific implant design (Kurtz and Devine, 2007).

There are limited studies on the wear of PEEK, but simplified pin-on-disc tribological studies have suggested that the friction and wear behaviour of PEEK depends on the surface roughness of the PEEK component and the counter-face on which it is articulating, as well as the temperature, the contact pressure between the bearing surfaces and the lubricant used (Cowie et al., 2014a,b; Scholes and Unsworth, 2010; Stolarski, 1992). The mechanical properties of PEEK can be tailored to an implant application by reinforcement with a volume fraction of carbon fibres, which has an effect on the wear of the PEEK (Wang et al., 1999). CFR-PEEK offers an improved wear rate over PEEK in certain bearing combinations, such as when articulating against a ceramic. However, it was recommended by Wang et al. (1999) that CFR-PEEK should not be used in a non-conforming contact situation where high contact stresses are present, such as in total knee replacement (Kurtz and Devine, 2007; Scholes and Unsworth, 2010; Wang et al., 1999). An increase in wear could result from the hard carbon fibre inclusions, which makes CFR-PEEK more abrasive than unfilled PEEK once the fibres are exposed (Harsha et al., 2003). However this would require direct investigation for articulation on UHMWPE. Although preliminary pin-on-plate wear tests of unfilled PEEK on UHMWPE by Cowie et al. (2014a,b) have shown promising results in comparison to CoCr on UHMWPE, there is little data in the literature relating to component level wear testing. A single conference abstract presented by Wang et al. (2011) reported an average of 41% reduction in UHMWPE wear for an injection moulded PEEK femoral component, articulating in a 6-station knee wear simulator after 3 million cycles. However, this gave no significant difference compared to UHMWPE wear with CoCr ($p = 0.08$). An average of 36% reduction in wear was measured for a machined PEEK femoral component under the same conditions, which gave a significant reduction in wear compared to CoCr on UHMWPE ($p = 0.048$). The tribology of this bearing combination needs to be investigated for application to each TKR design. This is being investigated as part of the larger PEEK knee project (led by Invibio Ltd) at the University of Leeds, so shall not be discussed further in this thesis.

2.1.4 Biocompatibility of PEEK-Based Materials

The biocompatibility of PEEK-based materials is supported by numerous studies. Combined with the ability to withstand repeated sterilisation with no significant effect on its mechanical properties, PEEK has good potential as a biomaterial for an articulating joint replacement (Brown et al., 2011; Godara et al., 2007; Hallab et al., 2012; Katzer et al., 2002; Morrison et al., 1995; Nieminen et al., 2008; Rivard et al., 2002; Utzschneider et al., 2010).

PEEK has displayed no signs of cytotoxicity with minimal response in animal models at 6 months implantation and healthy cell cultures after 96 hours; neither did it display any traits of mutagenicity as confirmed through the Ames test (Katzer et al., 2002; Morrison et al., 1998; Williams et al., 1987). PEEK has also been shown to have a stimulatory effect on the osteoblast cell protein content without inhibiting that of fibroblasts in a study by Morrison et al. (1995), which may indicate cell growth. This suggests that bone tissue growth may be encouraged around a PEEK implant *in vivo*, however, the chemical properties of PEEK may inhibit any adhesion at the bone-implant interface (Rivard et al., 2002).

The resonance stabilised effect of the PEEK molecular chain results in the characteristic unreactive nature of the biomaterial, as discussed in section 2.1.2, leaving it bioinert. Therefore the bioactivity of PEEK is minimal (Kemmish et al., 2011; Kurtz, 2011; Kurtz and Devine, 2007; Walton and Lorimer, 2000).

Attempts have been made to improve the bioactivity of PEEK by tailoring the polymer surface to stimulate bone cell deposition and adhesion. One method is to create composites with calcium phosphate containing molecules, such as hydroxyapatite (HA), which are bioactive and encourage bone growth (Kurtz and Devine, 2007; Tan et al., 2003). A pure titanium (Ti) surface coating can also be applied to PEEK by electron beam deposition. This has been shown to increase the bioactivity and wettability of the PEEK substrate during *in vivo* animal studies (Han et al., 2010). Dual-coating with Ti and then HA provides the bone with a more biocompatible and rough implant surface once the HA has been absorbed (Ha et al., 1997).

Another method used in the literature to improve the bioactive nature of PEEK without using a coating or bioactive-filler compound is plasma surface activation. This has been achieved by using a plasma (ionised gas) mixture of argon and ammonia (a technique discussed further in section 2.5.3), which generates functional groups capable of bonding biomolecules on the PEEK molecules at the surface of the component, without toxic effects. Briem et al. (2005) used this technique to achieve cell proliferation and differentiation of primary fibroblasts and osteoblasts through plasma-induced chemical micro-patterning. Oxygen plasma treatment has been used to increase the surface energy of PEEK to promote cellular adhesion in a study by Poulsson et al. (2013). However, although their results showed good early bone formation, their presentation at the 1st International PEEK Meeting (April 2013, Philadelphia, PA, USA), showed that there was no significant difference in the histomorphometry results for bone integration with treated and untreated PEEK. Although there was a difference in pull-out strength tests between machined and injection moulded surfaces, a difference with surface modification wasn't identified.

Nonetheless, for application to cemented TKR, a bioinert response may be more favourable in terms of cellular response to wear particles, dependent on the size of the particles. This requires specific investigation for this purpose (Black and Hastings, 1998; Freeman et al., 1982; Goodman et al., 2013; Kurtz, 2011).

2.1.5 Current Use of PEEK in Biomedical Implant Applications

PEEK is currently used or under development for use in several biomedical applications. In the spine, PEEK is used as a biomechanically successful, biocompatible, radiolucent implant material, particularly for load-sharing spinal fusion applications (Kurtz et al., 2013). PEEK rods have also been developed for spinal fusion, exhibiting superior creep resistance in comparison with other polymer systems and comparable stability with Ti rod systems. The lower modulus of PEEK rods also provides improved load-sharing with the bone, promoting fusion of the vertebrae (Kurtz and Devine, 2007).

The radiolucency of PEEK allows easy observation of bone-implant integration on x-rays, however, the bioinert nature of PEEK results in limited fixation with bone. The current techniques used for fixation of PEEK to bone *in vivo* involve the use of Ti and HA coatings to create a bioactive interface, often with the addition of mechanical fastenings (bone screws), or the use of bone screws alone. Calcium phosphate inclusions in PEEK spinal implants aim to accelerate the fusion process (Kurtz, 2011). In tissue engineering, scaffolds have been manufactured from HA/PEEK composites using selective laser sintering as a platform on which cells can develop with the aim to regenerate specific and functional human tissues (Tan et al., 2003).

CFR-PEEK femoral stems have been investigated for use in hip arthroplasty as an isoelastic alternative to metal stems with the aim to reduce stress shielding effects. CFR-PEEK also shows promising results as acetabular cup components for total hip replacement and resurfacing hip replacement in terms of wear rate when articulating against ceramic femoral heads (Kurtz and Devine, 2007; Scholes et al., 2008). Initial results from clinical trials are mixed and a presentation at the 1st International PEEK Meeting (April 2013, Philadelphia, PA, USA) by Richard Field, warned that CFR-PEEK is a bearing material that may cause high friction torque at the bone-implant and head-trunnion interfaces in THR (Field, 2013).

A uni-condylar knee replacement has been developed using CFR-PEEK as the bearing material for the tibial component articulating against a metal femoral component showing promising pre-clinical wear results even though it was recommended originally by Wang et al. (1999) that CFR-PEEK was not suitable for this application (Scholes and Unsworth, 2009). The degree of conformity between two articulating surfaces may affect the wear rate, as abrupt changes in radii may reduce the life of plastic tibial components before serious delamination occurs. The bearing surfaces of a unicondylar implant are more conforming than those in a total knee replacement, potentially accounting for superior wear results with a unicondylar prosthesis (Blunn et al., 1997).

In the dental industry, patient specific denture bases are manufactured from a single disc of PEEK-OPTIMA by Juvora$^{\mathrm{TM}}$ (Juvora Ltd, UK), with the aim to improve patient comfort through the material properties and specific design. PEEK dental implants were presented by Marya et al. (2011) in a study with three cases receiving a dental implant manufactured from a PEEK (80%), beta tricalcium phosphate and titanium dioxide (20%) composite. They commented on the radiolucency of the composite observed on radiographs, but saw a dense bone region surrounding the implant after 6 weeks, showing the implant position and good integration.

2.2 Acrylic Bone Cement

Self-curing polymethylmethacrylate (PMMA) bone cement has been used for fixation of implants to bone in joint replacement surgery since the 1960s (Navarro et al., 2008). The bone cement forms an intermediary mantle between the implant and the bone, and acts as a grout, which transmits applied forces and body weight to the surrounding bone and tissue (Basgorenay et al., 2006; Webb and Spencer, 2007). The following sections describe the composition, preparation and resulting properties of bone cement, for use as a fixation medium in orthopaedic implant applications.

2.2.1 Composition and Preparation

Bone cement is generally composed of a liquid monomer part (methylmethacrylate) and a powder part, containing pre-polymerised PMMA (polymethylmethacrylate) beads. When mixed together, the liquid monomer undergoes an addition polymerisation reaction to form an initially viscous dough, which is still fluid enough to be inserted where it is required in the patient's bone to polymerise fully, forming solid bone cement (Lewis, 1997).

The exact composition of the cement depends on the manufacturer, but the powder part will often contain a radiopacifier, such as barium sulphate, and a polymerisation initiator, benzoyl peroxide. The liquid monomer typically contains a stabiliser additive (hydroquinone) to prevent premature polymerisation and an accelerator (N,N-Dimethyl-p-toluidine) which will allow polymerisation to begin when it is mixed with the powder, initiating cold curing of the polymer (Lewis et al., 2007; Webb and Spencer, 2007). The accelerator causes the benzoyl peroxide initiator in the powder part to decompose and generate free radicals, which initiate an addition polymerisation reaction of the monomer and pre-polymerised PMMA beads. Commercial systems may also contain chlorophyll which acts as a dye, allowing surgeons to distinguish more easily between the cement and bone.

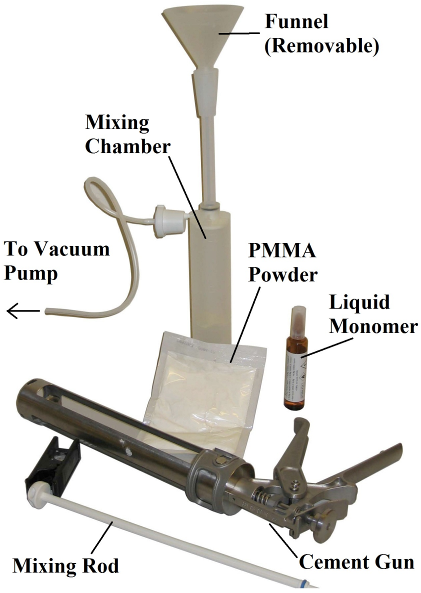

Figure 2.7: A third generation vacuum mixing cement system (modified from (Briscoe, 2006))

The mixing methods of bone cement have developed over time from basic hand mixing in a bowl to vacuum syringe mixing systems, but each remains highly user dependent. First generation mixing took place in an open air bowl with the use of a spatula, and was inserted in to the bone by hand, resulting in a cement with a high porosity content

(Dunne and Orr, 2001). Second generation mixing introduced cement guns for improved insertion of the cement in the bone, in order to achieve increased interdigitation with trabecular bone, and thus enhanced fixation, as the cement hardens. The cement-bone interface relies on interdigitation as a means of fixation (discussed further in sections 2.4.4 and 2.5), however a study by Kopec et al. (2009) showed no difference in interdigitation penetration depth achieved with a cement gun and hand packing. The third generation cementing technique involved vacuum mixing in a cement gun, as shown in Figure 2.9 (under reduced pressure), which was developed to reduce porosity and increase the strength of the bone cement (Chandler et al., 2006; Haydon et al., 2004). Porosity can have a significant effect on the mechanical properties of the bone cement and therefore on the lifetime of the implant-cement-bone construct *in vivo*. Hence, minimising porosity during curing may be a contributor to success (Dunne et al., 2003; Hoey and Taylor, 2009).

The polymerisation of bone cement is an exothermic process, reaching temperatures in the region of between 67 and 124°C in the centre of the mantle (Lewis, 2008; Stanczyk and van Rietbergen, 2004). The temperatures reached in polymerisation have been reported to depend upon the size of the polymer beads and nature of the bone cement additives (Basgorenay et al., 2006). Dunne and Orr (2002) showed that the mixing method also has a role in the maximum temperature reached during polymerisation. Excessive heat generation over 47°C can cause thermal necrosis (death) of the surrounding bone cells (Lundskog, 1972). However, interfacial temperatures have been measured by Reckling and Dillon (1977) to be below this, and suggested that necrosis may occur as a result of mechanical injury or damage to blood supply.

Bone cement also undergoes shrinkage during polymerisation as well as a thermal shrinkage due to the exothermic nature of the reaction. This occurs late in the curing cycle after the cement has obtained its solid properties, resulting in the formation of residual stresses. Orr et al. (2003) reported that shrinkage was greater in vacuum mixed cement compared to hand mixed cement due to the porosity content, which may counteract the shrinkage through expansion. Their results implied that cement cracks are present at the time of implantation, and that residual stresses at implant and bone interfaces may act as a source of crack initiation if they exceed the tensile strength.

2.2.2 Cement Viscosity

Viscosity describes the ratio of an applied shear stress to the velocity gradient it produces, the shear rate (Callister, 1997). Commercial bone cements are available in different viscosity formulations which vary the mixing and working time of the cement, the time in which the cement can be forced through the delivery device, penetrate the bone interstices and allow the implant to be manipulated in to the correct position (Lewis, 1997). This is also known as the doughy stage, when the cement has formed a polymerised cement ‘skin’.

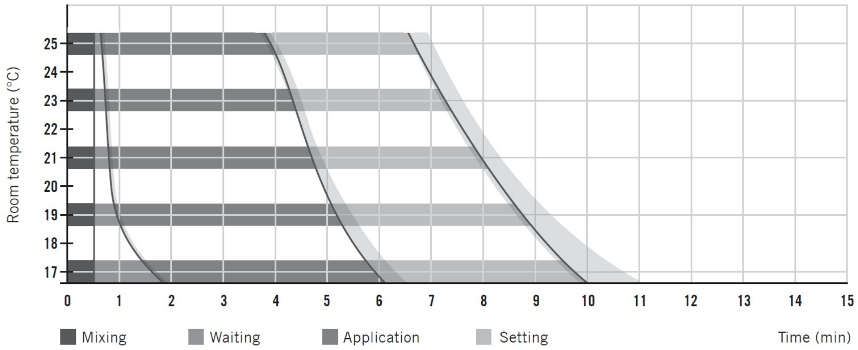

(a) High viscosity

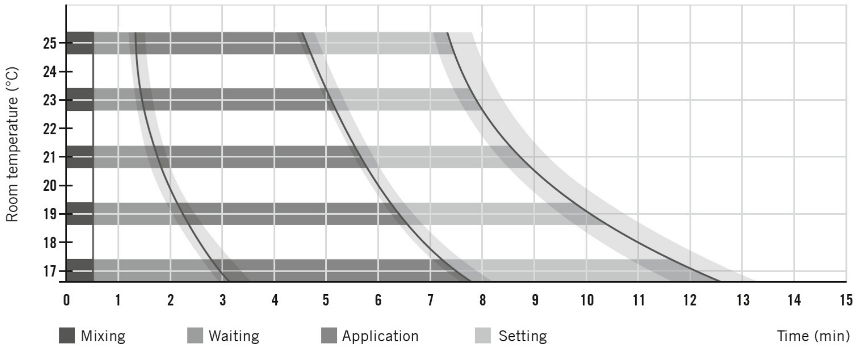

(b) Medium viscosity

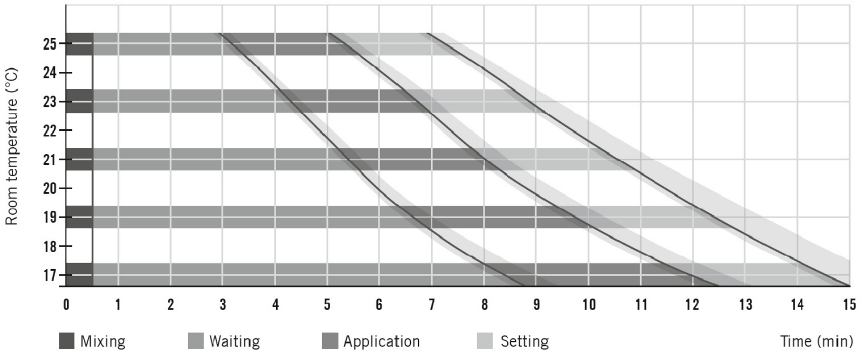

(c) Low viscosity

Figure 2.8: Working times for the manual mixing of high, medium and low viscosity Palacos bone cements (Heraeus Medical GmbH, Wehrheim, Germany)

Generally, viscosity increases in all acrylic cements as the polymer chains lengthen during polymerisation. The material is also pseudoplastic during the working time, so the viscosity decreases with an increase in shear rate. The working times of high, medium and low viscosity Palacos (Heraeus Medical GmbH, Wehrheim, Germany) bone cements are shown in Figure 2.10. Low viscosity cement formulations have a long mixing time and a short working time where the viscosity rapidly increases, whereas high viscosity cements have a short mixing time and a long working time where the viscosity remains fairly constant until a very short hardening phase. Medium viscosity cement has a long working time where the viscosity increases slowly (Webb and Spencer, 2007).

Viscosity is an important consideration when choosing a suitable cement for a specific application. For example, a low viscosity cement can be difficult to handle as it flows more easily and can be displaced by blood pressure, but it will penetrate the bone more easily, potentially achieving an improved micro-interlock. On the other hand, a low viscosity cement can be more forgiving for a surgeon because it has a long working time when positioning an implant (Chandler et al., 2006).

2.2.3 Material Properties of Bone Cement

The mechanical properties of a range of acrylic bone cements have been summarised by Lewis (1997), shown in Table 2.2. These properties may be affected by the composition of the cement, the mixing technique, and the curing and ageing conditions.

Property	**Range**	**Units**
Ultimate tensile strength	24 – 49	MPa
Ultimate compressive strength	73 – 117	MPa
Flexural strength	50 – 125	MPa
Elastic modulus	1.5 – 4.1	GPa
Fracture toughness	1.03 – 2.32	MPa$\sqrt{\text{m}}$

Table 2.2: Overview of the mechanical properties of acrylic bone cement (Lewis, 1997)

Due to its viscoelastic behaviour, the creep of bone cement may lead to prosthesis subsidence, as demonstrated in a study by Yetkinler and Litsky (1998). Constrained dynamic creep tests (representative of the cement surrounded by the bone and implant) are necessary to obtain the data required when making an assessment of potential subsidence effects *in vivo*. The cement should also be loaded under dynamic conditions, as well as static, when evaluating creep behaviour because the material has the opportunity to relax after each loading cycle.

Bone cement has a fracture toughness similar to that of PEEK (section 2.1.3). The fracture toughness of bone cement has been correlated with low impact and fatigue strength, and may be affected by porosity (Ries et al., 2006). As previously mentioned, inadequate mixing method and inclusion of air bubbles when mixing bone cement can lead to porosities, which have been shown to enhance the formation of micro-cracks that contribute to crack propagation, reduction in fatigue life and thus the implant lifetime (Dunne and Orr, 2001).

Residual stresses and porosities can be classed as stress raisers, which contribute to the fatigue failure of bone cement (Sinnett-Jones, 2007). It was shown in a study by Dunne et al. (2003) that even though reduced pressure mixing systems reduce porosity, crack initiation may still originate at single macropores which could lead to fatigue failure of the cement mantle, implant loosening and revision surgery. Therefore porosity and stress raisers in bone cement should be minimised in order to preserve the lifetime of the implant *in vivo*. However, it is also important to note that the implant stability and interfacial strength between the bone and the cement will be highly dependent on the amount of interdigitation of the cement into the bone (Mann et al., 1997).

2.3 Bone

The structural properties and the behaviour of bone must be considered when designing and implanting any prosthesis, to predict any response within the bone itself. As a living material, bone is able to adapt its structure depending on the mechanical usage experienced. The following sections (2.3.1 and 2.3.2) comprise a brief overview of bone structure and function from the article ‘Normal bone anatomy and physiology’ by Clarke (2008), and the books ‘Bone’ by McLean and Urist (1968), ‘Basic Orthopaedic Biomechanics and Mechano-Biology’ by Mow and Huiskes (2005) and ‘Handbook of Biomaterial Properties’ by Black and Hastings (1998). A review of periprosthetic bone response then follows in section 2.3.3. It is acknowledged that bone maintenance is a complex biological process, but for the interests of this thesis, the behaviour is presented from a mechanical perspective.

2.3.1 The Structure of Bone

As the implantation sites of the femoral and tibial components, the femur and tibia bones are of greatest interest at the knee joint for TKR. These are classed as long bones, which have a rounded epiphysis section above the growth plate (nearest the articulating surface) and a tapered metaphysis section below the growth plate at either end of the bone, which are connected by a hollow shaft, the diaphysis. The diaphysis is primarily composed of a cortical bone structure and the metaphyses and epiphyses are predominantly cancellous bone of a sponge-like trabecular structure with a thin cortical bone shell. Figure 2.11 shows a cross-section of the bone structure in the distal femur. A TKR femoral component is supported by the cancellous bone and a peripheral dense cortical shell. The bone cement provides fixation with the bone by interdigitating with the trabeculae of the cancellous bone.

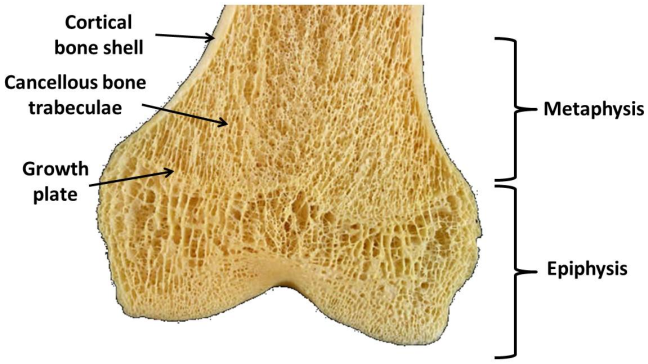

Figure 2.9: Bone anatomy of the distal femur

Bone has a tiered hierarchical structure, with three main cellular components associated with specific functions:

- Osteoblasts are bone forming cells
- Osteocytes are bone maintenance cells
- Osteoclasts are bone resorbing cells

As a tissue, both the cortical and trabecular bone are composed of osteons. Cortical osteons are the Haversian systems which have a cylindrical structure with layers of concentric lamellae. Large numbers of lacunae connnected with canaliculi containing osteocytes are present in the Haversian systems; at the centre is the Haversian canal which contains blood vessels. Lamellar bone is formed with collagen fibrils which are laid down in alternating orientations, making it mechanically strong. Woven bone is formed when collagen is laid down in a disorganised manner as osteoblasts produce osteoid rapidly; this results in a bone which is much weaker, but it is gradually converted to lamellar bone. The periosteum is a fibrous connective tissue sheath around the cortical bone which contains blood vessels, nerves, osteoblasts and osteoclasts. The endosteum is a membrane covering the inner surface of the cortical bone, the trabecular bone and blood vessel canals, containing blood vessels, osteoblasts and osteoclasts. The cancellous bone is up of trabeculae which form a rod and plate structure composed of concentric lamellae. Figure 2.12 shows the overall hierarchical structure of the bone.

2.3.2 Bone Remodelling

During adult life, bone is maintained through a process known as remodelling, in which old bone is resorbed and new bone is formed to reverse accumulation of microdamage and preserve the mechanical strength. The exact trigger for the onset of the remodelling process is generally not known, but the cycle is thought to be divided

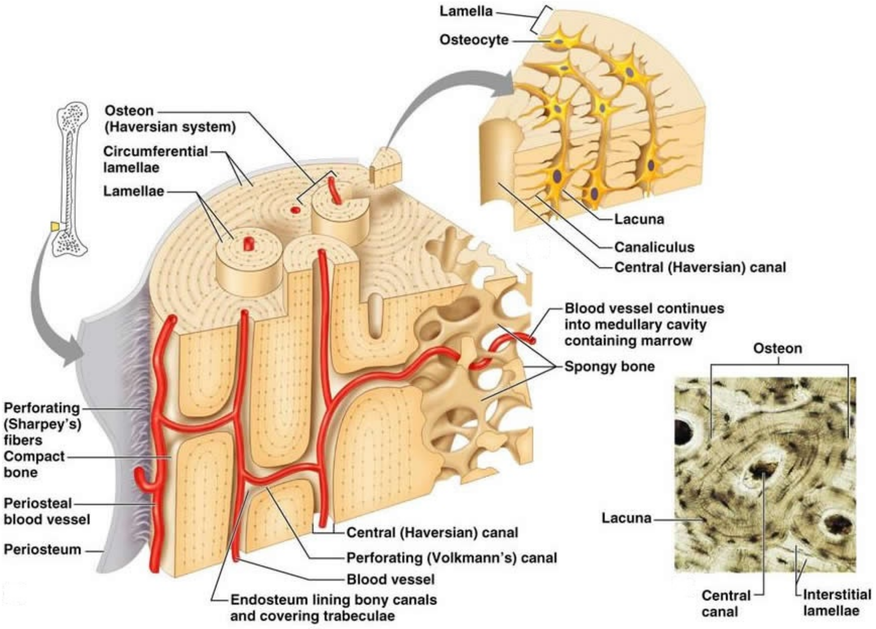

Figure 2.10: The hierarchical structure of cortical and cancellous bone

in to four stages, outlined in Figure 2.13. The activation cycle involves recruitment of pre-osteoclasts from the circulation and the formation of sealed zones around bone-resorbing compartments beneath multi-nucleated osteoclasts. Osteoblasts are thought to express the biochemical signal, RANKL, which attracts pre-osteoclasts (which express RANK, the receptor of RANKL) from the marrow and stimulates the differentiation and activation of osteoclasts. The osteoclasts then resorb the bone in the remodelling stage and pre-osteoblasts are recruited to begin bone formation in the inversion stage, which is thought to be governed by the strain gradient in the lacunae. As osteoclasts resorb bone in a conical manner, a strain gradient is left in the lacunae with strain reduced in front and increased behind. Osteoclasts are thought to be activated by reductions in strain and osteoblasts are thought to be activated by an increase in strain. The growth factor TGF-β is released during resorption and is also thought to link to bone formation, stimulating osteoblast bone formation. Bone formation occurs as osteoblasts produce a new collagenous matrix which is mineralised as calcium and phosphate, as osteoblasts become osteocytes. The result is the formation of a new osteon in either cortical or trabecular bone, with the rate of trabecular bone remodelling much higher for mineral metabolism.

2.3.3 Peri-Prosthetic Bone Response

Bone requires the stimulus of mechanical strain in order to maintain its structure and will respond and remodel in accordance with its local stress environment, as described

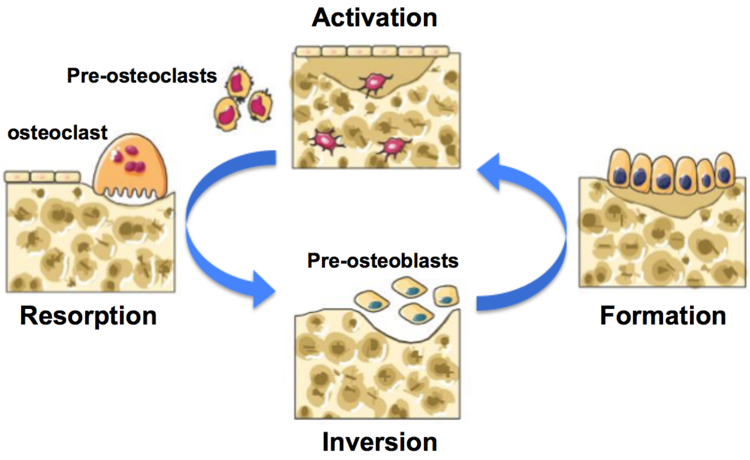

Figure 2.11: Schematic of the bone remodelling cycle (modified from Brandi (2009))

by Wolff's law and bone's mechanostat (An and Draughn, 2000; Frost, 2003). When a prosthesis is inserted into bone, it provides structural reinforcement and shares the applied load, resulting in a decrease in stresses generated in the surrounding tissue as the load bypasses the bone (Huiskes et al., 1987; van Lenthe et al., 1997). Insertion of implants of greater stiffness than bone will greatly alter the stress distribution experienced by the bone during activity (van Lenthe et al., 2002). If the bone surrounding an implant is no longer subjected to strains necessary for maintenance, it can slowly resorb and redistribute over time, as in the case of stress shielding.

It is believed that as the osetocytes are subjected to mechanical loads at tissue-level, the resulting strain causes signals to be transmitted. These signals inhibit the natural action of the osteoclasts and osteoblasts to remove and lay down new bone respectively, maintaining the current bone structure (Martin, 2000). Bone remodels around an implant as a result of strain energy density within the bone tissue (Huiskes et al., 1987). The minimally effective strain threshold range for bone modelling (maintenance) is thought to be within 1000 to 2000 $\mu\varepsilon$. When the strain stimulus is low in the bone tissue, within the threhold range for disuse (50 - 400 $\mu\varepsilon$), the osteocytes generate less signals to inhibit the action of osteoclasts and bone resorption increases, leading to a net loss of bone mass. If an implant provides structural support such that the load bypasses the adjacent bone, it will become porotic, weakening the bone structure and potentially leading to implant loosening (Frost, 2003; Kurtz and Devine, 2007; Scholz et al., 2011; van Lenthe et al., 1997; Williams et al., 1987). Loss in periprosthetic bone mineral density (BMD) is commonly reported in the literature following metallic TKR (Jarvenpaa et al., 2014; Karbowski et al., 1999; Soininvaara et al., 2004; Spittlehouse et al., 1999), regardless of fixation type (Abu-Rajab et al., 2006). BMD loss is also reported following metallic unicondylar knee replacement (Soininvaara et al., 2013).

When the strain stimulus increases and exceeds approximately 3000 $\mu\varepsilon$, the operational microdamage threshold, the osteoblast inhibition signal is decreased, resulting in a net gain of bone mass (Frost, 2003). This is also the point at which bone begins to yield and woven bone formation replaces lamellar bone formation. Bone densification has been reported to occur near the proximal edges of the anterior and posterior flange and around the fixation pegs of metallic femoral components and in the tibial metaphysis (below the tibial component) as a result of increased bone strain at these locations (Soininvaara et al., 2013; van Lenthe et al., 1997). However, in clinical studies a net reduction in BMD dominates in each region of interest of the distal femur, particularly the central metaphysis (Abu-Rajab et al., 2006; Soininvaara et al., 2013).

An immune response to particulate wear debris (primarily PE and PMMA) may also result in periprosthetic osteolysis dependent on the size, composition and dose of particles present (Black and Hastings, 1998; Freeman et al., 1982; Goodman et al., 2013). Clinically, this can lead to aseptic loosening of the implant, significant bone loss and pathological periprosthetic fracture (Archibeck et al., 2000).

Management of bone loss remains the most challenging aspect of TKR revision surgery, which highlights the need for a more bone preserving device (Lombardi et al., 2010; Panegrossi et al., 2014). As discussed in section 2.1.3, a PEEK femoral component with increased compliance has the potential to reduce the stress shielding effect of bone observed with high modulus metallic devices.

Even though there is an inevitable modulus mismatch between PEEK and bone, this is significantly smaller than that imposed by traditional metallic orthopaedic alloys used in joint replacement, which have a modulus of approximately 220 GPa, 10 to 20 times greater than the surrounding bone (Black and Hastings, 1998). Therefore, a more compliant PEEK implant may transfer greater load to the bone in which it is implanted, rather than sustaining the load itself and shielding it from the bone.

2.4 TKR Biomechanics

The aim of TKR can be briefly summarised as relief from pain, restoration of function, durability (relative to the lifetime and lifestyle of patient) and reliability. In order to translate these aims to a functional TKR design, the biomechanical criteria, shown in table 2.3 must be specified for each aim such that the design may be optimised for purpose.

The following sections define the construct and the current state-of-the-art in TKR, before discussing the biomechanical environment that the TKR must endure. Findings

Aim	**Biomechanical Criteria for TKR**
Pain relief	Replacement of articular surfaces, ideally without micro-motion between the implant and bone
Restoration of function	TKR motion closely replicating the normal knee. Soft tissue balance, laxity and muscle lever arms within the range of the normal knee
Durability	Surrounding tissue stress within the range of the healthy knee and interface stress within the strength and durability limit of the materials. Minimal wear of articulating surfaces.
Reliabiltiy	Insensitive to variation in kinematics and sizing between patients.

Table 2.3: Aims for TKR and the associated biomechanical criteria (modified from (Mow and Huiskes, 2005))

from studies in the literature regarding the performance of the implant-cement interface and strength of adhesion at the interface are also reviewed, with a particular interest in application to a PEEK TKR.

2.4.1 TKR Femoral Implant Construct

The entire implant-cement-bone structure is referred to in this thesis as the construct. The mechanical integrity of the construct is a key factor governing the long term stability and success of the implant (Cristofolini et al., 2008). There are a number of factors to be considered when assessing the integrity of the construct. The interfacial strength and fracture toughness between the cement and the implant, as well as between the cement and the bone are equally important as the intrinsic properties of the implanted materials, the structural characteristics of the implant design, and the external loading modes which the implant construct is subjected to (An and Draughn, 2000).

2.4.2 State of the Art TKR

There are currently various designs of total knee replacement prostheses available, each offering certain advantages and disadvantages. Generally, TKRs consist of a metal femoral component, mainly cobalt chromium alloys, articulating on an ultra high molecular weight polyethylene (UHMWPE) tibial component. The tibial component is often modular with a metal tray backing, which has a mobile or fixed bearing insert. Certain design forms of TKRs retain the posterior cruciate ligament (see Figure 1.2), whereas others substitute it and often the patella is also resurfaced with a UHMWPE component (Bellemans et al., 2005; Lee and Goodman, 2008; Mow and Huiskes, 2005).

Different TKR designs are designed with different constraints and laxity. The constraint of a TKR is the resistance to a particular degree of freedom in knee movement, such as internal-external rotation. Laxity is the resultant displacement and rotations possible when forces are applied; hence laxity is the opposite of constraint (Walker and Sathasivam, 2000). A mobile bearing TKR has the potential to reduce the constraint of the system, whilst achieving higher conformity and larger contact areas in comparison with fixed bearing TKRs. However, studies have shown that increased wear and instability may result (Bellemans et al., 2005; Huang et al., 2008).

Fixation of TKRs can be achieved using acrylic bone cement (see section 2.2), a cementless design or a hybrid fixation method, in which the femoral component is cemented and the tibial component is uncemented. In cemented TKR, both the tibial and femoral components are cemented and in cementless TKR, a tight interference between the prosthesis and the surrounding bone is used to achieve the initial component stability. A coating on the internal surface exposed to bone, such as hydroxyapatite (HA), encourages ossointegration (bone ingrowth) over time, supplementing the press-fit fixation (Burgers et al., 2008). In addition to these 3 methods, other design features such as stems, pegs, screws and textured internal surface finishes (achieved through shot-blasting, for example), are incorporated into TKR prostheses to promote implant fixation.

Cemented implants allow more variability of prosthesis positioning, offer good initial stability and can be used in patients with weaker supporting bone. Cementless fixation aims to preserve bone stock and avoids the complications that may arise from using bone cement. However, the revision rate of uncemented TKRs is greater than that of cemented designs at 7 years, as shown in Figure 1.4 in section 1.1, and it is now understood that aseptic loosening results mainly from UHMWPE wear debris and stress shielding, rather than cement particles (Beckmann et al., 2011; van Lenthe et al., 1997). It is likely that patient selection and the surgeon play key roles in the success of the implant, as another study over 14 years found no significant difference between the survival rate of cemented and cementless TKRs and concluded that there was no advantage for either fixation type (Park and Kim, 2011).

2.4.3 Biomechanical Environment of the Knee Joint

The mechanical scenario *in vivo* must be considered when designing and testing a new total knee replacement prosthesis. Figure 2.14 shows the reference directions for the knee joint as described by Goodfellow and O'Connor (1978). The knee joint consists of the distal femur, (the end furthest from the torso, which forms the upper part of the joint), the patella (kneecap) and proximal tibia bone (the end nearest to the torso, which forms the lower part of the joint) (see Figure 1.2 in section 1.1). During gait, the articular bone at the distal femur and the proximal tibia will predominantly be loaded in compression and also experience shear forces as the joint contact areas roll, slide and rotate over one another. The ligaments and muscles (soft tissues) bear the tensile forces (Darwish and Al-Samhan, 2008; Goodfellow and O'Connor, 1978).

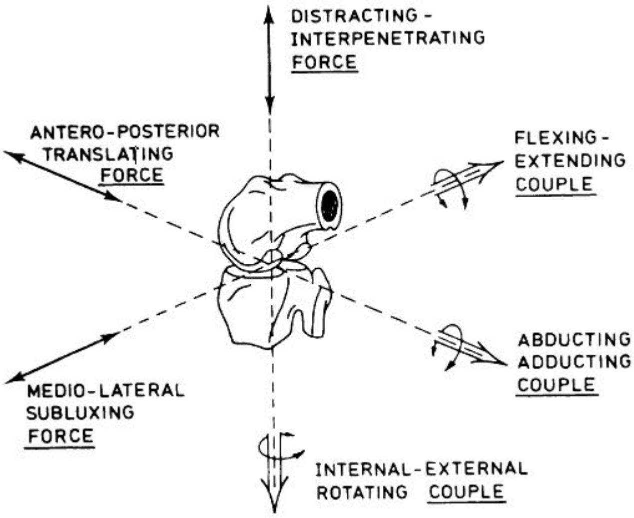

Figure 2.12: Reference directions and forces at the knee joint (Goodfellow and O'Connor, 1978)

The forces in the natural knee joint have been estimated by using multiple camera motion capture systems, EMG and force plates, to measure ground reaction forces of subjects during gait and other activities, before using computer modelling to calculate joint contact and muscle forces (Hurwitz et al., 1998; Shelburne et al., 2006; Taylor et al., 2004; Winby et al., 2009). Winby et al. (2009) calculated an average peak tibia-femoral (TF) force of 3.9 times body-weight (BW) from 11 subjects in the first half of the gait cycle (near contralateral toe-off) of which the external load contributed 42% (average, range 26-55%) and the muscles contributed the remainder. Shelburne et al. (2006) reported a maximum TF force of 2.7 BW occurring at contralateral toe-off, estimated from a human model (178 cm, 71 kg) averaged from measurements from 5 males. Medial compartment loading was found to be predominantly governed by the direction of ground reaction force and lateral compartment loading due to muscles and ligaments. However, they used modelling alone to calculate the loads at the knee joint, so the values reported are considered more of an estimation than those by Winby et al. (2009), who used motion capture, EMG and force plates to make measurements prior to modelling. In a study of four THR patients with intact knee joints, Taylor et al. (2004) reported that high TF contact and shear forces were generated during weight bearing at knee flexion angles greater than approximately 15 degrees during gait and stair climbing. The average resultant peak force during stair climbing and walking was 5.4 BW and 3.1 BW respectively, as calculated from a muscoskeletal model following clinical gait analysis that used two force platforms and six infrared cameras to measure ground reaction forces and motion respectively. Kuster et al. (1997) studied the kinematics and TF forces of 12 subjects (49 - 90 kg, average 70.8 kg) and reported peak loads of 3.4 and 3.9 BW during level gait for male and female subjects respectively, at a flexion angle of 20 degrees. However, when the flexion angle increased during downhill walking, the TF load increased to 7 and 8 BW for male and female subjects respectively. Hence in activities other than normal gait, the TF forces can be much higher in the normal knee. However, this is before the kinematics are altered by introducing a TKR (Alice et al., 2015; Bull et al., 2008).

Whilst the same techniques as used in the study of natural knee joint can be used to evaluate tibiofemoral forces with total knee replacement, studies have used instrumented telemetric knee implants to directly measure axial forces and moments. Taylor et al. (1998) presented a study of one patient (69 kg) with telemetric knee implant using a rotating knee hinge, which resected the cruciate ligaments. Peak forces averaging 2.26 BW were measured during gait with a peak axial torque of 8 Nm at the internal rotation of tibia. The highest forces at the knee joint were experienced in descending stairs (2.8 BW), then ascending stairs (2.5 BW), and the lowest forces were experienced in level walking. *In vivo* peak TF forces of 2.9 to 3.4 BW were recorded from telemetric knee implants in 2 patients (100 kg and 92 kg) by Trepczynski et al. (2012), with little variation between patient data with activity type (shown in Figure 2.15). However, the calculated patello-femoral (PF) joint contact forces were much more variable, from 1 BW during walking up to 3 BW during high flexion activities. As a result, it was suggested that the TF and PF joint contact forces must be considered together in order to fully understand the *in vivo* loading conditions at the knee joint. Zhao et al. (2007) also measured TF forces using a telemetric implant in a single patient (68 kg). A maximum load of 2.2 BW was measured during gait, which raised to 3.5 BW during a step down.

More recently, DeMers et al. (2014) used a telemetric implant and modelling to evaluate variation in muscle activity and TF forces with a single patient (64 kg). This study demonstrated the sensitivity of the compressive TF forces to activation of muscles during patient activity, although the model did not allow for internal-external rotation and abduction-adduction, so there may have been errors in force predictions for each muscle. DeMers et al. (2014) predicted that introducing these degrees of freedom would increase muscle activation and TF forces. Another study using a telemetric TKR has shown that adaption of gait kinematics can reduce TF forces (Fregly et al., 2009).

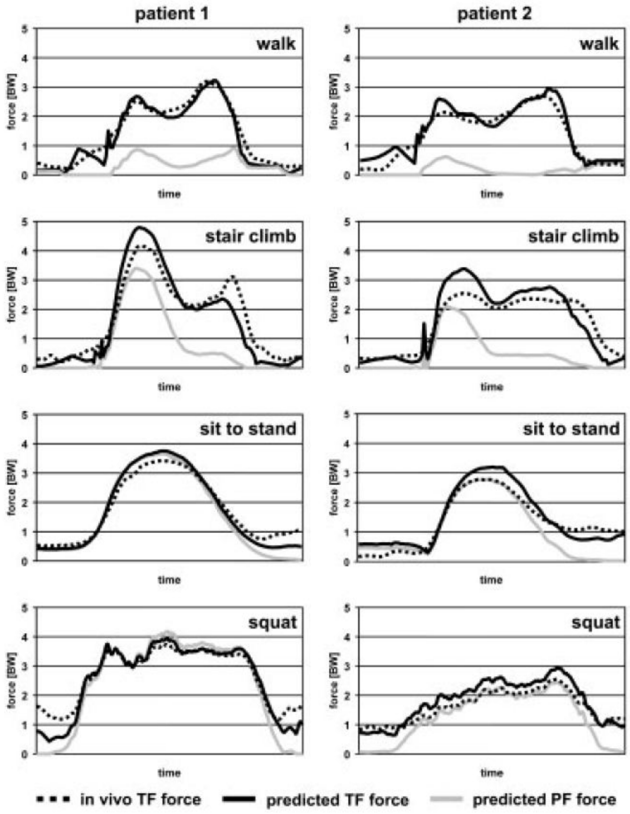

Figure 2.13: Tibio-Femoral (TF) joint contact forces recorded during different patient activities in a study by Trepczynski et al. (2012) (patient 1: 64 years, 100 kg, 19 months post-operative; patient 2: 78 years, 92 kg, 8 months post-operative)

The current international test standard for TKRs (wear testing), which follows a gait cycle load pattern replicated from gait analysis studies, specifies a maximum load of around 3.7 BW (70.8 kg european average), 2600 N, occurring at heel strike (BS ISO 14243-1, 2009; Walpole et al., 2012). However, a more recent study by Bergmann et al. (2014a) has shown that test standard BS ISO 14243-1 (2009) for wear of TKR may be out of date. Using telemetric implants in 8 subjects, Bergmann et al. (2014a) reported that the peak load in gait occurs at contralateral heel-strike, rather than in contralateral toe-off off as in BS ISO 14243-1 (2009). Data was grouped by patients with an average BW of 75 kg and a high BW of 100 kg (all data is available on the Orthoload website (Bergmann et al., 2014b)). Figure 2.16 shows a comparison of the load components and knee flexion for patients in the 100 kg group with those in BS ISO 14243-1 (2009).

It should also be considered that during deep flexion of the knee (flexion angles >90°) the posterior load component increases significantly. In a study of the normal knee in deep flexion, Nagura et al. (2002) reported that the net posterior force increases by two thirds in single and double leg descents and raises (0.62 BW average) compared to

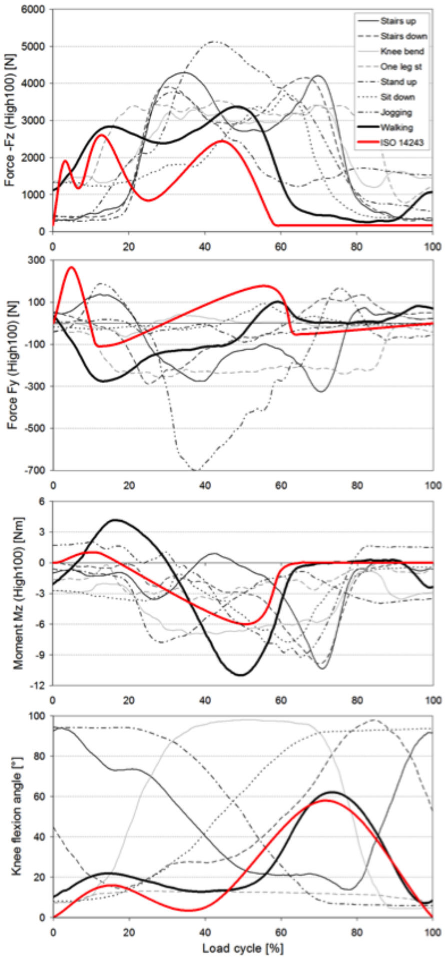

Figure 2.14: Load components and knee flexion angle for different activities measured by Bergmann et al. (2014a), compared with wear test standard ISO 14243, for subjects with a weight of 100kg (HIGH100)

gait (0.39 BW), as the inferior forces decrease (0.71 BW average compared to 1.12 BW during gait). High posterior forces during deep flexion could compromise the posterior region of fixation or the structural integrity of the implant itself (Zelle et al., 2011b). Thambyah and Fernandez (2014) and Zelle et al. (2011b) modelled deep flexion squatting with TKR and reported high tensile stress in the anterior flange of a CoCr femoral component, which could compromise fixation. However, a more compliant PEEK component has the potential to reduce anterior flange stresses, as shown in a study by Ruiter et al. (2014) which followed the loads of BS ISO 14243-1 (2009), although higher posterior cement stresses were predicted. Therefore it can be speculated that in deep flexion, a PEEK component may be more susceptible to high stress in the posterior region, however, this would require investigation. Deep flexion and squatting related activity is common in Asia cultures, which increases the demand for high flexion components that allow the range of motion required (Murphy et al., 2009; Narayan et al., 2009).

A significant limitation in the design process for TKR is that forces are not known for certain and will vary from patient to patient. Each of the studies in the literature that have presented telemetric data were for specific designs of TKR, which are usually posteriorly stabilised (the cruciate ligaments have been resected). Therefore the implant takes all of the load rather than sharing with the ligaments. If prostheses of different designs are implanted such as posterior cruciate retaining or rotating platforms (mobile bearing), unknown portions of the load components presented in studies such as those by Bergmann et al. (2014a) and DeMers et al. (2014) could be taken up by the ligaments rather than the implant alone (Seon et al., 2011). However, Seon et al. (2011) reported that posterior stabilised designs have more favourable kinematics compared to cruciate retaining implants. Lower forces measured in the study by Taylor et al. (1998), may be attributed to the hinge design of the TKR.

The contact area of the bearing surfaces of TKRs, determined by the radii of curvature of the surfaces, and the implant size (relative to BW) affect the contact stresses experienced by the prosthesis during day-to-day activities, as shown in a review by Walker and Sathasivam (2000). The construct must be able to endure the highest forces generated at the knee joint in order to survive *in vivo* and prevent failure of trabecular bone from excessive varus-valgus moments. The shear forces and torques act across the implant-bone interface and can affect fixation, potentially leading to crack propagation (Walker and Sathasivam, 2000).

As described by An and Draughn (2000), there are three modes of loading that a crack can experience, shown in Figure 2.17. Mode I describes a crack which is subjected to a principal load applied normal to the crack plane causing the crack to open (opening mode). A mode II crack is subjected to a loading force parallel to the crack propagation direction, causing one crack face to slide against the other, known as in-plane shear mode. In mode III loading, the crack is subjected to a load normal to the crack propagation direction (out-of-plane shear), causing it to twist and tear.

A crack within a material or at an interface between two materials can be loaded by a combination of these modes (known as mixed-mode loading). After consideration of the forces experienced at the knee joint, it can be deduced that the TKR implant-cement-bone construct will be subject to mixed mode loading *in vivo*, so this must be considered when determining the interfacial properties. In any case, a crack will tend to propagate along the path of least resistance (Anderson, 2005). In an implant-bone construct this commonly occurs at the interfaces (An and Draughn, 2000; Hung and Chang, 2010; Pittman et al., 2006; Scheerlinck et al., 2008; Zelle et al., 2011a; Zhang et al., 2008).

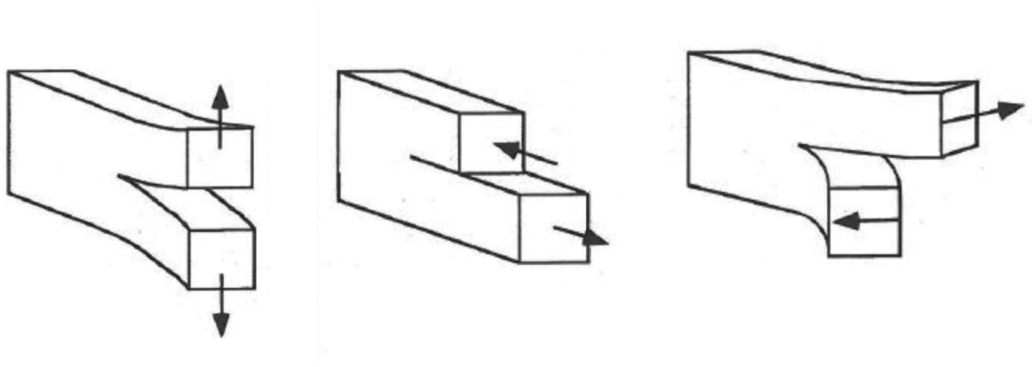

(a) Mode I (b) Mode II (c) Mode III

Figure 2.15: Three loading modes that a crack can experience: (a) mode I, opening mode (tension); (b) mode II, in-plane shear mode; and (c) mode III, out-of-plane shear (tear) mode (modified from Anderson (2005))

2.4.4 Implant-Cement Interface

The behaviour at the interfaces between the implant, cement and bone plays a key role in the success of total knee replacement and these interfaces have been considered the 'weak-link zones' in the construct (An and Draughn, 2000; Lewis, 1997).

The surface roughness between the implant and the cement may determine the interfacial strength alone if adhesive chemical bonding is not present between the implant and the cement, as it affects the degree of mechanical keying between the materials (see section 2.5). The material and surface finish of a femoral stem in a total hip replacement can greatly affect the timing and degree of debonding at the stem-cement interface (Ramaniraka et al., 2000). Prostheses with a smooth polished surface may then be expected to debond more readily than those with a rough surface, although greater microcrack activity has been recorded with rough surfaces (Qi et al., 2007).

In a study by Zelle et al. (2011a), the greatest shear and tensile interface strength between steel and bone cement was achieved with the greatest surface roughness investigated ($R_a = 2.76\ \mu m$). This confirmed findings in studies by Zhang et al. (2008) and Pittman et al. (2006). However, Pittman et al. (2006) also reported that the rotational loading experienced by a 'macro-surfaced', (waffle patterned macro-texture), tibial TKR component may leave it vulnerable to interfacial failure. For the femoral component, this may be dependent on the rotational alignment, which affects interface loads and ligament balance (Victor, 2009). In addition, poor cementing of the posterior condyles, which is common due to the surgical technique of TKR, could accelerate the loosening of the femoral component (King and Scott, 1985; LaButti et al., 2003). In any case, failure of a rough interface could cause increased wear and lead to revision surgery (Verdonschot and Huiskes, 1998).

Another factor affecting the interfacial strength and durability of the construct is potential interfacial defects between the implant and the cement mantle. Interfacial defects have been experienced with femoral stems in total hip replacement, possibly caused by (a) porosity in the cement accumulating at the implant surface, (b) micromovement of the implant during implantation (during curing or mechanical loading), (c) thermal expansion of voids with vaporised monomers during cement polymerisation or (d) cement shrinkage (Orr et al., 2003; Scheerlinck et al., 2008). An interfacial defect could propagate as an interfacial crack, causing interfacial failure.

The degree of interdigitation between the cement and the bone affects the strength of the cement-bone interface, and hence, the overall strength of the implant construct. The cement-bone interface transfers applied loads and may experience strain softening, the ability to support substantial decreasing loads post-yielding with increasing interface displacement (Mann et al., 1997). In addition, the mechanical strength of the cement-bone interface has been found to be greater in shear than in tension, with the same post-yield softening response (Mann et al., 1999). The orientation of the architecture of the trabeculae in the distal femur differs between the superior region and the inferior region, giving relationships between bone mineral apparent density and properties such as differences in modulus of elasticity and stress values (Burgers et al., 2008). This must be taken into consideration when designing and testing the fixation of a femoral component, particularly for press-fit scenarios. Funk and Litsky (1998) evaluated the interfacial shear strength between bone and cement and concluded that the stiffer material determined the shear behaviour at the interface. This may be significant for comparative strengths between polymer and metal implant materials.

2.5 Adhesion

To further consider the efficacy of the fixation of the TKR construct, one must consider the factors governing the adhesive strength of the interfaces. As described by Marshall et al. (2010), interfacial adhesion is achieved through the interaction between two materials at a molecular scale; cohesion involves two similar materials and adhesion involves two dissimilar materials, as in the case of the implant-cement interface of the TKR construct. The three main types of adhesion occur as a result of:

- **Chemical bonding**: mainly covalent, ionic or metallic bonding between two substrates (primary bonding)

- **Physical bonding**: van der waals forces, polar forces, dipole-dipole interactions and hydrogen bonding between two substrates (secondary bonding)
- **Mechanical interlock**: meshing together of two surfaces with interface roughness providing anchorage

A bimaterial construct can either fail in an adhesive manner, along the interface between the two materials, or cohesively, through the material substrate (Marshall et al., 2010). The strength of adhesion achieved between PEEK and PMMA bone cement may be limited by the type of contact between the two materials.

PMMA bone cement is described in the literature as a grout rather than an adhesive, transferring the load from the implant to the surrounding bone (Lewis, 1997; Webb and Spencer, 2007). However, the interaction between the PEEK and the cement is still an act of adhesion. In any case, the fracture at the mechanical interlock line between these two dissimilar materials may be treated as adhesive fracture from both a continuum mechanics viewpoint, as well as from an energy concept in a fracture mechanics approach, relative to the phase angle of loading (Bennett et al., 1974; Brown, 2006; Lane, 2003). Hence for this thesis, PEEK is considered the adherend substrate and the PMMA bone cement is considered the adhesive. The following sections cover the factors governing the adhesive strength of the implant-cement interface, with the aim to outline the factors capable of enhancing the fixation strength of the PEEK with cement.

2.5.1 Surface Energy

The excess energy associated with the presence of a surface determines the contact between the two surfaces (Packham, 2003). This is known as the surface energy per unit area in Gibbs (G^S), which contributes towards the formation of adhesive bonds. The surface tension, γ, is also referred to as the surface energy as it is often not possible to measure the free energy of the surface.

The energy balance at the solid material interface can be determined from the surface energies using Young's equation, (2.1), the components of which are illustrated in Figure 2.18 (Kinloch, 1980). Here, θ is the contact angle, γ_{sl} is the solid/liquid interfacial free energy, γ_{sv} is the solid surface free energy and γ_{lv} is the liquid surface free energy.

$$\gamma_{sv} = \gamma_{sl} + \gamma_{lv} cos\theta \tag{2.1}$$

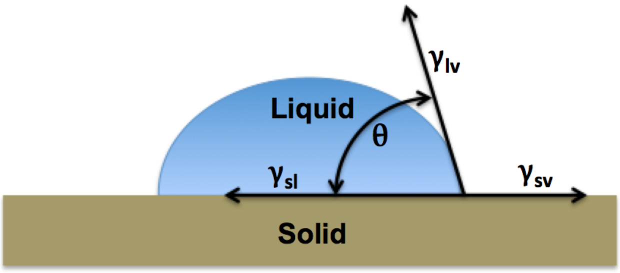

Figure 2.16: Components of surface energy calculation using Young's equation

The contact angle between the adhesive as a liquid and the solid adherend can be measured to determine the wettability of the surface, which determines the degree of adhesion that can be achieved. A high contact angle ($> 90°$) indicates a low surface energy with poor wettability, consistent with hydrophobic surfaces. A low contact angle will be achieved when the surface has enough energy to compete with the cohesive forces in the liquid, giving a better spread across the surface, as in the case of hydrophilic surfaces. The wettability of a surface is often evaluated by measuring the contact angle of liquid (usually water) to the surface (Marshall et al., 2010; Packham, 2003).

The surface energies are associated with the failure of an interface in the work of adhesion, W_{ab}, between two surfaces, a and b (equation 2.2), which involves forming new surfaces with respective appropriate surface energies (Watts et al., 2005). The materials in contact must interact to reduce the total energy of the system, forming the interface through adhesion. If there is not a net reduction in energy, the materials will reduce the interaction contact area; this can be likened to water beading on a hydrophobic surface as a result of the surface tension (Marshall et al., 2010).

$$W_{ab} = \gamma_a + \gamma_b - \gamma_{ab} \tag{2.2}$$

Chemical and physical bonding to surfaces hydrophobic in nature with relatively low surface energy (high contact angles), such as PEEK, may be unlikely (Comyn et al., 1996). Consequently, to maximise the adhesion, it may be necessary to alter the surface topography of the adherend substrate (PEEK).

2.5.2 Surface Topography

Interfacial roughness can improve adhesion by facilitating mechanical bonding through keying of the two surfaces at the macro, micro and nano length scales. By increasing the surface area, adhesion strength is improved as long as the roughness does not impair the contact. The loading mode controls the mechanical interlock effect as the stress distribution generated at the interface controls the deformation and failure characteristics (Kim et al., 2010). Roughness can increase the surface energy and wettability of a surface but this relies upon the adhesive being able to penetrate pores or features in the topography of the surface (Packham, 2003).

On a nano scale, polymeric chain entanglement can occur causing nano-interdigitation, which is reported to be common in dental acrylic bone cements. The liquid monomer diffuses into the polymer adherend surface and polymerises. With immiscible polymers, chemical bonding does not occur but the resulting entanglement of polymer chains is enough to enhance the adhesion strength noticeably (Marshall et al., 2010). A rough surface greatly increases the 'true' surface area and energy available for adhesion. Surface roughness on the nanometre to micron length scales may strengthen an interface with increased fracture energy by allowing bulk energy dissipating processes to be activated when the bond is stressed. These processes may include energy involved in chain pull out or scission, and bulk plastic and elastic deformations (Packham, 2002).

Prolongo et al. (2006) used a lap shear test setup to evaluate the effect of substrate roughness at the micro length scale on adhesive joint strength. They concluded that the optimal surface roughness depends on the penetration ability of the adhesive material; the joint strength then depends on density and depth of protuberances on the substrate surface. In addition, Janarthanan et al. (1997) reported that adhesion could be enhanced in an immiscible polymer bilayer by using orientated macroscopic roughness to introduce stick-slip friction at the crack front. This was shown to increase the fracture toughness of the interface, with small pitch and deep grooves creating the highest density of barriers to the crack front. Li et al. (2012) carried out a computational study of a two-order hierarchical sinusoidal interface, which was found to enhance the fracture toughness compared to a flat or pure sinusoidal interface. As a result of the hierarchical structure, the stress distribution at the interface was altered and the wavy crack was subjected to normal resistant forces as well as tangential forces. Another study by Kim et al. (2010) used micro patterns to enhance adhesion strength of polymer-metal interfaces; they concluded that to increase the adhesion strength, the failure mode must be moved from adhesive to cohesive. Undercuts in the surface geometry can provide the ideal mechanical keying, but these can be difficult to manufacture, especially through injection moulding processes.

As discussed in section 2.4.1, studies of the implant-cement interface strength have found that increased surface roughness has the greatest influence on mating strength, but this must be approached with caution as a debonded rough interface can lead to interfacial wear and generation of third body wear particles (Pittman et al., 2006; Qi et al., 2007; Verdonschot et al., 1998; Wang et al., 2003; Zelle et al., 2011a).

Surface topography may also be altered to improve the adhesive properties by changing the surface chemistry. This is discussed in the following section for application to PEEK.

2.5.3 Surface Activation of PEEK

Surface activation of PEEK substrates may be achieved through chemical or physical treatments to enhance the adhesive properties. Both chemical etching and oxygen plasma treatment have been shown to cause the PEEK surface topography to become irregular with higher roughness due to its spherulitic structure, enhancing the adhesive bond strength through mechanical methods (Ha et al., 1997). The wetting angle of PEEK is also lowered and the polarity of the surface is increased by addition of oxygen molecules to the surface (increasing the surface energy); this enhances the adhesive bond strength by facilitating chemical and physical bonding (Bhatnagar et al., 2012).

Chemical etching is a wet treatment whereby a suitable acid is applied to the PEEK, which randomly erodes the surface resulting in a porous structure. Schmidlin et al. (2010) showed that bonding strength of a dental resin cement to PEEK was greatest when the surface was chemically pre-treated with sulphuric acid compared with an air-abraided pre-treatment. No adherence could be achieved on polished PEEK. On the other hand, Stawarczyk et al. (2013) showed that a greater bond strength to veneering resin was achieved with an air-abrasion pre-treatment compared to acid etching using the same treatment parameters. This shows the specificity of each surface treatment to each material application.

Plasma treatment is a physical method where a plasma is produced by separating electrons from the molecules in a gas state, usually through ionisation. The free electrons gain energy from an imposed electric field and collide with neutral gas molecules, transferring energy to form free radicals and ions. These interact with the surface of the solid substrate placed in the plasma allowing surface modification to take place (Kaplan and Rose, 1991; Liston et al., 1993). In the case of plasma treatment of PEEK, oxygen gas and a radio frequency glow discharge plasma source may be used to form additional polar chemical groups on the surface, such as —COOH, making autohesive bonding of PEEK possible (Awaja et al., 2010). A greater surface oxygen to carbon ratio has been observed with oxygen plasma treatment of PEEK compared to chemical etching, but carbon-oxygen functional groups are formed with both treatments (Comyn et al., 1996; Ha et al., 1997). Atmospheric pressure plasma treatment was shown to be more effective than low-pressure plasma treatment by Iqbal et al. (2010) when trying to improve the bond strength of PEEK to an epoxy adhesive. This was linked to the increase in surface roughness achieved with the atmospheric pressure technique. However, this could suggest that there was greater damage to the surface by ion bombardment, which can result in breakage of C=O bonds and opening of benzene rings (Liston et al., 1993). Iqbal et al. (2010) also highlighted the importance of material stiffness and fracture toughness in the strength of an adhesive bonded joint, concluding that PEEK has low toughness and stiffness compared to fibre reinforced polymers, so stress concentrations at bonded interfaces may result in failure.

Comyn et al. (1996) noted that a reduction of around 14% in peel strength resulted after ageing the plasma-treated PEEK surface for 90 days when investigating the use of plasma treatment for enhancement of the adhesive bonding of PEEK films. The degraded plasma-treated PEEK surface was still stronger than the untreated PEEK surface, but this result demonstrates the shelf-life of the plasma-treated surfaces. Cognard (2006) described the same duration as long term efficiency. The efficacy of plasma treatment is therefore very application dependent.

2.6 Evaluation of TKR Construct Properties

Static testing techniques may indicate the effect of different femoral component backing surface finishes on the performance of the implant-cement interface and hence be used to optimise the design of the component for fixation *in vivo*. The overall implant design influences the periprosthetic bone response (section 2.3.3), as well as the interfacial strain at full construct level. Bone's mechanostat suggests threshold strain values for bone modelling, remodelling and damage responses within the tissue structure (Frost, 2003). Hence, methods for the evaluation of strain within the construct can allude to the risk of stress shielding and bone loss. In this section, different techniques used for strength and strain assessment in studies in the literature are discussed for characterisation of the implant-cement interface and TKR construct respectively.

2.6.1 Interfacial Strength

Since the TKR implant construct is mainly subject to compressive and shear forces *in vivo*, it is beneficial to measure the shear strength of the interface between the construct materials, rather than the tensile strength alone. However, standards for testing the interfacial strength between the implant, cement and bone have not been established to date. Coupon level tests, representative of an area of the full specimen, can be carried out to give an estimation of a unit measurement for a specific material property. This can then be used to advise the full scale design prior to full construct tests which come at greater cost, specimen complexity and test resources, as commonly used in the building block test approach in the aerospace industry (Grant and Rousseau, 2001).

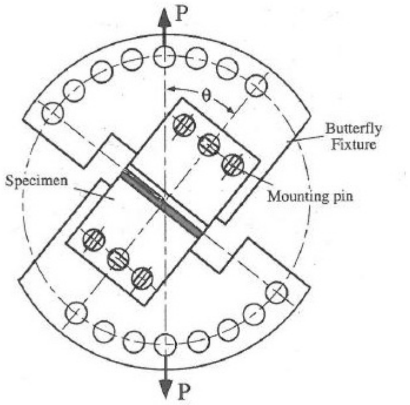

Figure 2.17: Butterfly loading setup for mixed mode testing(An and Draughn, 2000)

In the literature, Zelle et al. (2011a) used a mixed mode test setup (butterfly jig, Figure 2.19) for carrying out tensile and shear tests on stainless steel-cement samples to determine the interfacial strength with varied surface roughness. Although it was established that the lowest interface strength resulted under a combination of tensile and shear loading (30° loading angle), it was noted that the measurement in the test setup was not sensitive enough for surfaces with lower roughness, leading to large standard deviations. The weight of the jig would add a considerable pre-stress to the interface before the application of test loading. This must be accounted for, especially for interfaces with increased compliance. Zelle et al. (2011a) concluded that smaller scale interface experiments could be more appropriate to characterise samples with low surface roughness.

Pittman et al. (2006) used rod samples to carry out tensile and torsional interface strength tests with varying surface finish Ti-6Al-4V and CoCrMo cemented samples. Mann et al. (1999) also used rod samples to carry out tensile strength tests between bone-cement samples. In the same study, short beam samples were used to measure the interfacial shear strength. Pull- and push-out tests were used by Zhang et al. (2008) and Walsh et al. (2004), respectively, to evaluate the interfacial shear strength with application to femoral hip stems of varying surface roughness. Hung and Chang (2010) used a lap shear test setup and rectangular beam shaped tensile samples to test the bone-cement interface strength. An alternative shear strength test method with Iosipescu specimens was used by Funk and Litsky (1998) to determine the interfacial strength between bone and cement with pure shear loading. With a bone implant interface, it was possible to cut a notch at the interface between the two materials to manufacture the Iosipescu shape. This could be more problematic with evaluation of the implant-cement interface.

Figure 2.18: Lap shear test specimen

The lap shear test is a simple method of measuring the shear strength between two materials with a known area of overlap; it is the most commonly used adhesive test in mechanical testing of adhesive joints with ease of manufacture and test setup. The cross section of the lap shear specimen is shown in Figure 2.20. A tensile load, P, is applied at the ends of the two material components parallel to the material overlap, generating a shear force at their interface, provided that the specimen is perfectly aligned with the applied loading direction. However, a non-uniform stress distribution exists at the interface with shear stresses increasing towards the ends of the overlap; in addition, if bending deformation occurs along the length of the sample, tensile stresses may be induced (Devries and Adams, 2002).

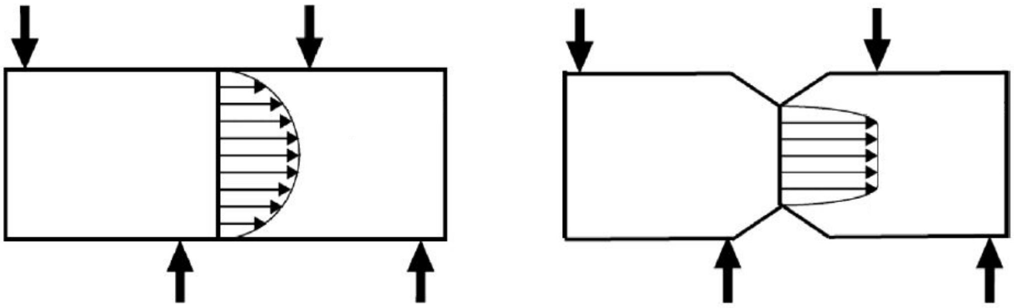

(a) Parabolic shear stress distribution with short-beam specimen

(b) Uniform shear stress distribution with Iosipescu specimen

Figure 2.19: Cross section of a short-beam shear specimen and Iosipescu specimen with corresponding interfacial shear stress distributions and locations of support (external large arrows) (modified from Krishnan and Xu (2011)

The short beam shear test is a similar method of measuring the shear strength of the interface, by subjecting it to a pure shear force. However, with both of these methods, alignment is critical and edge stress intensities are generated leaving a non-uniform stress distribution (Bennett et al., 1974). On the other hand, the Iosipescu shear test set-up minimises stress intensities and a near constant shear stress variation is experienced at the material interface. The Iosipescu specimens have a notch feature at the interface between the two materials, providing a uniform shear stress field when the specimen is loaded. A compressive force is applied to one half of the specimen, whilst the other half is supported rigidly, inducing a shear stress at the interface. The short beam shear specimen and the Iosipescu test specimen are shown in Figure 2.21a and 2.21b respectively, with the corresponding shear stress distributions (Krishnan and Xu, 2011).

In each case the interfacial shear strength is calculated from the applied load at failure, P, and the area of the interface, as shown in equation 3.1 (Callister, 1997).

$$\text{Interfacial Shear Strength (MPa)} = \frac{\text{Failure Load (N)}}{\text{Interfacial Area (mm}^2\text{)}} \tag{2.3}$$

In order to test the shear strength of the interface between two dissimilar materials, in this case the PEEK implant and PMMA bone cement, lap shear tests, short beam shear tests and Iosipescu shear tests are three possible methods which have been identified from the literature (Bennett et al., 1974; Funk and Litsky, 1998; Hung and Chang, 2010; Mann et al., 1999; Walrath and Adams, 1983). For tensile interface strength, simple rod interface samples would be appropriate (Mann et al., 1999; Pittman et al., 2006).

Interfacial tensile and shear test methods yield the nominal measure of strength of the interface, but not the fracture resistance. In order to estimate the resistive fracture properties of the interface in terms of energy or stress intensity required to propagate an interfacial crack, a linear elastic fracture mechanics approach can be adopted, assuming linear elasticity and isotropy. The critical stress intensity factor, K_c, (the magnitude of stress at the crack tip when it starts to propagate) and the critical energy release rate, G_c, (the driving force for crack propagation) for each crack loading mode (Figure 2.17) can be determined to define the interfacial fracture toughness between two dissimilar materials (An and Draughn, 2000). Although the interfacial fracture toughness is an important consideration for the performance of the TKR interface, it is outside the remit of this thesis so shall not be discussed further.

2.6.2 Contact Strain Measurement Techniques

2.6.2.1 Strain Gauges

Traditionally, strain measurement has been carried out on a wide variety of materials using electrical resistance strain gauges, making this one of the most established techniques for bone strain evaluation, with hundreds of studies in the literature (An and Draughn, 2000). By bonding the gauge directly to the surface, strain can be measured in a single direction with a uniaxial strain gauge and the direction and magnitude of principal strains can be monitored with a triaxial or strain gauge rosette

(Cristofolini and Viceconti, 1997). However, the accuracy of the strain measurement depends on the quality of the bonding of the gauge to the specimen, as the specimen must transmit surface strain in to the strain gauge (An and Draughn, 2000). Electrical strain gauges work by altering their electrical resistance as the foil grid deforms, allowing the strain at the surface to be calculated by dividing the change in resistance by the initial strain gauge resistance and the gauge factor (specified for each grid material) (Mordan, 2009). In the field of TKR, Completo et al. (2008) used strain gauges to evaluate the stress shielding effect of different revision TKRs on distal femoral bone strain. They showed that whilst the use of long-stemmed implants may increase initial stability, reductions in bone strain may result, which could contribute to bone loss. Although this is a low cost, accurate, well established technology for measuring strain, it is limited to average point measurements so it does not allow full field strain measurement across the entire specimen's surface (An and Draughn, 2000; Mordan, 2009). Local reinforcement affects may also arise from the stiffness of strain gauges when used on lower modulus materials (Ajovalasit et al., 2007).

Strain may also be calculated from displacement measurements obtained using extensometers (including clip-on electro-mechanical devices, dial gauges and linear variable differential transducers (LVDTs)) (An and Draughn, 2000). Whilst extensometers are very useful for interfacial displacement measurements and evaluation of prosthesis micromotions (Britton et al., 2004; Claes et al., 2000), the strain calculation is made over a gauge length of constant cross-sectional area, which limits its application for whole bone strain evaluation in the TKR construct (Morgan and Keaveny, 2001). They are also sensitive to temperature change, vibration and contact friction within the system, which can lead to measurement errors (Britton et al., 2004). Optical (video) extensometers offer a non-contact displacement measurement technique which eliminates error from slip at the contact and allows changes in gauge length and diameter to be assessed, however an average strain is still calculated for each gauge length (Kurtz et al., 1998).

2.6.2.2 Fibre Bragg Grating Sensors

Fibre Bragg gratings (FBG) are applied to glass fibres to make fibre optic strain sensors. A FBG is a fringe pattern applied to a short section of a glass fibre using UV radiation, which periodically varies the refractive index (Kang et al., 2007). A broad-band light source of a known wavelength transmitted down the fibre will experience shifts in wavelength as it passes through the FBG as a result of any axial deformations from strain or temperature changes in the surrounding material to which it is bonded. By interrogating the resulting signal (the Bragg wavelength) relative to a control FBGs (experiencing no strain or temperature changes) it is possible to measure strain and temperature effects within a material in real-time, provided that the fibre is fully bonded to the material (Iodice et al., 2005). FBGs have a wide bandwidth, a dynamic response and are very small with a diameter of 125 μm (Smart Fibres Ltd). This makes it possible to use FBGs for strain measurement at small regions of interest, which is not possible with traditional strain gauges and extensometers.

FBGs are increasingly used for dynamic measurements in bioengineering applications due to their size, sensitivity, chemical inertness and immunity to electromagnetic interference. They enable measurement of strain within a body (not just surface strain), contact pressure, temperature change and displacement measurements, depending on test setup (Al-Fakir et al., 2012; Chuang and Ma, 2008; Kang et al., 2007; Ren et al., 2007). Relating to orthopaedic biomechanics, Talaia et al. (2007) assessed bone-plate strains in femurs during fracture fixation, which is not feasible using strain gauges. At the implant-cement interface, a study by Ramos et al. (2012) used FBG sensors to measure strain and temperature in the cement mantle around a Total Hip Replacement (THR) stem as it polymerised and validate a finite element model, achieving good agreement between their experimental and numerical results. With an uncemented prosthesis, Reikeras et al. (2011) measured the strain at the THR stem implant-bone interface using FBGs and compared this to external strain gauge measurements on the cortical bone surface to evaluate measurement patterns for implant loosening. The mismatch in their results brought them to the conclusion that stem loosening could not be evaluated from external cortex strains alone, and that internal interface strains should also be measured in future studies. Direct application of FBGs to the articular joint was investigated by Dennison et al. (2010) who reported a method for using an FBG sensor for simultaneous contact force and fluid pressure measurement in intact cadaveric hip joints, showing that FBG sensors can be implanted without dissection or disarticulation of the joint. During TKR, Mohanty et al. (2007) mapped the pressure using an FBG instrumented tibial spacer for malalignment detection and evaluation of distribution of contact stress in flexion and extension during surgery.

Regarding the TKR fixation interface, FBG assessment of dynamic interfacial strain has not been reported in the literature to the author's knowledge. Whilst FBG sensors show great potential in the literature for strain assessment within the TKR construct, this would require a large investment in an FBG interrogator system, software and additional training which was not feasible for this project. Therefore, this thesis shall concentrate on the use of non-contact strain assessment tools for full-field evaluation of strain.

2.6.3 Non-Contact Strain Measurement Techniques

Non-contact techniques offer a method of full field surface strain measurement. A brief summary of these techniques follows in the context of application for bone strain measurement.

- **Moiré interferometry**: A technique which measures surface strain by the interference effect between a specimen diffraction grating and a reference diffraction grating as the test surface deforms. The diffraction grating is difficult to apply to a 3D surface, therefore the technique is mostly used on flat surfaces, limiting its application to bone (Gungor, 2009).
- **Photoelastic stress analysis**: A partially non-contact, optical strain measurement technique which requires an expensive, thin epoxy coating to be applied to the specimen surface. As the specimen deforms, the induced photoelastic fringes can be viewed under polarised light and the strains and shear stresses can be calculated (Dubey, 2009). However, this assumes that the specimen material is homogenous and isotropic, making it unsuitable for application to bone.
- **Digital speckle pattern interferometry**: A technique which measures the interference between a reflected laser beam and the original laser beam signal. The reflected signal has further to travel when the specimen deforms, creating a set of fringes related to the out of plane displacement from which strain measurements can be derived (Pierron, 2009). This technique is limited to flat diffusive surfaces, however it has been used in previous biomechanical studies to assess the strain on femur bone (Horta et al., 2003; Su et al., 2005).
- **Thermal Stress Analysis (TSA)**: A technique which uses the thermoelastic effect of materials to analyse surface stress and strain by monitoring small temperature changes with an infra-red detector (Eaton-Evans, 2009). TSA was successfully employed by Kohles and Vanderby (1997) and Shah et al. (2012) to measure femoral bone strain but this technique requires dynamic cyclic loading of the specimen.
- **Digital Image Correlation (DIC)**: A technique whereby images taken of a specimen with a random pattern at different stages of deformation are compared and blocks of pixels are tracked, so that surface displacement can be measured. 2D and 3D surface deformation vector fields can then be calculated and in-plane strain maps formed for heterogenous anisotropic materials, such as bone (McCormick and Lord, 2010).

2.6.3.1 Digital Image Correlation

Digital Image Correlation (DIC) has been identified as the most appropriate non-contact technique for surface strain measurement across a TKR construct specimen. DIC is a non-contact image analysis technique for shape and deformation measurement, allowing full field strain assessment of the complex 3D surface geometry of heterogeneous, anisotropic materials (Sutton et al., 2009). As detailed by Sutton et al. (2009), the local-approach image correlation technique employs an algorithm that tracks the displacement of a random speckle pattern by matching subsets, with an area of unique grey level pixel values, spaced centre to centre by a specified step size, between images obtained before and after deformation. Hence, the subset size defines the spatial resolution of the displacement measurements. The displacement resolution depends on the number of pixels, the field of view and the scale of the image relative to the surface pattern. The strain is calculated from the grid of displacement data points, positioned at the centre of each subset, by interpolating from the surrounding points to form a Green-Lagrange strain tensor for each point in the grid. These strain tensors are then smoothed over a decay filter ('filter size' or 'strain window') of a specific number of data points to reduce noise. Therefore, this controls the spatial resolution of the strain measurement (filter size x step size + subset size). Stereo DIC employs two cameras at a known angle to one another, which are calibrated using a target with known marker size and spacing, such that a common 3D co-ordinate system can be determined for both cameras. This makes it possible to measure deformation across a 3D surface, resulting in a technique that is insensitive to out-of-plane deformations. Multiple stereo camera DIC has also been shown to be possible by Chen et al. (2013), allowing a large area to be assessed without losing resolution and accuracy.

DIC is an optimisation method which requires appropriate experimental setup and selection of data analysis parameters (subset, step and filter size) in order to produce valid results and minimise noise, bias and systematic errors during the correlation analysis (Crammond et al., 2013; Wang et al., 2009; Yaofeng and Pang, 2007). Studies should be presented in a way that explicitly states analysis parameters to the reader to demonstrate the reliability of the results, whatever the application, especially for their use in validation of finite element models (Dickinson et al., 2011; Grassi et al., 2013). However, this information is not always included in the documentation of biomechanical studies in the literature, such as those by Dickinson et al. (2012); Mann et al. (2014); Moerman et al. (2009); Scott et al. (2013); Terrier et al. (2014); Tiossi et al. (2012); Vaananen et al. (2013), to specify a few.

Figure 2.22 shows an example of subset size (7 pixels), step size (3 pixels) and filter size (5 data points) to illustrate their influence in DIC measurement spatial resolution.

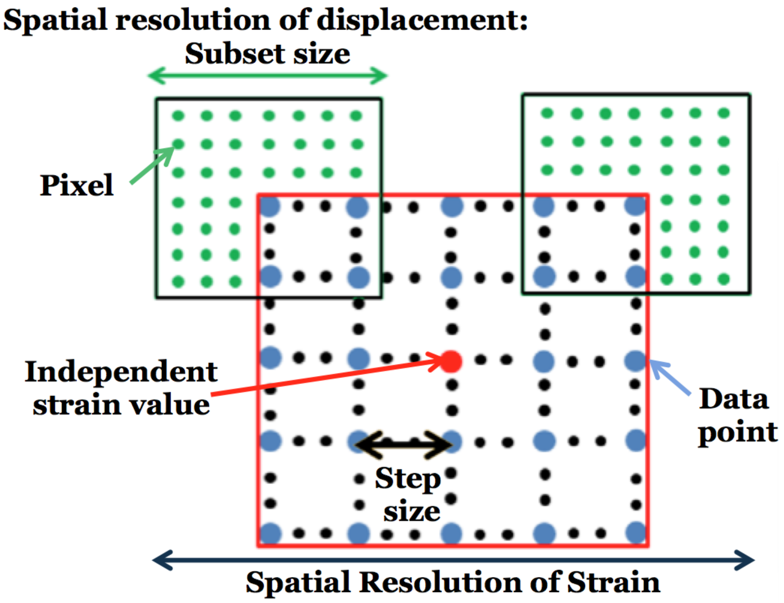

Figure 2.20: Illustration of Digital Image Correlation parameters and corresponding spatial resolution of measurements

Each green dot represents the centre of a pixel, each blue dot represents a displacement data point and each black dot shows the step size spacing between subsets. The correlation criterion algorithm (cost function, χ^2) chosen for the optimisation process of matching these subsets, and hence tracking the deformation, depends on the speckle pattern and surface lighting, plus any changes in lighting post-deformation. These factors influence the raw image contrast, which determines the spread of pixel grey value intensity data (0-255 for an 8 bit image) and how well the data is likely to correlate. Ideally, the pixel intensity range should lie between 20-230 in order to avoid saturation so that sub-pixel accuracy can be achieved. Saturated pixels due to reflections on the specimen surface will cause measurement errors because the intensity will change within these regions, resulting in bias from the correlation calculations (Sutton et al., 2009).

Bias in the displacement calculation and subsequent strain calculation can arise from systematic errors in the subset matching process, affecting the accuracy of DIC. This may arise through interpolation or noise. Interpolation is used between sample points (pixels) to approximate pixel intensity values at non-integer locations, such that sub-pixel accuracy can be achieved, but this induces errors in the optimisation process. The accuracy of the correlation strongly depends on the phase accuracy of the interpolation filter. High-order interpolation methods with smaller phase errors, such as an 8-tap optimised interpolation filter, have been shown by Shreier et al. (2000) to reduce systematic errors. By increasing raw image contrast (increasing intensity value gradients), it is possible to reduce the contribution of bias from pixel intensity patterns, decreasing the displacement errors significantly (Wang et al., 2009). Random image noise also contributes to bias in DIC, since the interpolation process acts as a low-pass filter for non-integer locations leading to amplitude errors. This introduces spatial correlation in the noise, lowering the variance of the filtered noise. Again, high-order optimised interpolation filters can greatly reduce this effect (Sutton et al., 2009). Larger subset sizes can also reduce the affect of image noise, but at the cost of decreasing the spatial resolution of measurement (Wang et al., 2009).

Surface strain measurement with DIC has allowed the behaviour of polymer and composite materials to be examined, facilitating the evaluation of interlaminar shear strain on the free-edges of laminates and composite lap-shear joints (Comer et al., 2013; Laurin et al., 2012; Lecomte-Grosbras et al., 2009; Poulain et al., 2013). The fracture toughness of materials can also be assessed with DIC by using displacement fields to calculate the stress intensity factors around a crack tip (Brynk et al., 2012). This may be particularly useful for assessment of the performance of a bimaterial interface, owing to the ability of DIC to measure strain across heterogeneous, anisotropic materials (Desai et al., 2012). However, in the case of crack propagation it is important to remember that DIC is a continuum mechanics technique. Thus, whilst DIC can measure displacement across a region of discontinuity, it can only accurately measure strain on the material surrounding a crack, so the crack area must be excluded from the region of interest (Nguyen et al., 2011; Sutton et al., 2009).

DIC is increasingly used in biomechanics for evaluation of cortical surface strain in various bone models including synthetic analogue, epoxy, murine, ovine and human cadaveric bone materials (Carriero et al., 2014; Cyganik et al., 2014; Ghosh et al., 2012a; Sztefek et al., 2010; Tiossi et al., 2012; Vaananen et al., 2013). Speckle patterning of bone tissue has most commonly been achieved using matt paints (water or solvent based) applied as an aerosol (Carriero et al., 2014; Cyganik et al., 2014; Ghosh et al., 2012a; Gilchrist and Guy, 2013; Grassi et al., 2014; Helgason et al., 2014; Mann et al., 2014; Sztefek et al., 2010; Terrier et al., 2014). One study reported using enamel paint on biological tissue, but no comments were made on the deformation behaviour of the enamel paint relative to the tissue, compared to acrylic paints (Zhang and Arola, 2004). Photocopier toner and iron oxide powder has also been used to create speckle patterns on bone (Liu et al., 2014; Thompson et al., 2007), and at greater magnification, no speckle pattern is required for microscopic-DIC of bone due to the existing texture (Budyn et al., 2012; Tang et al., 2015). Whichever way the speckle pattern is applied, it must deform with the material and not delaminate from the surface or this will give rise to errors in measurement (Sutton et al., 2009).

Previous work has demonstrated a good correlation between strain measurements from

DIC and strain gauges on Sawbone using a similar DIC system and DIC measurements have been used to validate finite element models for subsequent predictive remodelling analysis (Dickinson et al., 2011; Ghosh et al., 2012a). However, it is important to note that the 2D strain measurements from DIC cannot be directly compared with the 3D strain predictions of FE models, but an equivalent strain ('Von Mises' in Vic-3D software) may be calculated for comparison based on a 2D principal plane strain formulation (Dickinson et al., 2011; Simonsen, 2011).

Vaananen et al. (2013) demonstrated the repeatability of DIC strain measurements on composite Sawbone (analogue) proximal femurs with very low intra-sample variability (high precision) when loaded to fracture. In this study, it was identified that the overall experimental variability in strain measurements originated from the inter-sample variability in the composite femurs themselves, with surface geometry, defects, stiffness and resulting ability to bear high strains differing from femur to femur. Whilst there was variation in potting angle, this was reported to not correlate with maximum load at failure (in their supplementary material). However, the resulting load contact location and area were not reported.

Recently, Grassi et al. (2014) presented a cadaveric study using stereo DIC to measure proximal femoral bone strain under physiological loading rates up to fracture (constant displacement rate of 15 mm/s), showing the ability of DIC to evaluate crack propagation behaviour at the femoral neck. Grassi et al. (2014) used a control plate to assess the DIC noise, rather than the surface of the bone itself, so the results presented were not bone deformation measurement resolutions, but the effect of test machine movement on DIC noise was shown to increase the noise on the plate by approximately 5 times.

To assess mechanically-induced bone response, DIC may be used as a tool to measure the local bone surface strain distribution. Sztefek et al. (2010) used DIC to establish the effects of load-induced adaptive changes in bone architecture on mouse tibiae, of which the right had been subjected to loading whilst in vivo and the left was used as an unloaded control. Whilst the mean strain values across the bone surfaces indicated no significant difference after the *in vivo* loading regime, this study highlighted the need for multiple specific regions of interest in order to make specific strain comparisons for evaluation of bone adaption. The full-field nature of DIC compared to a single point measurements achieved using strain gauges makes this possible for evaluation of strain response to loading. This response may be used as an indicator of changes in tissue structure or stimuli for bone adaption following a variable change, for example, loading regime or introduction of a prosthesis.

Regarding periprosthetic bone strain distribution, Dickinson et al. (2012) have used DIC to evaluate the pelvic cortical bone strain following implantation with different acetabular cup materials, showing the potential of a composite implant to induce cortical bone strains closer to the physiological case. Implant induced bone strains have also been assessed for dental prostheses using DIC, which validated the surface strain predictions of FE models used to investigate the bone-implant interface (Tiossi et al., 2011, 2012, 2013). Tiossi et al. (2012) used DIC to measure the supporting bone strain distribution of dental implants using an epoxy resin model, showing that there was a significant difference between veneering materials, but the study did not compare this with a physiological strain distribution (i.e. pre-operative state) so could not make any assumptions on which implant material was more appropriate for maintaining bone stock. In the knee, Scott et al. (2013) carried out a DIC study to evaluate unicompartmental knee implant design and Malinzak et al. (2014) used DIC to evaluate tibial component design in TKR by measuring tibial surface strain following implantation, both in Sawbone models. Mann et al. (2014) used DIC to evaluate micro-motion, in addition to periprosthetic bone strain, on the tibiae of post-mortem-retrieved total knee replacements, and related time in service to greater micro-motions and increased bone strains. However, to the authors' knowledge, there are no studies in the literature that have used DIC to measure femoral bone strain for comparison of TKR geometry or material.

2.6.3.2 Digital Volume Correlation

Digital Volume Correlation (DVC) is a three-dimensional extension to the image correlation technique made possible by advances in volumetric imaging which have allowed 3D positioning and measurements of internal material features (Sutton et al., 2009). Confocal microscopy, magnetic resonance imaging (MRI) and x-ray Computed Tomography (CT) are three examples of non-destructive imaging techniques that generate volumetric data for analysis using DVC. The latter shall be described in this section with use of a local-approach DVC technique for the interests of this thesis.

μ-CT is an x-ray imaging technique whereby x-ray projection images are obtained at angles of view throughout 360° of an object's axis, resulting in radiographs with a spatial resolution in the micrometre range (Ritman, 2011). A 3D image stack of trans-axial slices composed of individual voxels providing quantitative densitometric (density and geometry data) through the object's volume is then created by use of a tomographic reconstruction algorithm such as filtered back projection (ASTM International Standard E1441, 2000; Landis and Keane, 2010). By loading or displacing a specimen *in situ*, local DVC may be used to exploit the micro-architectural texture within certain materials, in order to track the displacement of small sub-volumes of interest, through optimisation of an objective correlation function, relative to a reference volume (usually unloaded) (Bay et al., 1999). Figure 2.23 illustrates how the cross correlation technique splits the reference and deformed volume into smaller non-overlapping sub-volumes (*f(x, y, z)* and *g(x+i, y+j, z+k)* respectively). The offset (i, j, k) between the corresponding sub-volumes can then be determined by maximising the normalised cross-correction coefficient (Equation 2.4), which allows the average displacement to be calculated (Palanca et al., 2015; Scarano, 2013). (X, Y, Z) refers to the co-ordinates (in voxels) at the same point in the reference and deformed volume. f and g are the grey level values at those co-ordinates, for the reference and deformed volumes, respectively. The estimated 3D displacement data may then be used to calculate the internal strain fields at full continuum-level (Bay et al., 1999; Sutton et al., 2009; Verhulp et al., 2004).

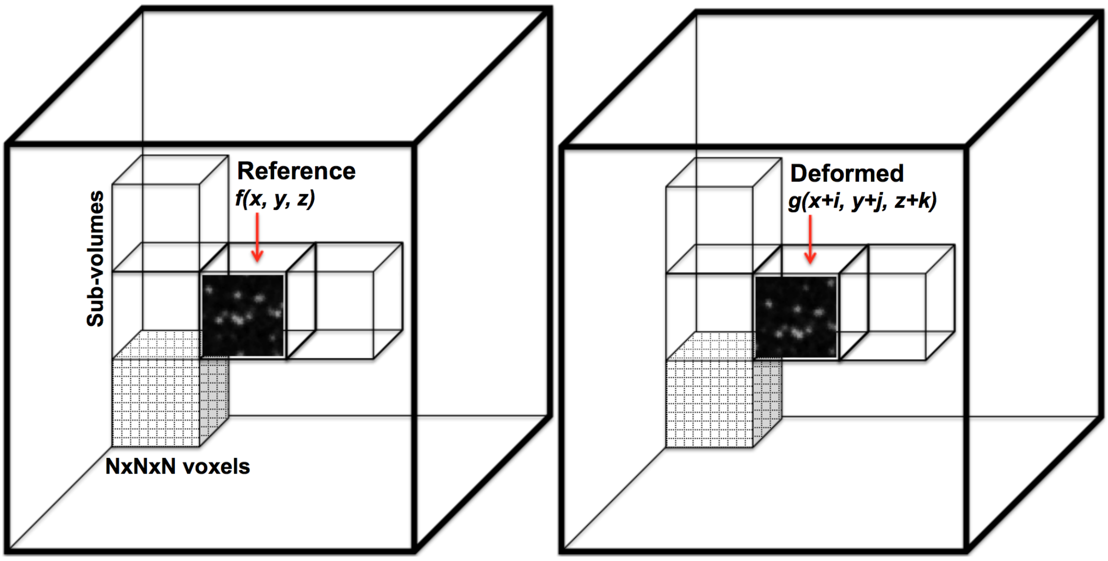

(a) Reference Volume (b) Deformed Volume

Figure 2.21: Reference and deformed volumes are divided into sub-volumes (NxNxN voxels) for cross correlation

$$r_{local} = \frac{\sum_{X,Y,Z} f(x,y,z) \cdot g(x+i,y+j,z+k)}{\sqrt{\sum_{X,Y,Z} f(x,y,z)^2 \cdot \sum_{X,Y,Z} g(x+i,y+j,z+k)^2}} \tag{2.4}$$

The resolution of strain measurement using DVC is defined as the minimum significant strain value regarded as a result of material behaviour and not noise artefacts from the CT data (Gillard et al., 2014). For a given DVC analysis, the measurement resolution may be evaluated from repeated scans under static, nominally-zero strain conditions and rigid translation tests, as this accounts for the difference between the calculated and true total displacements (Dall'Ara et al., 2014; Gillard et al., 2014; Hardisty and

Whyne, 2009; Liu and Morgan, 2007; Palanca et al., 2015; Sukjamsri et al., 2015). Possible systematic errors (bias) in the results are indicated by the mean values, and random errors arising from noise are indicated by the standard deviations. Hence, the accuracy and precision of displacement and strain measurements from DVC are quantified by the mean and standard deviations, respectively (Liu and Morgan, 2007; Sukjamsri et al., 2015). Gillard et al. (2014) highlighted that a good subvolume correlation is necessary to obtain accurate strain measurements, so any subvolume with a correlation coefficient less than 0.9 should be discounted. The length scale of the displacement and strain measurements, i.e. the subvolume size, defines the spatial resolution of measurement (Madi et al., 2013). A recent study by Palanca et al. (2015) compared three DVC methods for the analysis of bone and concluded that with every method, sufficiently large subvolumes must be used in order to achieve reasonable accuracy and precision. Hence, as with DIC, the DVC measurements are a compromise between spatial resolution and accuracy of strain (Dall'Ara et al., 2014; Sutton et al., 2009).

The naturally occurring micro-architecture of bone trabeculae makes it well-suited to DVC analysis; as such, it has been used to develop the DVC technique since its inception by Bay et al. (1999) and it is the most widely used material in DVC studies to date (Roberts et al., 2014). DVC on trabecular bone has shown adequate precision for measurement of elastic strains, although variation in DVC performance among different bone types has led to the recommendation that DVC is restricted to the yield and post-yield behaviour of bone (Bay et al., 1999; Liu and Morgan, 2007). At whole bone level, Hussein et al. (2012) applied the DVC technique to full human vertebrae and reported higher strain errors than studies using trabecular bone alone, which they attributed to attenuation of the x-ray signal as it passed through the cortical shell (decreasing the trabecular bone signal) and a decrease in signal to noise ratio from multiple stitched scans in order to achieve acceptable resolution of the whole bone for the DVC analysis. Hardisty and Whyne (2009) also evaluated whole bone strain using DVC, however, they used a rat vertebrae which enabled a higher resolution scan.

Relating to the bone-implant interface, Sukjamsri et al. (2015) recently used DVC to evaluate interfacial micromotion by measuring the displacement of a thin coating of porous titanium on the PE implant surface and the displacement of the surrounding bone. Tozzi et al. (2014) used DVC at the bone-cement interface to assess micro damage within the interdigitated layer, however they did not assess the measurement resolutions, nor report correlation values and CT scan resolution, which makes it difficult to interpret their results reliably, although they did present strain measurements within the cement volume.

DVC shows good potential for measurement of strain in the bone at the interface with the cement in the PEEK TKR construct. However, at full-construct level, the strain measurement would be limited to within the bone itself at the resolution achievable with current μ-CT hardware. Local scanning techniques make it possible to reconstruct specific volumes of interest within a specimen at much higher resolution and the smaller the voxel size, the less the partial volume effects present at material boundaries in these regions (Ritman, 2011). There is potential to use the radiopacifier particle pattern within the cement to track the deformation, as shown in a study by Gates et al. (2011), who used silica beads ranging from 50-250 μm in size within a polymer matrix for DVC analysis, imaged at 10 and 20 μm resolution using μ-CT. The zirconium dioxide radiopacifier particles in Palacos cement have a mean diameter of 1-5 μm with a propensity to agglomerate as particles of 50-200 μm in diameter (Neut et al., 2010).

The limitations of DVC are mostly reported to be due to μ-CT resolution and the pattern within the material, which relates to both poor correlation in regions of the volume and spatial resolution (Gillard et al., 2014; Hardisty and Whyne, 2009; Hussein et al., 2012; Madi et al., 2013; Palanca et al., 2015; Sukjamsri et al., 2015). In addition, care must be taken in the DVC process to identify discrepancies between reconstructed values and the 'true' attenuation coefficient, known as CT artefacts, which can arise due to physical processes in the CT system, for example, beam hardening, sample movement, aliasing, photon scatter and detector saturation (Boas and Fleischmann, 2012; Limodin et al., 2011). Ultimately, any limitations with DVC are overcome by the volumetric full-field strain measurements, which are not obtainable with other techniques.

2.6.4 Finite Element Analysis

Finite element analysis (FEA) is the most commonly used computational numerical technique for structural evaluation. As detailed by (Moaveni, 2008), in FEA, a large structural problem is broken down into smaller sub-regions (elements) then, assuming a solution that approximates their behaviour (Hooke's Law in deflection, for example), equations are developed for application to the elements in order to approximate solutions at discrete points (nodes). These are assembled for continuity at inter-elemental boundaries with specified boundary conditions and loads to achieve the global solution.

FE models have been used in studies in the literature to evaluate bone remodelling, peri-prosthetic stresses and implant wear (Dickinson, 2014; Huiskes et al., 1987; Knight et al., 2007; Liau et al., 2002; Ramaniraka et al., 2000; Taylor, 2006; van Lenthe et al., 1997, 2002; Zelle et al., 2011b). For validation, predictions from FEA of implanted bone must be compared with experimental data. This allows an FE model to be used for further simulations and probabilistic analysis to assess the response with different implant geometry for example, without the time and cost of experimental setup (Anderson, 2005; Arsene and Gabrys, 2013; Bessho et al., 2007; Laz et al., 2006; Tuncer et al., 2013).

2.6.4.1 An FE Model of the PEEK TKR Construct

A finite element (FE) model was developed at the start of this project by Dr Alex Dickinson and Dr Mamadou Bah, two research fellows in the Bioengineering Science Research Group, as part of the conceptual study for the PEEK TKR (Bah et al., 2012). The FE model was employed in this project to predict the shear stresses at the TKR femoral PEEK implant-cement interface in order to set acceptance criteria for the shear strength required between PEEK and cement. The next section summarises the FE simulations presented at 1st International PEEK Meeting in Philadelphia, PA, USA, used for comparison with experimental results presented in Chapter 3 (Rankin et al., 2013).

A femur model generated from CT scan data of a male angiography patient, was implanted with a left cruciate retaining TKR femoral component of generic geometry with a 4 GPa Young's modulus and a Poisson's ratio of 0.36 (Figure 2.24a), using an interdigitated layer of bone cement. The femoral component was positioned according to typical surgical techniques and attached to the bone using either a bonded contact or a simplified slip-stick Colomb friction contact model (coefficient of friction = 0.3). The femur was cut at two thirds of the shaft length above the knee, as the proximal part was outside the region of interest. The implanted femur was meshed using dense linear tetrahedral elements, with a side length of 1.5-2 mm in the implant, distal bone and cut bone, and 5-6 mm in the diaphyseal bone outside the region of interest (Figure 2.24b).

Heterogeneous isotropic material properties were applied to the bone elements from the grey scale values of the CT-scan voxels using Bonemat, with a relationship of $E = 6950\rho^{1.49}$ between bone density (ρ) and Young's Modulus (E) (Istituto Ortopedico Rizzoli, 2007). The density was linearly correlated to the CT scan Hounsfield Unit (HU) with 1.73 g/cc for a dense cortical diaphyseal location (1.73 g/cc) and 0 g/cc for a non-mineralised location in the medullary cavity. Shell elements with a constant Young's modulus of 10 GPa and a thickness of 0.5 mm were applied to the external surface of the bone to reproduce thin cortical bone removed as a result of CT scan segmentation or partial volume effects. The thickness of the interdigitated cement

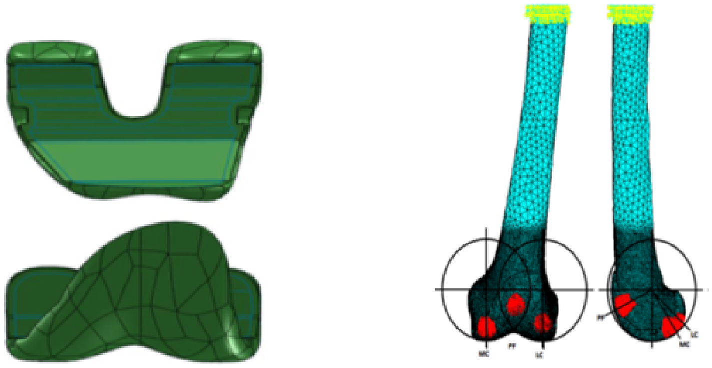

(a) (b)

Figure 2.22: (a) Generic femoral component geometry and (b) boundary conditions used for heel strike showing Medial Condyle (MC), Patellofemoral (PF), Lateral Condyle (LC) loading and diaphyseal constraint

layer was varied between 2 mm and 4 mm, according to a study by Vaninbroukx et al. (2009), to investigate if it would alter the interfacial stresses. For each specific cement thickness, all FE elements of the distal femur part (cancellous bone alone) associated with nodes within 2 mm of the implant surface were modelled as bone cement with a Young's modulus of 2.5 GPa. Boundary conditions were applied to the model representing heel strike (van Lenthe et al., 1997). Joint contact forces were applied to the FE model at the medial and lateral condyles, and at the patellofemoral contact (Table 2.4) directly to nodes on the implant or subchondral bone bearing surface. The forces were applied across 10 mm radius contact patches (Figure 2.24b), whilst the diaphyseal cut surface was constrained against displacement in all directions.

Force location	**Resultant force, N**	**Flexion, °**	**Adduction, °**
Medial condyle	1651.8	34.4	0.97
Lateral condyle	990.5	47.9	0.94
Patellofemoral contact	1753.2	-64.3	-24.2

Table 2.4: FE model load conditions for heel strike case

The FE results showed that the maximum interfacial shear stresses occurred anteriorly near the left flange in both the bonded (2.9 MPa) and frictional contact (4.3 MPa) cases during heel-strike. As the cement thickness increased from 2 to 4 mm, the magnitude of the highest stresses remained approximately the same as did the stress distribution around the implant surface. An increase in the cement thickness did not result in a significant change in the magnitude of maximum tensile and compressive stresses within the cement layer and when the cement thickness was greater than 2 mm, a slight decrease (2.7 to 2.5 MPa) in shear stress was predicted.

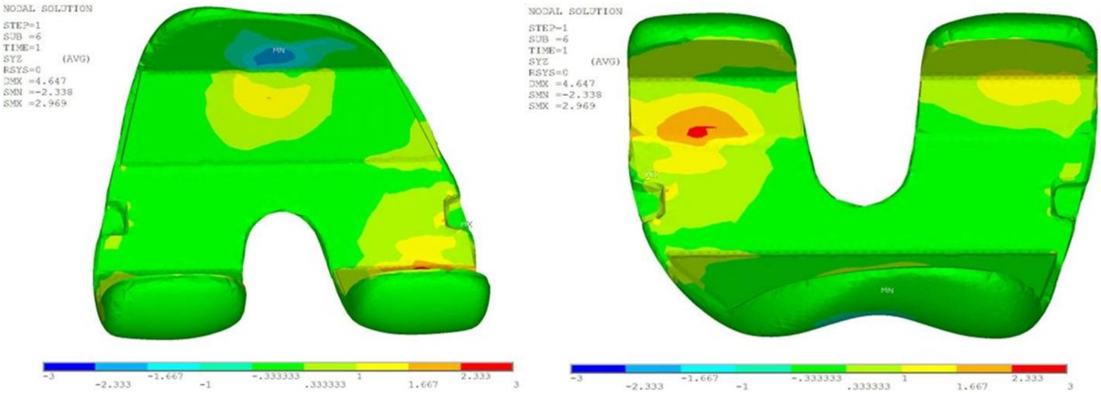

Figure 2.23: Shear stresses plot from an FE model of a PEEK femoral component with 2 mm cement thickness in the bonded state at heel strike loading (anterior flange view, left, and posterior flanges view, right) (Bah et al., 2012)

Figure 2.25 shows the predicted shear stresses at the PEEK-cement interface during heel strike with a cement thickness of 2 mm. This suggests that the shear stresses experienced in the knee joint are likely to peak below 3 MPa during normal gait, provided that the cement is bonded to the PEEK implant. However, it is important to note that this prediction is for a single femur geometry and the implant is of a generic geometry without fixation features.

2.7 Summary

A review of the literature has demonstrated that the properties of PEEK make it a promising candidate as a biomaterial capable of fulfilling the requirements of a femoral component for total knee replacement. PEEK is bioinert, resistant to sterilisation and insensitive to temperature at the working conditions *in vivo*. It is now widely accepted as a radiolucent alternative to metallic implants, with a modulus comparable to that of bone, potentially reducing stress shielding effects and bone resorption. Induced regions of stress shielding in the distal femur with considerable reductions in strain energy density, have be related to areas of bone loss after total knee replacement with a metallic femoral component (Tissakht et al., 1996). Hence a lower modulus PEEK femoral component has the potential to greatly reduce these effects by transferring more physiological loads.

Nevertheless, the chemical inertness of PEEK implies that it has limited fixation with bone alone, but this is not an issue if the PEEK implant is to be cemented. The fixation of PEEK is a critical issue for use in a femoral component, as its increased compliance could give it a propensity to debond at the interface with high interfacial strains. Fixation to date has mainly been achieved through Ti and HA coatings, and mechanical fastenings. For application in a total knee replacement, bone cement is most realistic choice in order to achieve good initial stability and greater variability for implant positioning.

The mechanical integrity of the cemented implant construct influences the long term stability of the implant and survivorship of the joint replacement (Lewis, 1997). In a previous all-polymer TKR, a polyacetal-on-UHMWPE bearing combination gave a significant reduction in wear rate compared with conventional metal-on-UHMWPE wear couples (Bradley et al., 1993; McKellop et al., 1993). However, these all-polymer knee replacements failed through poor sterility and fixation *in vivo*, highlighting the importance of developing an optimal implant fixation system prior to clinical trials. Therefore the interfacial properties of the PEEK-cement construct must be characterised for TKR, which in addition, is a topic that has not been published in previous studies in the available literature. After consideration of the forces experienced at the knee joint, it can be deduced that the TKR construct will be subject to mixed mode loading *in vivo*. The weakness in the TKR construct often lies at the interface leading to implant loosening and revision surgery. Therefore the interface strength must be optimised to meet the requirements of the stresses generated during daily activities. However, it appears that despite the clinical relevance of failures, there is not a standard test protocol available to test the long-term implant-bone fixation of TKR *in-vitro*. Thus test protocols will be developed accordingly.

The findings from the literature survey can be summarised as follows.

- Polyetheretherketone, PEEK, is considered an isoelastic material for implant applications and has the potential of reducing stress shielding effects experienced with traditional high modulus orthopaedic materials. It is also highly biocompatible, bioinert, resistant to sterilisation and radiolucent to x-rays.
- The mechanical properties of PEEK can be tailored to an implant application by reinforcement with carbon fibres. Despite this, carbon fibres are stiffer and hence more abrasive than PEEK alone, so may increase the wear rate of a softer polyethylene tibial component, making unfilled PEEK a more suitable femoral bearing material.
- Acrylic bone cement can be used to achieve rapid fixation of a joint replacement prosthesis. The composition and mixing method of the cement are key in determining its mechanical properties. Porosity content, influenced by the mixing method, may act as stress raising defects within the cement, potentially causing crack propagation and failure of the cement mantle. Cement shrinkage can also leave residual stresses within the cement or at the cement-implant interface.
- The polymerisation of bone cement is an exothermic process, however, the temperatures experienced at the implant-cement interface are unlikely to have any effect on the mechanical properties of PEEK.
- The TKR construct will be subjected to mixed mode loading *in vivo*, with the articular surfaces predominantly loaded in compression and shear, as the contact areas slide, roll and rotate over one another during gait.
- It was predicted by an FE model that shear stresses may reach 3 MPa at the PEEK-cement interface.
- A higher interfacial surface roughness between an implant and cement mantle may give a higher interfacial shear strength. The interfacial shear strength between PEEK and cement can be determined through lap shear tests, the short beam or Iosipescu shear test method. The tensile interface strength may be achieved with a tensile rod test setup.
- PEEK has poor adhesive properties due to its low surface energy. The type of bond achieved between a PEEK implant and PMMA bone cement has not been determined from the literature available. However, it is likely that mechanical keying between the materials at the interface controls the interfacial strength alone. This may be achieved through surface roughness at the nano, micro and macro length scales.

- Surface activation through oxygen plasma-treatment offers a clean, dry method of increasing the surface polarity of PEEK to enhance its adhesive properties.
- The induced surface cortical bone strains in the PEEK TKR construct may be evaluated with Digital Image Correlation (DIC), compared to a conventional metallic implant, to assess stress shielding. DIC allows full-field, 3D surface strain measurement of heterogeneous, aniosotropic materials. However, DIC is an optimisation method which requires suitable experimental setup and parameter selection in order to produce valid results. Therefore a DIC protocol must be developed for measurement of femoral bone strain.
- To assess the remodelling stimulus within the cancellous bone, Digital Volume Correlation (DVC) may be employed at full construct level using micro-focused computed tomography scans with *in situ* loading to measure the bone strain under different loading modes through a 3D volume. There is also potential to use the radiopacifier particles within the cement as a pattern for volumetric strain measurement using DVC.
- In order to assess the interfacial strain between the PEEK implant-cement-bone interface using DVC, a feasibility study is required to determine if the radiopacifier particles within the cement may be used as a marker to track deformations through the 3D volume. The DIC technique may also be used in 2D to assess the interfacial strain distribution between PEEK and cement at a coupon level.

While the literature supports the concept of a PEEK based knee implant, new test methods need to be developed for characterisation of the device due to the differences in material properties compared with traditional metallic orthopaedic implants, which form the basis of current test standards.

Chapter 3

Evaluation of the Fixation Strength of the PEEK-Cement Interface

3.1 Introduction

Adequate pre-clinical testing is vital in ensuring the safety and suitability of orthopaedic prostheses to evaluate the performance of new devices versus existing designs, under representative *in vivo* conditions (Steele et al., 2011). In order to determine suitable experimental and computational preclinical test methods for a novel implant, it is first necessary to determine a mechanical variable associated with the progress of failure (Prendergast and Maher, 2001). The review of the literature suggests that fixation is a critical issue in the success of total knee replacement. Since a novel material with increased compliance is proposed for this application, the femoral component could have a propensity to debond as a result of increased interfacial strains. Therefore evaluation of the interfacial properties of the construct are key in ensuring the implant is safe and effective.

The main variables concerning the fixation of the PEEK femoral component have been defined as the interfacial strength between the PEEK and cement and the interfacial strength between the cement and the bone. It is hypothesised that the interfacial shear strength shall be governed by the mechanical interlock or keying between the two materials rather than chemical interactions due to the inert nature of PEEK. The following chapter concerns an investigation of the fixation strength of PEEK with PMMA bone cement at the coupon level, with the aim to determine how to enhance the adhesion at this interface most effectively. The FE model, described in section 2.6.4.1, estimated a peak shear stress value of 3 MPa at the PEEK-cement interface (Bah et al., 2012). This was used as the acceptance criterion for determination of a sufficient PEEK-cement interfacial shear strength in the present study.

Prior to the commencement of the PEEK-cement fixation study, a discussion was held with Invibio Ltd regarding commercially viable methods of enhancing the fixation strength of the PEEK femoral component. The study was limited to surface design features and dry treatments that could be applied during the manufacture process of a

PEEK medical implant. In addition, the test protocol was chosen for ease of implementation at Invibio Ltd. This led to the formulation of three studies of the PEEK-cement interface strength:

1. Preliminary study of smooth and grit-blasted PEEK and CFR-PEEK
2. Surface topography study of injection moulded PEEK
3. Plasma treatment surface activation study of PEEK

First, the preliminary investigation of the PEEK-cement interfacial shear strength sought to evaluate any change in interfacial shear strength through premature cementing (applying the cement whilst it is still in the waiting phase of polymerisation, as discussed in section 2.2.1). This is hypothesised to promote improved wetting of the PEEK surface and thus an improved mechanical interlock. A premature cementing technique was used in the methodology of Zelle et al. (2011a), whose results for steel-cement shear strength were to be used for comparison. Two PEEK materials were investigated, unfilled PEEK and CFR-PEEK, with a smooth and roughened surface finish achieved through grit-blasting.

The second phase of this fixation study investigated the effect of surface topography of injection moulded unfilled PEEK on the interfacial shear strength with cement. The aim of this study was to improve the mechanical bond strength between PEEK and cement by determination of suitable surface topography to improve the mechanical keying. An injection moulded surface topography was chosen due to the risk of third body inclusions from the grit-blasting process.

The shear strength of the PEEK-cement interface may also be increased through surface activation of PEEK which has been reported to enhance adhesive bonding in the literature (outlined in section 2.5.3). By modifying the surface chemistry of PEEK using oxygen plasma treatment, it may be possible to improve the interfacial strength bone cement further; this is evaluated as an additional hypothesis in study 3.

3.2 Preliminary Study

3.2.1 Methodology

A preliminary study of interfacial shear strength between PEEK and bone cement was carried out using two PEEK based materials, for comparison of strength values to those presented by Zelle et al. (2011a) for steel-cement interfaces, with a grit-blasted surface finish.

3.2.1.1 Materials

Injection moulded test plates with dimensions of 60 x 25 x 6 mm (incorporating a 5 degree edge chamfer for removal from the injection mould tool) were supplied by Invibio Ltd (Thornton Cleveleys, UK). PEEK-OPTIMA® (unfilled, referred to as PEEK) and MOTIS® (30% chopped fibre reinforced, referred to as CFR-PEEK) sample material groups were used to investigate the effect of carbon fibre reinforcement on the interfacial shear strength with bone cement. The material properties for each PEEK material have been shown in Table 2.1 in section 2.1.3.

Twenty plates of each PEEK-based material were grit-blasted with polymer beads to create a roughened surface finish, similar to that used in the cement pockets of the contemporary CoCr femoral component of the Maxx Freedom Knee® (Maxx Orthopedics, Inc., PA. USA). Ten plates of each material remained untreated as a control (Figure 3.1).

Figure 3.1: An example of each test plate used - From right to left: PEEK smooth injection moulded and grit-blasted finishes, and CFR-PEEK injection moulded and grit-blasted surface finishes

Palamed medium viscosity cement (E = 2.92 GPa) (Palacos MV, Heraeus Medical GmbH, Wehrheim, Germany) was used for the preliminary study of interfacial shear strength with the PEEK and CFR-PEEK samples. The preparation method is detailed in section 3.2.1.3.

3.2.1.2 Measurement of Surface Roughness

To assess the surface roughness of the samples for comparison with the corresponding interfacial strength values, the R_a and R_z value of each sample were measured according to ISO 4288. The R_a value is the arithmetic mean deviation of the roughness line profile. This is derived from the primary surface line profile by suppressing any long-wave component, which corresponds to the waviness of the surface, using the profile filter λ_c (the cut-off). Very high frequency data is often attributed to vibrations of surface debris, so this must also be filtered from the line profile measured. The R_z value is the maximum height measurement of the surface from the lowest profile valley to the highest profile peak.

For an accurate measurement of R_a and R_z, a suitable evaluation length must be chosen depending on how rough the surface is. Table 3.1 shows the evaluation and sampling lengths for different ranges of R_a value. The sampling length is equal to the cut-off. The software associated with the surface roughness measurement equipment then uses signal processing and statistics to analyse the stored line profile data (BS EN ISO 4288, 1998).

R_a, μm	Sampling Length, mm	Evaluation Length, mm
$0.006 < R_a \leq 0.02$	0.08	0.4
$0.02 < R_a \leq 0.1$	0.25	1.25
$0.1 < R_a \leq 2$	0.8	4
$2 < R_a \leq 10$	2.5	12.5
$10 < R_a \leq 80$	8	40

Table 3.1: Roughness sampling lengths for measurement of R_a (BS EN ISO 4288, 1998)

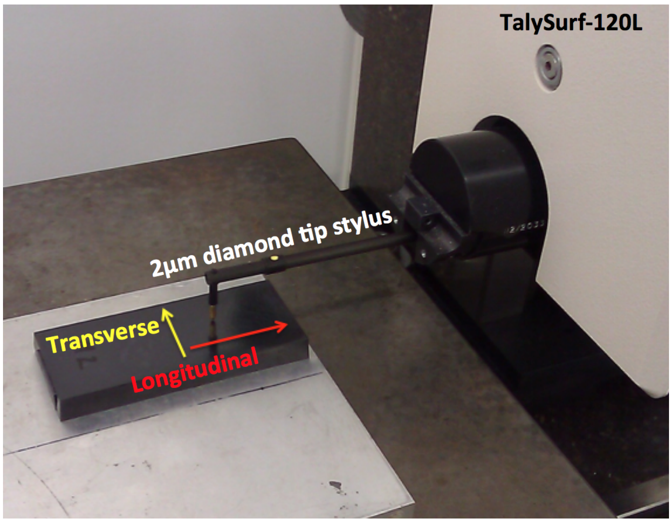

Figure 3.2: TalySurf-120L contact profilometer and roughness measurement directions)

A TalySurf120L (Taylor Hobson, Leicester, UK) contact surface profilometer was used to measure roughness parameters of each PEEK surface finish. The TalySurf120L retracts a 2 μm radius diamond tipped stylus across the sample's surface to measure the surface profile height relative to the height of the stylus (Taylor-Hobson, 2011). Sampling lengths of 0.8 and 2.5 mm were used with gaussian filtering for the smooth injection moulded finish samples and grit-blasted samples, respectively, when determining the roughness value. Ten measurements were taken across each sample in the longitudinal and transverse directions (relative to lap-shear specimen loading direction, Figure 3.2), which were then averaged for comparison.

3.2.1.3 Lap Joint Sample Preparation

A polyethylene mould was manufactured to facilitate the cementing of the PEEK plate samples (60 x 25 x 6 mm) with a 25 x 25 mm^2 single lap joint. Palamed medium viscosity cement (Palacos MV, Heraeus Medical GmbH, Wehrheim, Germany) was manually mixed in open air before application to the PEEK and CFR-PEEK samples. The working time for the Palamed cement at different room temperatures (not pre-chilled or vacuum assisted) is shown in Figure 3.3. The manufacturer's mixing instructions were used as a standard protocol with the mixing and application times calculated from Figure 3.18 according to the environmental conditions.

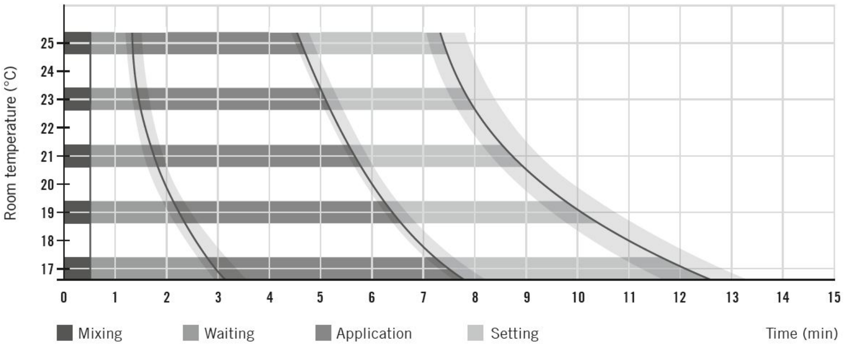

Figure 3.3: Working time for the Palmed bone cement (not pre-chilled or vacuum mixing) (Heraeus Medical GmbH, Wehrheim, Germany)

The cement powder and liquid monomer were mixed together for 30 seconds in an open glass beaker, then a waiting time of 1 minute 30 seconds was taken, before the cement reached the doughy stage in which it was applied to the mould by finger packing. The doughy stage occurs during the 'application' time period, referred to in this study as the working phase. With the use of G-clamps, the mould was clamped closed and the cement was left to cure under compression for 15 minutes before removal. This was performed in a fume cupboard to remove the monomer fumes and prevent inhalation of cement powder. This cementing procedure was carried out for ten plates of each PEEK and CFR-PEEK material surface finish. The mould (with samples ready for cementing) and mixing equipment used is shown in Figure 3.4, and the samples upon removal from the mould are shown in Figure 3.5.

A second cementing method was used for a further ten plates of grit-blasted PEEK and CFR-PEEK samples. A premature cementing technique was carried out by immediate application of cement to the mould after 30 seconds of mixing. This was to

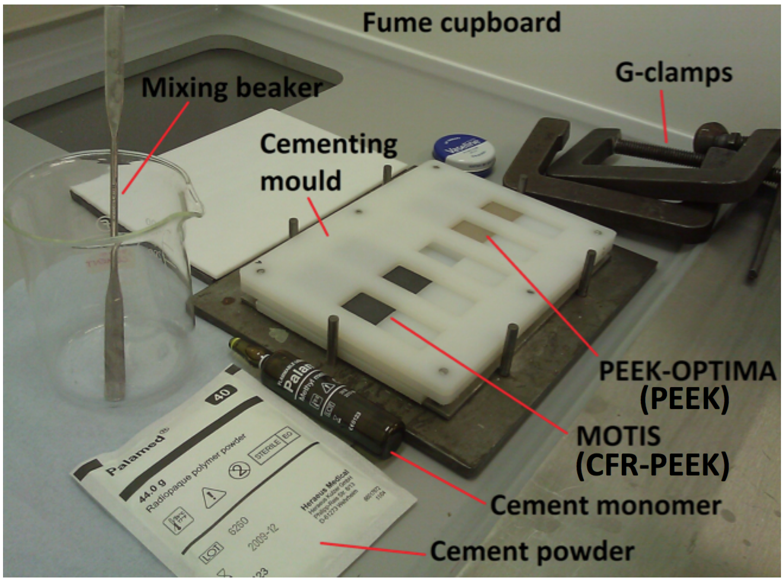

Figure 3.4: Moulding jig with PEEK and CFR-PEEK samples

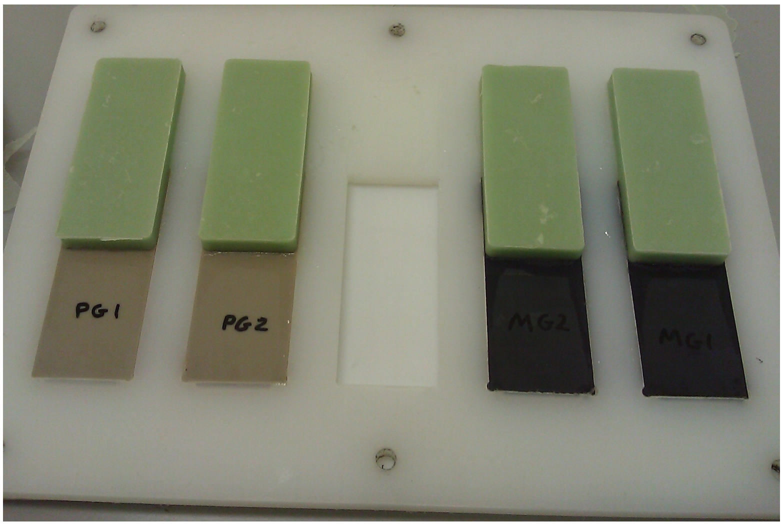

Figure 3.5: Moulded PEEK-Cement samples upon removal from the cementing mould

determine whether this technique would have any effect on the interfacial shear strength values measured or if there was any change in chemical interaction between the cement and the PEEK. Each sample group was removed from the cementing mould after 15 minutes and was left to cure fully for 72 hours prior to the lap shear tests.

3.2.1.4 Lap Shear Test Procedure

The cemented samples were mounted in the jaws of an Instron 5569 electromechanical test machine (Instron Inc., IL, USA) with 6 mm thick aluminium alignment plates (Figure 3.6), such that an equal area was supported in the grips, with the mechanical axis aligned with the PEEK-cement interface.

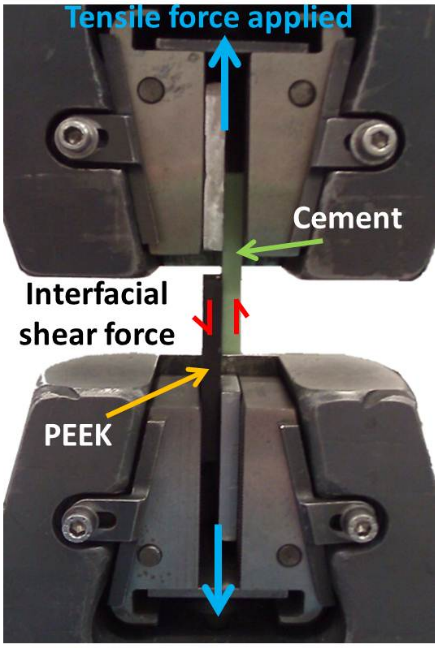

Figure 3.6: Lap shear test sample mounted in jaws of the test machine

Each sample was subjected to a ramped displacement of 2 mm/min to induce shear stress at the PEEK-cement interface, until the sample failed with complete separation of the PEEK and cement components. Failure was defined as adhesive if the sample failed along the interface, cohesive if the sample failed through either the cement or the PEEK substrate, or both adhesive and cohesive if the sample failed along the interface in addition to through the cement or PEEK substrate. The peak failure load was recorded using Bluehill Materials Testing Software (Instron Inc., IL, USA) and the interfacial strength was calculated from equation 3.1, with an assumption of uniform interface stress.

$$\text{Interfacial Shear Strength (MPa)} = \frac{\text{Applied Load (N)}}{\text{Interfacial Area (mm}^2\text{)}} \tag{3.1}$$

3.2.1.5 Imaging of Fracture Surfaces

A Nikon Wild M420 Makroscope (Nikon Metrology NV, Leuven, Belgium) was used for examination of the interfacial shear fracture surfaces to identify any features for examination under high magnification using a scanning electron microscope. Full examination of uneven fracture surfaces is not possible under optical microscopes at higher magnifications due to the relatively shallow depth of field and narrow field of view. The macroscope has the advantage of a wide field of view, but has a maximum magnification of 32x. Therefore, scanning electron microscopy (SEM) was used to achieve a greater depth of field on the fracture surfaces at very high magnification, with the aim of determining where the failure initiated from - at the interface or within the cement or the PEEK substrate.

In SEM, electrons are accelerated into a high energy beam that interacts with the atoms in the surface of the specimen, causing some particles to emerge (for example electrons, x-rays and photons) which are then detected. This has many advantages over optical microscopy, which are particularly useful in the microstructural-characterisation of fracture surfaces. Optical microscopy is only capable of 1000x magnification and has a relatively small depth of field, so depends upon the surface being smooth. In comparison, SEM is capable of magnifications up to 1,000,000x with a resolution of up to 1 nm, and has a large depth of field, allowing the majority of the specimen surface to be in focus regardless of the surface roughness (Vernon-Parry, 2000). It can also provide compositional and crystallographic information.

A JEOL thermal field emission scanning electron microscope JSM-6500F (FEG SEM) (JEOL GmbH, Freising, Germany) was used in this investigation (Wang, 2002). This was capable of accelerating voltages of 0.5-30 kV, magnification up to 500,000x, resolution of 1.5 nm at 15 kV, 5 nm at 1 kV, secondary electron and backscattered electron imaging (along with electron backscattered diffraction) and energy dispersive X-ray (EDX) microanalysis (Oxford Inca 300). Due to the non-conductive nature of the polymer samples, gold coating was applied with a Hummer 6.2 gold sputter machine (Anatech USA, CA, USA) before SEM scanning, to prevent the accumulation of static fields caused by the electron irradiation. A 5 kV accelerating voltage was used in the SEM for the PEEK and cement surfaces.

3.2.1.6 Statistical Analysis - Independent Samples T-test

The interfacial shear strength results were analysed by using an independent samples t-test to determine any significant difference between the sample means, with variances unknown and not assumed equal. The null hypothesis, H_0, was no significant difference (Δ_0) between the mean interfacial shear strengths (x_1 and x_2), with H_1 as the alternative hypothesis for all comparisons made.

H_0: $x_1 - x_2 = \Delta_0$

H_1: $x_1 - x_2 \neq \Delta_0$

As explained by Montgomery and Runger (2007), equation 3.2 calculates the t-test statistic, with $\bar{x}_1$, $\bar{x}_2$, S_1^2 and S_2^2 as the sample means and variances, respectively, and n_1 and n_2 as the number of samples tested in each group.

$$t_0 = \frac{\bar{x}_1 - \bar{x}_2 - \Delta_0}{\sqrt{\frac{S_1^2}{n_1} + \frac{S_2^2}{n_2}}} \tag{3.2}$$

This is distributed approximately as t with degrees of freedom, ν, (referring to the number of independent observations in the data) given in equation 3.3. If ν is not an integer, it is rounded down to the nearest integer.

$$\nu = \frac{\frac{(S_1)^2}{n_1} + \frac{(S_2)^2}{n_2}}{\frac{\left(\frac{(S_1)^2}{n_1}\right)^2}{n_1 - 1} + \frac{\left(\frac{(S_2)^2}{n_2}\right)^2}{n_2 - 1}} \tag{3.3}$$

All mean comparisons were carried out at a significance level of $\alpha = 0.05$ with the rejection criteria

$$-t_{\alpha/2} < t_0 \quad \text{or} \quad t_0 > t_{\alpha/2}$$

Critical values of t were looked up in a table of percentage points $t_{\alpha,\nu}$ of the t-distribution for the relevant number of degrees of freedom shown in (Montgomery and Runger, 2007) (p.711).

3.2.2 Results

3.2.2.1 Surface Roughness

An example of the roughness line profile measurement obtained on the PEEK smooth injection moulded and grit-blasted surfaces are shown in Figures 3.7 and 3.8, respectively, in the longitudinal direction.

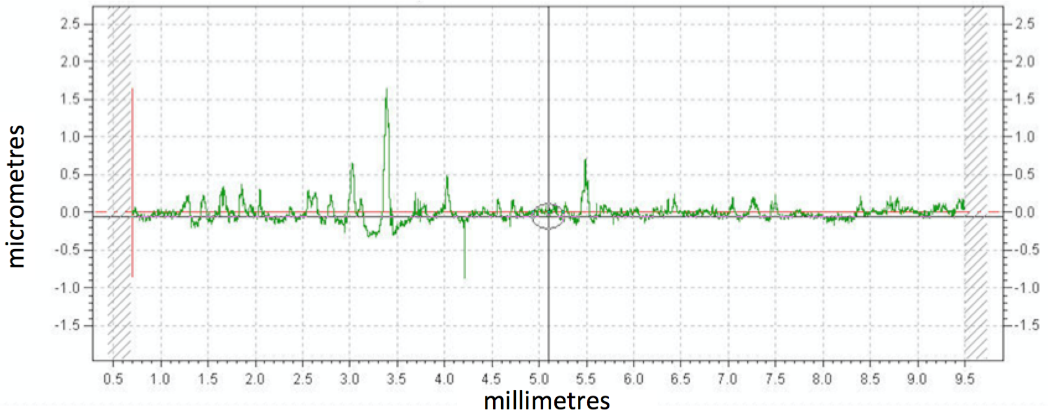

Figure 3.7: Roughness line profile on smooth injection moulded PEEK, with height in μm and length in mm

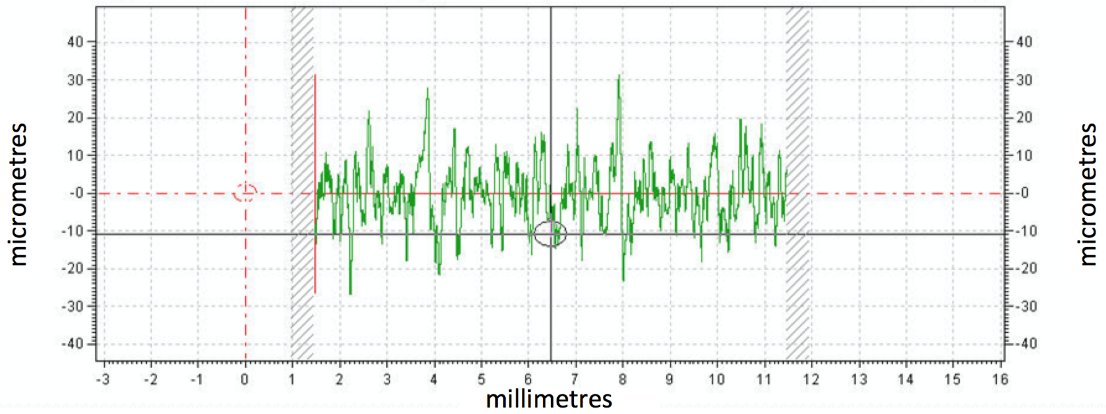

Figure 3.8: Roughness line profile on grit-blasted PEEK, with height in μm and length in mm

For comparison, an example of the roughness line profile measurement obtained in the longitudinal direction on the CFR-PEEK smooth injection moulded and grit-blasted surfaces are shown in Figures 3.9 and 3.10, respectively. Qualitatively, a similar magnitude and density of surface peaks was observed on the grit-blasted PEEK and CFR-PEEK surfaces. However, the smooth injection moulded CFR-PEEK surface had a greater density of surface peaks compared to the injection moulded PEEK surface.

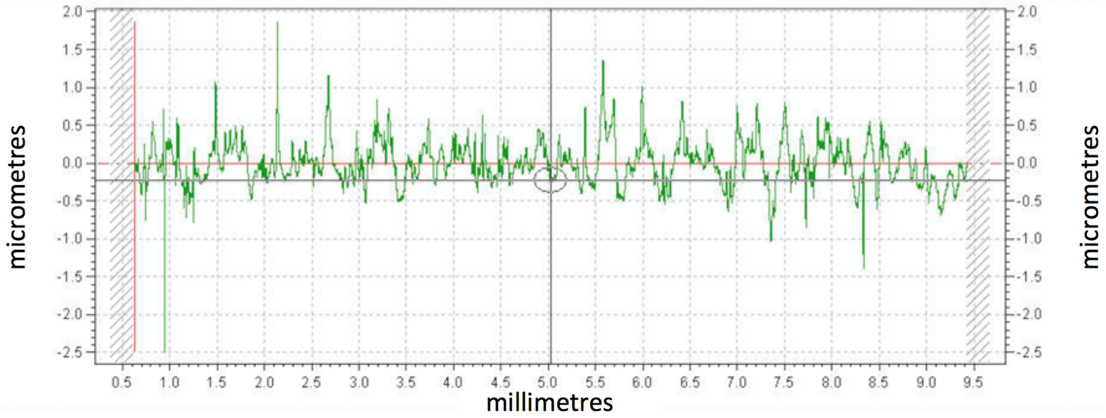

Figure 3.9: Roughness line profile on smooth injection moulded CFR-PEEK, with height in μm and length in mm

The average R_a and R_z measurements of the PEEK and CFR-PEEK samples are shown for each surface finish in Tables 3.2 and 3.3, in the longitudinal and transverse directions, respectively. The smooth injection moulded surface mean R_a of CFR-PEEK was twice that of the PEEK surface. The PEEK injection moulded finish showed directionality in the mean R_a and R_z values in the longitudinal and transverse directions, whereas the CFR-PEEK did not. The R_z values on the grit-blasted CFR-PEEK surfaces were of greater magnitude than on the PEEK surfaces, but the R_a values were of comparable magnitude.

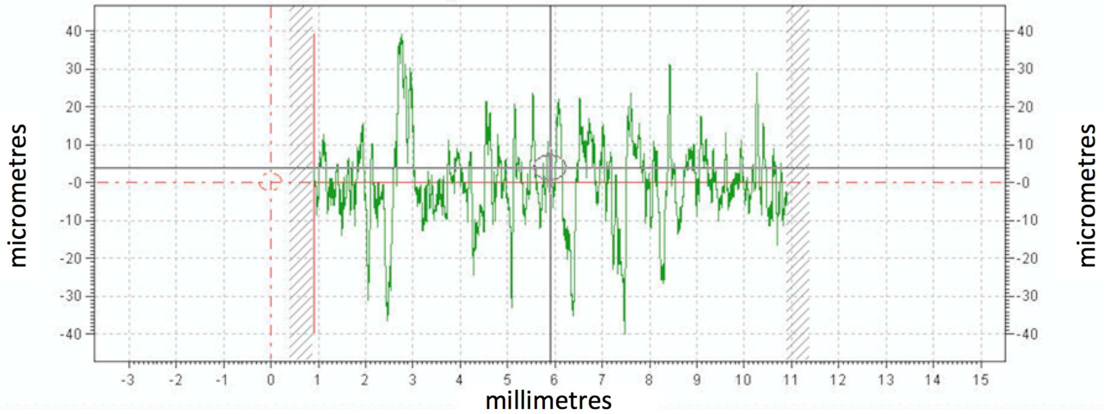

Figure 3.10: Roughness line profile on grit-blasted CFR-PEEK, with height in μm and length in mm

Material	**Surface Finish**	**Longitudinal Direction**			
		R$_a$ μm		**R$_z$ μm**	
		Mean	**S.D.**	**Mean**	**S.D.**
PEEK	Injection moulded	0.07	0.04	0.48	0.27
PEEK	Grit blasted	5.51	0.72	36.93	5.04
CFR-PEEK	Injection moulded	0.23	0.04	1.52	0.21
CFR-PEEK	Grit blasted	5.90	1.08	45.50	6.53

Table 3.2: R$_a$ and R$_z$ longitudinal surface roughness measurements

Material	**Surface Finish**	**Transverse Direction**			
		R$_a$ μm		**R$_z$ μm**	
		Mean	**S.D.**	**Mean**	**S.D.**
PEEK	Injection moulded	0.14	0.03	1.40	0.28
PEEK	Grit blasted	5.34	0.43	37.14	3.11
CFR-PEEK	Injection moulded	0.23	0.03	1.58	0.42
CFR-PEEK	Grit blasted	5.92	1.13	45.15	11.39

Table 3.3: R$_a$ and R$_z$ transverse surface roughness measurements

3.2.2.2 Interfacial Shear Strength

All of smooth injection moulded surface finish PEEK and CFR-PEEK substrates separated from their cement counterparts upon removal from the cementing mould, so could not be tested. A summary of the interfacial shear strength results of the grit-blasted surface finish PEEK and CFR-PEEK samples cemented in the working phase (WP-C) and the premature phase (Pr-C) are shown in Table 3.4. A box plot showing the distribution of the measurements is shown in Figure 3.11.

The results from the Student's t-test are shown in Table 3.5 with each comparison used to determine if there was any significant difference between the shear strength obtained with PEEK or CFR-PEEK, or cementing in the working or premature phase.

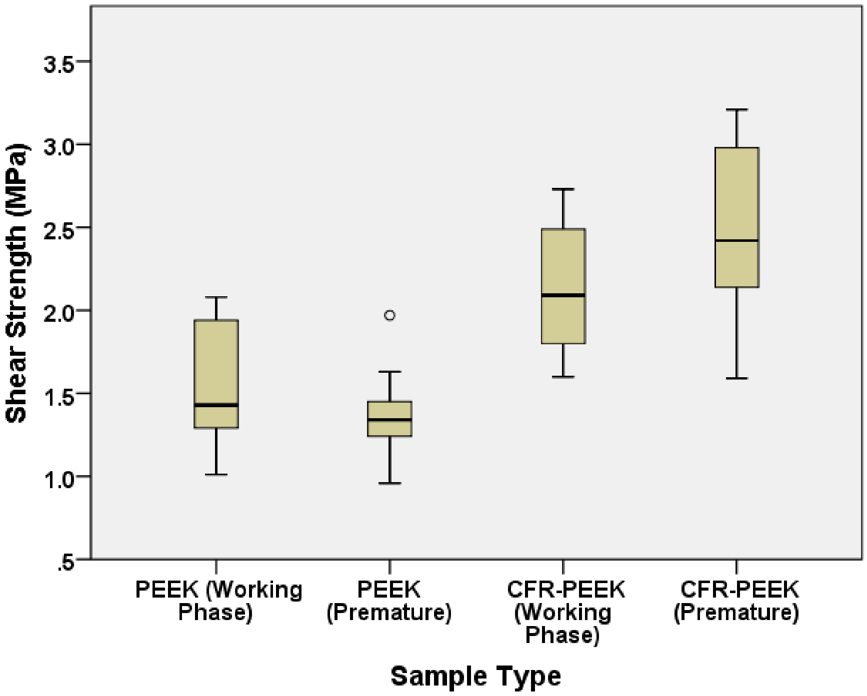

Figure 3.11: Boxplot of shear strength results for the grit-blasted PEEK and CFR-PEEK samples, grouped by the cementing technique (○ = outlier)

Material	Cementing Technique	N	Shear Strength, MPa			Failure Mode
			Mean	S.D.	S.E.	
PEEK	WP-C	10	1.53	0.35	0.11	A
PEEK	Pr-C	10	1.38	0.26	0.08	A
CFR-PEEK	WP-C	10	2.14	0.40	0.13	A+C
CFR-PEEK	Pr-C	10	2.50	0.50	0.16	A+C

Table 3.4: Lap shear strength results for grit-blasted PEEK and CFR-PEEK substrates with cementing in the working phase (WP-C) and premature phase (Pr-C) including number of samples tested, N, standard deviation, S.D., and standard error, S.E.. Failure modes are shown as adhesive (A) (along the interface), or cohesive (C) (through the substrate), or a combination of both (A+C).

There was no significant difference in the shear strength values obtained through cementing in the working phase and premature cementing for either substrate material, but the CFR-PEEK-cement combinations were significantly stronger than the PEEK-cement combinations.

3.2.2.3 Fracture Surface Inspection

The shear fracture surfaces of the grit-blasted PEEK and corresponding cement component can be seen in Figures 3.12a and 3.12b respectively, as observed under the macroscope. Given the colour of each material, there was no clear transfer of material

Two Sample t-test	x	S^2	ν	t_0	$t_{critical}$	**Conclusion**	**Significant**
PEEK, WP-C	1.53	0.12	17	3.63	2.110	reject H_0, $p<0.05$	Yes
CFR-PEEK, WP-C	2.14	0.16					
PEEK, WP-C	1.53	0.12	16	1.09	2.120	accept H_0, $p>0.05$	No
PEEK, Pr-C	1.38	0.07					
CFR-PEEK, WP-C	2.14	0.16	17	1.78	2.110	accept H_0, $p>0.05$	No
CFR-PEEK, Pr-C	2.50	0.25					
PEEK, Pr-C	1.38	0.07	13	6.29	2.160	reject H_0, $p<0.05$	Yes
CFR-PEEK, Pr-C	2.50	0.25					

Table 3.5: Two sample t-test results for the comparison of interfacial shear strength with PEEK and CFR-PEEK materials, and cementing in the working or premature phase, at the 5% significance level.
(G-B = Grit-Blasted, WP-C = Working-Phase-Cemented, Pr-C = Premature phase cemented, x = mean interfacial shear strength (MPa), S^2 = variance, ν = degrees of freedom, t_0 = t statistic)

from either the cement to the PEEK or vice versa. In contrast, transfer of CFR-PEEK material was seen on the cement fracture surface (Figure 3.12d), but no visible transfer of cement to the CFR-PEEK surface was observed (Figure 3.12c).

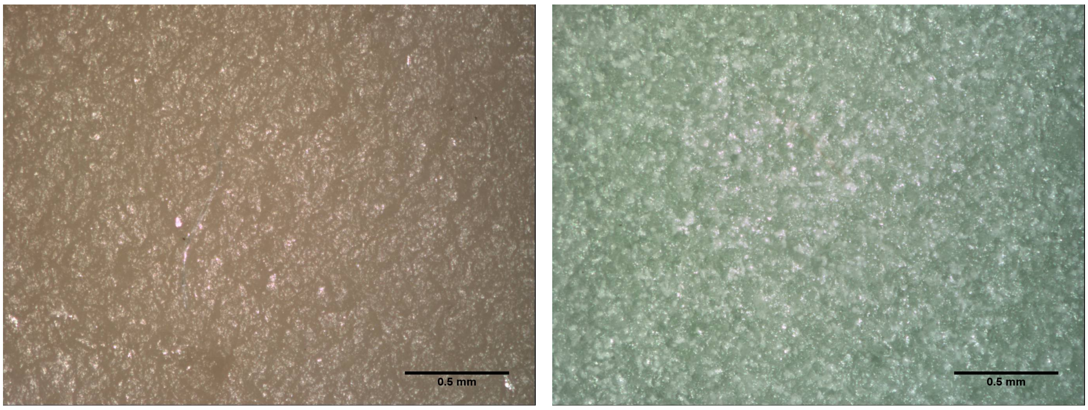

(a) PEEK

(b) Cement (corresponding to PEEK)

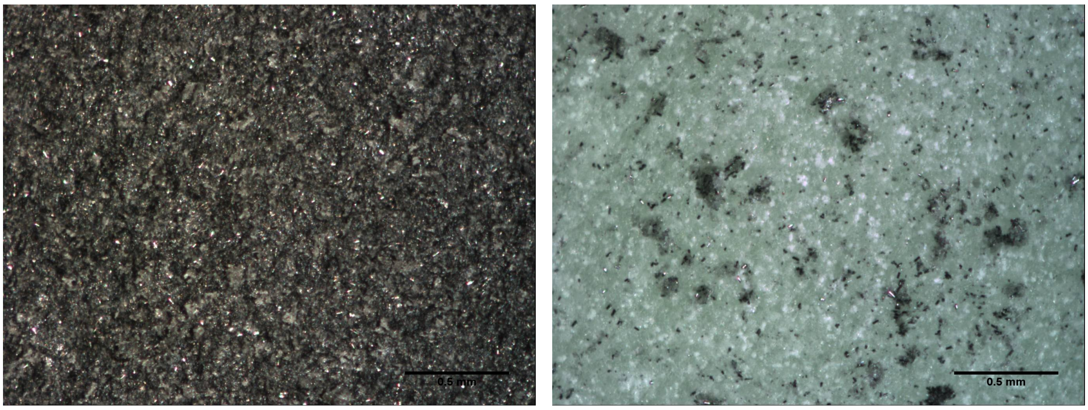

(c) CFR-PEEK

(d) Cement (corresponding to CFR-PEEK) with black CFR-PEEK particles visible

Figure 3.12: Macroscope images of the interfacial shear fracture surfaces at 32x magnification

The PEEK, CFR-PEEK and corresponding cement fracture surfaces were examined at greater magnification using SEM (Figures 3.13 and 3.14). The potential crazing of cement transferred to the PEEK surface was observed with fibril features and round beads of PMMA visible (Figures 3.13b, 3.13d and 3.13f, with the corresponding cement surface in Figure 3.13e). The general shear fracture surface of PEEK is shown observed at 100x and 250x magnification (Figures 3.13a and 3.13c).

The CFR-PEEK fracture surfaces were observed under SEM, with surface cavities suggesting fibre pullout (Figures 3.14a and 3.14b). Fibres were not clearly observed on the corresponding cement fracture, although there are tube-like ridges (Figures 3.14c and 3.14d).

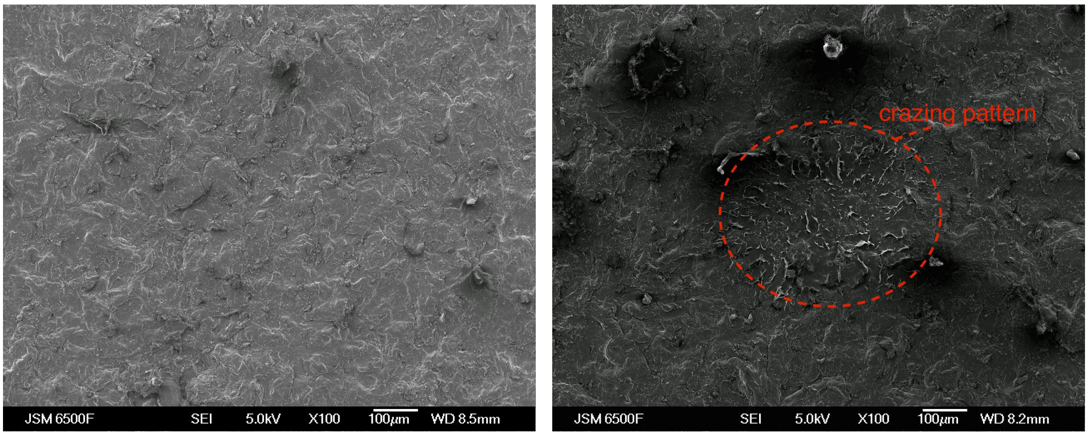

(a) General observation of PEEK fracture surface, x100 magnification

(b) Local observation of PEEK fracture surface with possible cement crazing, x100 magnification

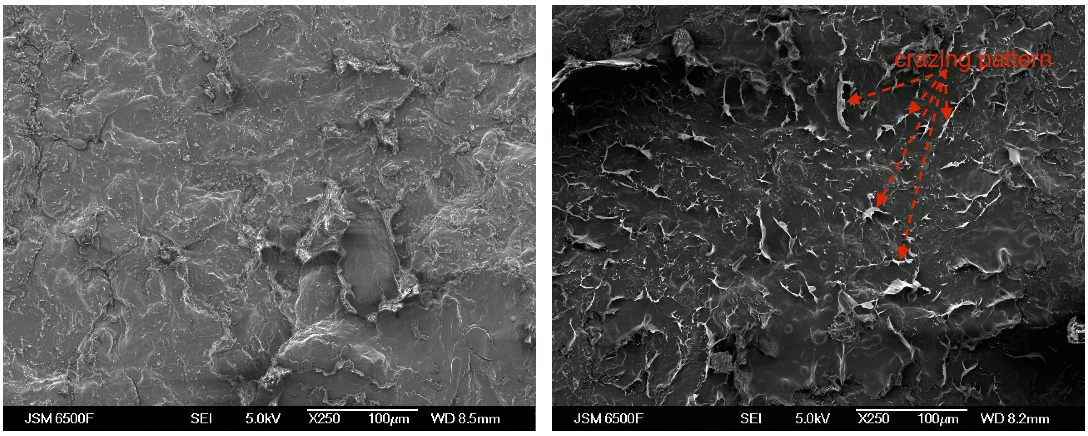

(c) General observation of PEEK fracture surface, x250 magnification

(d) Local observation of PEEK fracture surface with possible cement crazing, x250 magnification

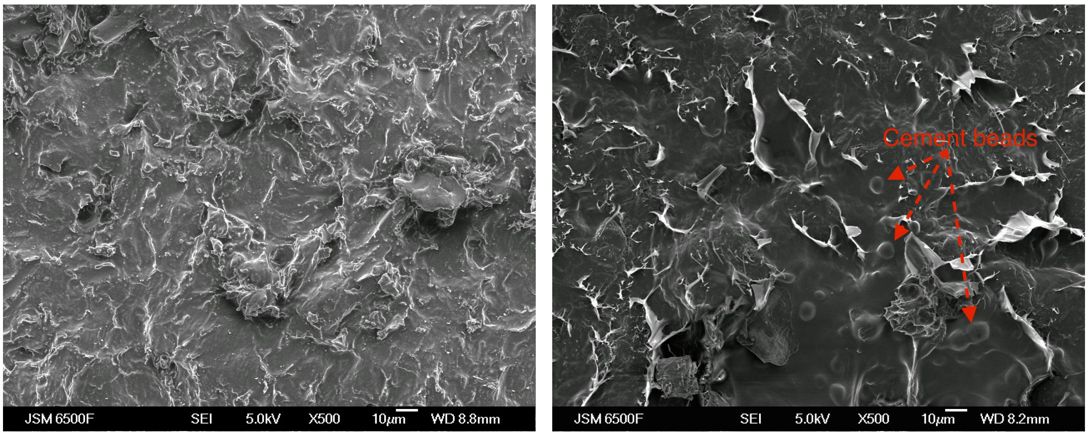

(e) High magnification of cement fracture surface corresponding to PEEK, x500 magnification

(f) Local observation of PEEK fracture surface with possible cement crazing, x500 magnification

Figure 3.13: SEM images showing possible crazing of bone cement on the shear fracture surface of PEEK

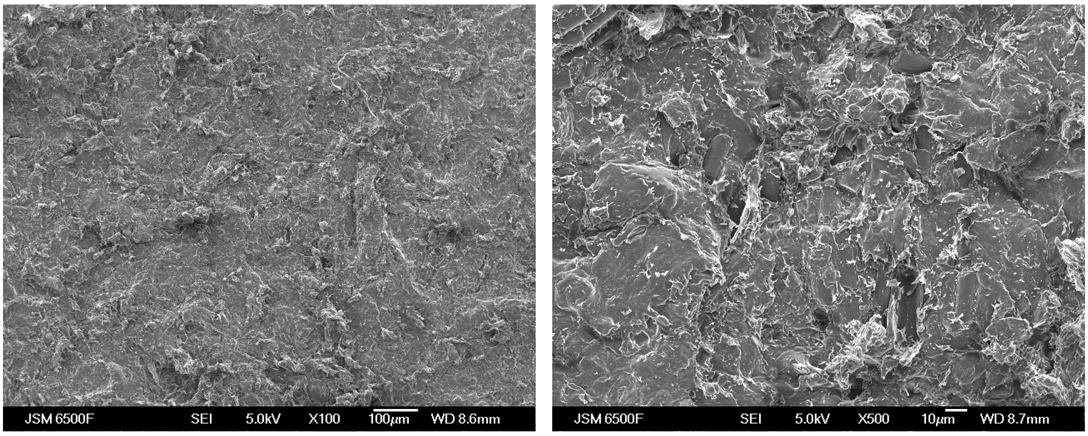

(a) CFR-PEEK fracture surface, x100 magnification

(b) CFR-PEEK fracture surface, x500 magnification

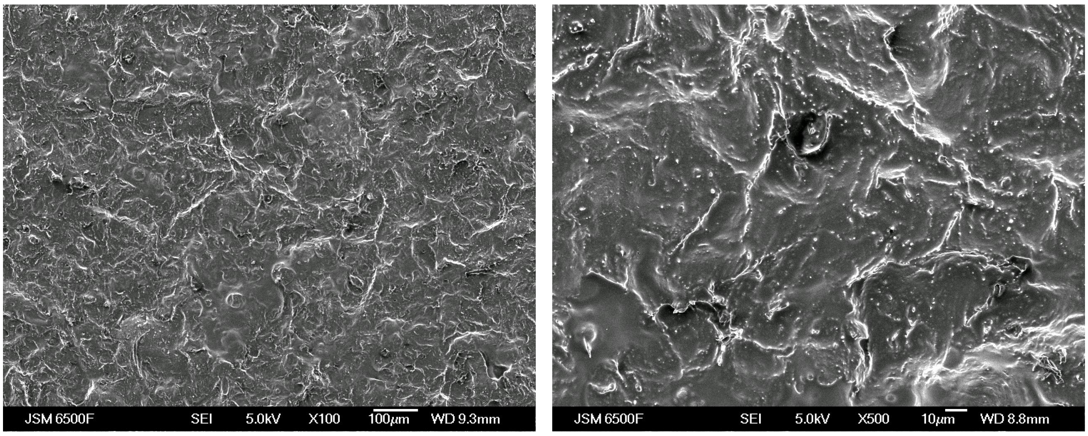

(c) Cement fracture surface corresponding to CFR-PEEK, x100 magnification

(d) Cement fracture surface (corresponding to CFR-PEEK), x500 magnification

Figure 3.14: SEM image of CFR-PEEK shear fracture surface and the corresponding cement shear fracture surface

3.3 PEEK Surface Topography Study

An investigation into the effect of surface topography on the PEEK-cement interfacial strength was carried out using sixteen different injection moulded textures to determine how to improve the interfacial shear strength at the femoral component-cement interface through mechanical keying.

3.3.1 Methodology

3.3.1.1 Materials

PEEK-OPTIMA® (PEEK) plates were used for the surface topography study, as the material of choice for the TKR femoral component. Twelve textures were created on

PEEK plates by different injection moulding tools. These textures were grouped into “micro-textures”, defined by the microscale surface features (short-wave component, surface roughness), “macro-textures without directionality” and “macro-textures with directionality”, defined by the macroscale surface features (long-wave component, surface waviness). The “micro-textures” group comprised of injection moulded grit-blasted effect surfaces ranging from a fine to a coarse grade (Figure 3.15a). The “macro-textures without directionality” were split into two further groups of male (outward) and female (inward) pattern types, (Figures 3.15b and 3.15c respectively), as were the “macro-textures with directionality” with male types (Figures 3.15d and 3.15e) and a female type (Figure 3.15f).

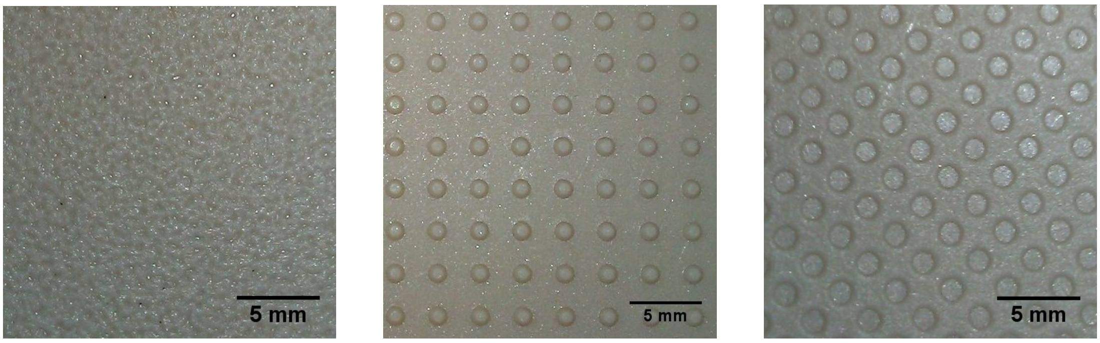

(a) Micro-textures: injection moulded grit-blasted effect

(b) Macro-textures without directionality: Convex conical frustums pattern (male)

(c) Macro-textures without directionality: Concave conical frustums pattern (female)

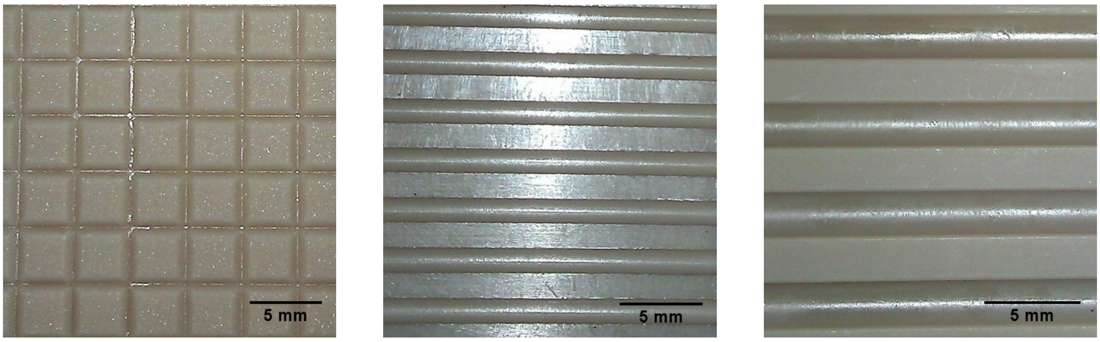

(d) Macro-textures with directionality: Waffle pattern (male)

(e) Macro-textures with directionality: Ribbed pattern (male)

(f) Macro-textures with directionality: Trough pattern (female)

Figure 3.15: Grouping of PEEK plates with injection moulded surface features

An additional sample group was then created to combine the short and long-wave components of roughness in a “micro-macro-textured” injection moulded PEEK plate, Figure 3.16, to determine if the interface strength could be further enhanced. Two surfaces were created with the same micro-texture and rib spacing, but with rib depths of 1 mm and 2 mm.

Figure 3.16: Sample group with a combination of short and long-wave roughness components: micro and macro injection moulded features

Seven plates of gritblasted CoCr were used as the metallic control group. Each plate was cemented using Palacos R bone cement ($E = 2.87$ GPa) (Heraeus Medical GmbH, Wehrheim, Germany) using the procedure described in the sample preparation section (3.3.1.3). As a different viscosity bone cement was used in this study, compared to the preliminary study, another set of grit-blasted PEEK plates were tested as the PEEK control group.

3.3.1.2 Surface Topography Analysis

A non-contact surface profilometer was used to scan the interface area of the textured PEEK plate samples, such that the interfacial surface contact area and cement interlock volume could be approximated for each surface finish. A 3D laser scanner profilometer (TaiCaan Xyris 2000 TL) was used to measure surface form with change in height from a reference point, through the use of a dual detector triangulation laser system with a 30 μm spot size (Figure 3.17). This system improves the accuracy of the sensor by allowing the range of the signal, (the distance travelled to the surface), to be validated (Blais, 2004). The 25 x 25 mm^2 surface areas were scanned to generate a 501 x 501 (lateral spatial resolution = 50 μm) data point cloud of vertical (z) height measurements in the lateral directions (x and y). The data was built into a 3D topological surface map using the TaiCaan Boddies software and a ‘volume/area calculation’ tool was used to measure the surface area and volume between boundary conditions of a set height (TaiCaan Technologies Europe, Southampton, UK).

Profile surface roughness could not be evaluated using the contact profilometer method in section 3.2.1.2 on all of the surfaces due to the maximum evaluation length available on the sample surface (25 mm) compared to that required by ISO 4288 for very rough surfaces. The Alicona Infinite Focus (Alicona Imaging GmbH, Graz, Austria) is an

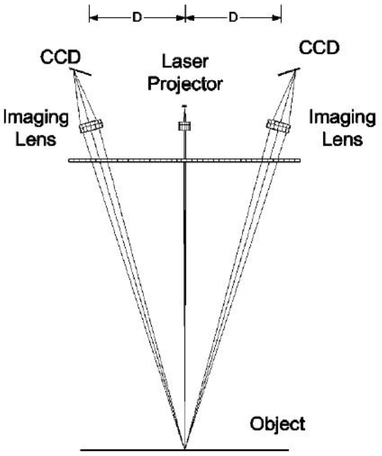

Figure 3.17: Dual detector triangulation system, as used in the TaiCaan Xyris 2000 TL (Blais, 2004)

optical 3D micro co-ordinate system that uses focus variation for form and roughness measurement. This was used to assess the surface roughness using line profile measurements and areal surface texture for 3D surface features. A sample region on each PEEK surface was selected to represent the entire surface topography. Complete 25 x 25 mm^2 interface area surface scans were not possible at the resolution necessary for surface roughness assessment, as the data captured within this region exceeded the capabilities of the computer and IF-MeasureSuite analysis software. Surface scans were carried out between specified vertical height boundaries such that a 3D surface topography could be obtained. A polariser was used to achieve optimal contrast across the PEEK surfaces with complex geometry, which suffered from saturation of the image pixel histogram due to surface reflections. The Alicona user manual was followed to select suitable objective lenses and cutoff values for the surface measurements (Alicona IF-MeasureSuite version 5.1 Manual, December 2013, Alicona Imaging GmbH, Graz, Austria). The ImageField function was used to scan across larger surface features exceeding the field of view. The line profile roughness measurements were compared for each sample type using R_a (arithmetic mean of the roughness profile), R_z (mean peak to valley height of the roughness profile), R_q (Root-Mean-Square roughness of the profile), and R_{sk} (skewness of the roughness profile). The surface area and volume measurements were obtained from the software, and an estimate was made for the complete interface area by multiplying the measurement by the proportion of the area that the sample region occupied. These measurements were then compared to those obtained using the TaiCaan laser profilometer and the corresponding mean interfacial shear strength measurements. The relationship between areal surface roughness and interfacial shear strength was also investigated, using S_a (average height of the area), S_z (maximum height of the area),

S_q (Root-Mean-Square height of the area), and S_{sk} (skewness of the area).

3.3.1.3 Lap Joint Sample Preparation

The textured PEEK plates were cemented using the same mould as in the preliminary study (Figure 3.4 in section 3.2.1.3), but Palacos R cement was mixed using the PALAMIX system (Heraeus Medical GmbH, Wehrheim, Germany) under vacuum assisted conditions to reduce porosity content.

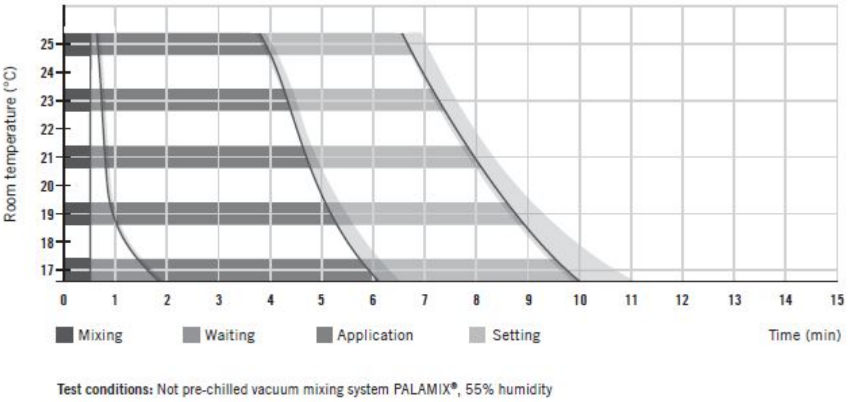

Test conditions: Not pre-chilled vacuum mixing system PALAMIX®, 55% humidity

Figure 3.18: Working time for the vacuum assisted mixing of Palacos R bone cement using a PALAMIX system, not pre-chilled (Palacos R, Heraeus Medical GmbH, Philipp-Reis-StraBe 8/13 61273 Wehrheim, Germany)

The cement was then injected onto the PEEK surface at the appropriate application time according to the manufacturer's guidance (Figure 3.18), before it was finger packed into the mould. After 15 minutes of cure time under pressure, the PEEK-cement samples were removed from the mould, and left for 72 hours before the lap shear tests were carried out. The grit-blasted CoCr control group was cemented using the same conditions.

3.3.1.4 Lap Shear Test Procedure

The cemented samples were tested using the same technique described for the preliminary study in section 3.2.1.4. An Instron 5569 electromechanical test machine was used to apply a tensile load to the lap joint sample (Figure 3.19) with a ramped displacement of 2 mm/min to induce shear stress at the interface, until failure occurred with complete separation of the substrates. The peak failure load was then used to calculate the interfacial shear strength (Equation 3.1 in section 3.2.1.4). Again, the failure mode was recorded as adhesive (A), cohesive (C) or a combination of both (A+C).

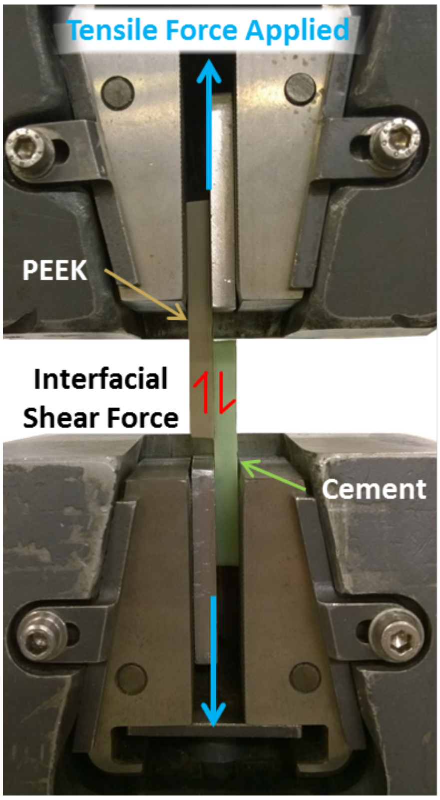

Figure 3.19: Lap shear test setup

3.3.1.5 Statistical Analysis - ANOVA Multiple Comparisons Test

As the independent samples t-test only allows for comparisons to be made between two samples at a time, the analysis of variance method (ANOVA) was employed to include all conditions of the independent variable, (in this case surface textures), in one comparative test of the difference in the dependent variable (interfacial shear strength). The ANOVA test measures the variability in scores between the conditions of the independent variable and variability in scores due to random factors and error by generating a variance ratio value, F (Hinton et al., 2004). The value of F indicates if there is large variability caused by an effect of the independent variable on the dependent variable, but not which conditions of the independent variable are causing it, i.e. which surface finish is producing a significantly higher shear strength. Further, post hoc, multiple comparisons tests then allow differentiation between conditions, to appreciate which condition of the independent variable is having what effect on the dependent variable.

The one factor independent measures design ANOVA was used to analyse the shear strength results data in IBM SPSS Statistics (version 20, IBM Corp. USA) at the 5% significance level. Fifteen comparisons were made with each sample surface finish type as the independent 'factor' and interfacial shear strength as the 'dependent list'. A

Tukey post hoc multiple pairwise comparison test was carried out for all possible condition combinations (with equal variances assumed), producing a significance value for the mean difference between the identifier group (I) and the second group for comparison (J) with 95% confidence intervals. The 95% confidence interval complements the significance level, indicating there may be a difference if the range is large and includes zero (i.e. it ranges from a negative value to a positive value), even if the significance value is greater than the test value ($p>0.05$).

3.3.2 Results

3.3.2.1 Surface Topography Analysis

The surface profiles of the micro- and macro-textured PEEK plates obtained with the laser profilometer are shown in Figure 3.20. The gritblasted PEEK and CoCr are shown in Figures 3.20a and 3.20b, respectively, for comparison with the injection moulded PEEK grit-blasted effect textures in Figures 3.20c to 3.20f. The random orientated textures are shown in Figures 3.20g and 3.20h and the conical patterns tested are shown in Figures 3.20i and 3.20j. The textures with directionality are shown in Figures 3.20k to 3.20n. The micro-macro-texture combination samples were injection moulded after the laser profilometer became unavailable for use, so cannot be presented for comparison using this technique.

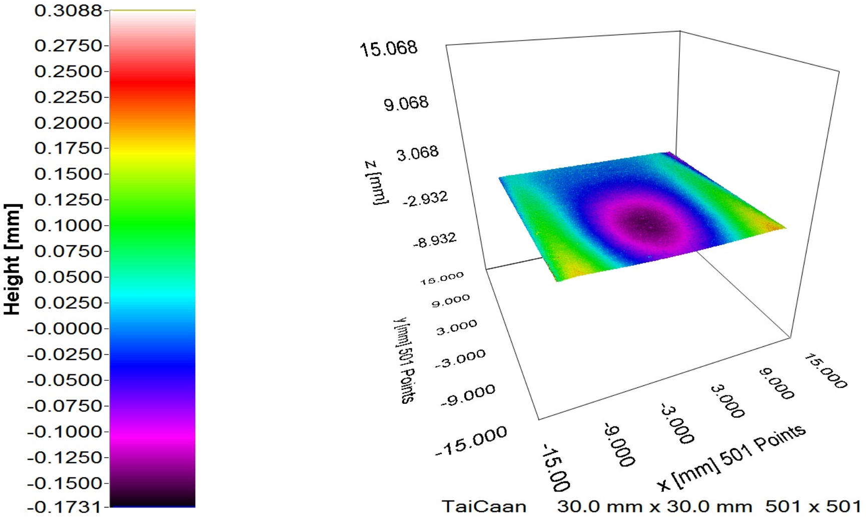

(a) Grit-blasted PEEK

Figure 3.20: 3D surface profile scans from the laser profilometer

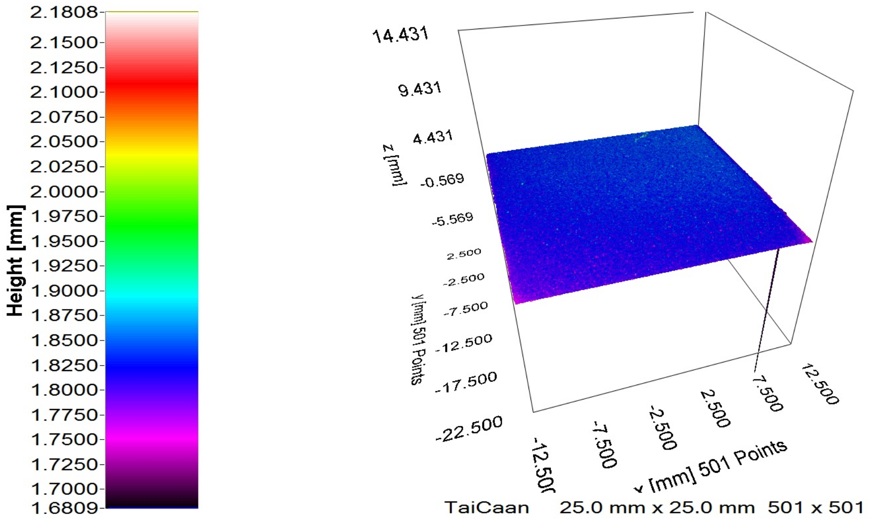

(b) CoCr (grit-blasted, control sample)

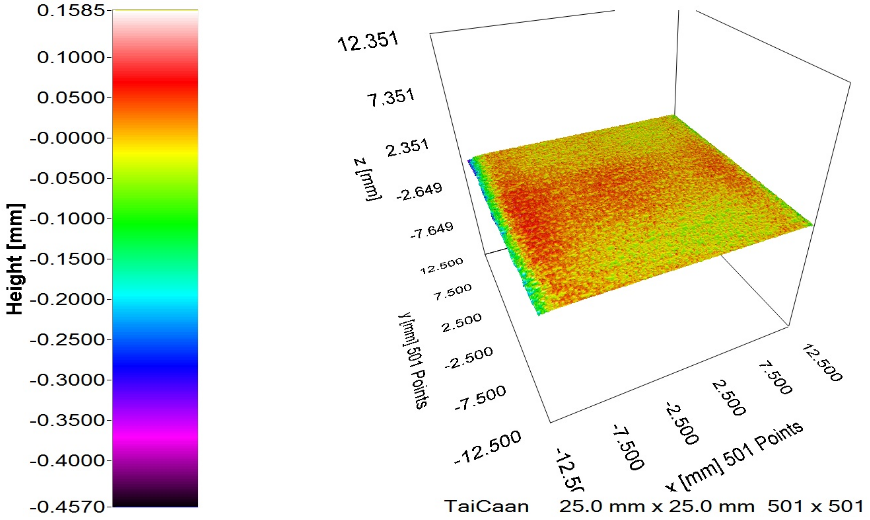

(c) Micro-roughened effect 1

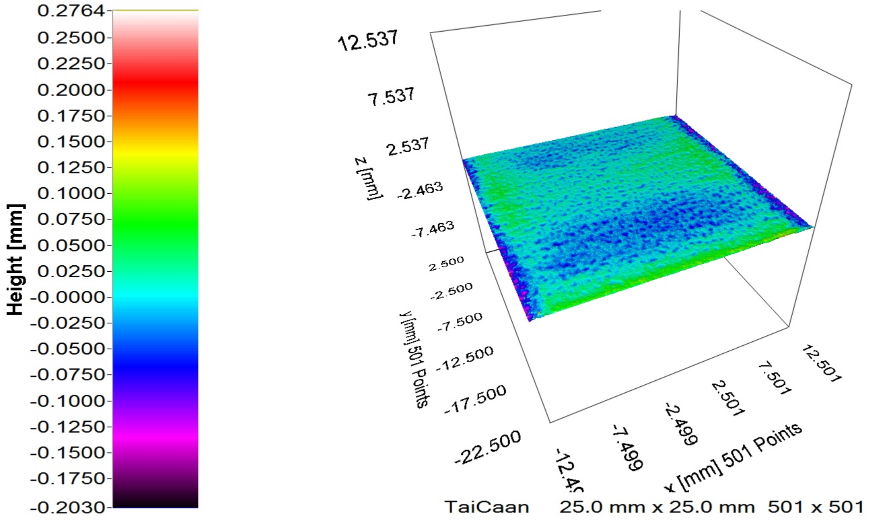

(d) Micro-roughened effect 2

Figure 3.20: 3D surface profile scans from the laser profilometer

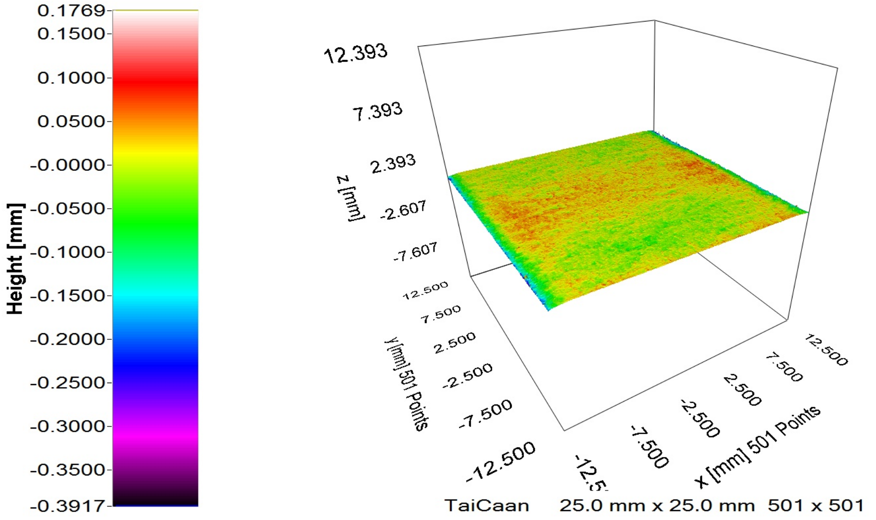

(e) Micro-roughened effect 3

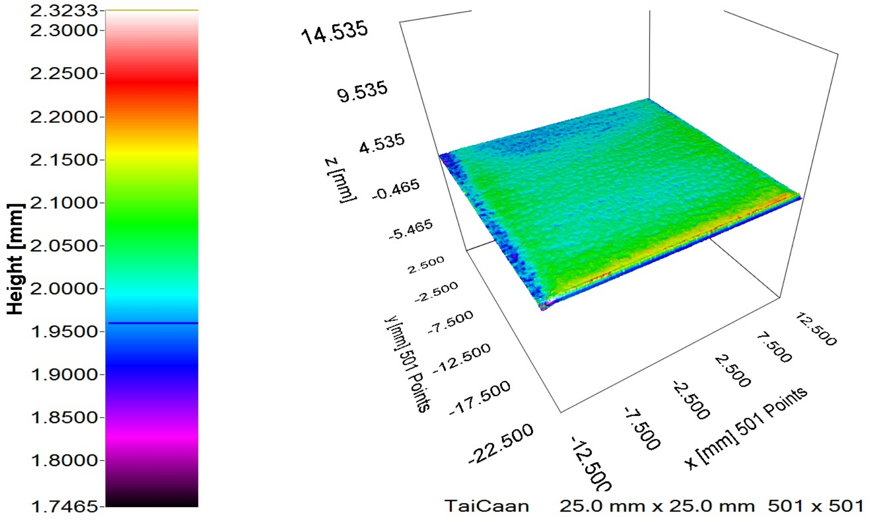

(f) Micro-roughened effect 4

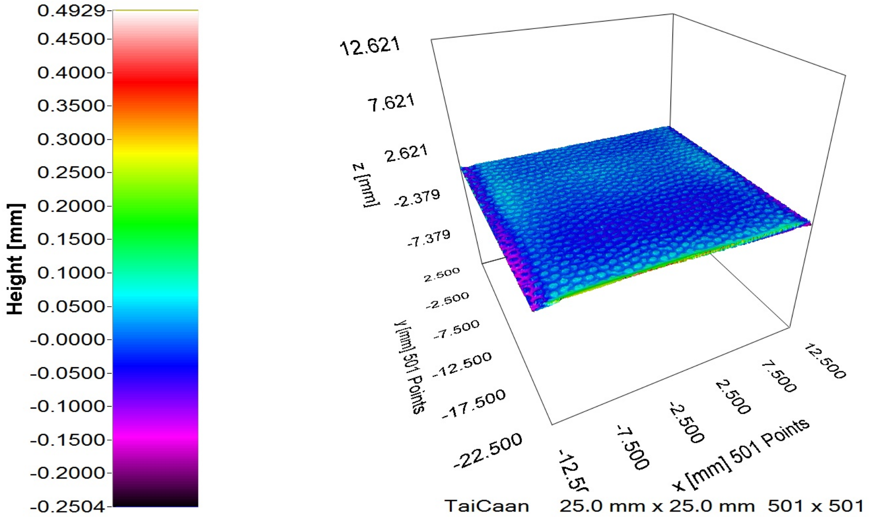

(g) Scaled effect

Figure 3.20: 3D surface profile scans from the laser profilometer

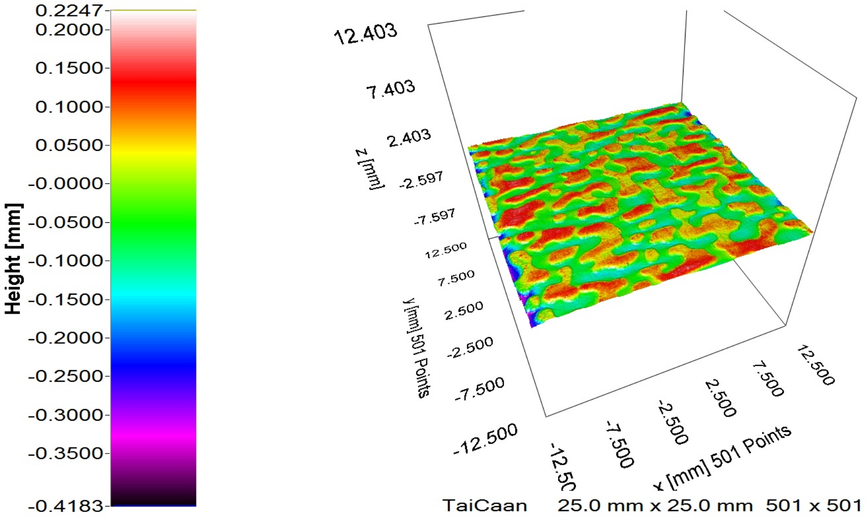

(h) Random protuberances

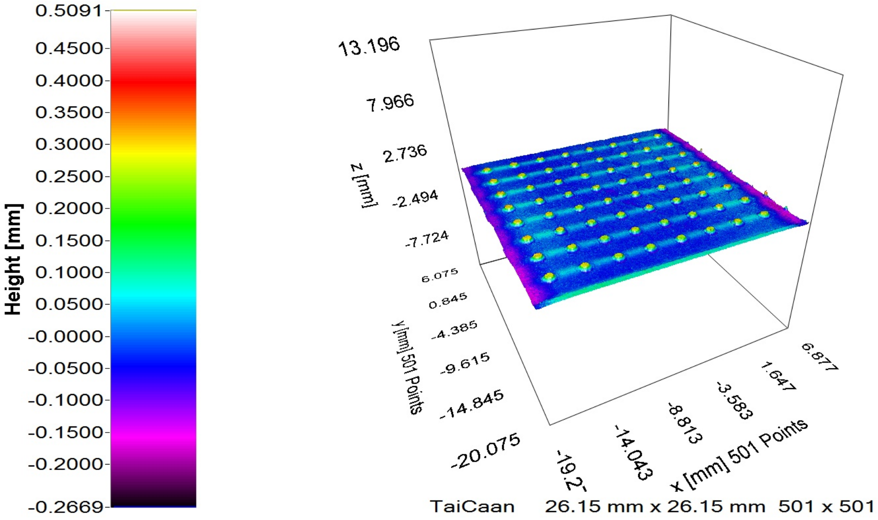

(i) Conical frustums

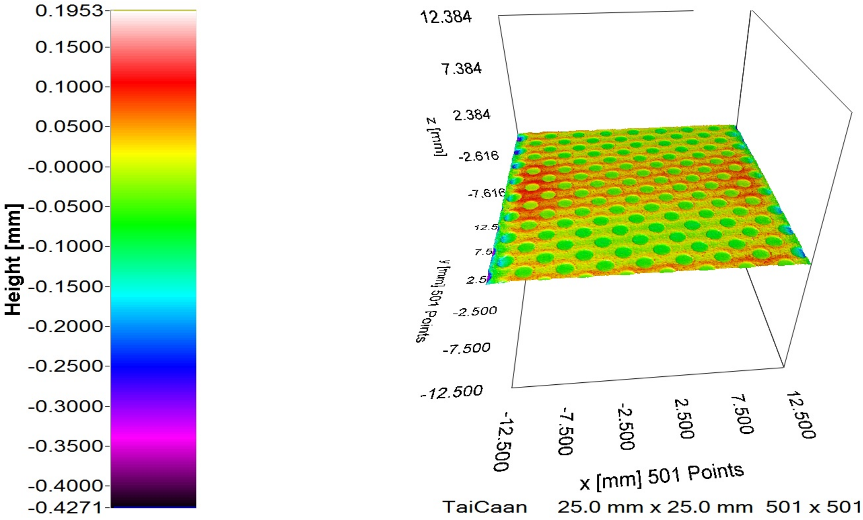

(j) Inverted conical frustums

Figure 3.20: 3D surface profile scans from the laser profilometer

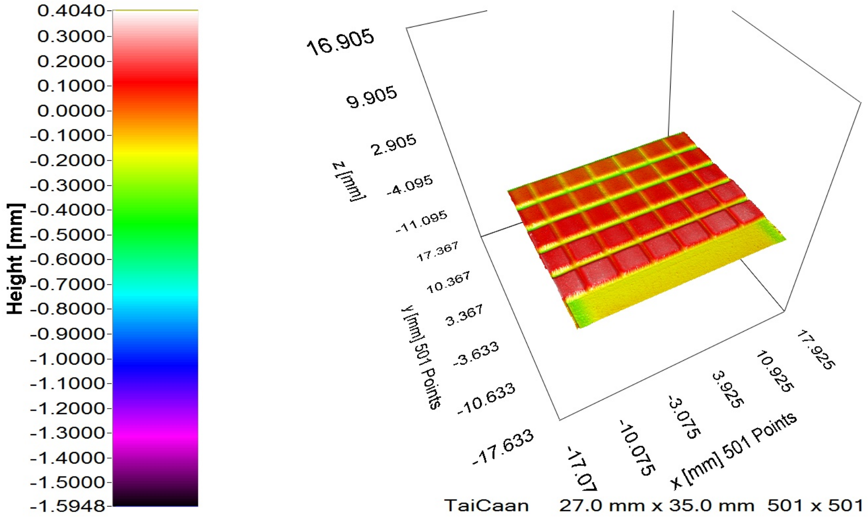

(k) Waffle

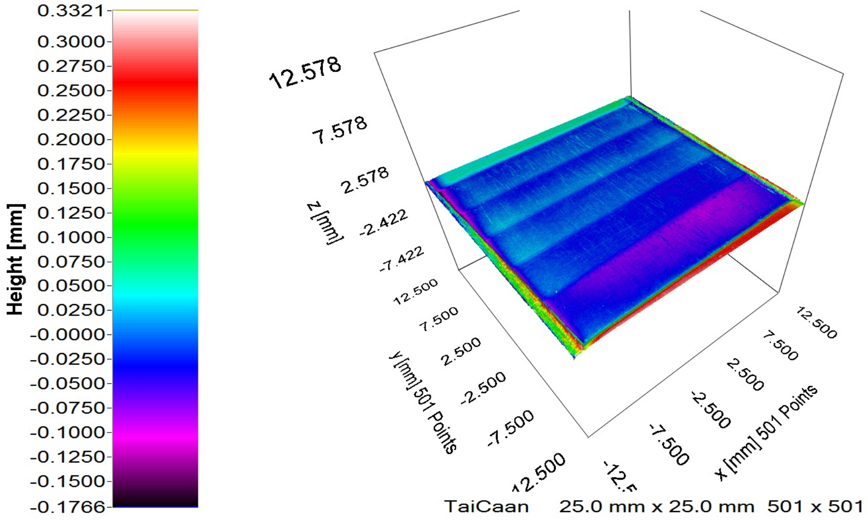

(l) Saw tooth

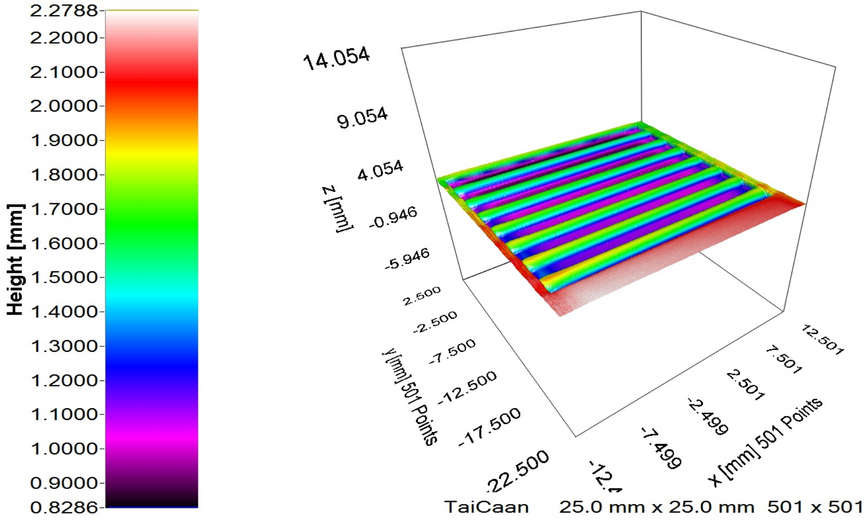

(m) Macro Ribbed

Figure 3.20: 3D surface profile scans from the laser profilometer

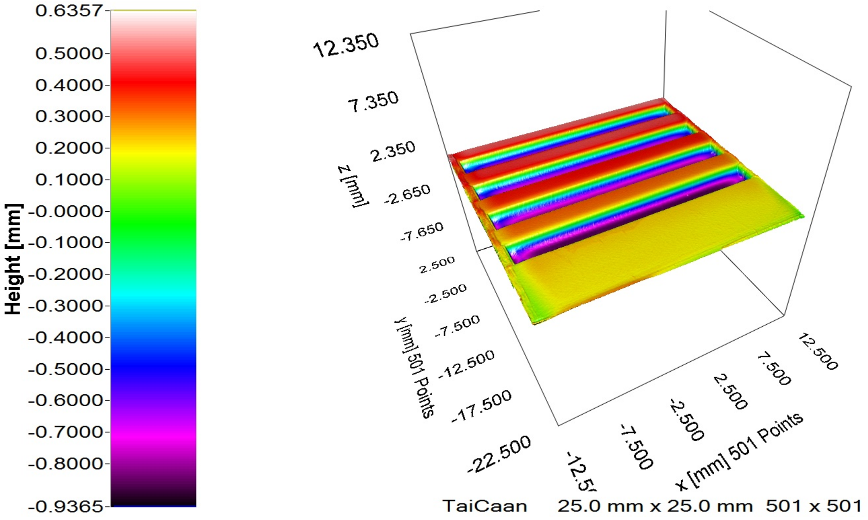

(n) Macro Troughed

Figure 3.20: 3D surface profile scans from the laser profilometer

The surface scans were used to calculate the surface interlock parameters (Table 3.6), which are plotted against the corresponding interfacial shear strength values in Section 3.3.2.2.

Sample Type	**Texture Group**	**Area, mm^2**	**Volume, mm^3**
Grit-Blasted	micro	644	30.2
CoCr (control)	micro	647	5.8
Waffle	macro (directional, male)	734	63.8
Conical frustums	macro (male)	731	20.6
Inverted conical frustums	macro (female)	691	21.4
Micro-roughened 1	micro	685	13.7
Scaled effect	micro	671	15.7
Micro-roughened 2	micro	662	12.8
Micro-roughened 3	micro	665	12.9
Micro-roughened 4	micro	646	12.2
Random protuberances	macro (male)	689	37.6
Macro Ribbed	macro (directional, male)	774	161.2
Macro Troughed	macro (directional, female)	775	194.5
Sawtooth	macro (directional, male)	659	20.2

Table 3.6: Interface surface area and interlock volume (male side) data for textured PEEK and CoCr control sample groups, predicted from the laser profilometer measurements

Three examples of the 3D surface topography maps obtained using the optical focus variation microscope system are shown for micro-, macro- and micro+macro- texture groups in Figures 3.21, 3.24 and 3.27 respectively.

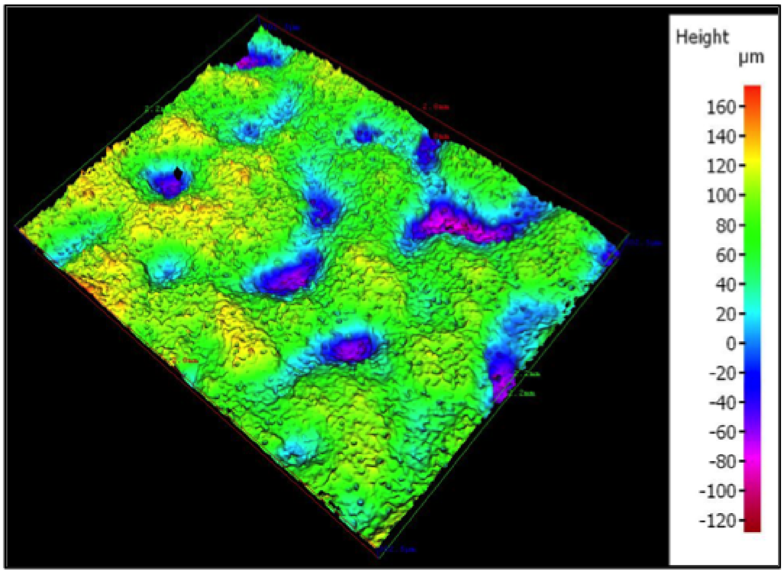

Figure 3.21: Example of micro-textured surface topography: Micro-roughened effect 4

The full sample region and analysis path for the line profile used on the micro-roughened PEEK surface is shown in Figure 3.22, with the corresponding roughness profile in Figure 3.23.

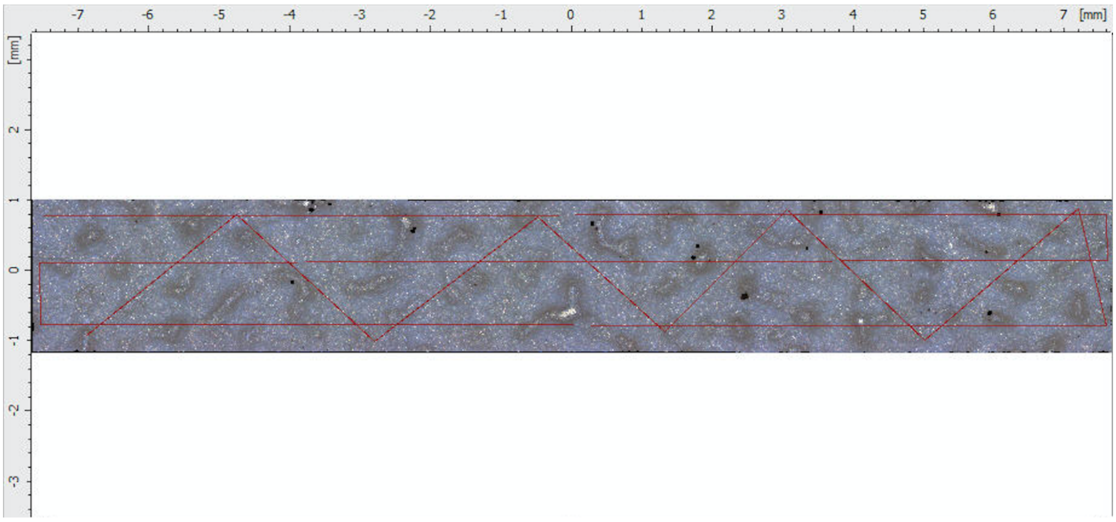

Figure 3.22: Line profile path on the Micro-roughened textured surface

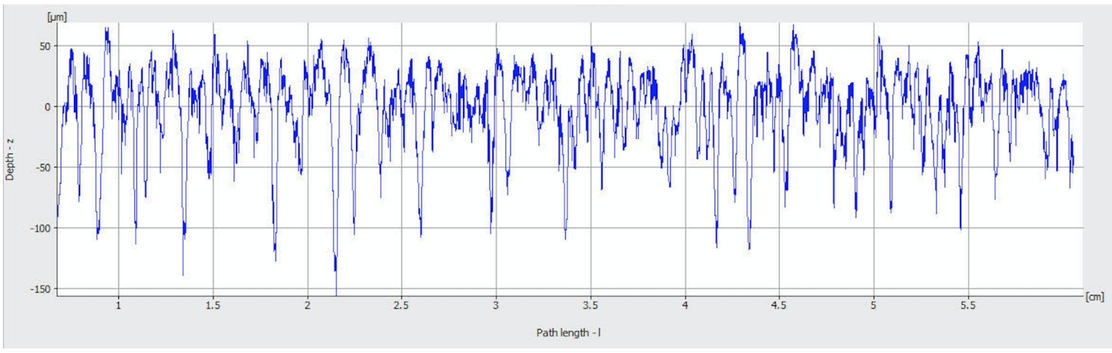

Figure 3.23: Line roughness profile (cut-off, $\lambda_c = 8000\ \mu$m) on the Micro-roughened textured surface, with $R_a = 26.4\ \mu$m, $R_z = 184.1\ \mu$m, and $R_q = 34.5\ \mu$m (x-axis = path length in cm and y-axis = depth in μm).

The majority of the surface features on the micro-textured surfaces could be captured using the optical focus variation microscope system, without large regions of missing data. However, the steep edges of the macro-textured surface features caused difficulty in imaging, and as a result, there were large gaps in the surface topography data (shown by the black regions in Figure 3.24). The full sample region and analysis path for the line profile used on the Macro Troughed textured PEEK surface is shown in Figure 3.25, with the corresponding roughness profile in Figure 3.26.

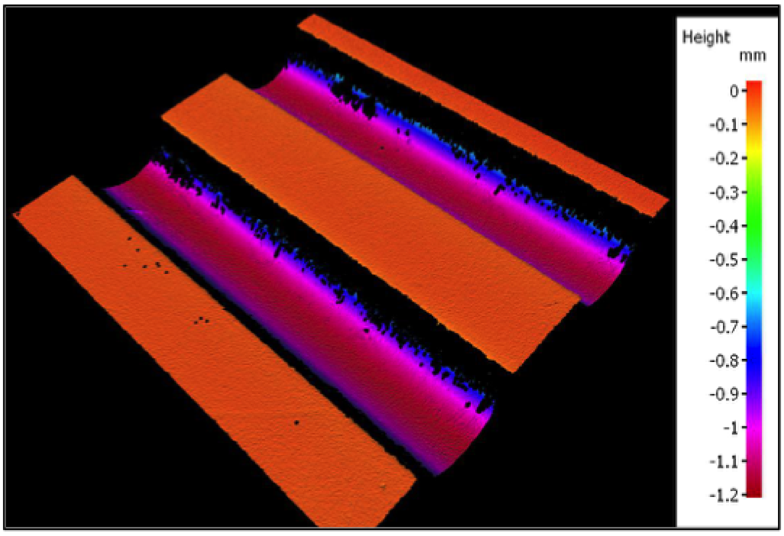

Figure 3.24: Example of macro-textured surface topography from the optical focus variation microscope system: Macro Troughed

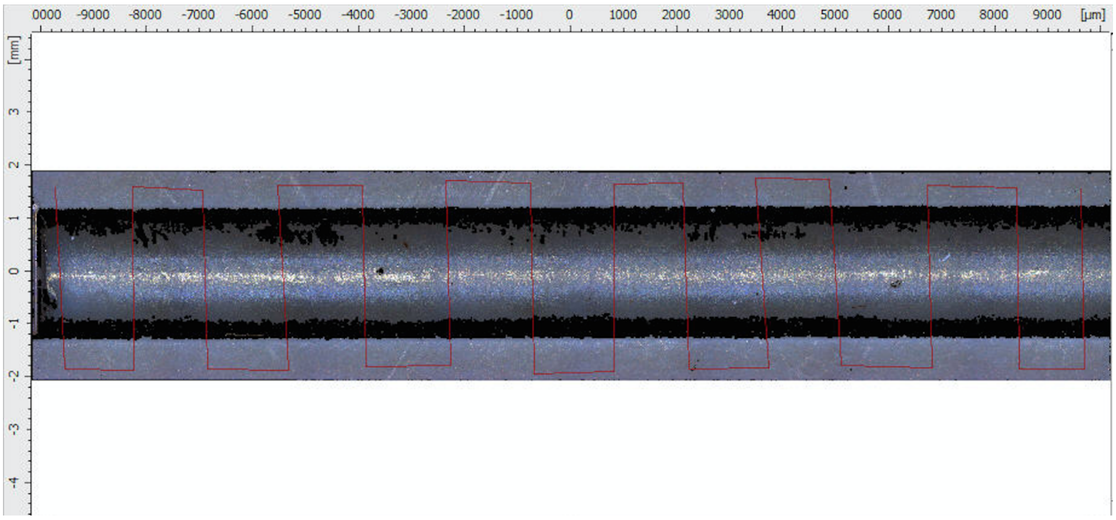

Figure 3.25: Line profile path on the Macro Troughed textured surface

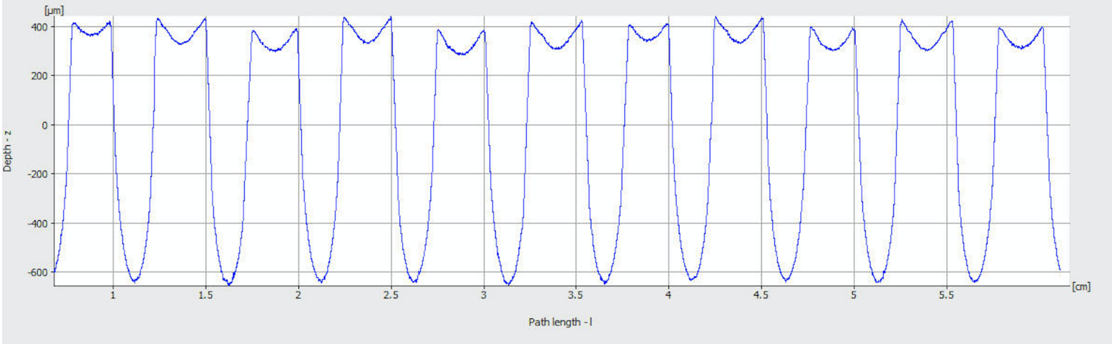

Figure 3.26: Line roughness profile (cut-off, $\lambda_c = 8000\ \mu$m) on the Macro Troughed textured surface, with $R_a = 392.1\ \mu$m, $R_z = 1100\ \mu$m, and $R_q = 416.6\ \mu$m (x-axis = path length in cm and y-axis = depth in μm).

The steep edges on the Micro-rough + Macro Ribbed textured surface also left gaps in the topography data (Figure 3.27). However, the use of the polariser enabled data capture across a larger proportion of the sample region on the surface, and reduced the large changes in contrast and intensity caused by the reflectivity of the PEEK surface.

The full sample region and analysis path for the line profile used on the Micro-rough + Macro Ribbed PEEK surface is shown in Figure 3.28, with the corresponding roughness profile in Figure 3.29.

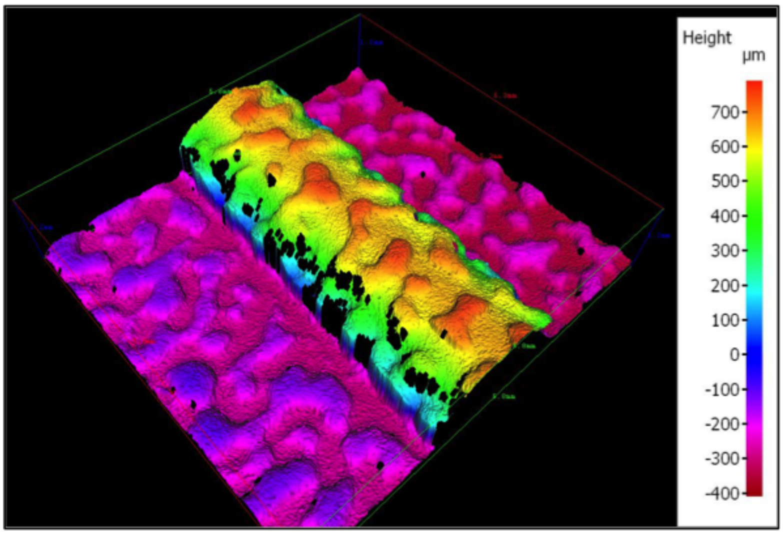

Figure 3.27: Example of micro+macro-textured surface topography from the optical focus variation microscope system: Micro-rough + Macro Ribbed (1 mm depth)

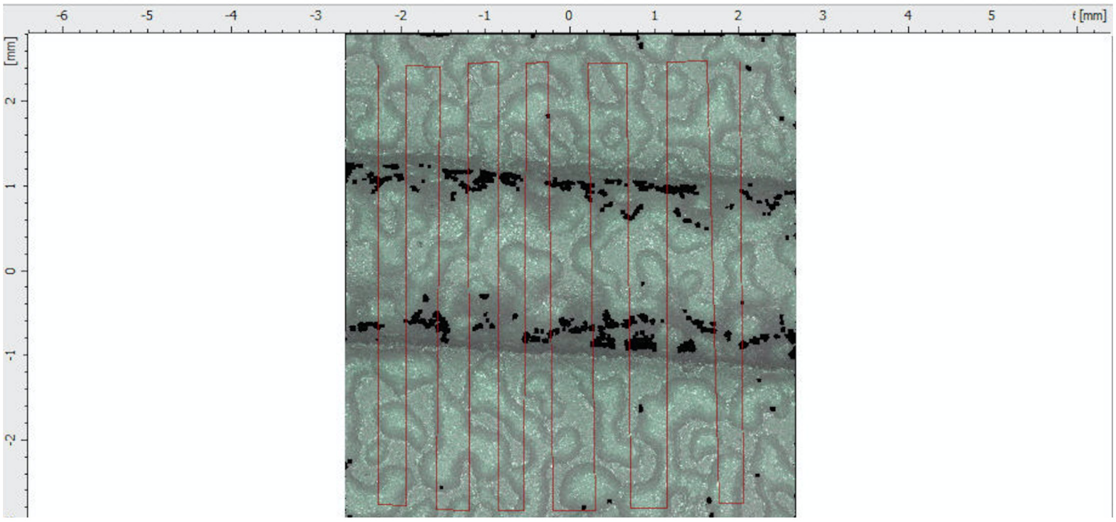

Figure 3.28: Line profile path on the Micro-rough + Macro Ribbed (1 mm depth) textured surface

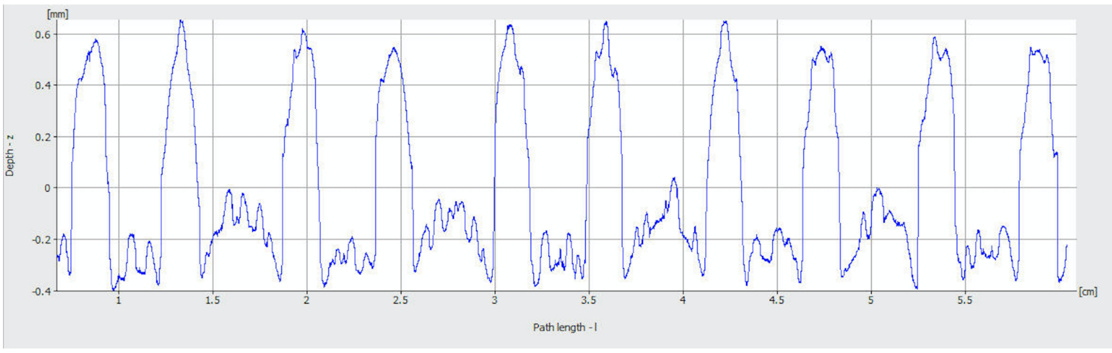

Figure 3.29: Line roughness profile (cut-off, $\lambda_c = 8000$ μm) on the Micro-rough + Macro Ribbed (1 mm depth) textured surface, with $R_a = 291.5$ μm, $R_z = 1000$ μm, and $R_q = 328.8$ μm (x-axis = path length in cm and y-axis = depth in μm).

3.3.2.2 Interfacial Shear Strength

The lap-shear test results for the textured samples are shown in Table 3.7 with their respective surface roughness magnitudes and failure modes. The box plot graph in Figure 3.30 shows the distribution in shear strength data for examples of each PEEK surface texture group. A box plot showing the distribution in shear strength data for every textured sample group tested is shown in Appendix 4 (Figure 1).

Sample	N	Mean Shear Strength, MPa	S.D., MPa	S.E., MPa	Failure Mode
Grit Blasted	10	1.23	0.22	0.07	A
Waffle	10	1.24	0.42	0.13	A
Conical frustums	10	1.06	0.31	0.10	A
Inverted conical frustums	6	0.77	0.04	0.02	A
Micro-roughened	6	0.91	0.33	0.13	A
Scaled	6	1.18	0.15	0.06	A
Micro-roughened 2	6	0.52	0.23	0.10	A
Micro-roughened 3	6	0.51	0.28	0.12	A
Micro-roughened 4	6	1.35	0.10	0.04	A
Random protuberances	6	0.94	0.32	0.13	A
Macro Ribbed	6	2.07	0.39	0.16	A+C
Macro Troughed	6	2.65	0.78	0.32	A
Sawtooth	6	0.52	0.40	0.16	A
Micro-rough + Macro Ribbed (1mm)	6	3.62	0.71	0.32	A+C
Micro-rough + Macro Ribbed (2mm)	6	3.42	0.25	0.11	A+C
CoCr (control)	7	8.08	0.64	0.23	C

Table 3.7: Summary of textured PEEK-cement lap shear strength results with number of samples, N, standard deviation, S.D., and standard error of mean, S.E.. A = adhesive failure and C = cohesive failure

An analysis of variance test (ANOVA) was used as a multiple comparisons test of the mean shear strength of the textured PEEK samples at a 5% significance level (Table 1 in Appendix 4). The PEEK samples were significantly weaker than the CoCr control group. However, it was observed that the PEEK-cement samples were bending across the interface region at high loads, indicating that peel stresses may have been induced. Therefore the lap shear-strength values shall be taken as the ‘apparent’ interfacial strength.

The directional macro-textures enabled significantly higher shear strengths than the micro-textures. The stepped plaque was too shallow (0.3 mm depth and 5 mm pitch) to enhance the shear strength. The Micro-rough + Macro-Ribbed textured samples had significantly greater interfacial shear strengths with cement than their micro and

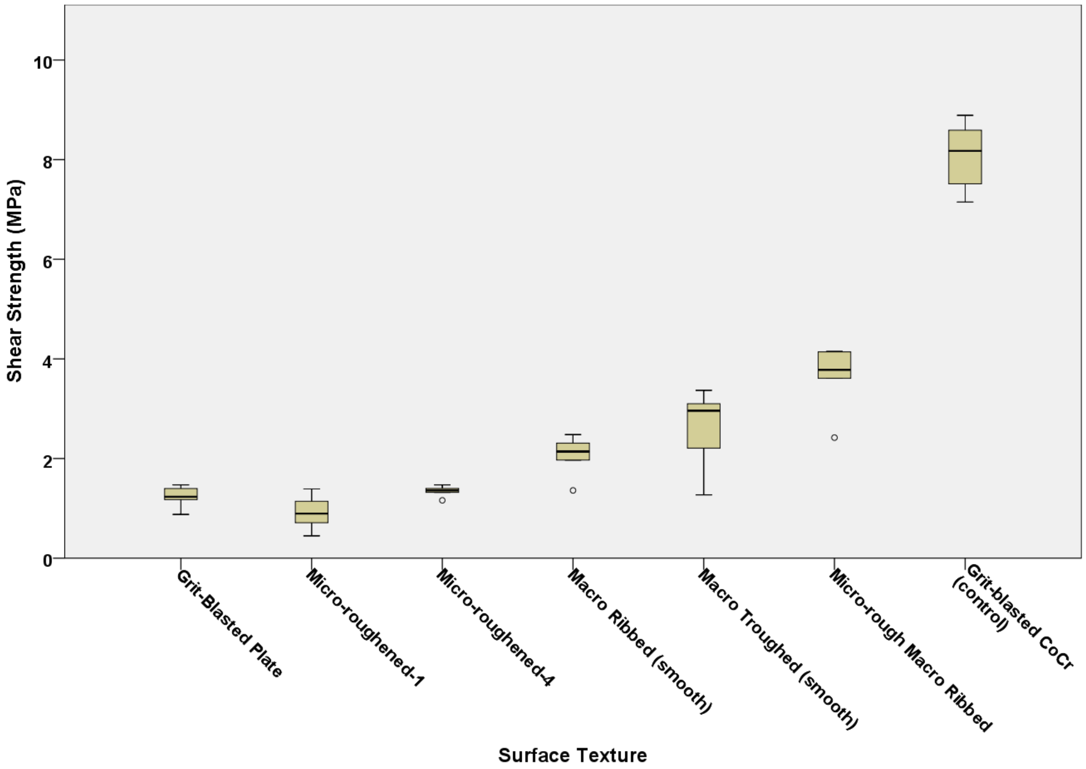

Figure 3.30: Box plot comparison of shear strength values with textured PEEK surfaces (○ = outlier)

macro components. By combining the micro and macro scale components of surface roughness, the shear strength was increased significantly at the 5% significance level and the acceptance criteria, set by the peak shear stress value predicted by the PEEK FE model (section 2.6.4.1 (Bah et al., 2012)), has been met.

The shear strength values were plotted against the corresponding area and volume measurements for each sample group, obtained from complete surface scans using the laser profilometer and estimated from sample regions using the optical focus variation microscope system (Figures 3.31 and 3.32). The corresponding best fit trend line and R^2 value is shown on each graph. The data from the optical focus variation microscope system includes the micro-macro textured PEEK surface, which could not be analysed with the laser profilometer as it was not available when these samples were produced. Relatively larger interlock volumes were estimated for the textured surfaces using the optical focus variation analysis technique (Figure 3.31b), compared to the measurements from the laser profilometer (Figure 3.31a), but a similar correlation was observed with the mean shear strength values. Wider scatter was observed in the relationship between the surface area and shear strength using the laser profilometer (Figure 3.32a). No correlation was observed with the surface area values estimated from the optical focus variation data (Figure 3.32b).

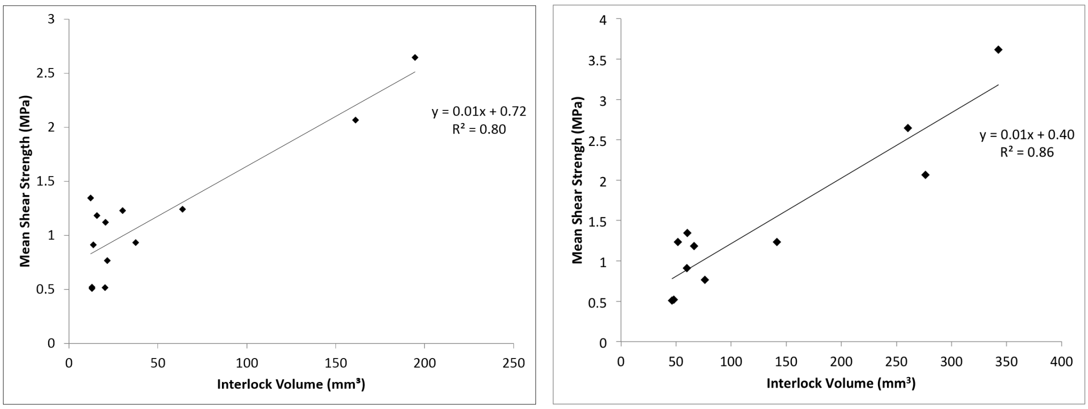

(a) Area data from the laser profilometer scans (b) Estimates for the full area from the optical focus variation data

Figure 3.31: Graphs of interfacial contact area vs. corresponding mean interfacial shear strength using data from two topography analysis techniques

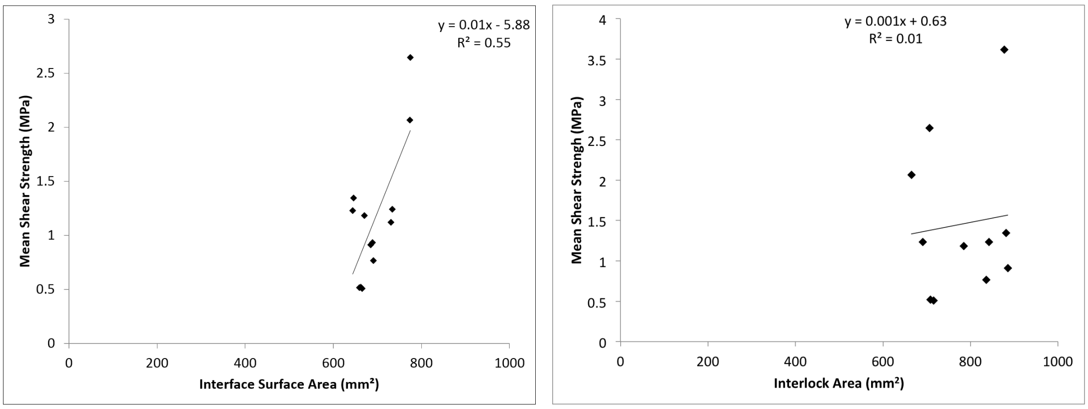

(a) Volume data from the laser profilometer scans (b) Estimates for the full volume from the optical focus variation data

Figure 3.32: Graphs of material interlock volume vs. corresponding mean interfacial shear strength using data from two topography analysis techniques

Selected parameters of the roughness profile for each sample group are plotted in Figure 3.33 against the corresponding mean shear strength values. The best fit in the relationship is shown for R_a (Figure 3.33a), R_z (Figure 3.33b), R_q (Figure 3.33c), and R_{sk} (Figure 3.33d) with the corresponding R^2 and equation for each trend line. The magnitude of R_a, R_z and R_q is closely related for each texture group, hence similar R^2 values are shown against the mean shear strength. There was a weak relationship between the skewness of the profile and the mean shear strength.

Accounting for 3D surface features, the surface texture of the sample area primary dataset showed a similar relationship when plotted against the corresponding mean shear strength values. Figure 3.34 shows the best fit trend line and R^2 values for the S_a (average height of the area, Figure 3.34a), S_z (maximum height of the area, Figure

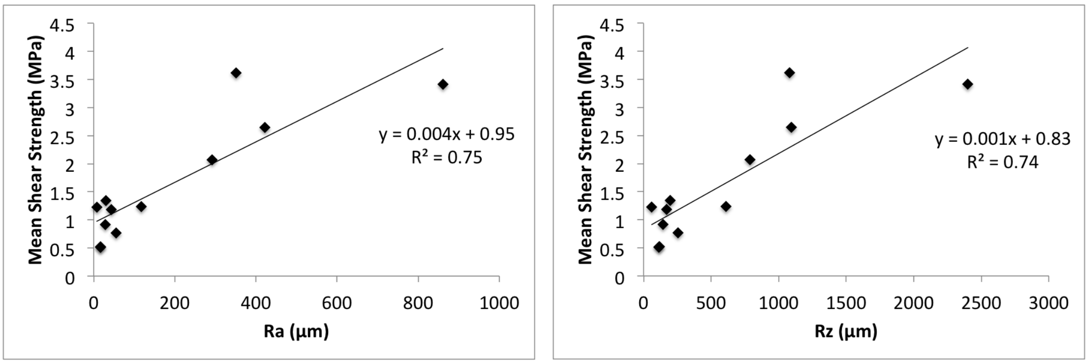

(a) R_a (b) R_z

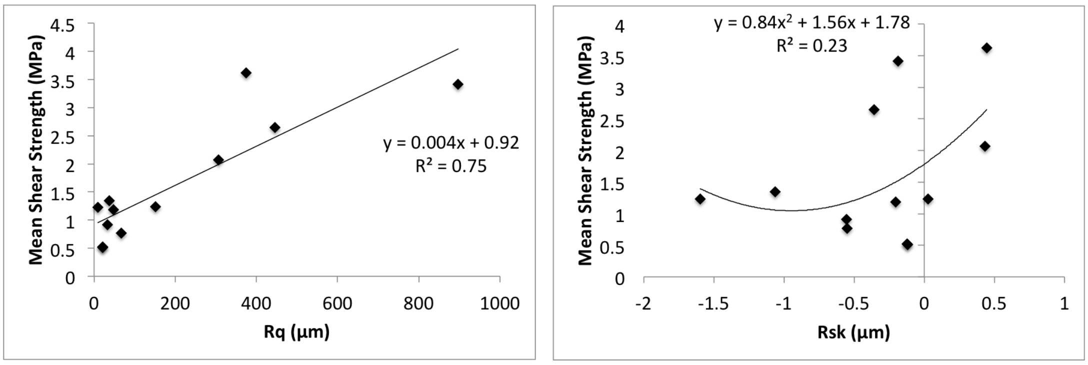

(c) R_q (d) R_{sk}

Figure 3.33: Mean shear strength plotted against the corresponding surface roughness values for each sample group (from the optical focus variation technique)

3.34b), S_q (Root-Mean-Square height of the area, Figure 3.34c), and S_{sk} (skewness of the area, Figure 3.34d) of each sample, against the mean shear strength data.

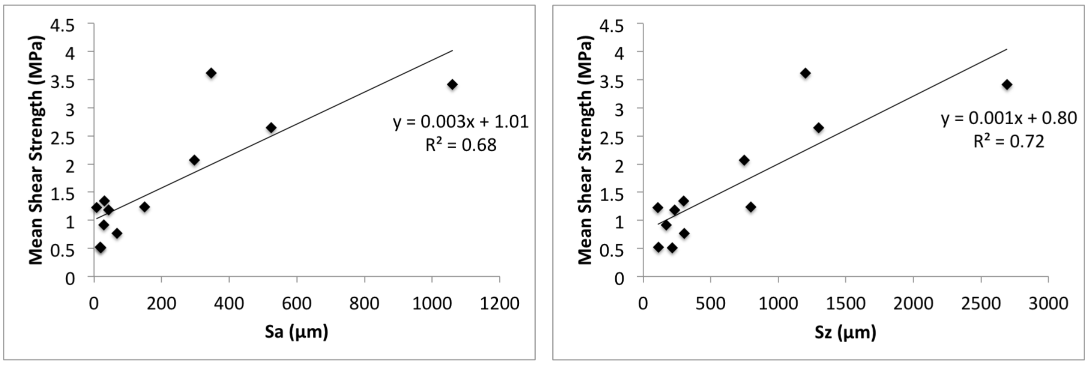

(a) S_a (b) S_z

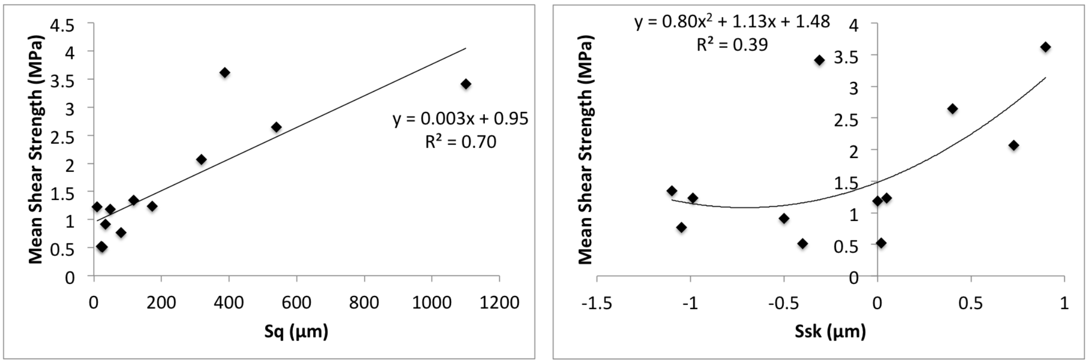

(c) S_q (d) S_{sk}

Figure 3.34: Mean shear strength plotted against the corresponding areal surface roughness values for each sample group (from the optical focus variation technique)

3.4 Surface Activation of PEEK

The third fixation study concerned an investigation into the surface activation of PEEK using oxygen plasma treatment to determine whether (a) the PEEK-cement interfacial shear strength would be enhanced and (b) which plasma treatment duration is optimal (using the equipment at the University of Southampton).

3.4.1 Methodology

3.4.1.1 Materials

A pilot study was carried out using plasma treated PEEK-OPTIMA® (PEEK) samples, with three surface topographies, which were supplied through Invibio Ltd for shear strength testing with bone cement. Smooth injection moulded plates, textured waffle pattern (Figure 3.15d) and conical frustum pattern samples (Figure 3.15b) were plasma treated with 5 minutes supply of oxygen and a plasma duration of 60 minutes at 100% generator power (unspecified).

In the second part of the study, through a collaboration with the Centre for Hybrid Biodevices in the Nano Research Group of Electronics and Computer Science, (Faculty of Physical Sciences and Engineering, University of Southampton), the effect of plasma treatment time on the contact angle with water was investigated on injection moulded PEEK plates, as an indication of the surface energy. The methodology is detailed in the next sections (3.4.1.2 and 3.4.1.3).

Once a suitable treatment time was established, plasma treatment was carried out on PEEK plates with waffle and conical frustum textures to allow a comparison with the surfaces used in the pilot study. In addition, Micro-roughened, Macro Ribbed and Macro Troughed textured PEEK samples were also plasma treated, to allow interfacial shear strength with bone cement to be measured, for comparison to that achieved with the untreated surfaces in section 3.3.2.2.

Palacos R bone cement (Heraeus Medical, Wehrheim, Germany) was used for all of plasma treated PEEK plates in this study.

3.4.1.2 Plasma Treatment

Smooth injection moulded PEEK plates were plasma treated using a Diener Femto low pressure plasma system with a radio frequency generator (RF, 13.56 MHz), outlined in the schematic of Figure 3.35 (Diener Electronic GmbH, Ebhausen, Germany).

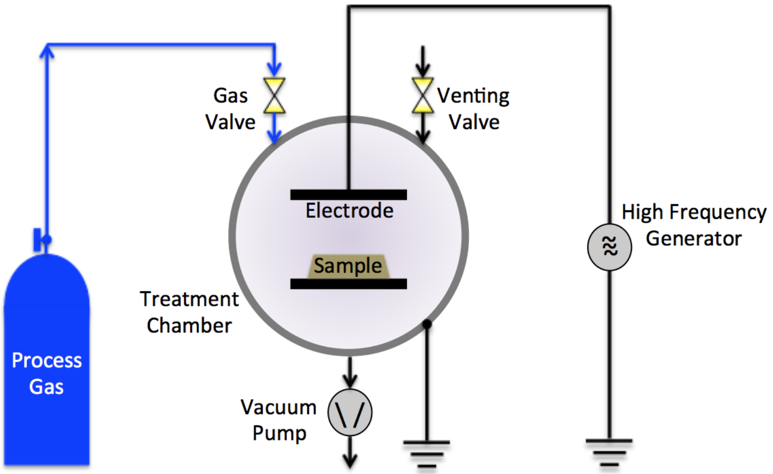

Figure 3.35: Schematic of the low pressure plasma system for oxygen-plasma treatment of PEEK

Prior to plasma treatment, the PEEK plate surfaces were cleaned with isopropanol wipes, then washed with deionised water and dried using compressed nitrogen. The plates were then positioned at the front of the chamber of the Femto system with the smooth surface for treatment exposed (Figure 3.36). The vacuum pump was activated to remove air from the chamber, reducing the pressure to below 100 Pa. Oxygen gas was then supplied for 5 minutes at a flow rate of 100% (90 cm^3/min) to flush any remaining air from the chamber prior to the ignition of plasma. The generator was set at 50 W power and the PEEK plates were treated for 30, 60, 360 and 500 seconds (with 5 plates in each treatment group). An untreated PEEK sample group was used as a control.

Figure 3.36: Plasma treatment of PEEK plates using a Diener Femto low pressure plasma system

3.4.1.3 Contact Angle Measurement

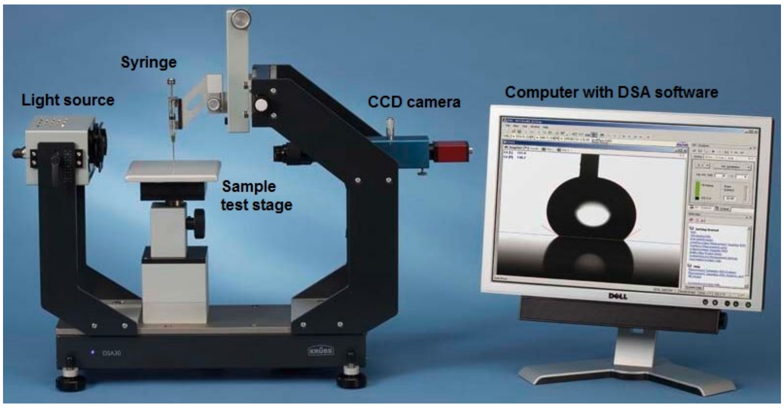

Figure 3.37: Krüss DSA30B contact angle measurement system (Krüss GmbH, Hamburg, Germany)

The contact angle of the smooth PEEK plates were measured using a Krüss DSA30B system (Krüss GmbH, Hamburg, Germany) with manual dosing of di-ionised water through a syringe on to the surface of the sample. Each drop was illuminated with a light source from behind the sample, an image of the drop was captured with a CCD camera and a contact angle measurement was made using the Krüss drop shape analysis (DSA) software. Six drop measurements were averaged along the surface of each sample before and after plasma treatment. The volume of the drops was approximately 14 μl.

3.4.1.4 Lap Shear Sample Preparation and Test Procedure

The optimal oxygen plasma treatment time determined in the contact angle study for maximum reduction in contact angle (30 seconds, see section 3.4.2.1) was used to treat the textured PEEK plates. The same protocol described in section 3.4.1.2 was followed.

All of the plasma treated PEEK plates were cemented using Palacos R bone cement, mixed under vacuum assisted conditioned with the PALAMIX system according to the manufacturer's instructions (Heraeus Medical, Wehrheim, Germany), using the cementing mould (Figure 3.4). The fresh plasma treated samples were cemented within 24 hours of oxygen plasma treatment. The pilot study samples were supplied in inert environment sealed foil bags to preserve the plasma treated surfaces prior to cementing.

The plasma treated PEEK-cement samples were then tested after 72 hours, using the lap shear method described in section 3.2.1.4. The ANOVA statistical test method described in section 3.3.1.5 was then used to compare the shear strength results of the plasma treated surfaces, with the untreated surfaces in the surface topography study (section 3.3.2.2).

3.4.2 Results

3.4.2.1 Contact Angle Results

The change in the contact angle of water on PEEK with increasing plasma treatment duration is shown in Table 3.8 and Figure 3.38. A high contact angle indicates a hydrophobic surface and a low contact angle indicates a hydrophilic surface. The contact angle did not change significantly with any plasma duration longer than 30 seconds. Therefore a 30 second treatment time was determined sufficient to increase the surface energy of the PEEK surface, with the equipment available.

Treatment Time (seconds)	Mean Contact Angle (°)	Std. Error (°)
0	80.41	0.17
30	30.58	0.58
60	29.03	0.86
360	22.43	0.56
500	25.73	0.59

Table 3.8: Contact angle measurements with increasing plasma treatment time

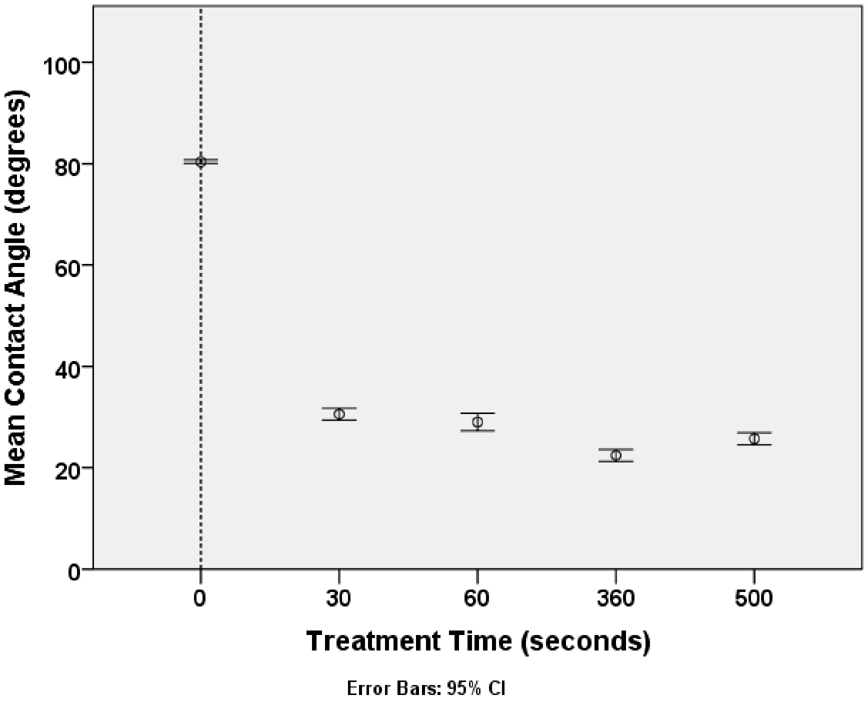

Figure 3.38: Graph showing the effect of plasma treatment time on contact angle at 50W (13.56 MHz)

3.4.2.2 Plasma Treated PEEK-cement Shear Strength Results

The plasma treated PEEK-cement interfacial shear strength results from the pilot study are shown in Table 3.9. These strength values were compared with untreated PEEK samples with the same texture surface finish in an ANOVA test (Table 2 in Appendix 4). The plasma treated samples were significantly stronger than their untreated counterparts at the 5% significance level. A change in failure mode was also observed; the waffle textured plasma treated samples failed cohesively through the cement as well as adhesively at the interface.

Plasma treated Sample	N	Mean Shear Strength, MPa	S.D., MPa	S.E., MPa	Failure Mode
Plate	3	0.37	0.29	0.17	A
Waffle	3	3.16	0.34	0.20	A+C
Conical frustums	3	2.39	0.26	0.15	A

Table 3.9: Summary of pilot study plasma treated PEEK-cement lap shear strength results with number of samples tested, N, standard deviation, S.D., and standard error of mean, S.E.. A = adhesive failure and C = cohesive failure.

The plasma treated PEEK-cement interfacial shear strength results using the samples treated at the University of Southampton are shown in Table 3.10. The strength values for the waffle and conical frustum textured PEEK samples were compared with the strength values achieved in the pilot study using the ANOVA test (Table 2 in Appendix 4). There was no significant difference between the interfacial shear strength values achieved with the samples plasma treated at the University of Southampton and those supplied by Invibio at the 5% significance level. However, the samples failed at the interface alone. In comparison to their untreated counterparts in the surface topography study (section 3.3.2.2), the plasma treated samples were significantly stronger at the 5% significance level. A change in failure mode was also observed for the Macro Troughed textured sample, which failed cohesively through the cement, as well as adhesively at the interface.

Plasma treated Sample	**N**	**Mean Shear Strength, MPa**	**S.D., MPa**	**S.E., MPa**	**Failure Mode**
Waffle	4	2.75	0.60	0.30	A
Conical frustums	4	2.08	0.46	0.23	A
Micro-roughness	4	1.54	0.19	0.10	A
Macro Ribbed	4	3.26	0.16	0.08	A+C
Macro Troughed	4	3.39	0.23	0.12	A+C

Table 3.10: Summary of mean plasma treated PEEK-cement lap shear strength results with number of samples tested, N, standard deviation, S.D., standard error of mean, S.E. and failure mode, A = adhesive failure and C = cohesive failure

A box plot comparison of the untreated PEEK-cement and the plasma treated PEEK-cement interfacial shear strengths values is shown in Figure 3.39. The mean shear strength value of both the Macro Ribbed and Macro Troughed PEEK samples now exceeds the shear stress value predicted by the PEEK FE model (see section 2.6.4.1 (Bah et al., 2012)).

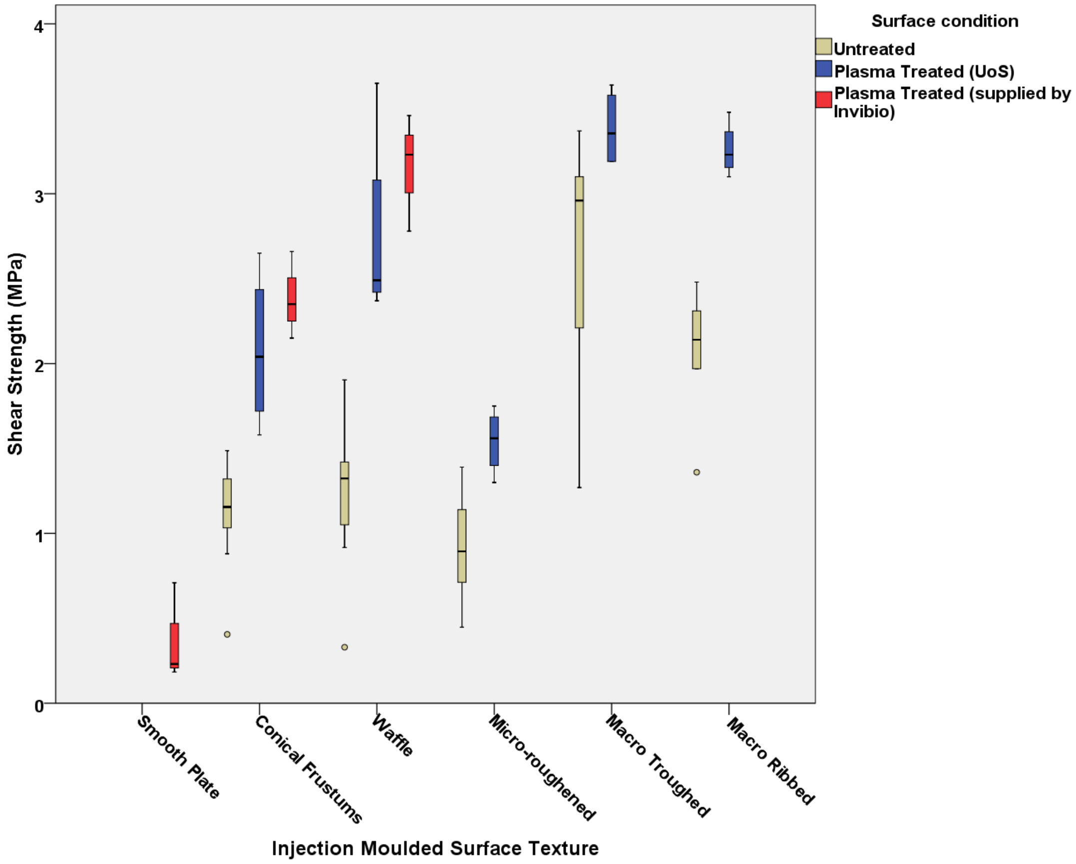

Figure 3.39: Box plot comparison of shear strength values with plasma treated PEEK and surface texture (PT = plasma treated, ○ = outlier)

3.5 Discussion

To the author's knowledge, this is the first study into the bonding performance of PMMA bone cement to PEEK. Consequently, shear strength results can only be compared to experimental interfacial strength studies with other material combinations published in the literature. The metallic TKR femoral component currently sets the benchmark for interface strength properties, but these may be overly conservative for enduring the forces at the knee joint. A finite element (FE) model was developed at the start of this project by Dr A Dickinson and Dr M Bah, two research fellows in the Bioengineering Science Research Group, as part of the conceptual study for the PEEK TKR (detailed in Section 2.6.4.1). The predicted shear stresses at the PEEK-cement interface peaked at 3 MPa during normal gait. This was used as an indicative pass criteria for the PEEK-cement shear strength in the present study.

In the preliminary study of fixation, adhesion was not achieved between smooth injection moulded PEEK and cement. Surface roughening was required for measurable adherence between the substrates, such that a mechanical interlock was achieved between the two components, confirming the study hypothesis. This is a common finding in studies with PEEK and dental resin cements (Hallmann et al., 2012; Schmidlin et al., 2010). Stawarczyk et al. (2013) showed that air abrasion of PEEK with alumina lowers the contact angle with water (from 74.6 to 55.7), improving the wettability and increasing the surface energy. This enhanced the shear bond strength with dental resin cement considerably (from 0.33 MPa to 9.33 MPa), although the highest shear bond strengths were achieved after acid etching of the PEEK surface, which did not lower the contact angle significantly. Cognard (2006) states that the roughness of a substrate is an important factor in the surface adhesion, providing mechanical anchorage of the adhesive due to increased surface contact. It is most likely that the adhesion between grit-blasted PEEK and cement in the present study was achieved through mechanical interlock. However, the contact angle prior to cementing must be measured for quantification of any change in wettability following grit-blasting, as it has been shown that surface roughness is related to surface wettability (Packham, 2003).

The results from the preliminary study showed that there was no significant difference between the shear strength of PEEK samples cemented in the working phase and prematurely, in the waiting phase, suggesting that there is no difference in chemical interactions or mechanical interlock achieved between the materials. Hence a valid comparison can be made with the steel-cement interface strength study by Zelle et al. (2011a). The greatest shear interface strength between steel and bone cement was achieved with the maximum surface roughness obtained through grit-blasting, an R_a value of 2.76 μm. This achieved a mean interfacial shear strength of 9.90 MPa, far greater than the mean interfacial shear strength between grit-blasted PEEK (mean $R_a = 5.51\mu m$) and cement of 1.53 MPa achieved in this study.

In the present study, the CoCr-cement control samples achieved an average interfacial shear strength value of 8.08 MPa, similar to the steel-cement shear strengths of Zelle et al. (2011a). The difference between the metal-cement and PEEK-cement shear strengths could partly be explained by the difference in surface topography achieved through grit blasting. It is postulated that a sharper form of surface undulations may exist on a metallic surface compared to a more rounded and uniform texture on a polymer as a result of the difference in modulus and deformation behaviour, which occurs through chain-sliding. Polymers have a much lower plasticity compared to metals. Different grit-blasting media (round or sharp-edged) can also achieve different surface topographies, which cannot be compared through R_a value alone (Bacova and Draganovska, 2004). This would require surface analysis of grit-blasted PEEK and CoCr at greater magnification using an SEM for quantification.

When comparing the interfacial shear strengths of the grit-blasted PEEK-cement (PEEK-OPTIMA®) and CFR-PEEK-cement (MOTIS®) samples, the CFR-PEEK-cement interface was significantly stronger which may also be accounted for by the transfer of material observed in the macroscope images (shown in Figures 3.12c and 3.12d). This suggests that cohesive failure was occurring at the interface with carbon fibre pullout. In the SEM images, tube-like ridges in the cement matrix resemble the structure of the carbon-fibres within the CFR-PEEK, however, similar features can be seen on the cement fracture surface corresponding to the PEEK sample in Figure 3.13e. To more accurately identify a change in surface features, PEEK and CFR-PEEK grit-blasted surfaces must be imaged by SEM prior to cementing.

Even though CFR-PEEK may have a higher interface strength with cement, it would not be a suitable material for a femoral component articulating on a polyethylene (PE) tibial component due to the hard carbon fibre inclusions, which are likely to increase the wear of the PE, once exposed (Harsha et al., 2003). As CFR-PEEK wears in a low congruency bearing with high contact stresses, the softer PEEK matrix is removed, exposing the wear resistant carbon fibres (Grupp et al., 2010). It has also been reported that release of these carbon fibres can cause third body abrasive wear of UHWMPE (Latour, 1995).

When observing the fracture surfaces of the PEEK samples under SEM, some cement transfer was identified where there were round polymer bead shapes. This suggests that there was some porosity at the interface between the cement and the PEEK. A pattern of fibrils on the surface suggests that crazing occurred during cohesive failure through a thin layer of cement as the interface failed adhesively. Crazing is a mechanism whereby the matrix of the polymer is weakened when the applied stress localises and concentrates at a flaw, void or crack front (propagation) due to the yielding of aligning molecular chains, which causes plastic deformation as the energy dissipates (Cognard, 2006; Grellmann and Seidler, 2001). However, this is a localised observation, suggesting overall adhesive interface failure.

As discussed in Section 2.1.2, PEEK is a relatively unreactive polymer, therefore it may be unlikely to generate any chemical coupling bonds with the bone cement. The bone cement will be in contact with the surface of the PEEK when in the doughy stage, whilst it is polymerising (Lewis, 1997). However, the type of bond achieved between the PEEK implant and the PMMA bone cement, if any at all, is unknown and no relevant information was found in the literature.

Molecular chain entanglement can occur at interfaces between immiscible polymers, as discussed in section 2.5.2, creating a mechanical interlock at the molecular scale (Brown, 1991, 2006; Silvestri et al., 2003). However, the polymerised PMMA skin that forms around the cement when it is in the viscous doughy stage (before it is implanted) may prevent any adhesive bonds forming or any chain entanglement from occurring, provided that the surgeon implants the cement within the working time frame. Van der Waals forces would be present between the materials in contact in any case, although these are very weak in comparison with adhesive bonding (Callister, 1997).

Therefore, if adhesive bonding is not present, the surface roughness between the implant and the cement alone may determine the interfacial strength. The greater the surface roughness, the greater the shear and tensile interfacial strength that may be achieved. This was confirmed through the surface topography study with injection moulded textured PEEK, where interfacial surface area and interlock volume correlated positively with shear strength. However, this correlation could have been more positive if the shear strength results were not affected by the bending of the lap-shear samples at high loads. Additionally, porosity found near the interface of multiple samples throughout this study may have contributed towards lower average shear strengths. This is important to note for future PEEK TKR concepts, as interfacial defects may affect the strength and durability of the implant *in vivo* by propagating as interfacial cracks, which could lead to implant loosening.

Directional macro-texture features enhanced the shear strength significantly more than the micro-texture features, however, this depended on the depth and orientation of the pattern in relation to the loading direction, i.e. grooves perpendicular to the loading direction. By combing micro and macro features, a hierarchical structure was created; this significantly increased the interfacial shear strength compared to using the micro or macro features alone and satisfies the strength criteria set by the shear stress predictions of the FE model. However, they do not allow for a safety factor. Similar conclusions have been drawn in studies of the effect of interfacial roughness on fracture toughness, where sinusoidal interface geometry has been shown to introduce resistant normal forces at the debond line and stick-slip crack mechanisms (Janarthanan et al., 1997; Kim et al., 2010; Li et al., 2012). Hierarchical structures are common in nature for providing adhesion strength at interfaces; geckos have three-tiered morphology to their setae (hairs on their feet), which promote an increased number of contact points and adhesion energy (Bhusan et al., 2006).

The interfacial shear strength is enhanced as the roughness of the adherend increases, resulting in a larger effective surface area and interlock volume. However, this effect appeared to peak before decreasing with increased depth of surface features in the micro-macro texture group, which could be accounted for by an increase in stress concentration at the debond line, as a crack progresses up the interface. Excessively rough surfaces are also reported to lead to poor surface wetting and void formation with adhesives (Prolongo et al., 2006). There was a weak relationship between the skewness of the roughness profile and the mean shear strength values. This may be due to the analysis path across the surface features, which accounted for multiple directions, rather than just the longitudinal direction in which the surface was tested. In addition, it was not possible to use the same line profile analysis path on each surface due to the size difference in the analysis region chosen to represent the entire surface texture. A confident conclusion cannot be drawn between the surface roughness and texture parameters and the mean shear strength data due to limitations of the lap shear testing technique. Bending at the lap joint interface may have skewed the shear strength distribution causing earlier failure of interfaces with greater roughness due to the increased deflection from the machine loading axis, without having as significant effect on samples with relatively low values. Any misalignment between the loading axis and the interface could also account for the wide variation in results within sample groups. The discrepancies between the interlock volume and surface area measurements from the two surface topography analysis techniques used (laser profilometer and optical focus variation microscope) could be due to missing data in areas of steep geometry, thus reducing the accuracy of the area and volume calculated. The triangulation laser system used on the laser profilometer is reported to be capable of measuring up to a 45 degrees angle relative to the surface tangent (Boltryk et al., 2008). After this the signal becomes too weak to make a measurement. The Alicona InfiniteFocus technical specification states that it can measure angles up to 87 degrees, but this depends on the reflectivity and lighting of the surface. Downsampling could help achieve a larger surface scan using the Alicona surface area analysis, but this would not solve the problem of missing data due to the reflectivity and steep edges of the PEEK textures.

In order to attempt to achieve chemical bonding to enhance the interface strength, the surface chemistry of PEEK must be altered. Ideally, peroxide groups would be added to the PEEK surface to achieve chemical bonding with PMMA. In the surface activation study, the increased interfacial shear strength of oxygen plasma treated PEEK and cement showed that the adhesion is improved significantly. Adhesion was achieved with smooth injection moulded PEEK samples which was not possible with the untreated PEEK, suggesting that some physical bonding may have occurred by addition of polar groups to the PEEK surface. In addition, by combining plasma treatment and macro-textures, the shear strength was increased significantly at the 5% significance level compared to using the macro-texture topography alone, as the measured strength almost doubled. The failure mode change from adhesive to cohesive, an observation also reported by Jha et al. (2010) when investigating the effect of plasma treatment on the lap shear strength of PEEK using an epoxy adhesive.

If etching of the PEEK surface is achieved through plasma treatment, the adhesion could be improved further.

The contact angle analysis showed that plasma treatment of PEEK lowered the contact angle of water, suggesting that the surface energy is increased as polar groups are added to the PEEK surface, transforming it from hydrophobic to hydrophilic. This would improve the wetting angle of the cement on the PEEK surface, which may have enhanced the adhesion strength. However, x-ray photoelectron spectroscopy (XPS) analysis would be required to identify any polar chemical groups which may have been added to the PEEK surface.

A 30 second oxygen plasma treatment time was identified as sufficient to increase the surface energy of PEEK with the facilities available at the University of Southampton. Although it was noted during testing that the plasma treated surface is very delicate and the effect can be removed by wiping the surface or by blowing compressed nitrogen across the surface (to remove dust). Therefore a strict protocol is required to remove the plasma treated samples from the treatment chamber and prepare the samples for cementing without contaminating the surfaces. This could pose a problem for a viable application to a PEEK femoral component backing for use in surgery.

Overall, the limitations of the lap-shear test method employed in this fixation study may have contributed towards relatively lower shear strength measurements of the PEEK-cement interface. A non-uniform stress distribution acts across the interface of a lap shear specimen upon loading; this induces normal stresses which are compressive in the central region and tensile at the ends of the overlap. In addition, the increased compliance of the PEEK-cement samples over the CoCr-cement samples could have led to greater bending of the sample at comparatively lower loads (CoCr > CFR-PEEK > PEEK for both stiffness and interfacial shear strength with cement). This would cause mode I stresses to be induced at the ends of the interface area and may lead to failure from peel stresses at lower loads, for lower stiffness materials. In the literature, lap-shear failure is reported as being more closely related to the induced tensile stresses than the shear stresses (Adams and Davies, 2002; Devries and Adams, 2002).

It could be postulated that a PEEK-cement construct may potentially exhibit relatively higher interfacial fracture resistant properties compared to a metal-cement construct due to the reduced compliance mismatch between the polymer materials. A metal-cement implant construct has a higher property mismatch than the potential PEEK-PMMA material couple, which has similar individual moduli. Therefore a higher bond strength may be achieved, dependent on the surface roughness at the implant-cement interface. A study by Darwish and Al-Samhan (2008) showed that increasing the Young's modulus of the prosthesis resulted in weakening the cement layer in a cemented TKR tibial component by increasing the stress at the interface. Krishnan and Xu (2011) showed that bi-material systems with a greater property mismatch exhibited a lower mode I interfacial fracture toughness and shear bonding strength compared to similar material interfaces. In a bimaterial with a large elastic modulus mismatch, the stress state at the debonding interface is altered such that a degree of shear stress is always acting on the crack tip. Crack propagation speed along a mismatched moduli interface may also be greater but this depends on the nature of the loading as well as contact at the crack tip (Xu and Needleman, 1996). Conversely, crack propagation normal to a compliant-stiff interface can lead to crack arresting mechanisms and crack deflection, should the crack initiate in the lower modulus material (Chen and Mai, 2010). The lap-shear test method was chosen for ease of sample manufacture. By carrying out shear strength tests using a double lap joint or a compressive block shear test method (ASTM D 4501), peel stresses could be reduced and the interfacial shear strength more accurately assessed.

Another shortcoming of the methodology in these fixation tests is that the environmental effects *in vivo* were not accounted for; consequently, the effect of moisture absorption on the PEEK-cement interface is unknown. Moisture absorption could potentially degrade the interfacial integrity and lead to accelerated loosening of the implant. Plasma treatment of PEEK could further improve the interface strength of the femoral component because physical bonds are reported to be less susceptible to degradation from environmental effects (Cognard, 2006). The feasibility of applying these surface treatments to a final PEEK femoral component has to be considered though. Plasma treated surfaces have a limited shelf life under laboratory conditions, such that there is a set timescale for its effectiveness (Comyn et al., 1996). This may not be practical for the medical market unless a suitable packing environment is used. Acid etching is another chemical treatment which could potentially improve the interface strength by producing undercuts and a porous surface finish (Schmidlin et al., 2010). However, this treatment may not produce the same pattern on each surface, and would require strict control in the manufacturing procedure of a medical device to prevent contamination of the articular surface.

Ultimately, the main goal of this fixation study was to establish the adhesive properties of PEEK to cement with varying surface treatments. It has been identified that the strength of the PEEK-cement interface is governed by the mechanical interlock between the two materials. The results presented give a qualitative indication of the interfacial strength due to the presence of interfacial bending and induced peel stresses. Without surface activation of the PEEK substrate, a hierarchical surface texture has been identified to provide a mechanical interlock which meets the interfacial shear strength acceptance criteria. However, it must be taken into account that if this interface debonds, the rough surface could lead to a rasping effect, causing release of cement particles and osteolysis. Cement shrinkage stresses could also increase the likelihood of debonding (Orr et al., 2003).

Chapter 4

Development of a DIC Analysis for Evaluation of the Influence of Implant Material on Femoral Bone Strain following TKR

4.1 Introduction

As discussed in section 2.3.3, a high modulus implant such as a traditional metallic total knee replacement ($E \approx 220$ GPa) can alter the strain field of the supporting bone *in vivo*, causing a phenomenon known as stress shielding. This may lead to an adverse redistribution of bone material, leaving the periprosthetic bone weak and porotic, necessitating revision surgery. Strain-adaptive bone remodelling theory suggests that bone cells react to local deviations in strain and predicts that below a certain threshold of strain, bone will be resorbed (Frost, 2003; van Lenthe et al., 1997). TKR implants manufactured from PEEK will have a stiffness similar to bone and therefore the potential to reduce stress shielding effects by allowing more physiological load transfer (Kurtz and Devine, 2007).

Preservation of long term bone quality is important in implant design. To demonstrate the efficacy of PEEK in promoting a more natural stress distribution, there are a number of established and emerging strain monitoring techniques available, as outlined in section 2.6.2. Digital Image Correlation (DIC) was identified as the most appropriate non-contact technique for surface strain measurement across the TKR construct.

In the present study, 3D DIC was used for analysis of distal femoral bone strain, with the null hypothesis that a compliant PEEK implant has the potential to promote a more physiological bone strain distribution compared to that induced by a contemporary metallic implant. A detailed methodology is presented in this chapter for the evaluation of implanted TKR constructs using an analogue bone model, as a basis for future investigation of cadaveric bone (Chapter 5).

First, a preliminary study is described in which the bone strain distribution after implantation of a PEEK implant and a contemporary metallic implant is compared (section 4.2), following a previously validated DIC technique (Dickinson et al., 2011), on an analogue bone model. The experimental setup and DIC analysis technique were then refined for robust measurement of strain on the distal femora. The final DIC method and results are described in section 4.3, before a discussion of all results in section 4.4.

4.2 Preliminary Analogue Bone DIC Study

4.2.1 Methodology

The distal third of three anatomical femur models (medium Foam Cortical Shell femur model, item 1121-20, Sawbones Europe AB, Malmö, Sweden) were sectioned and potted in Technovit® PMMA resin. Each bone was aligned to represent static stance, such that the anatomical axis was 6 degrees adducted from the mechanical axis, 3 degrees to the vertical axis ((Pickering and Armstrong, 2013)), using the surgical distal cut alignment tool, a spirit level, and a retort stand, clamp and boss.

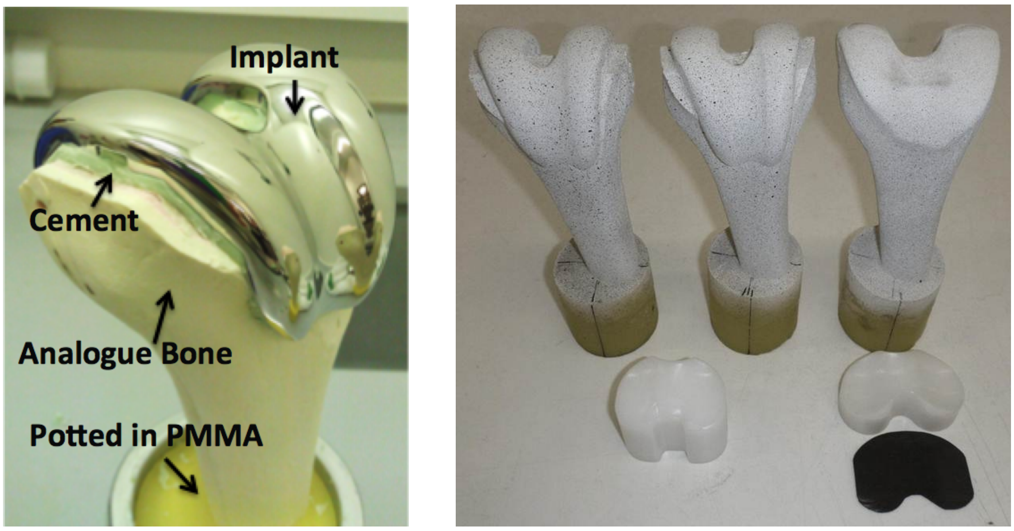

(a) Implanted test specimen (b) Test femurs with speckle pattern applied

Figure 4.1: Potted analogue femur test specimens (with speckle pattern applied, left to right: CoCr implanted, PEEK implanted and intact)

One distal femur was implanted with a size C cruciate retaining metallic (Cobalt Chromium, CoCr) femoral component from the Maxx Freedom Knee commercial implant system and another femur was implanted with a PEEK-OPTIMA® (PEEK) femoral component of the same size and geometry, using the corresponding Freedom

Knee surgical instrumentation. Both components were fixed in place using Palacos R acrylic bone cement ($E = 2.9$ GPa) mixed under vacuum to the manufacturer's instructions (Heraeus Medical GmbH, Wehrheim, Germany) (Figure 4.1a). The final femur section was left intact for reference to represent the physiological strain case.

To allow surface strain measurement, each femur was sprayed with a thin layer of matt white paint (Plasti-Kote Ltd, Wokingham, UK), then a black acrylic paint speckle pattern was applied using a brush flicking technique (Figure 4.1b).

Dual 2 MP cameras (1624 x 1232 pixels) (Limess GmbH, Krefeld, Germany) were used to acquire images of the speckled surfaces with an exposure time of 12.5 ms. The cameras were positioned at a distance of 300 mm from the surface of the bone with an aperture of f12 and calibration images were obtained using a 12 x 9 grid of 5 mm spot targets at multiple orientations. Three fibre-optic light sources were used to illuminate the anterior, lateral and posterior bone surfaces with a diffuse LED light source positioned behind the cameras.

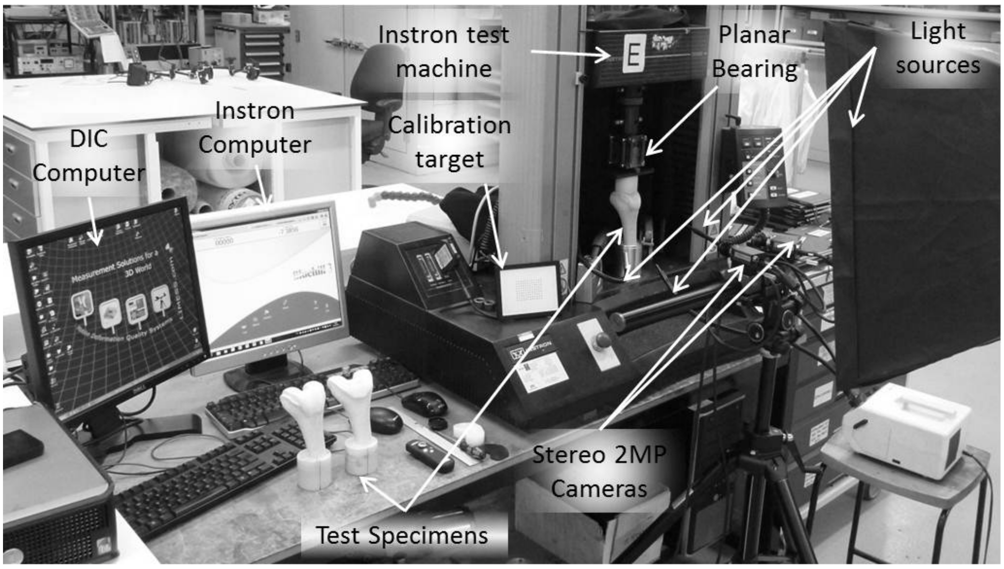

Figure 4.2: DIC test setup

Each bone was loaded in fixed increments up to 1000 N joint contact force to determine the optimal load for signal-to-noise ratio. The corresponding Freedom Knee UHMWPE tibial component size was used to load the bone with a planar bearing to ensure each construct was loaded solely in compression. For the intact bone, a 2 mm thick rubber sheet was used to represent cartilage and to promote uniform contact with the UHMWPE tibial component. Load was applied axially using an Instron 5569 electromechanical test machine (Instron Inc., IL, USA) with a 50 kN load cell. In each load increment, a ramped displacement was applied until the target load was attained, at which point the crosshead was held in position at a constant displacement and six consecutive photos of the surface were taken (2 fps). Six repeat load cycles were performed for each femur on the anterior and lateral bone surfaces to assess measurement variability and tibial component positioning. Six repeat unloaded datasets for each bone in each view were collected to assess measurement sensitivity. The test setup is shown in Figure 4.2.

The speckle image data was compared at different loads using Vic-3D software (Correlated Solutions, Inc., USA) which calculates strain fields under loading by tracking blocks of pixels to measure surface displacement. A subset pixel grid size of 31 and 41 were used with a step size of 7 for the anterior and lateral sides respectively to process surface deformation parameters from the displaced speckle pattern pixels before generating 3D deformation vector fields and in-plane strain maps. The strain measurements were averaged within fifteen and sixteen 5 mm^2 virtual strain gauge regions of interest (ROI) across the anterior and lateral bone surfaces, respectively, for comparison (Figures 4.3a and 4.3b). The boundary co-ordinates for each ROI were defined from X and Y plots of each analysed bone surface in the anterior and lateral view. This allowed a quantitative comparison of strain induced on each bone, by averaging data points across each region.

The principal strain values were plotted for each ROI on the intact versus implanted cases, and the regression score (R^2) and gradient (β) were calculated using IBM SPSS Statistics 20 (IBM Corp. USA) as well as the Pearson's correlation coefficient to evaluate the strength of the relationship. Perfect agreement between the implanted and intact cases would give $R^2 = 1$ and $\beta = 1$, ($y = x$).

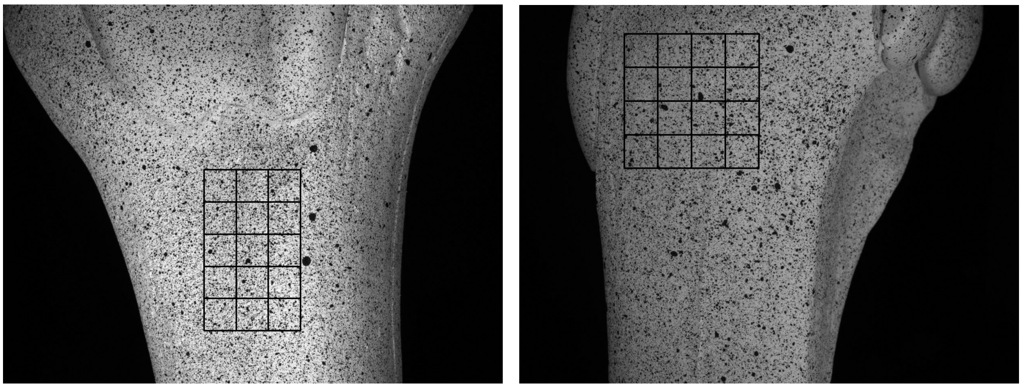

(a) Anterior (b) Lateral

Figure 4.3: Strain gauge areas within which the DIC strain measurements were averaged

4.2.2 Preliminary Analogue Bone Strain Results

The minimum sensitivity of strain measurements (mean + 3(standard deviation)) was calculated from sequential unloaded images to be an average of 135 $\mu\epsilon$ (63+3(24)), 138 $\mu\epsilon$ (63+3(25)) and 97 $\mu\epsilon$ (43+3(18)) for the intact, PEEK and CoCr implanted bones respectively, on the anterior surfaces within the virtual strain gauge area regions. On the lateral surfaces the minimum sensitivity of strain measurements was 116 $\mu\epsilon$ (62+3(18)), 139 $\mu\epsilon$ (61+3(26)) and 130 $\mu\epsilon$ (73+3(19)) for the intact, PEEK and CoCr implanted bones respectively. At 750 N load, the maximum six sigma experimental error between the six repeat tests (± 3 standard deviations) was ±230 $\mu\varepsilon$, or 8.5% of the peak strain in the strain gauge region, 2700 $\mu\varepsilon$. Therefore it was determined that 750 N load gave an acceptable signal-to-noise ratio for the analogue bones tested.

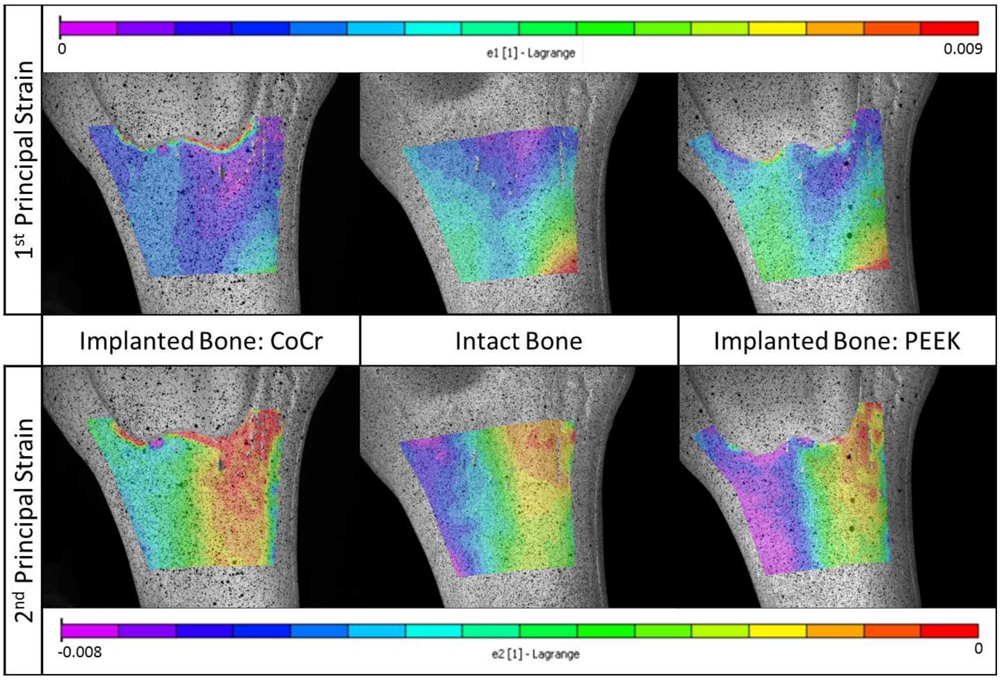

Figure 4.4: Principal strain maps for the intact and implanted DIC tests on the anterior bone surface at 750N (1^{st} principal = tensile, 2^{nd} principal = compressive)

The principal strain maps show the qualitative difference in strain distribution for the anterior and lateral surfaces of the bone (Figures 4.4 and 4.5, respectively). Compared to the intact bone tests, high strains were measured on the bone surface adjacent to the CoCr implant and relatively low strains were measured on the bone surface distant from the implant in both the lateral and anterior views. The PEEK implant promoted a strain distribution more similar to the intact bone tests than the CoCr implant.

Comparing the strain gauge region measurements quantitatively, a wide scatter was observed between the CoCr implant dataset and the intact bone dataset on the lateral side of the bone ($R^2 = 0.424$ with slope $B = 0.451$, Pearson's correlation coefficient =

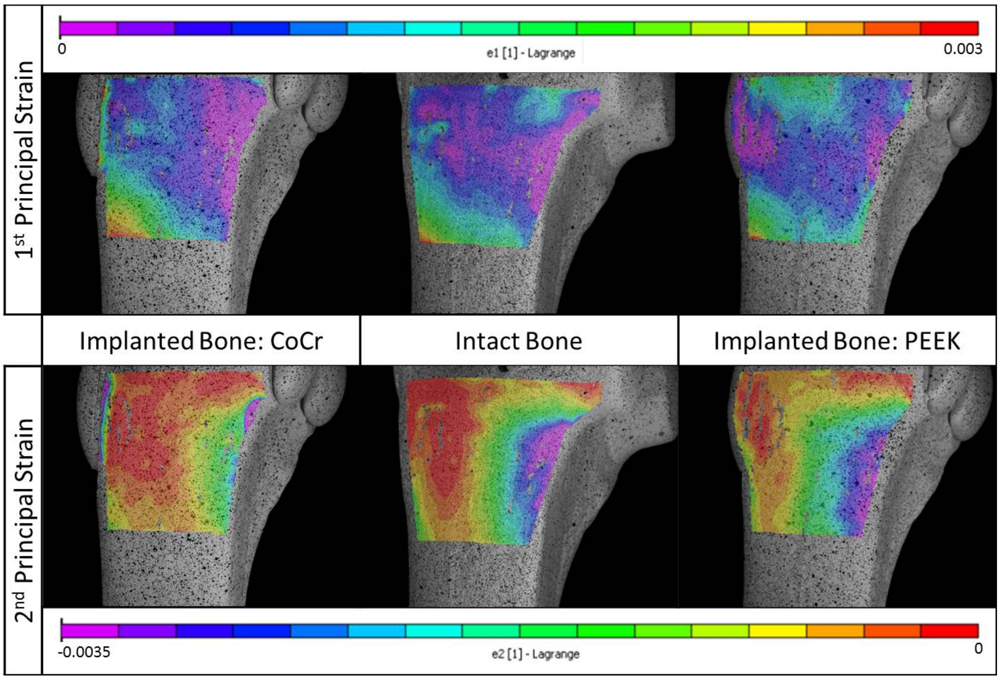

Figure 4.5: Principal strain maps for the intact and implanted DIC tests on the lateral bone surface (1st principal = tensile, 2nd principal = compressive)

0.651). A closer agreement was shown between the strain distribution of the PEEK implant dataset and the intact bone dataset ($R^2 = 0.771$ with slope $B = 1.270$, Pearson's correlation coefficient = 0.878) (Figure 4.6).

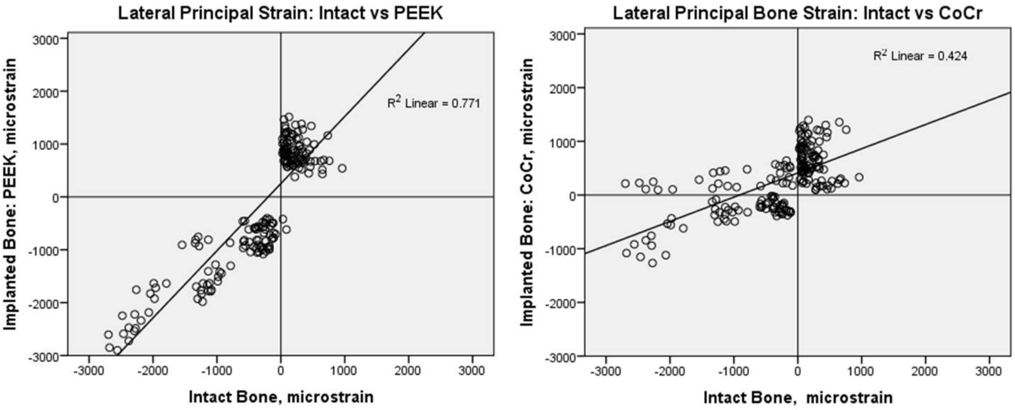
Lateral Principal Strain: Intact vs PEEK

Lateral Principal Bone Strain: Intact vs CoCr

Figure 4.6: Graphical comparison of principal strains in the intact and implanted cases on the lateral bone surface

This scatter was less pronounced on the anterior bone for both PEEK ($R^2 = 0.982$ with slope $B = 1.209$) and CoCr ($R^2 = 0.973$ with slope $B = 0.547$), compared to the intact dataset (Figure 4.7). However, the closer agreement between the PEEK implant and the intact bone dataset remained.

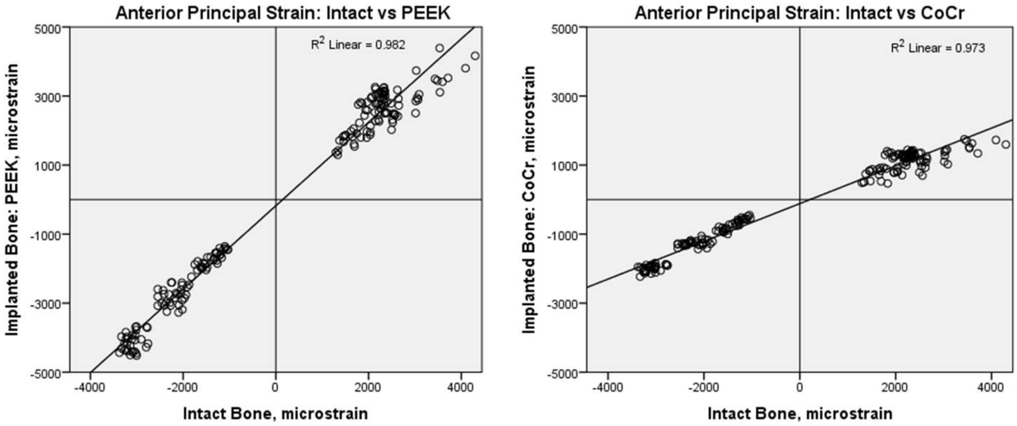

Figure 4.7: Graphical comparison of principal strains in the intact and implanted cases on the anterior bone surface

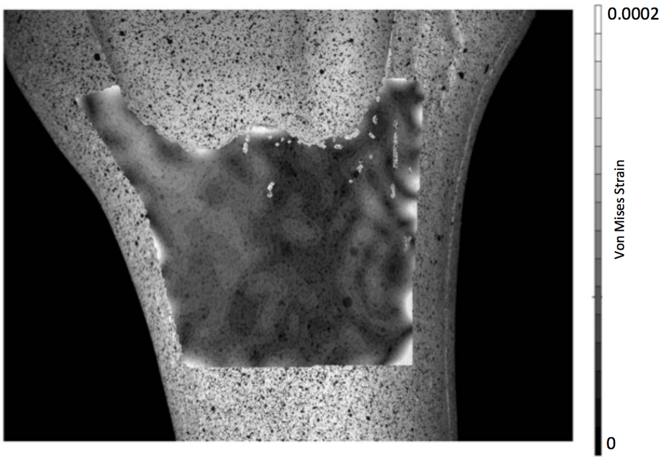

(a) Anterior

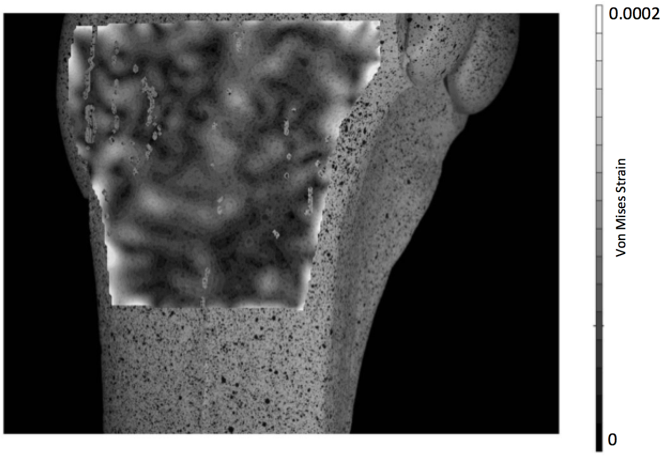

(b) Lateral

Figure 4.8: Example strain plots showing the noise distribution across the femoral surfaces from sequential unloaded speckle datasets

Strain maps under nominally zero strain conditions show the distribution of noise in strain measurement for the anterior and lateral views (Figures 4.8a and 4.8b, respectively). Higher noise values are located at the edges of the DIC analysis region.

4.3 Full DIC Analysis Analogue Bone Study

4.3.1 Methodology

It was concluded from the preliminary study that for further comparison with clinical and FE data, the DIC cameras needed to be translated vertically to include the distal section of bone in contact with the distal face of the femoral component. A zone on the distal lateral surface was identified from the literature as the region of particular interest for DIC analysis of metaphyseal bone surface strain in the implanted and intact states (see Section 2.3.3 (Abu-Rajab et al., 2006; Jarvenpaa et al., 2014; Soininvaara et al., 2004)). Whilst a similar experimental setup was used, a parameter selection protocol was employed (Section 4.3.1.2) to evaluate the reliability and accuracy of measurements on the distal femoral surface.

4.3.1.1 DIC Test Technique

The intact and implanted analogue femur models used in the preliminary study (section 4.2.1) were used again in the full DIC study, with the same DIC equipment. The speckle pattern coverage across each specimen was approximated by converting images to binary to assess the speckle size and percentage coverage using ImageJ software (National Institutes of Health, MD, USA) (Lecompte et al., 2006).

Covering the lateral side of the distal extent of the femur, the cameras were positioned with a relative pan angle of 25°, with a baseline of 139mm and a focal length of 308 mm, resulting in a spatial image resolution of $\approx$40 μm/pixel. Each femur was illuminated using the same lighting setup as in the preliminary study (Figure 4.2).

Each distal femur was loaded to 750 N, as established from the preliminary study, using the corresponding polyethylene (UHMWPE) tibial component and a planar bearing on an Instron 5569 electromechanical test machine. Six repeat tests were carried out to assess experimental error and account for any variation in tibial component positioning. The tibial component was removed between tests.

In each test, a ramped displacement was applied until the target load was attained, at which point the crosshead was held in position at a constant displacement while six consecutive images were taken (2 fps) to account for measurement variability due to sensor noise. Pre- and post-test static images were obtained for each bone under nominally zero strain conditions to quantify the displacement and strain resolutions. A vertical translation was performed in order to assess the ability of the software to perform a rigid body movement correction and determine any effect on the strain resolution.

4.3.1.2 Displacement and Strain Calculation

Vic-3D software was used to calculate the displacement and strain fields under loading. The same analysis area was used on each femur with the hole in the lateral surface (from manufacture) masked out. The selected displacement calculation method employed the normalised sum of square differences correlation criterion (NSSD), which is robust to changes in specimen lighting during deformation, and the optimised 8-tap spline interpolation method, which minimises interpolation bias (Sutton et al., 2009). To determine the optimum subset and step size in terms of maximum strain gradient sensitivity versus noise, the standard deviations (SD) of horizontal and vertical displacements (U and V, respectively) were evaluated, under nominally zero strain conditions, both static and after rigid body correction (Figure 4.9).

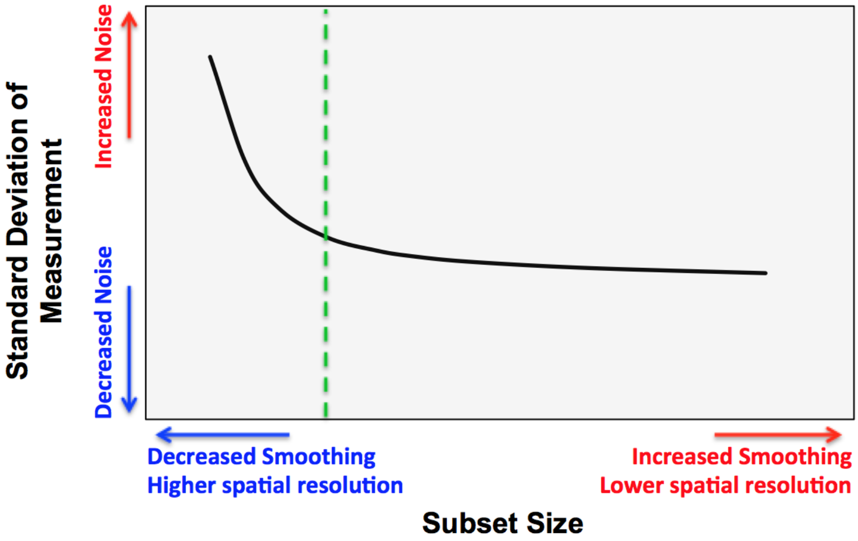

Figure 4.9: Selection of subset size: a trade-off between noise and smoothing of the data under nominally zero strain conditions (example curve)

Using the same conditions, a suitable decay filter size for the computation of the Green-Lagrangian strain field was determined from the SD of strain across a range of subset and step sizes. The mean and SDs of the displacement and the strain under nominally zero strain conditions were taken as the respective measurement bias (systematic error) and resolution. The bias gives a measure of the accuracy of the DIC technique (Figure 4.10). The raw image noise was assessed by comparing the standard deviation of pixel difference between consecutive unloaded images.

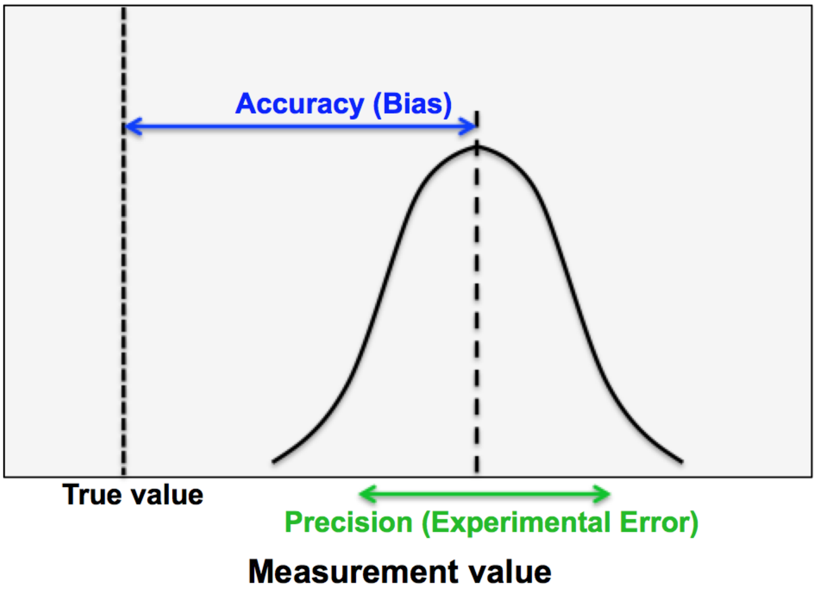

Figure 4.10: Schematic to show the accuracy and precision of measurement, determined by the bias and experimental error in the DIC technique

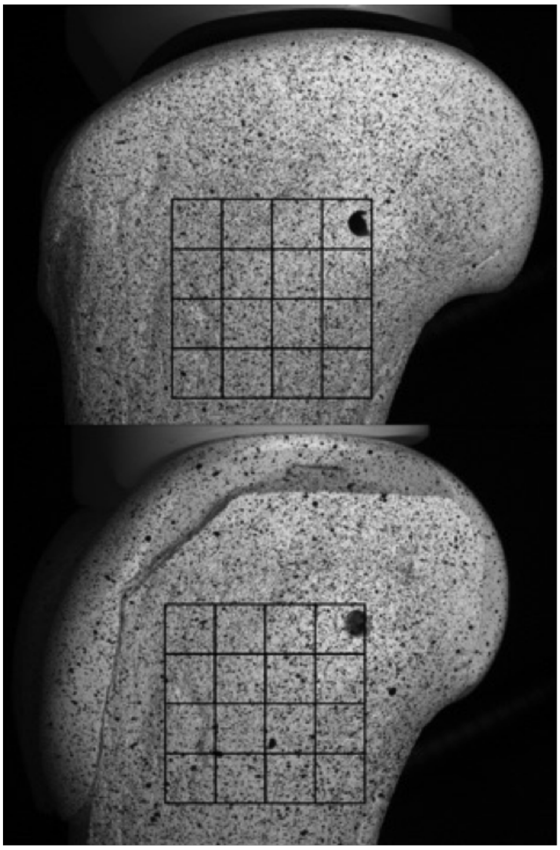

Figure 4.11: Virtual strain gauge regions of interest on the intact (top) and implanted (bottom) bone surfaces

The 1st (major, tensile) and 2nd (minor, compressive) principal strain measurements under load were averaged within sixteen 5 mm^2 virtual strain gauge ROIs across the lateral side of each bone for quantitative comparison using Matlab software (MathWorks, MA, USA) (Figure 4.11). The measurement variability was calculated from the SD of the strain measurements in each repeat test across the ROIs to give a measure of the precision or experimental error (Figure 4.10). As in the preliminary study, the principal strain values from each ROI were plotted for the intact versus implanted cases, and the regression score (R^2) and gradient (β) were calculated to evaluate the strain relationship (ideal case R^2 = 1 and β = 1) (IBM SPSS Statistics 20, IBM Corp., USA). A Wilcoxon Signed Rank Test was used to test the null hypothesis that there would be no difference between the strain at relative ROI locations on the intact and implanted bone surfaces at the 5% significance level.

The bone strain distributions were then compared to those predicted by an FE model of the analogue bone experimental setup.

4.3.1.3 Finite Element Computational Model

In Solidworks (SolidWorks Corp., Concord MA, USA), a block cutter geometry was created around the parasolid (.x_t) geometry of the Maxx Freedom Knee femoral component, and saved as a surface mesh (.stl) file (Figure 4.12). The implant backing surface was defeatured to simplify the geometry for meshing, removing features that would not affect load transfer (Figure 4.13b). The full implant geometry is shown in Figure 4.13a for reference.

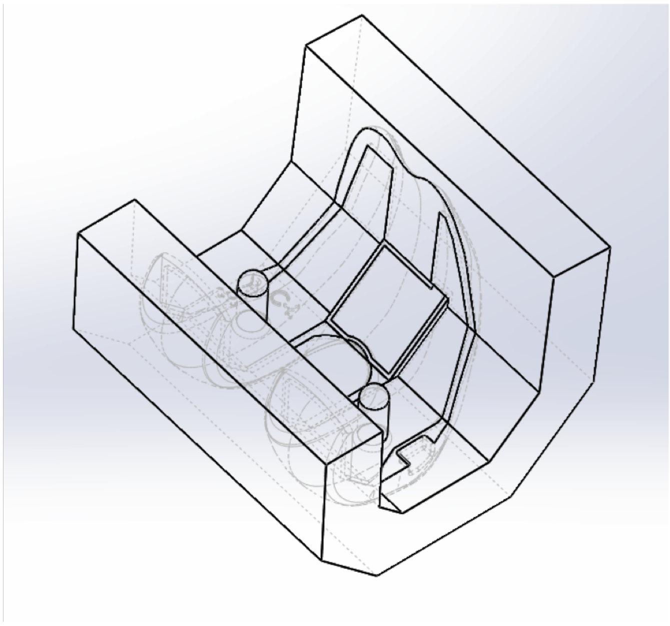

Figure 4.12: Bone cutter geometry aligned with implant

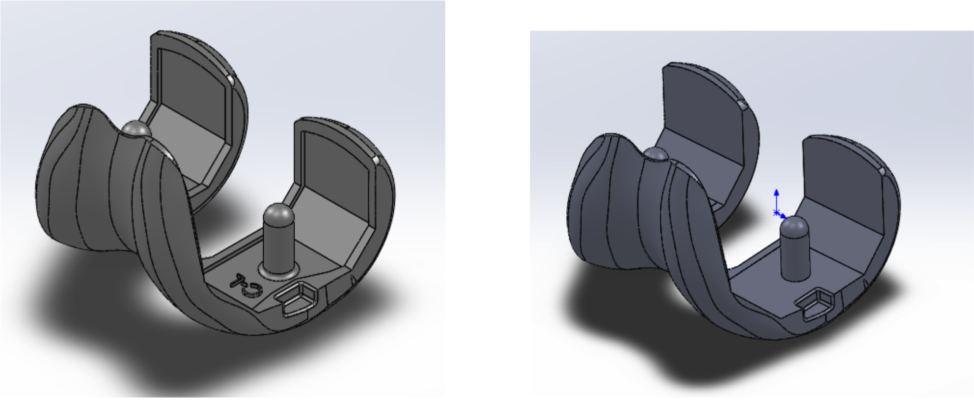

(a) Maxx Freedom Knee femoral component

(b) Defeatured component

Figure 4.13: Maxx Freedom Knee femoral component (Maxx Orthopaedics Inc., PA, USA) and defeatured geometry

An .stl model of the Sawbone femoral geometry (cortex and cancellous components) was then implanted using boolean split operations with the cutter model geometry in Rhinoceros software (Robert McNeel & Associates, WA, USA). μCT scans of the PEEK implanted femur DIC test specimen (described in section 6.2.2.1 of Chapter 6) were used to align the cutter and implant relative to the intramedullary canal. This ensured the model's implant positioning accurately represented the physical test. The shaft was cut, leaving the distal third, as used in the experimental setup. The cortex, cancellous and implant model constituents were then imported into ICEM CFD software (ANSYS Inc., Cannonsburg PA, USA) where the geometries were healed and meshed. Dense first order tetrahedral elements were used with a maximum size of 3 and 2 mm for the bone and implant parts, respectively. An intact bone model was also meshed using the same size elements, for reference.

The meshes were exported to ANSYS 14.0 (ANSYS Inc., Cannonsburg PA, USA) for analysis. Material properties were applied to the cancellous and cortex regions with a Young's modulus of 200 and 6000 MPa, respectively, and a Poisson's ratio of 0.3. Young's modulus values of 4 GPa and 220 GPa were applied to the PEEK-OPTIMA and ASTM F75 CoCr implanted models respectively, with a Poisson's ratio of 0.3. Boundary conditions were applied with a 50 mm fixed region at the cut end of the shaft, representing the length of the bone potted in resin. The loading contact patch radius was selected from the surface nodes at maximum distal extent of the intact and implanted condyles to a surface depth of 2 mm. A 750 N load was uniformly divided across these nodes before the model was solved. The meshed intact and implanted models are shown in Figures 4.14a and 4.14b.

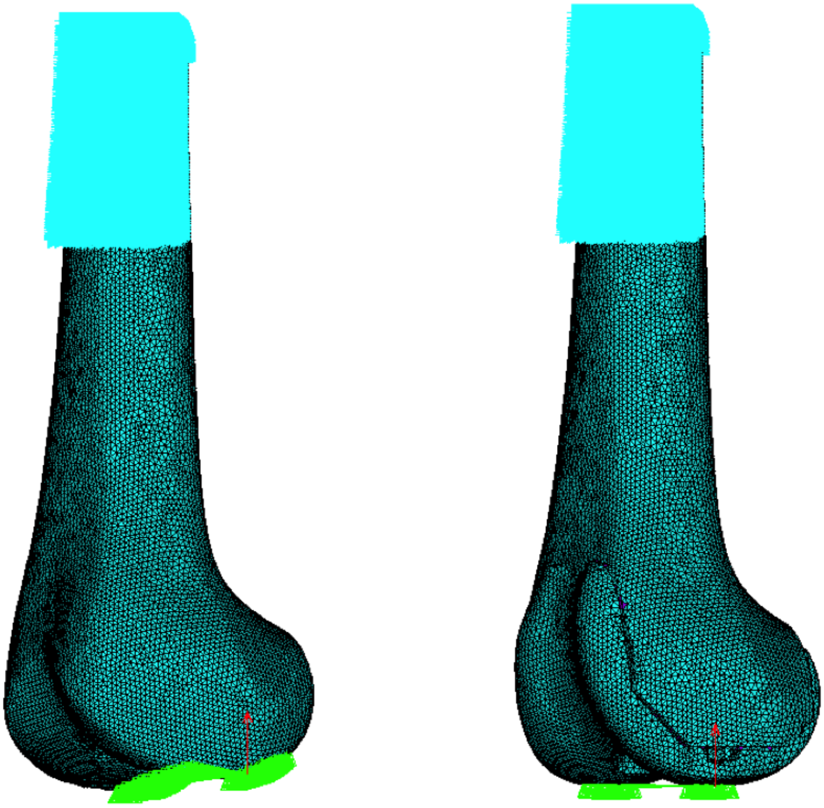
(a) Intact Model (b) Implanted Model

Figure 4.14: Meshed intact and implanted femur models with loading contact patches (green) and fixed potted region (blue)

4.3.2 Results

4.3.2.1 Speckle Pattern

The analogue femur specimens had a speckle pattern coverage of approximately 28%, 25% and 22% on the intact, PEEK implanted and CoCr implanted bones, respectively. The diameter of speckles ranged from 2-30 pixels (Figure 4.15).

4.3.2.2 DIC Parameter Selection

Evaluation of grey level pixel difference (range 0-255) from one consecutive static raw image to the next gave a maximum SD of 2.846, which occurred in the implanted PEEK speckle images, corresponding to ~1% raw image noise value (Figure 4.16).

The highest displacement and strain SDs under static nominally zero strain conditions were also measured for the implanted PEEK case. Hence the DIC analysis parameters

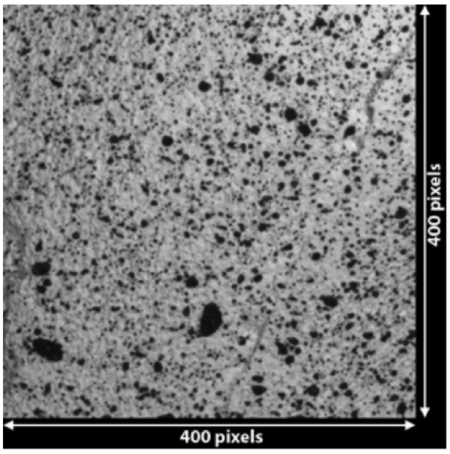

Figure 4.15: Resulting speckle pattern achieved on analogue bone surface

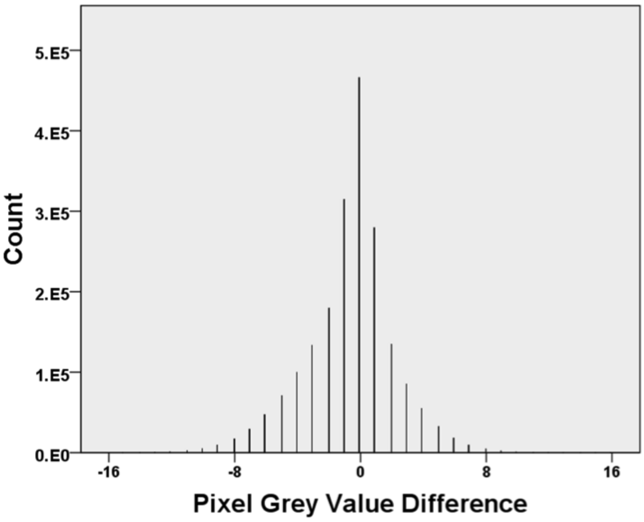

Figure 4.16: Assessment of raw image noise from pixel grey value difference (0-255 full grey scale range)

were determined from this test specimen and the consequent measurement resolutions are presented as the worst case for the DIC technique used.

The SD of displacement and strain under static zero strain conditions with increasing subset size were plotted to aid analysis parameter selection (Figures 4.17 and 4.18, respectively). A subset size of 41 x 41 pixels was chosen as a balance between noise and smoothing of the displacement field, whilst providing a large amount of unique data (speckle diameter range 2 to 30 pixels). A step size of 7 pixels and a filter size of 15 data points were chosen using the same criteria for the strain field across the bone surface (resulting in >16000 data points). The step size had a negligible effect on the displacement SD with this test specimen geometry ($p = 0.121$).

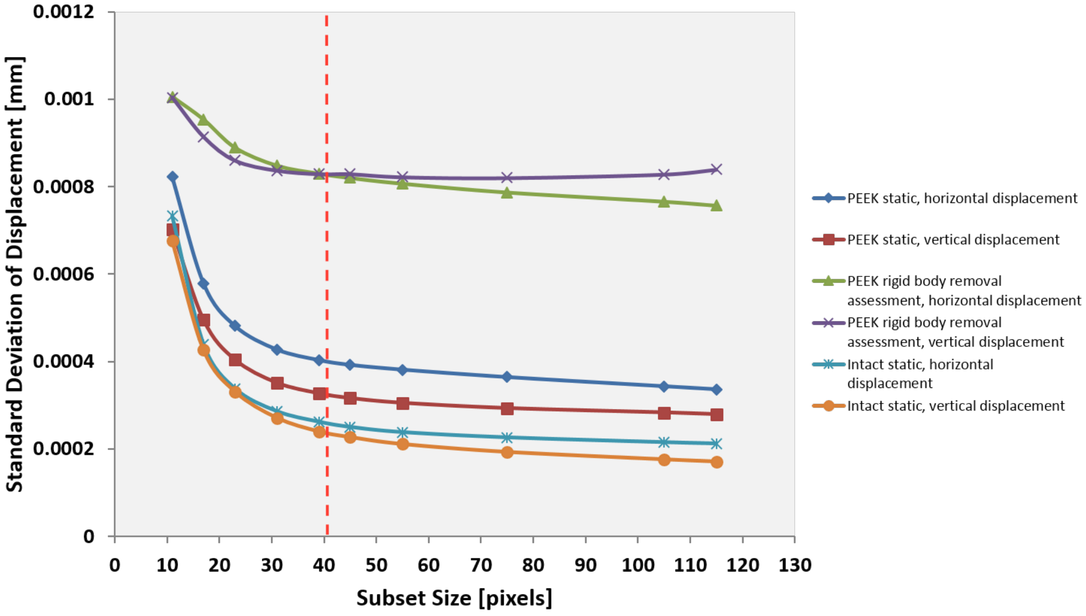

Figure 4.17: DIC parameter selection graph showing variation in SD of displacement with subset size for the analogue bones (red dashed line = chosen subset size)

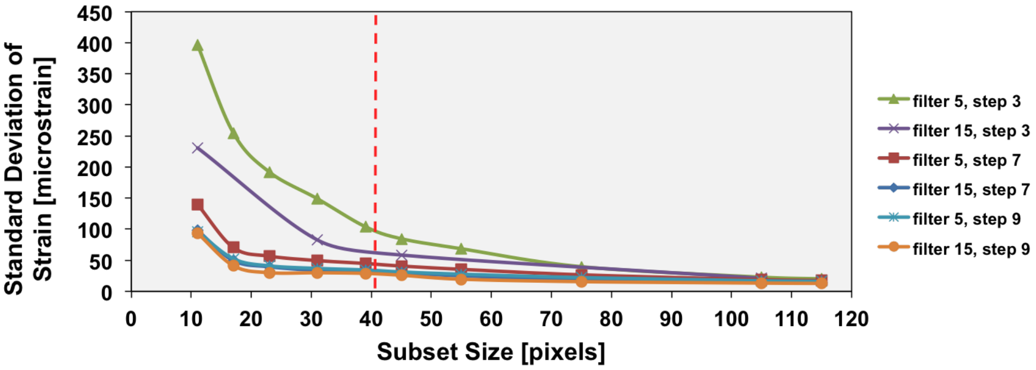

Figure 4.18: DIC parameter selection graph showing variation in SD of strain with subset size, step size and strain filter (red dashed line = chosen subset size)

4.3.2.3 DIC Resolution

With the subset size of 41 x 41 pixels and a step size of 7 pixels, under static conditions the maximum displacement resolution (SD) was 0.008924 pixels or 0.36 μm with a mean bias value of 0.00635 pixels, or -0.25 μm. The maximum strain resolution with a filter size of 15 data points was a SD of 30 $\mu\epsilon$ with a mean bias value of 38 $\mu\epsilon$. After the translation test under nominally zero strain conditions, the rigid body correction performed by the software gave a maximum strain resolution SD of 46 $\mu\epsilon$ with a mean bias value of 72 $\mu\epsilon$.

4.3.2.4 Experimental Error

The experimental error of strain measurement was ±71 $\mu\epsilon$, ±33 $\mu\epsilon$ and ±24 $\mu\epsilon$ for the intact, PEEK, and CoCr implanted bone surfaces respectively. This gave a maximum six sigma experimental error (representing ± 3 S.D. or 99.7% spread of data error) of ±213 $\mu\epsilon$ or 9.7% of the maximum strain in the virtual gauge region, 2200 $\mu\epsilon$.

4.3.2.5 Strain Measurements

The principal strain maps show the qualitative difference in surface strain distribution for the three cases (Figure 4.19). Comparatively low strains were measured on the model with the CoCr implant relative to the intact case, whereas the PEEK implant induced a strain distribution closer to the intact case. However, there was a shift in the strain path away from the posterior towards the anterior distal region of the lateral bone surface implanted with PEEK.

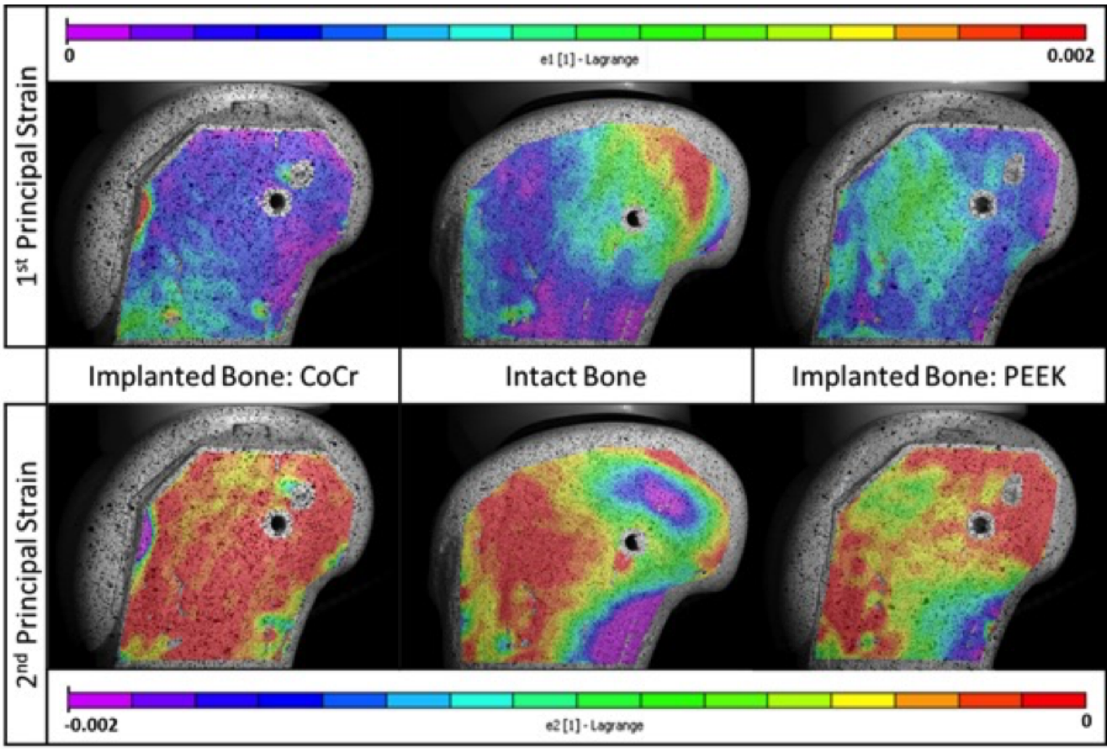

Figure 4.19: Principal strain maps for the intact and implanted test specimens in the lateral view

Quantitatively, a larger deviation was observed between the CoCr implanted bone dataset and the intact bone dataset at each ROI ($R^2 = 0.6178$, slope $\beta = 0.4314$) with significantly different strain measurements at the 5% significance level ($p = 0.014$) (Figure 4.20). A closer agreement was found between the strain distribution of the

PEEK dataset and the intact dataset at each ROI ($R^2 = 0.7972$ with slope $\beta = 0.939$) with no significant difference ($p = 0.231$).

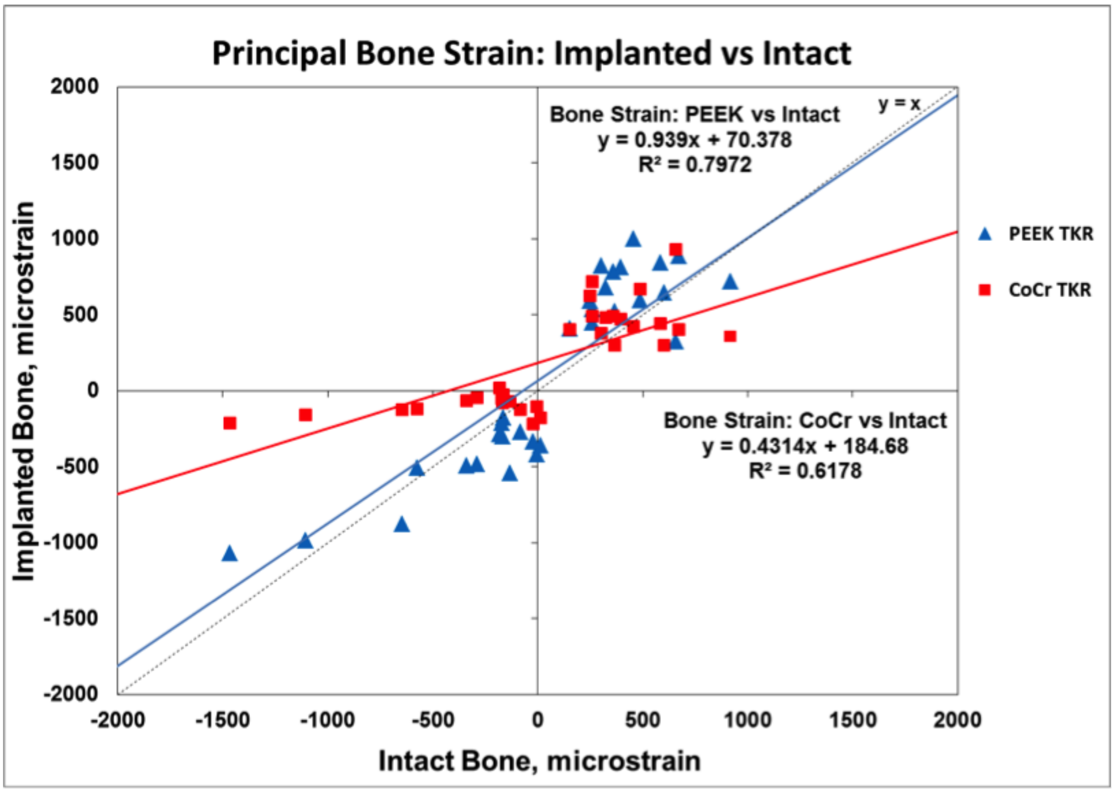

Figure 4.20: Quantitative comparison of principal strain on the intact bone with the implanted bone surfaces

4.3.3 FEA Results

A comparison of the strain distribution measured on the lateral bone surfaces using DIC with those predicted by the femur FE model shows that qualitatively the distribution is similar. Figure 4.21 and Figure 4.22 show the compressive and equivalent strain distribution on the lateral bone surfaces, respectively. The 2D compressive surface strain measurements from DIC (zero through thickness) cannot be directly compared with the 3D predictions of the FE model, but the equivalent strain ('Von Mises' in Vic-3D software) allows for strain magnitude comparison, based on a 2D principal plane strain formulation (Dickinson et al., 2011; Simonsen, 2011). Nevertheless, the equivalent strain plots show similar strain distributions for each case.

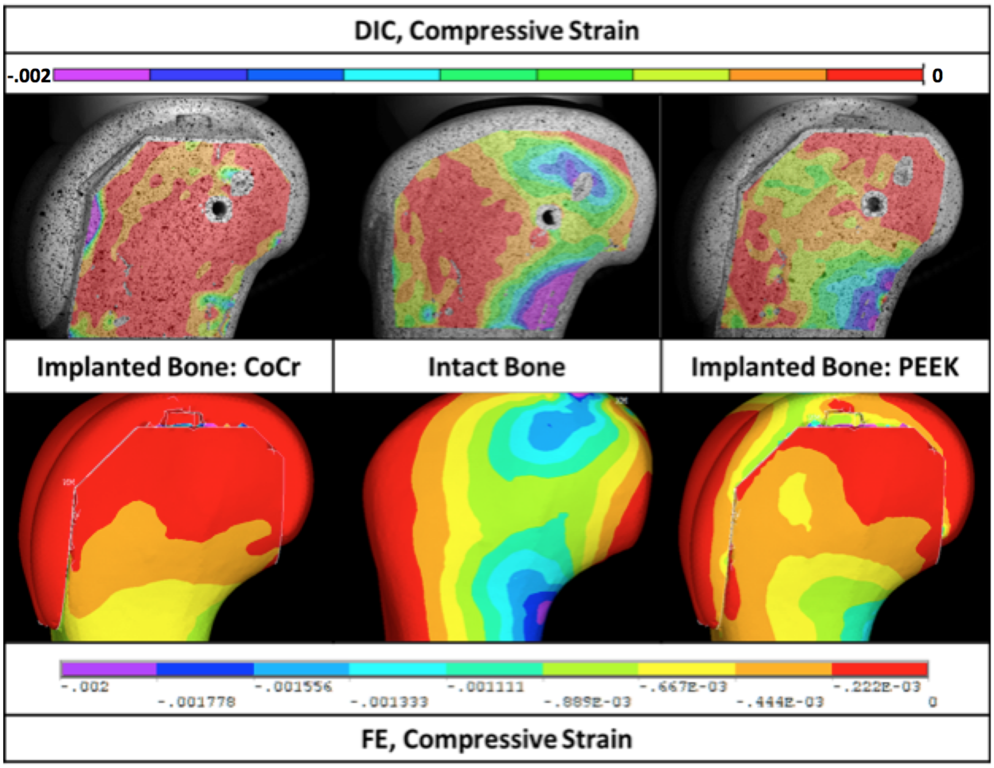

Figure 4.21: Comparison of the compressive strain measurements from DIC and predictions from FEA

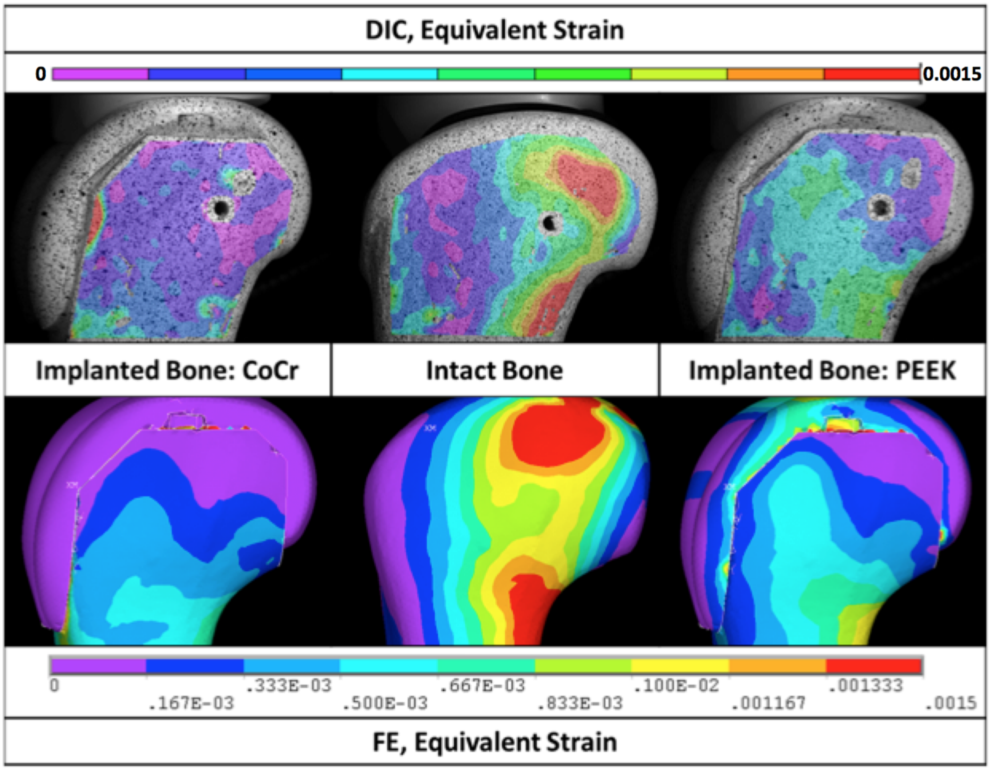

Figure 4.22: Comparison of the equivalent strain measurements from DIC (Von Mises) and predictions from FEA

4.4 Discussion

The purpose of this Chapter was to present a DIC method, developed using an analogue bone model, as a means of assessing the stress shielding effect of TKR femoral component designs and materials. The influence of PEEK and CoCr femoral component materials on distal femoral analogue bone surface strain has been presented, in comparison to an intact reference model.

In the preliminary study, relatively higher bone strain in regions close to the CoCr implant can be attributed to the high stiffness mismatch between implant and bone where the bone is constrained to the implant by the cement. Due to the implant geometry, bone in the central metaphyseal region of the femur is not so constrained by the CoCr implant and subsequently much lower compressive strains are observed compared to the intact bone case. This suggests that stress shielding is occurring which could lead to bone resorption *in vivo* if the local strains are below the modelling threshold strain criterion for bone maintenance (Frost, 2003).

These findings are consistent with clinical observations from bone mineral density scans of implanted metallic TKRs in the literature, which have shown a reduction in bone density in the low strain regions observed with the CoCr implanted bone, where the bone mass has reduced after stress shielding (Soininvaara et al., 2004). High strain gradients induced near the stiff CoCr could potentially compromise implant fixation, also leading to component loosening. The compressive strains in the PEEK implanted bone were similar to those in the intact case suggesting that bone would be maintained in these regions. This supports the hypothesis that a compliant PEEK implant could promote more physiological bone strains and promote bone preservation in the long term.

Clinical studies have shown that the central metaphyseal region experiences the greatest loss in bone mineral density (Soininvaara et al., 2004; van Lenthe et al., 1997). This was out of view in the preliminary study and it was that for further comparison with clinical and FE data, the DIC cameras needed to be translated vertically to include the distal section of bone in contact with the distal face of the femoral component. In addition, as DIC is an optimisation technique, it requires a rigorous parameter selection protocol in order to achieve valid results for each experimental scenario and to inform the reader of the study fully. This is not commonly reported in biomechanical studies using DIC, so was included as a development for the full DIC study.

In the full DIC study, statistically significantly lower strains were measured across the lateral metaphyseal surface of the bone implanted with CoCr compared to the intact reference model, whilst the PEEK implanted cortex strain was not significantly different. This further supports the hypothesis that a more compliant PEEK implant could promote a more physiological strain distribution compared to that induced by a contemporary metallic implant, thus indicating the potential for successful long term bone maintenance.

The anterior shift of the strain path observed in both implanted cases compared to the intact case (Figure 4.19) may be caused by the change in geometry of the articular surface, causing an anterior translation of the tibio-femoral contact. This was also observed in the FEA results. The strain distribution on the CoCr implanted bone in the distal region confirms the postulations of the preliminary study and is corroborated by studies in the literature, examining the metaphyseal bone directly. Clinical measurements of longitudinal BMD changes around metallic TKRs, have reported a reduction in density particularly in the central metaphyseal region due to stress shielding and reduced patient activity following surgery (Abu-Rajab et al., 2006; Jarvenpaa et al., 2014; Soininvaara et al., 2004). However, these represent the changes in bone density throughout the entire mediolateral or anterioposterior extent (in the lateral and anterior views, respectively), so do not give local density information.

Whilst DIC gives local surface strain information, FEA allows interrogation of internal bone strain.

The experimental measurement of distal femoral bone strain following implantation of a TKR implant has not been previously investigated to the author's knowledge, so direct comparisons to other studies could not be made. Previous knee implant studies used DIC to assess bone strain have focused on the tibial bone surface (Malinzak et al., 2014; Mann et al., 2014; Scott et al., 2013). A DIC study on periprosthetic bone strains with postmortem retrieved TKR tibial components carried out by Mann et al. (2014) suggested that a reduction in BMD leads to higher bone strains which could lead to an increased risk of failure. This suggests that if a PEEK implant promotes a mechanical strain stimulus closer to that of the physiological case, it could reduce the risk of a reduction in BMD and potentially reduce the risk of failure. In a study of the effect of unicompartmental knee implant design on proximal tibial strain in a Sawbone model, Scott et al. (2013) reported that metal-backed implants induced more strain shielding compared to an all-polyethylene design, as was observed with the metallic and polymeric implants in this study. However, it was also concluded that the all-polymer design was also associated with bone damage at the microscopic level due to its compliance and it was advised that these devices should be used with caution in patients likely to induce high loads. This requires further investigation for the all-polymer PEEK femoral component within a cadaveric model, as a firm conclusion cannot be drawn from an analogue Sawbone model and the implant design parameters vary greatly. Digital Volume Correlation (DVC), a three-dimensional extension of DIC, has recently shown great potential for more accurate quantification of this potential interfacial micro-damage (Tozzi et al., 2014). A feasibility study for the use of DVC to assess strain at the PEEK-cement interface is discussed in Chapter 6.

Regarding the test specimens used in this study, a thin layer of paint was used so that the deformation of the paint was the same as the underlying bone. The paint layer applied would not affect the surface properties any more than applying a strain gauge to the surface with an adhesive. It was reported by Crammond et al. (2013) that a black pattern on a white background produces less measurement error, as applied in these tests. The accuracy of the DIC strain measurements are dependent on the resolution of the speckle images, the speckle pattern applied and the subset size used in the calculation of displacements. To minimise the error from the speckle pattern, an even distribution of speckle sizes with unique features and randomness is required to maximise the correlation function response as the speckles are tracked within the image subsets (Crammond et al., 2013). However, there is a finite number of pixels within the pattern so smaller speckles are less unique and more difficult to track.

Therefore there is an optimal size range for speckles, depending on the experiment, which affects the subset size required for analysis (Lecompte et al., 2006).

The brush-flicking technique used to apply acrylic paint produced a wide distribution of speckle size (2-30 pixels). However, the speckle pattern could have been more densely populated to reduce the subset size and improve the resolution of strain measurement (Yaofeng and Pang, 2007). The spatial resolution of the strain field obtained using DIC is limited by the maximum size and minimum spacing density of the speckle pattern used (maximum speckle diameter 30 pixels and approximate speckle coverage of 22% on the intact bone surface). Hence, a larger subset size was required to track the deformation of the pattern on the bone surface without leaving gaps in the data, as similarly reported by Carriero et al. (2014). Nonetheless, the geometry (low curvature) and material of the distal femur surface was such that there were no severe strain gradients which would require small subsets for accurate measurement, and the DIC parameters used were considered sufficient for this application (Lecompte et al., 2006). In order to increase the number of pixels in the speckle pattern, images could be obtained at higher magnification in a smaller region of interest. A wide field of view was used in these tests so that the entire width of the anterior and lateral surface of the bone was captured with the implant. The cameras used had fixed lenses, but macro lenses could be used to achieve a higher magnification.

Errors in DIC measurement arise in areas of high curvature, however, compared to the proximal femur, the anterior and lateral surfaces of the distal femur have more gradual curvature, so errors would be contained within the edges of those regions (Dickinson et al., 2011). The strain in the unloaded reference images for the anterior view, Figures 4.8a, and lateral view, 4.8b, show that the error in the measurement is low compared to the peak strains measured under load. The strain resolution value (standard deviation under nominally zero strain conditions) and bias (mean under nominally zero strain conditions) were of similar magnitude between the preliminary and full DIC studies after selection of appropriate analysis parameters. To use a measure of sensitivity as the mean plus 3 standard deviations (as used by Dickinson et al. (2011)) is now considered excessively strict. Whilst this gives 99.7% confidence in the spread of the data, it is a measure of the sensitivity range, which doesn't translate directly to the resolution of measurement. A technique can be precise (high resolution), yet inaccurate (bias from systematic errors), or vice versa, which indicates that the use of a mean value as a measure of bias, and the standard deviation as a measure of resolution (uncertainty) is more appropriate for DIC (Roux et al., 2012).

The experiments could be repeated with strain gauges to measure finite strain values at known locations to validate the DIC measurements. This was carried out in a previous study which demonstrated good correlation between strain measurements from DIC and strain gauges on a composite hemi-pelvis (Ghosh et al., 2012a). However, strain gauges carry their own disadvantages as discussed in Section 2.6.2.1 of the literature review, such as large average point measurements, local stiffness effects and problems with bonding the gauge to the test specimen.

The rough surface of the anatomical analogue femur models used in this study introduced some difficulty in achieving even lighting of measurement regions which could lead to errors (Sutton et al., 2009). Even though four light sources were used in the DIC tests, shadows were cast across the bone surface. This resulted in some holes in the strain field data post-analysis, where the displacements could not be calculated from speckles across narrow valleys on the bone surface. However, this was a repeated effect for each comparative bone test and the measurement bias was evaluated for each.

Considering the materials used in this study, the anatomical femur models used were more flexible than real bone, which would amplify the comparative strain signal in the DIC experiments. Therefore, any higher strains at the edge of the PEEK implant may be explained by the lower modulus of the anatomical femur model used which introduces some implant constraint and is a limiting factor for this study; nonetheless the results are still comparable. In a real femur, the cortical bone would have a modulus slightly greater than that of the PEEK femoral component, which implies that the PEEK implant would not be constraining the bone so the loads transmitted would be even closer to those in the intact femur.

It should be noted that these results are only comparative due to the use of analogue femur models and a single load case. However, the geometry and material properties of the analogue femora are nominally the same and therefore direct comparisons are possible, unlike cadaveric models with inter- and intra-patient variability which may lead to greater disparity in the induced strain fields. In the absence of well-matched pairs of cadaver bone samples, this would require a larger population for sufficiently powerful statistical analysis.

This study is limited by a single load case, static stance, which was necessitated by the lower modulus bone model used in order to reduce bending at the fixation point. In order to compare this study with finite element (FE) analysis predictions from models generated from femoral CT data, DIC tests need to be conducted on real bone (cadaveric models) to evaluate absolute strains and also to investigate other load cases such as heel strike (a worst case load scenario in gait). It may be difficult to apply a speckle coating to the surface of a cadaveric bone due to the moist surface, which could reduce the accuracy of the results. However, there is a precedence that suggests it is possible using the appropriate technique (Ghosh et al., 2012b).

A limitation of DIC is that it only measures strains on the specimen surface. Therefore, in the case of implanted bone, only the external cortical bone strains can be measured. In Total Knee Replacement, the implant should be supported by the cortex to relieve cancellous bone strains (Bourne and Finlay, 1986). Whilst measurement of cortical bone strains give an indication of the induced bone strains, it does not directly inform about the cancellous bone strain state, an area which could experience bone resorption, directly behind the implant. If an FE model of the implanted bone can be corroborated by DIC results, this can then be used to further predict the cancellous bone strain distribution, the remodelling stimulus, and possibly the progression of remodelling.

The DIC measurements of the induced strain fields in the PEEK, CoCr and intact bone cases qualitatively corroborate the strain distribution predictions of the FE model in this study. Variations in the equivalent strain distributions between the DIC and FEA results may be due to an unrealistic load distribution and contact area, as well as the exclusion of an interdigitated cement layer in the implanted models. Variation in the size and angle surgical bone cuts would also be present in the experimental models due to the tolerance between the blade and the cutting jig. For use as a quantitative validation tool, the FE model geometry, material properties, and load case need updating to replicate a real patient case fully. Predictions of the cancellous bone strain state could then be made. The presented DIC protocol has been prepared for translation to a cadaveric bone model, which is investigated in Chapter 5.

Chapter 5

TKR Femoral Bone Strain Assessment using a Cadaveric Model

5.0.1 Introduction

Following on from Chapter 4, the work in this chapter aimed to investigate the practicalities of applying the DIC technique to cadaveric bone, the test material most representative of bone *in-vivo*, for reliable assessment of the effect of implant material on femoral bone strain.

New challenges arise when applying a suitable speckle pattern to a moist cadaver bone surface. The majority of DIC studies using biological bone materials have used spray paints applied using an aerosol or an airbrush (Carriero et al., 2014; Cyganik et al., 2014; Ghosh et al., 2012a; Gilchrist and Guy, 2013; Grassi et al., 2014; Mann et al., 2014; Sztefek et al., 2010; Terrier et al., 2014). Liu et al. (2014) used iron oxide nanoparticles and Thompson et al. (2007) used photocopier toner, but both of these studies were carried out at higher magnifications than the others. At the microscopic-level on cortical bone, it has been shown to be possible to use the texture of the bone as a speckle pattern for DIC (Budyn et al., 2012; Tang et al., 2015). Zhang and Arola (2004) used a black enamel paint speckle pattern on existing light surfaces, and on top of a thin uniform layer of white enamel paint for darker surfaces on biological tissues.

In the present study, the bone strain distribution was measured on two intact cadaver femurs using the DIC technique developed in Chapter 4, before each cadaver was implanted with a CoCr or PEEK femoral component and re-tested. Therefore each cadaver acted as its own intact reference model, such that the strain distribution could be compared after implantation. The analogue bone strain distribution results were then compared with cadaver bone results to evaluate the technique.

5.0.2 Methodology

Two fresh-frozen femurs, free from disease, were selected from 15 cadaver femurs (Innoved Institute LLC, IL, USA) for size C Maxx Freedom knee femoral components (Maxx Orthopaedics Inc., PA, USA) (width in AP = 58 mm, width in ML = 61.5 mm). For each bone, the AP and ML dimensions were approximated using vernier callipers, whilst some soft tissue remained on the surface of the bone. The bone was then sectioned at 150 mm from the distal end (Figure 5.1a). The soft tissues were removed from the surface using a scalpel and fine tipped forceps, in order to remove as much of the periosteum sheath (the fibrous layer covering the bone surface) as possible. The bone surface was dried with absorbent paper as thoroughly as possible. The resulting bone surface is shown in Figure 5.1b.


(a) Prior to resection (b) Prepared bone surface

Figure 5.1: Resection of soft tissues from the distal cadaver section

The DIC preparation method described in section 4.2.1 of Chapter 4 was then followed, with the intact bone potted in PMMA resin, oriented such that the loading axis of the test machine would represent stance (Figure 5.2a). A speckle pattern was then applied using a thin uniform layer of matt white spray paint and black acrylic speckles, taking care to produce as dense a pattern of small speckles as possible (Figure 5.2b). The distal lateral bone surface was chosen for strain assessment as a particular region of interest for stress shielding and change in bone density, identified in section 4.3.

Subsequently, the full DIC method from Chaper 4 (Section 4.3) was followed, with speckle pattern coverage assessment using ImageJ software, for comparison with the speckle pattern achieved on the analogue bone models.

In the DIC experimental setup, each cadaveric bone was fixed in place on an Instron 8874 hydraulic test machine with a 25 kN load cell and the same dual 2 MP camera setup as with the anatomical Sawbone femur models (section 4.2.1). The cameras were calibrated with a baseline (distance between the cameras) of 88 mm and 103 mm for the 1st (for the CoCr implant) and 2nd (for the PEEK implant) donor cadaver bones respectively. With a focal length of 313 mm, the resulting spatial image resolution was

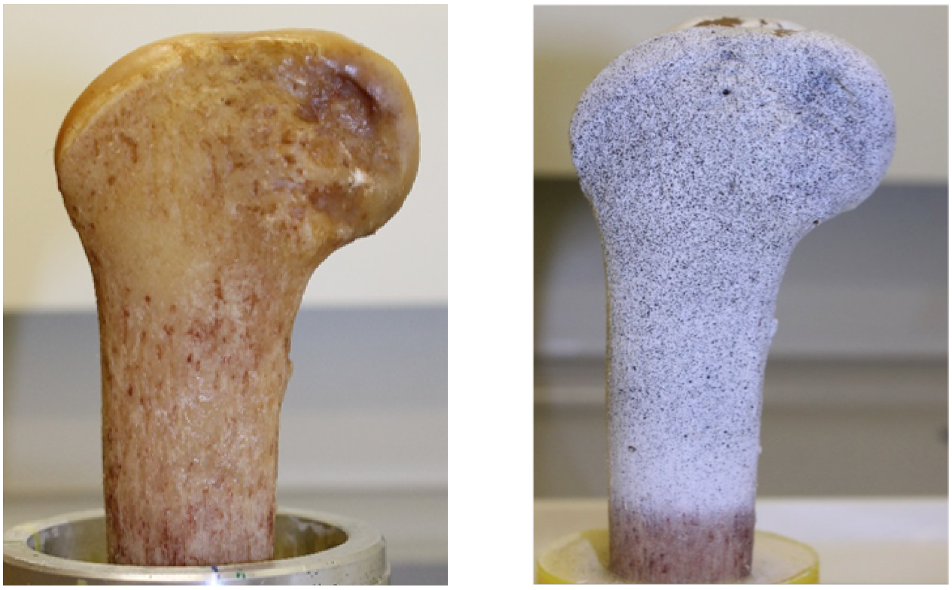

(a) Potted bone prior to speckle painting (b) Resulting speckled bone surface

Figure 5.2: Speckle patterning of the intact distal femur

$\sim$43 μm/pixel. Three fibre optic light sources were used to illuminate the anterior, lateral and posterior surfaces of the cadaver bone surface with a diffuse halogen light source positioned behind the cameras.

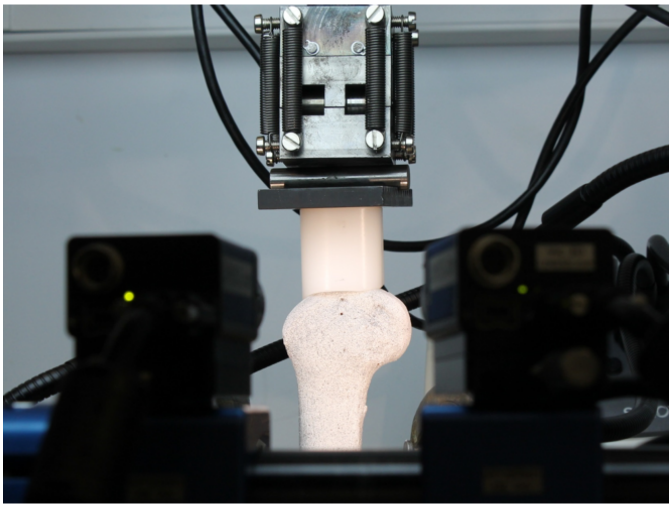

Figure 5.3: Loading setup with the intact bone and DIC stereo cameras in the foreground

The bone was then loaded with a planar bearing and a roller, through the tibial component, up to 2.5 times bodyweight (BW), to account for the different body weights of each donor (donor 1 = 94 kg and donor 2 = 61 kg). The bones were then tested in 0.5 kN increments from 1 kN up to 2.5 kN, to ensure that the best signal to noise ratio was achieved (Figure 5.3). At each load increment, six consecutive images were obtained to assess the experimental error. After each loading cycle, six consecutive images were taken under nominally zero strain (unloaded) conditions to assess the measurement resolution due to noise. This image capturing protocol was carried out in six repeat experiments for each intact bone. The images captured under zero strain conditions in each test repeat were used as the reference in the calculation of displacement vectors from the deformation images taken under load.

After the intact bone strain reference data had been obtained, the bone was removed from the test machine and the articular surfaces were prepared for implantation using the Maxx Freedom knee surgical instrumentation and an oscillating saw. The speckle pattern from the intact bone tests was retained on the bone surface during implantation. Bone debris generated on the lateral surface was wiped away using absorbent paper with care not to damage the painted surface (Figure 5.4).

Figure 5.4: Bone debris and fat produced on the speckle pattern while cutting the distal face of the femur

Once the distal face of the intact femur had been cut, the bone size was checked for the corresponding femoral component size and the alignment screws for 3 degrees of internal rotation were located for size C (Figure 5.5a). The cutting jig was then used to guide the anterior and posterior cuts using an oscillating saw (Figure 5.5b and 5.5c). The prepared cuts before implantation are shown in Figure 5.5d.

The size C femoral component was then fixed in place using Palacos R acrylic bone cement ($E = 2.9$ GPa) mixed under vacuum to the manufacturer's instructions (Heraeus Medical GmbH, Wehrheim, Germany). One cadaver bone was implanted with the CoCr femoral component currently used by the Maxx Freedom Knee implant system and the other cadaver bone was implanted with the PEEK-OPTIMA® femoral component of the same size and geometry. The intact and implanted bones are shown for comparison in Figures 5.6a and 5.6b, respectively, for the CoCr test (donor 1), and in Figures 5.7a and 5.7b, respectively, for the PEEK test (donor 2).

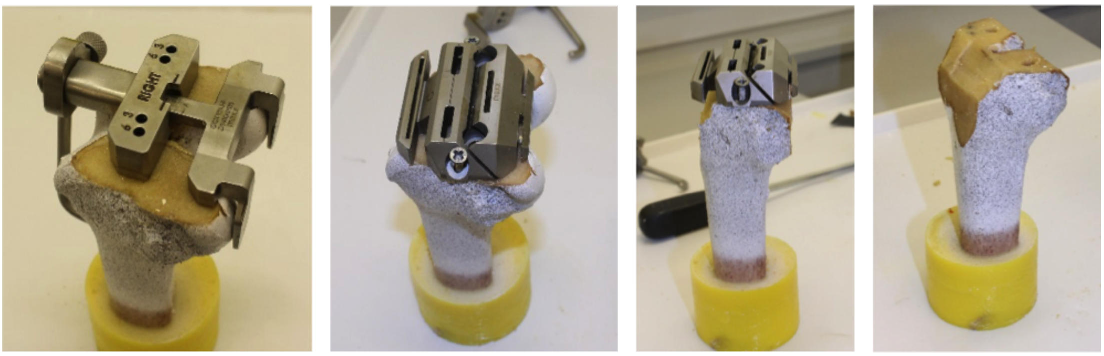

(a) Sizing of the femur after the distal cut

(b) Positioning of cutting jig

(c) Anterior and posterior cuts made using jig alignment

(d) Resulting surgical cut surface

Figure 5.5: Cadaver implantation

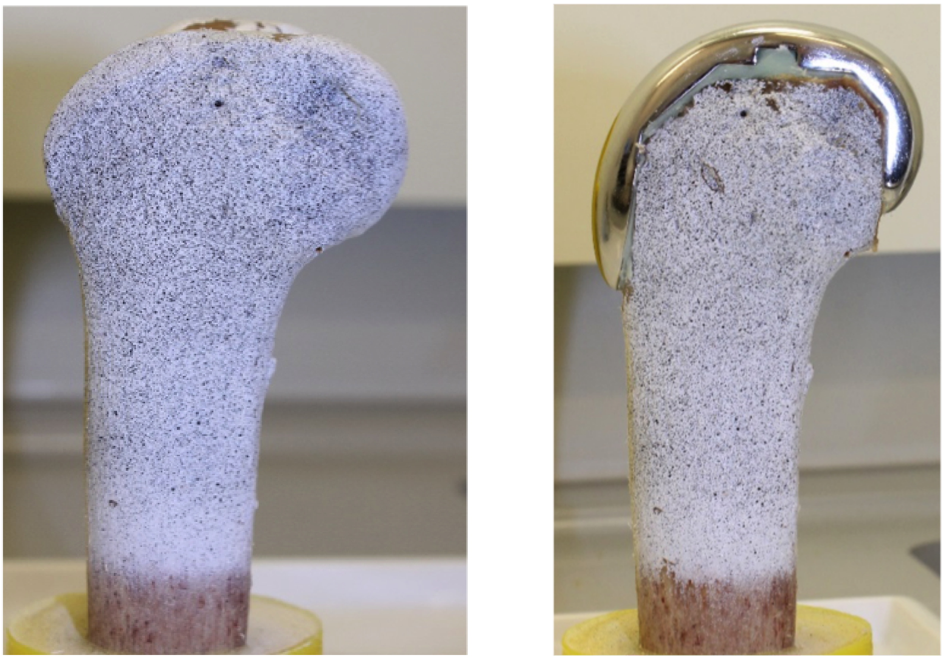

(a) Intact cadaver (donor 1)

(b) Cadaver implanted with CoCr

Figure 5.6: CoCr cadaver test specimen

The implanted bone was then replaced on the test machine, and the stereo cameras were re-calibrated using the 12 x 9 calibration target for the Vic-3D system. The loading and image capture process was then repeated for the implanted femur case.

The DIC analysis for displacement and strain calculation for the intact and implanted cases followed the methodology of Section 4.3.1.2. The strain measurements were averaged within sixteen 5 mm^2 virtual strain gauge regions of interest (ROI) for quantitative comparison of bone strain between each intact and implanted case. The positions of the ROIs across the intact and implanted bones were located in the central

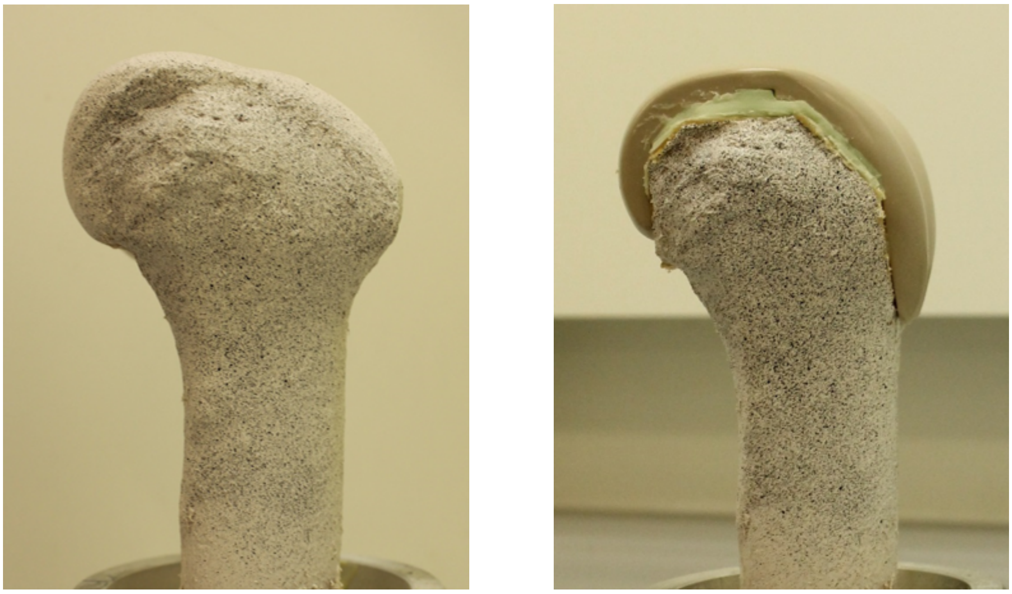

(a) Intact cadaver (donor 2) (b) Cadaver implanted with PEEK

Figure 5.7: PEEK cadaver test specimen

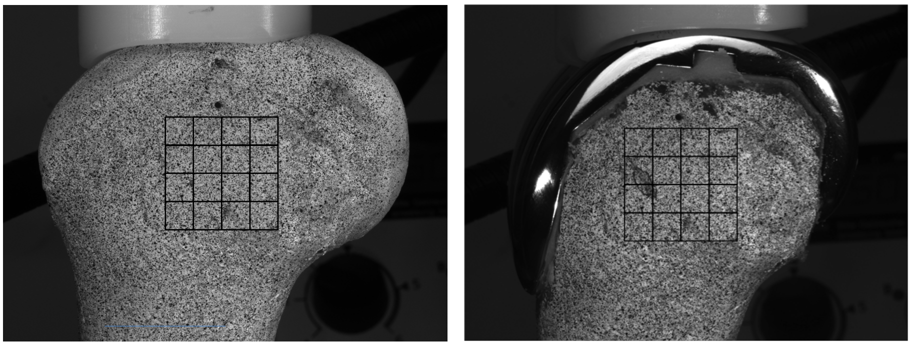

(a) Intact cadaver ROI (b) implanted with CoCr ROI

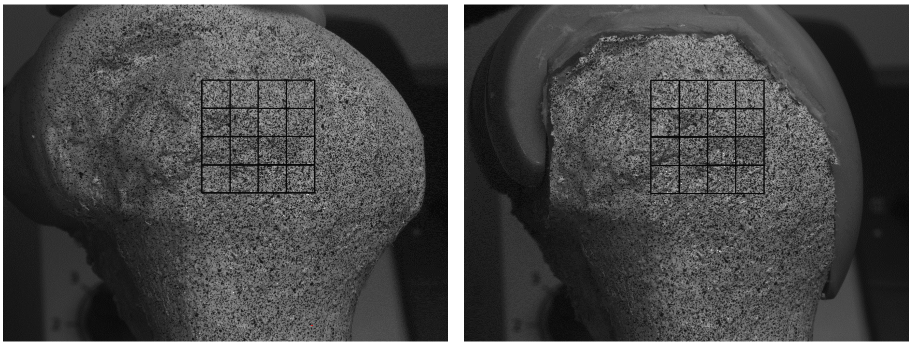

(c) intact cadaver ROI (d) implanted with PEEK ROI

Figure 5.8: Regions of interest across each cadaver in the intact and implanted states

metaphyseal region, avoiding the higher noise regions at the edge DIC analysis area (Figures 5.8a and 5.8b, respectively, for the CoCr bone and 5.8c and 5.8d, respectively, for the PEEK bone). The principal strain values from each ROI were plotted for each intact and implanted cadaver bone case. The regression score (R^2) and gradient (β) was calculated to evaluate the strain relationship between the intact and implanted bone strain, for each femoral component material (ideal case $R^2 = 1$ and $\beta = 1$) (IBM SPSS Statistics 20).

The raw image contrast was assessed on each cadaver for comparison to the analogue bone using ImageJ software. A comparison of strain results with the normalised sum of square differences (NSSD) and zero-normalised sum of square differences (ZNSSD) correlation criterion was carried out to assess which was most reliable for the raw image contrast achieved during testing. While the NSSD is robust to change in contrast, the ZNSSD is reported to be more robust to shifts in histogram during image capture as well (Sutton et al., 2009).

5.0.3 Results

5.0.3.1 Speckle Pattern

A speckle pattern coverage of 37% and 39% was achieved on the CoCr and PEEK cadavers respectively. With smaller maximum speckle diameters (2-12 pixels), a greater spatial density was achieved compared to that on the analogue bones in Section 4.3.2.1 of Chapter 4 (28%, 22% and 25% across the intact, CoCr and PEEK implanted bones, respectively). Figures 5.9a and 5.9b show a comparison of the speckle patterns on the cadaver and analogue bone surfaces, respectively.

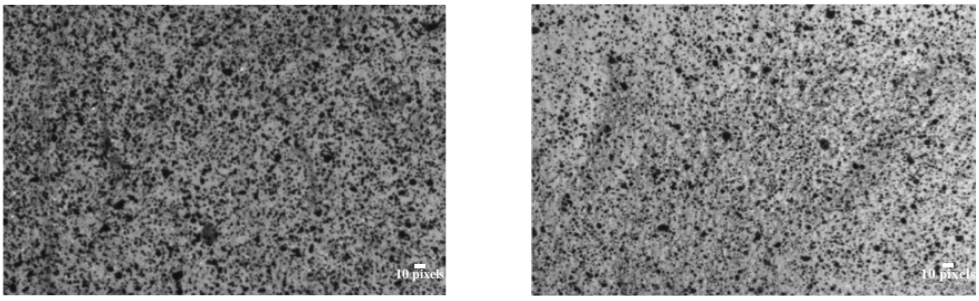

(a) Speckle pattern on cadaver bone (b) Speckle pattern on analogue bone

Figure 5.9: Comparison of speckle pattern coverage on the cadaver and analogue bone models (10 pixel scale bar)

5.0.3.2 DIC Parameter Selection and Resolution

Evaluation of grey level pixel difference (range 0-255) from one consecutive static raw image to the next gave a maximum SD of 2.586 and 2.164 on the CoCr (donor 1) and

PEEK (donor 2) cadaver specimens, respectively. This was comparable to the noise in the analogue bone images, corresponding to ∼1% raw image noise value.

Plotting the displacement SD under nominally zero strain conditions (static and post-rigid body translation correction) with increasing subset size indicated that a subset size of 31 x 31 pixels gave an optimal balance between noise and smoothing, whilst providing a large amount of unique data (speckle diameter range 2 to 12 pixels) (Figures 5.10).

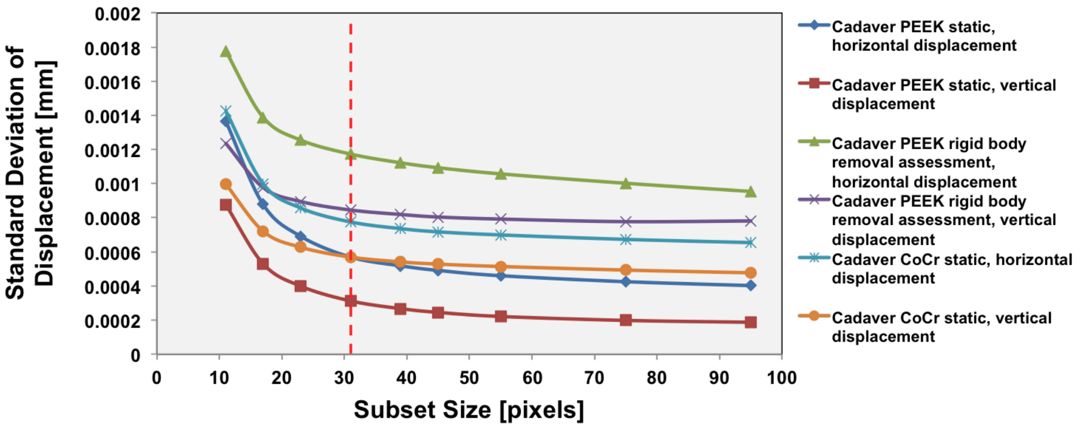

Figure 5.10: DIC parameter selection graph showing variation in SD of displacement with subset size for the cadaver bone

A step size of 7 pixels and a filter size of 15 data points were chosen using the same criteria for the strain field across the bone surface as in Section 4.3.2.2. The subset size of 31 x 31 pixels and a step size of 7 pixels gave a maximum displacement resolution (SD) of 0.78 μm with a mean bias value of -2.29 μm. The maximum strain resolution with a filter size of 15 data points was a SD of 63 $\mu\epsilon$ with a mean bias value of 90 $\mu\epsilon$, which occurred on the CoCr bone. The maximum strain resolution on the PEEK bone was a SD of 56 $\mu\epsilon$ with a mean bias value of 71 $\mu\epsilon$. After the translation test under the same conditions, the rigid body correction performed by the software gave a maximum strain resolution SD of 65 $\mu\epsilon$ with a mean bias value of 90 $\mu\epsilon$.

5.0.3.3 Experimental Error

The experimental error of strain measurement was ±33 $\mu\epsilon$ and ±36 $\mu\epsilon$ on the intact and CoCr implanted cadaver (donor 1), and ±46 $\mu\epsilon$ and ±47 $\mu\epsilon$ on the intact and PEEK implanted cadaver bone (donor 2) surfaces respectively. This gave a maximum six sigma experimental error (representing 99.7% spread of data error) of ±141 $\mu\epsilon$ or 10.6% of the maximum strain within the ROI, 1335 $\mu\epsilon$, at the maximum load of 2.5 kN (4 BW or 4 times the estimated load in normal standing stance for donor 2 (Bergmann et al., 2014b)). Therefore the signal to noise ratio was comparably lower than on the analogue bone surface.

5.0.3.4 Strain Measurements

The 1st (major, tensile) and 2nd (minor, compressive) principal strain distribution maps are shown for the cadaver bones for the intact and implanted states in Figure 5.11.

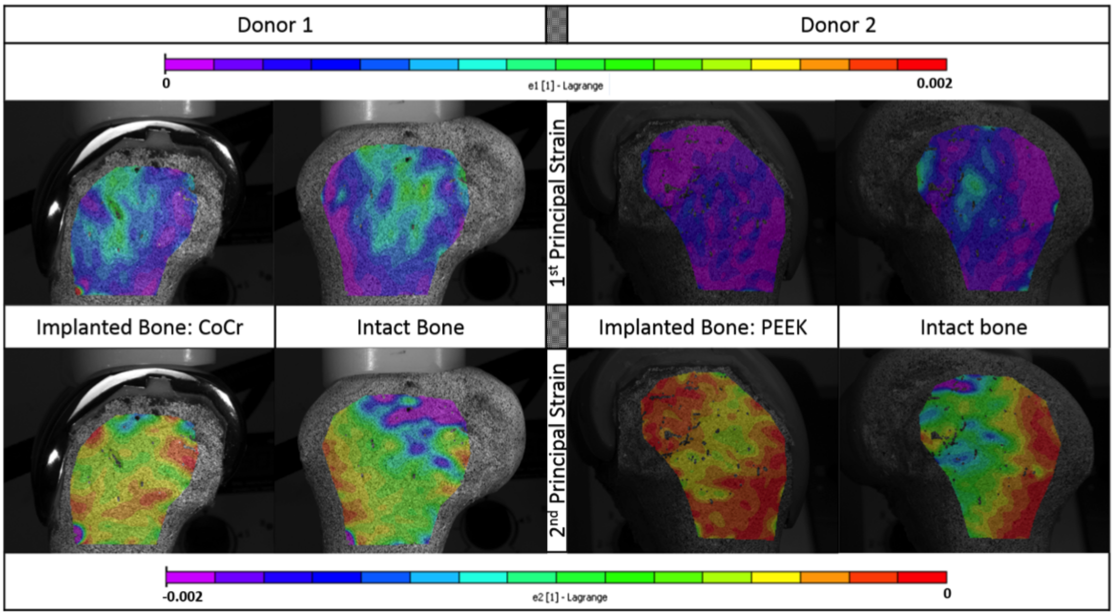

Figure 5.11: Principal strain maps for the intact and implanted cadaver bones

Qualitatively, a similar strain distribution was observed on the cadaver bone surface compared to that observed on the analogue bone surfaces, although the magnitude of bone strain on the CoCr implanted cadaver was greater than on the analogue bone. (Figure 5.12). As in the analogue bone case, there was a shift in the strain path away from the posterior towards the anterior distal region of the lateral bone surface implanted with PEEK.

A quantitative comparison at each ROI of intact versus CoCr implanted cadaver bone strain gave a slope of $\beta = 0.5421$ ($R^2 = 0.9176$), similar to that observed with the analogue bone (Figure 5.13). However, the strain magnitude on the PEEK implanted cadaver was much lower than that of the intact case with a slope of $\beta = 0.5472$ ($R^2 = 0.6977$) (Figure 5.14).

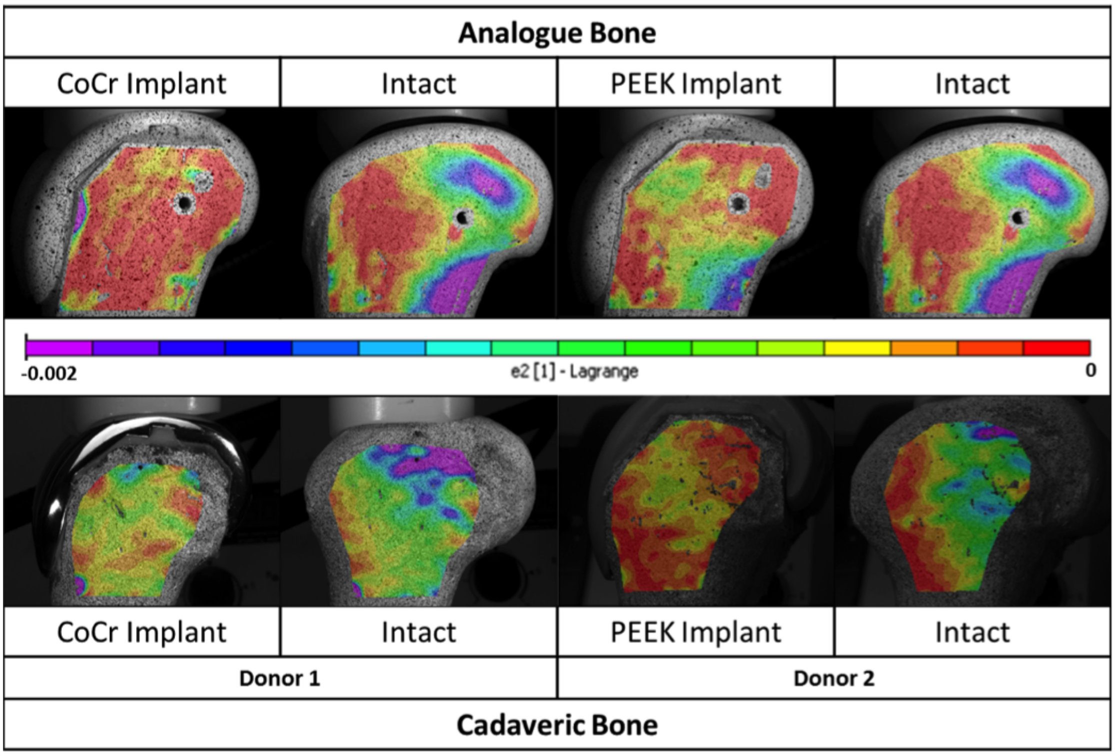

Figure 5.12: Compressive strain maps for the intact and implanted cadaver specimens in comparison to the distribution on analogue bone

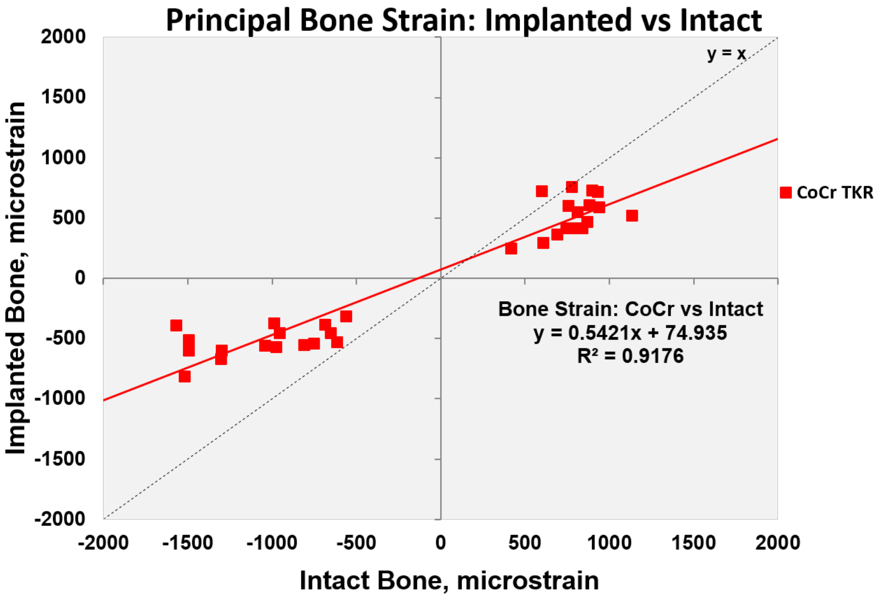

Figure 5.13: Graph of intact vs CoCr implanted cadaver bone strain

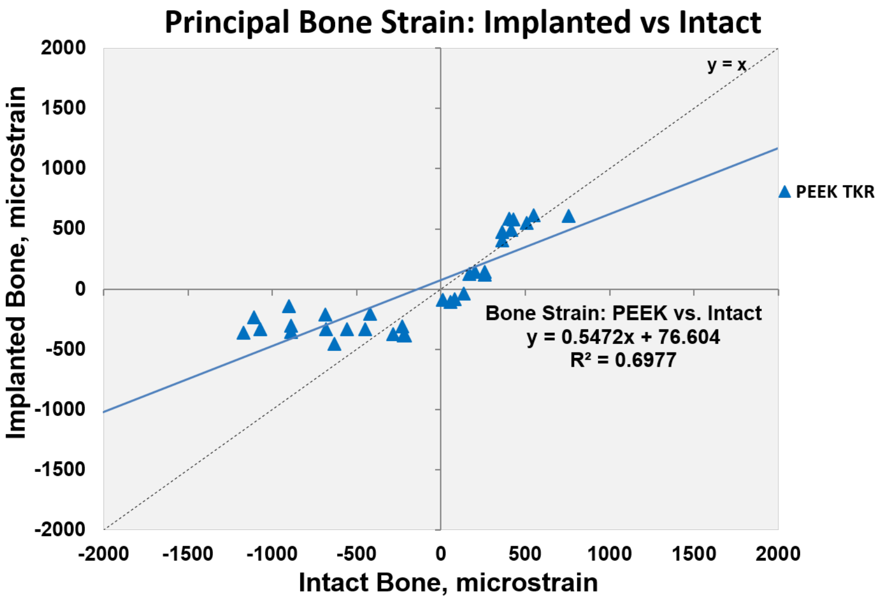

Figure 5.14: Graph of intact vs PEEK implanted cadaver bone strain

5.0.3.5 Raw Image Contrast

To verify whether the analysis method had an influence upon the discrepancy between the strain magnitude and distributions on the analogue and cadaver bone materials, the raw image contrast was checked for saturation. Compared to the contrast achieved on the analogue bones (Figure 5.15), a good contrast with a wide histogram of pixel grey scale values was observed for the cadaver bone implanted with CoCr (Figure 5.16). However, some pixels were saturating at 255 within the ROI (range 18-255).

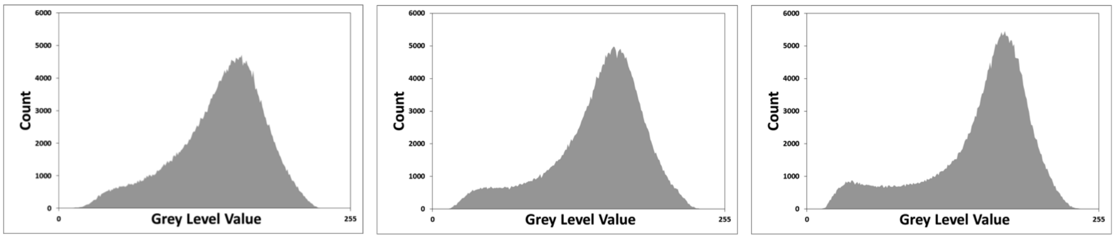

(a) Intact (b) PEEK Implanted (c) CoCr Implanted

Figure 5.15: Raw image contrast with analogue bone

A narrower histogram of grey scale values (range 7-255) was observed for the cadaver bone implanted with PEEK and again, whilst it's not visible on the graph in Figure 5.17, some pixels were saturating at 255. It was difficult to achieve even lighting on the surface without local saturation, so the surface lighting intensity was turned down resulting in a poorer contrast.

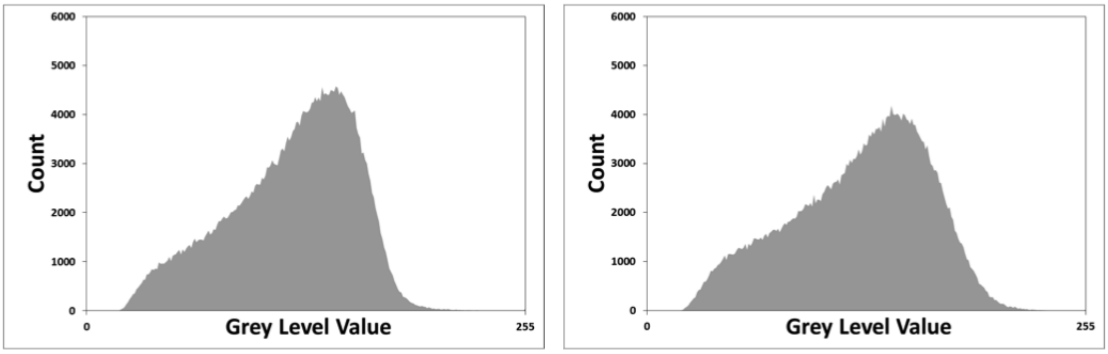

(a) Intact (b) Implanted

Figure 5.16: Raw image contrast on donor 1 cadaver surface (CoCr)

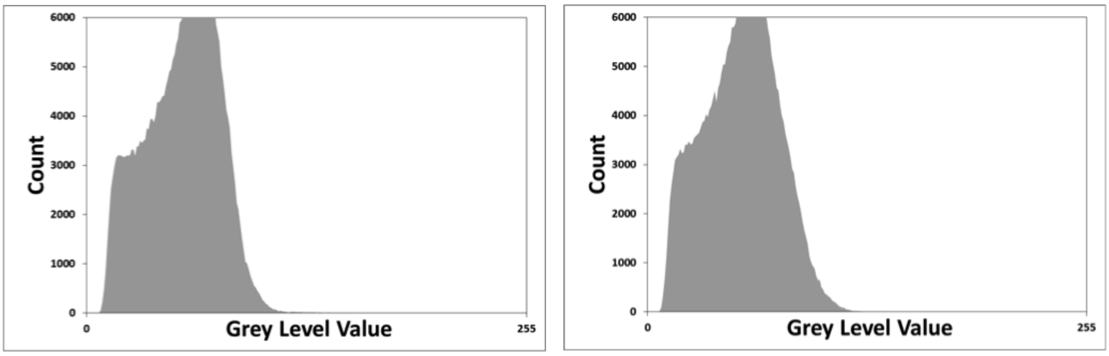

(a) Intact (b) Implanted

Figure 5.17: Raw image contrast on donor 2 cadaver surface (PEEK)

The ZNSSD correlation algorithm (Figure 5.18b) produced no difference in strain distribution compared to the NSSD algorithm (Figures 5.18a). Therefore it was established that the NSSD was sufficient for this analysis and any bias in the data resulting from the pixel intensities could not be accounted for any further.

5.0.4 Discussion

In this Chapter, the DIC methodology developed using an analogue bone model in Chaper 4 was applied to cadaver bone, with the aim to investigate the practicality of the technique for reliable assessment of the effect of TKR implant material on femoral bone strain.

In comparison to the change in analogue bone strain distribution from the intact to PEEK implanted case, a similar trend was observed on the cadaver bone (donor 2). However, whilst the strain magnitude appeared to reduce on the cadaver implanted with CoCr, the change in strain path was less pronounced on the principal strain maps. A quantitative comparison of the intact bone strain versus implanted bone

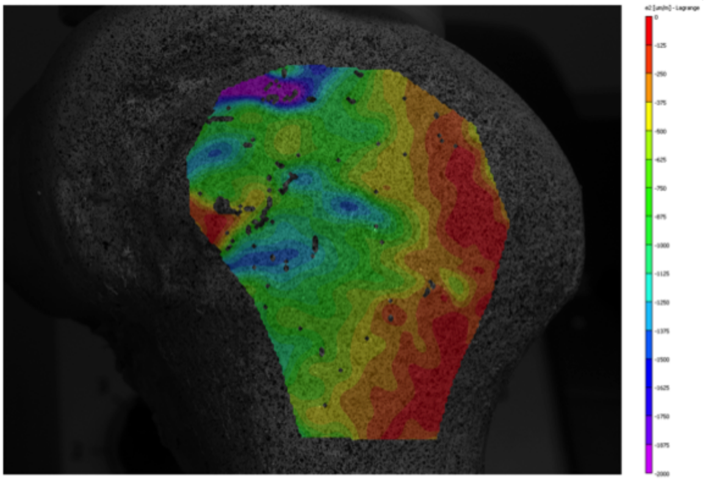

(a) Normalised sum of square differences

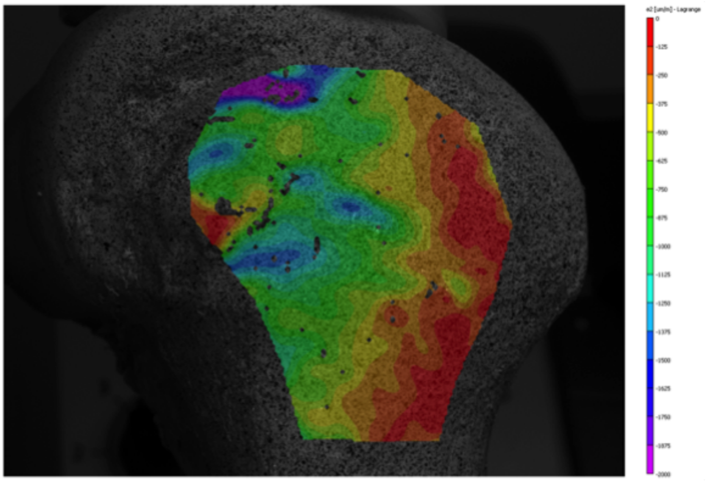

(b) Zero normalised sum of square differences

Figure 5.18: Comparison of strain maps with correlation criterion for the PEEK cadaver (scale: -2000 - 0 $\mu\epsilon$)

strain for both cadavers showed a large reduction in strain magnitude with both implant materials, indicative of stress shielding. This was unexpected for the PEEK material, which has a stiffness closer to that of bone and showed less of a stress shielding effect using analogue bone.

The shift in strain path is again likely to be related to positioning of the tibial component, and the different contact areas on the intact and implanted bones. The sliding of the tibial component on the femoral implant means that it preferentially loads anteriorly rather than posteriorly. The curvature of the intact articular surfaces of the cadaver which was implanted with CoCr (donor 1), was such that the tibial component was positioned more anteriorly than on the intact cadaver that was implanted with PEEK. The width of the tibial component used for loading, relative to the width of the intact cadaver bone, would also have influenced the surface strain distribution.

The saturation of some pixels in the ROI on the cadaver bones could have led to bias in the correlation calculations, resulting in measurement errors (Sutton et al., 2009). According to Sutton et al. (2009), the pixel range should be kept within 30-230 to avoid bias. However, this was not possible on the cadaver speckled surface without excessively degrading the contrast. In addition, to account for changes in contrast using the ZNSSD correlation criterion instead of the NSSD had no influence on the strain measurements with the analysis parameters selected. It was concluded that the pixel saturation was due to moisture formation on the cadaver surface (as well as bone marrow and fat from surgery), which caused reflections. Moisture evaporation can also cause heat waves which may be detrimental to DIC measurements. Poor painting technique could also lead to a shiny surface. The uneven surface of the cadaveric bone, which contained micro-holes, also made it difficult to achieve even lighting on the bone surface. This meant that strain measurement was not possible at the lateral collateral ligament attachment site in the posterior metaphyseal region. This may be reflected in the resolution (SD) and bias (mean) measurements on the cadavers, which were twice that measured on the analogue bone under nominally zero strain conditions. A denser pattern of smaller diameter speckles on the cadaver surfaces facilitated the use of a smaller subset size for the DIC analysis (31 x 31 pixels), which could result in greater noise. However, if the subset size was matched to that used in the analogue bone analysis (41 x 41 pixels), allowing more smoothing and thus an improved strain resolution value, the maximum resolution and bias values would still have been greater on the cadaver bone (displacement SD = 0.74 μm and mean = -1.70 μm, strain SD = 45 $\mu\epsilon$ and mean = 67 $\mu\epsilon$).

For the cadaver model, using the same speckle pattern on the intact and the implanted bone reduced the intra-model uncertainty in comparison of strain measurements. In addition, the experimental error values were lower on the cadavers in comparison to the analogue bones. During the implantation procedure, bone debris spread onto the speckle pattern surface (Figure 5.4) and whilst care was taken to remove this, some damage was sustained during the cutting procedure. However, this didn't affect the correlation within the ROI and no gaps were present in the data.

Cadaver bones have been widely used in biomechanics for determination of human bone properties. Whilst there can be great variation in cadaver bone quality, it is the closest test material to healthy human bone *in-vivo*. In the literature, a small number of DIC studies have used cadaveric bone for biomechanical analysis of fracture behaviour and implanted bone strain (Gilchrist and Guy, 2013; Grassi et al., 2014; Mann et al., 2014; Terrier et al., 2014). Regarding the study of implanted bone, Mann et al. (2014) showed that in the tibia, higher bone strains corresponded to patients with lower BMD and higher BW. This may account for the higher magnitude of bone strains measured on the bone implanted with CoCr. Although the BMD is not known, this donor had a BW of 94 kg, yet similar AP and ML dimensions to the femur implanted with PEEK, (from a donor with a BW of 61 kg), suggesting that they may have lived a sedentary lifestyle and had a low BMD. However, Mann et al. (2014) also note that BW is not a predictor of bone strain, so DEXA scans would have to be carried out for this study in order to investigate this postulation. Mann et al. (2014) did not state resolution or bias values for their measurements on the bone surface in that experimental setup, only the spatial resolution of the raw images which was 30 μm/pixel. Error values were quoted from a pilot calibration study (no details given) with a root mean squared error (RMSE) of 32.8 $\mu\epsilon$ with 95% confidence intervals of 19-42 $\mu\epsilon$. DIC was also used to evaluate the micro-motions at the implant bone interface, which were quoted have a peak mean of 32 μm and a peak median of 17 μm, with a minimum of 1.5 μm and a maximum of 105 μm. Again, the error in these measurements was quoted from a pilot study to be an RMSE of 1.1 with 95% confidence intervals of 0.54-1.16 μm. Without evaluation of the specific signal to noise ratio and bias for each experimental setup, the precision and accuracy of measurements is not known and valid comparisons cannot be made between studies. Terrier et al. (2014) used DIC on cadaver bone to evaluate the strain around a total ankle replacement for validation of an FE model. They used a dynamic extensometer (Instron 2620-603) to evaluate the systematic and random axial strain errors, which were quoted as 140 $\mu\epsilon$ and 230 $\mu\epsilon$ respectively. However, the extensometer had a clip-on fixture (Instron Inc., IL, USA), which may not have been a reliable reference method if slip occurred, although the fixation method to the bone was not described in the experimental setup. In both of these studies, the DIC analysis parameters were not described, nor was the speckle pattern used on the cadaver bone surfaces.

To the author's knowledge, this is the first study to carry out DIC analysis to measure the femoral bone strain following TKR on cadavers. While the study is limited by a single axial load case, the aim of the study was to apply the technique established on analogue bone to cadaver bone. However, compared to the analogue bones, which had nominally matched geometry, the strain distribution on cadaver bone could be affected by increased variability in test setup parameters due to bone geometry variation. There was difficulty in potting the cadaveric femurs at the same angle as one another, as it was not possible to use the same reference points as on the analogue bone. As a result, the CoCr bone appears to be in hyper extension, which may contribute towards the difference in strain distribution on the intact bone, compared to the PEEK bone. Any varus or valgus femoral axis angle that the donor may have had was unknown.

The experimenter, (the author), remained the same for all tests, but other than having observed TKR surgery, was not a trained surgeon. Another problem with using different donors is variation in bone density which alters the magnitude of the strains measured on the surface of the cortical bone (Mann et al., 2014). Each cadaver was used as its own intact reference case prior to implantation, making intra-specimen comparisons possible. However, the absence of inter-specimen comparison is a limitation in this study.

During implantation, the dimensions of the resected femur (Figure 5.5d) may have varied due to the tolerances between the oscillating saw blade and the distal cutting guide (Figure 5.5b and 5.5c). Any inclination or declination of the angle of the saw blade from parallel within the cutting guide slot causes a variation in the cement mantle thickness which could alter the induced surface strain distribution. It was also noted during implantation that large tolerances in the anterior sizing tool for the Freedom knee (Figure 5.5a) could lead to inaccurate measurements and result in mis-sizing of the femoral component required during surgery. Nevertheless these are design limitations of the implant system rather than the experimental method used.

The size of femoral component chosen for implantation could also alter the induced strain fields, particularly in the medial and lateral regions of the distal femur. While the mediolateral (ML) dimension of a femoral component is associated with patella tracking during flexion and can alter the induced patellofemoral forces, the anteriorposterior (AP) dimension is considered most important because it governs normal gait, flexion-extension of the leg and accurate balancing of ligaments. Therefore, the size of the majority of TKR implants is chosen from the AP dimension of the patient's femur.

In addition, the difference in femur aspect ratio vs. implant size and bone density could also influence strain magnitude. The aspect ratio, defined as the ML dimension divided by AP dimension, of the majority of knee implant systems (including the Maxx Freedom knee) is fairly constant within each system. However, it is observed that morphologically, smaller femurs in the AP plane tend to have a higher aspect ratio compared to femurs larger in the AP plane (Hitt et al., 2003). There is also a significant difference in the aspect ratio of male and female femurs, with female femurs having a smaller mean aspect ratio for ML to AP suggesting sexual dimorphism (Guy et al., 2012; Lonner et al., 2008; Yue et al., 2011). The medium right femur Sawbone analogue bone was geometrically of male Caucasian origin and measures with an ML dimension of 75 mm and a maximum extent in the AP plane of 61 mm. The AP measurement using the anterior referencing system is 53 mm, placing it between a size C and D of Freedom knee femoral component. If a half-size is measured during surgery, the surgeon would most commonly downsize the component and translate it anteriorly to avoid prosthesis overhang in the ML plane and femoral notching respectively (Tietjens, 2009). This verified the choice to implant a size C Freedom knee component in the Sawbone femur which resulted in a 6.5 mm overhang of bone medially and laterally.

The cadavers were both of female Caucasian origin. Even though they were selected based on their AP and ML sizes, only estimations could be made because of the soft tissue on the bone surface. Although, this is representative of the sizing scenario applied during surgery, an error in femoral component size selection may result. Using the sizing guide prior to implantation, donor 1 (CoCr), was measured as a size D and donor 2 (PEEK) was measured as a size C in the AP direction. However, the measurement across the transepicondylar axis in the ML direction with the soft tissues resected was 72 mm on donor 1 (3 mm smaller than the Sawbone) and 76 mm on donor 2 (1 mm larger than the Sawbone). This may also contribute towards the relatively larger strain magnitudes measured on the cadaver implanted with CoCr, compared to those on the analogue bones.

The Maxx Freedom knee was designed specifically for the Asian population, who have a different anthropometric range when compared to Caucasian femurs. Studies in the literature show that Asian femurs are typically smaller in the mediolateral dimension for a given anterioposterior dimension, resulting in a smaller aspect ratio compared to Caucasian geometry (Chaichankul et al., 2011; Hitt et al., 2003; Ho et al., 2006; Mahfouz et al., 2012; Vaidya et al., 2000). The size C Freedom knee femoral component has a smaller aspect ratio compared to other generic total knee replacement systems in current clinical use, to account for these differences with Asian femur geometry. However, this may lead to an increased overhang of bone mediolaterally if an Asian specific design is implanted on a male Caucasian, as seen in the analogue bone experiments. The effect of difference in aspect ratio between femoral component and native femur on functional and clinical outcomes has not been reported in the literature to date to the author's knowledge. Medial and lateral overhang of bone is common in total knee replacement implantation x-rays and photos available from open sources on the internet. Surgeons aim to avoid medial or lateral overhang of femoral component as it may result in soft tissue irritation, interference with ligament balancing, loss of range of motion, increased patellofemoral force, incomplete correction of deformities and pain (Asada et al., 2013; Chang et al., 2014; Incavo et al., 2004; Kawahara et al., 2012; Lo et al., 2003; Tietjens, 2009). In contrast, undersizing in the mediolateral plane may lead to placement of the implant on weaker cancellous bone which could lead to bleeding and open access to cancellous bone for wear debris, leading to osteolysis, ultimately reducing the effectiveness of the implant in the long term (Hitt et al., 2003). It is also postulated that the undersizing of component aspect ratio may lead to reduced medial and lateral bone strain, which could potentially result in resorption of bone in these regions.

In conclusion, this study has shown that DIC has sufficient resolution to measure physiological strain levels, although signal to noise ratio and bias should always be evaluated for each experimental setup. A rigorous DIC protocol must be carried out and reported in order to ensure meaningful and reproducible results. Optimal image contrast and speckle patterning are fundamental in the correlation and the validity of strain measurements. A large population of cadaveric donors would be required to determine the absolute effect of TKR implant material on bone surface strain, and care must be taken to account for the potential differences between diseased and healthy bone. However, paired bone models would be a suitable way forward for a comparative study with reliable statistical analysis. For future cadaver DIC studies, it is advised that the speckle surface is dried with absorbent paper during testing to avoid moisture formation causing reflections that introduce measurement uncertainty from pixel saturation. The correlation criterion and lighting on the uneven cadaveric surface are also important considerations with changes in raw image contrast during testing. Instead of loading the intact cadaver with the tibial component, a more representative contact area could be obtained by taking a moulding of the distal femoral articular surface geometry, in the absence of the tibia geometry. An improved jig design is also required for more accurate potting of cadaver geometry. This could be achieved by carrying out μCT scans of each bone, such that a specific potting jig model could be designed and 3D printed to ensure that the bone is potted at a specific angle, relative to its mechanical axis. Alternative loading angles could then be investigated.

Chapter 6

Development of a Methodology for Volumetric Strain Analysis of the Implanted PEEK TKR Construct

6.1 Introduction

3D-DIC provides surface strain measurement data, but it does not inform on the strain through the volume of the test specimen. The internal TKR construct strain state is likely to be important in describing the load transfer from the implant through the cement to the bone. Digital Volume Correlation (DVC), is a volumetric extension to DIC, which uses internal material features to track deformation. However, as with the DIC technique, the accuracy and reliability of the DVC measurements are dependent on appropriate scanning conditions and parameter selection for the analysis of each unique specimen.

In the present study, a DVC method for local *in situ* strain analysis within the PEEK TKR construct was developed using μCT scan volumes of two specimens. The full PEEK TKR construct was analysed using the trabecular foam region (analogue cancellous bone) for deformation tracking. Following that, a bone cement specimen was analysed to determine the feasibility of using the zirconium dioxide radiopacfier particle pattern to track deformation. In both cases, the aim was to carry out a DVC noise study to determine the optimal analysis parameters, and to assess the accuracy of the technique by imposing artificial strain value on the specimen with a change in magnification using the scan parameters. By minimising sources of error, a robust validated methodology was developed for volumetric strain analysis within the TKR construct.

6.2 Methodology

6.2.1 Materials

Two specimens were used for the DVC tests. The first was an analogue femur implanted with a PEEK femoral component, as used in the DIC study (section 4.2.1). The second test specimen was a bar of Palacos R bone cement, which was manufactured using the moulding technique, described in section 3.3.1.3, and cut into a 6 x 6 x 30 mm (width by depth by height) specimen using an IsoMet 4000 diamond saw (Buehler Inc., IL, USA).

6.2.2 μCT Volumes

μCT volume data was obtained for both specimens using a custom 225 kV Nikon Metrology HMX ST x-ray CT scanner (Nikon Metrology NV, Leuven, Belgium) at the μ-VIS centre[1] (University of Southampton). The specific scan parameters and methodologies used for each specimen are detailed in sections 6.2.2.1 and 6.2.2.2.

6.2.2.1 TKR Construct Scans

The implanted femur model was held in a 3-jaw chuck within the HMX CT scanner. Using a 1 mm aluminium filter, the gun voltage and power were set at 120 kV and 7.6 kW, respectively, based upon the histogram of grey scale values in the radiographs. The exposure time was set at 354 ms for 3142 projections with 8 frames per projection.

The scan configuration was then set as follows:

- 1 hour warm up scan
- Scan 1: Reference scan
- Scan 2: Repeat scan in same position as scan 1
- Scan 3: The specimen was translated up by 10 pixels (0.65 mm)
- Scan 4: The specimen was kept in the same translated (vertical) position as Scan 3, but the magnification was increased by 10 pixels, by moving the femur 0.65 mm closer to the x-ray gun

Each μCT dataset was reconstructed using CT-Pro 3D software (Nikon Metrology NV, Leuven, Belgium) which uses back-filtered projection (Landis and Keane, 2010). The

---

[1] www.southampton.ac.uk/muvis

centre of rotation was obtained, and the beam hardening correction and noise reduction were set at 2 and 1, respectively. A resolution of 64.8 μm was achieved in scans 1 to 3 (0.064817 mm) and, with a change in magnification (distance from the detector to the femur), a resolution of 64.7 μm was achieved in scan 4 (0.064654 mm). Each 32-bit real raw volume (2000x2000x2000 voxels, 29.8 GB) was imported into ImageJ, and cropped to a size of 1200x1200x800 voxels using the macro function, to remove as much of the air volume outside the specimen as possible. The 32 bit histogram of grey levels was scaled to 0-255 and the volumes were converted to 8 bit to reduce the computational resources necessary for the DVC analysis (1.07 GB).

6.2.2.2 Bone Cement Scans

The bone cement was held in a 3-jaw chuck within the HMX CT scanner, and the top region of cement was scanned. The gun voltage and power was set at 120 kV and 7 kW, respectively, without the use of a filter. The exposure time was set at 250 ms for 3142 projections with 8 frames per projection. Again, specimen shuttling was used at 15 pixels to reduce ring artefacts.

The scan configuration was then set as follows:

- 2 hour warm up scan
- Scan 1: Reference scan
- Scan 2: Repeat scan in same position as scan 1
- Scan 3: The specimen was translated up by 10 pixels (0.063 mm)
- Scan 4: The specimen was kept in the same translated (vertical) position as Scan 3, but the magnification was decreased by 10 pixels, by moving the femur 0.063 mm closer to the x-ray detector

As with the TKR construct scans, each μCT dataset was reconstructed using CT-Pro 3D software. The centre of rotation was obtained and the beam hardening correction and noise reduction were set at 3 and 1, respectively. A resolution of 6.32 μm was achieved in scans 1 to 3 (0.0063174 mm) and, with a change in magnification (distance to the cement), a resolution of 6.33 μm was achieved in scan 4 (0.00633417 mm). Care must be taken when reconstructing scans using CT-Pro 3D, as it will round the resolution (in mm) to 4 decimal places. This is significant when comparing volumes with resolutions smaller than 10 μm.

Each reconstructed 32-bit real raw volume (2000x2000x2000 voxels, 31.2 GB) was imported into ImageJ, and cropped using the macro function, to a size of 1000x1000x1400 voxels (the width of the cement specimen, removing the surrounding air volume). The cement volumes were converted to 8 bit (including scaling the histogram of grey levels to 0-255) to reduce the computational resources necessary for the DVC analysis (1.3 GB).

6.2.3 DVC Analysis

The μCT volumes were grouped for 3 DVC analyses (Table 6.1). The static noise analysis aimed to assess the strain noise (resolution) and bias (systematic error) from the CT scanning technique under nominally zero strain conditions. The rigid body translation noise analysis aimed to to assess the ability of the software to perform a rigid body correction, and to assess the resulting strain noise and bias. The magnification strain analysis aimed to assess the precision of strain measurement, with volumetric deformation imposed through the change in scan resolution.

μCT Volumes		**DVC Analysis Test**
Reference	**‘Deformed’**	
Scan 1	Scan 2	Static noise analysis
Scan 1	Scan 3	Rigid body translation noise analysis
Scan 3	Scan 4	Magnification strain (imposed isotropic strain) analysis

Table 6.1: μCT scan volumes corresponding to each DVC analysis test

The DVC analysis was performed using LaVision DaVis software (LaVision GmbH, Goettingen, Germany) to obtain the displacement vectors describing the deformation within the specimen. For each analysis, the two μCT volumes (reference and ‘deformed’) were imported into the DaVis software, using the original scan resolution (i.e. without a magnification change). The DaVis software uses the local correlation approach for DVC with the normalised cross correlation coefficient (see Figure 2.23 and Equation 2.4 in section 2.6.3.2) and a linear shape function with 12 degrees of freedom to map the displacements between the reference and deformed images in smaller sub-volumes (Figure 6.1). Feature recognition can be carried out in one of two ways using the DaVis software. The first uses a 3D fast Fourier transform (FFT), referred to from here onwards as the DaVis-FFT, with trilinear interpolation. The second uses a direct coupling method, referred to from here onwards as DaVis-Direct, with spline interpolation. The estimated full-3D displacement field is computed using analysis steps with decreasing sub-volume sizes and 2 passes for improved accuracy (predictor-corrector approach), and a local Gaussian intensity interpolation around the correlation peak (Palanca et al., 2015; Scarano, 2013).

Both the DaVis-FFT and the DaVis-Direct methods were used for the analysis of the TKR construct and bone cement specimens, to investigate any difference between the

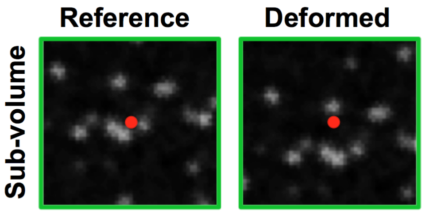

Figure 6.1: Example sub-volume corresponding to the reference and deformed volumes of bone cement

resulting strain measurements, resolution and bias. A range of sub-volume sizes were tested for each specimen (Table 6.2), using both correlation methods. The optimal size was determined from the balance between noise and spatial resolution of measurements, using the standard deviations (σ) from the static and rigid body translation tests (Figure 6.2). This decision was informed by the distribution of correlation values using each sub-volume size and correlation method. A good sub-volume correlation is necessary to obtain accurate strain measurements, so it is recommended that any sub-volume with a correlation coefficient less than 0.9 should be discounted (1 = perfect correlation, 0 = no correlation) (Gillard et al., 2014). Using the DaVis-Direct correlation, the spline interpolation order was selected from that which gave a distribution of correlation values closer to 1, along with lower noise values (standard deviations) in the static tests. A 50% overlap gave displacement measurements at half of the sub-volume size with both the DaVis-FFT and the DaVis-Direct methods.

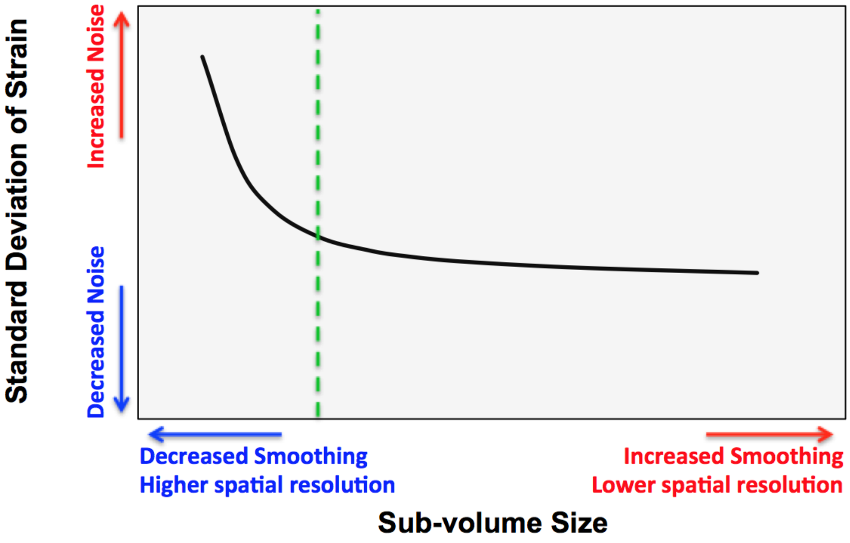

Figure 6.2: Selection of optimal sub-volume size: the trade-off between noise and smoothing of the data under nominally zero strain conditions (example curve)

To assess the ability of the DaVis software to perform a rigid body correction, a coarse

Sub-volume Size Tests (voxels)			
TKR Construct		**Bone Cement**	
DaVis-FFT	**DaVis-Direct**	**DaVis-FFT**	**DaVis-Direct**
32x32x32	32x32x32	24x24x24	24x24x24
48x48x48	48x48x48	32x32x32	32x32x32
64x64x64	64x64x64	48x48x48	40x40x40
72x72x72	72x72x72	64x64x64	48x48x48
96x96x96	96x96x96	96x96x96	64x64x64
128x128x128	128x128x128		

Table 6.2: Sub-volume sizes tested for each specimen using the DaVis-FFT and DaVis-Direct correlation methods

DVC analysis was first performed on the translated test volume using a large sub-volume size (large enough to cope with the rigid body shift). The translation co-ordinates of the correction required were then implemented by importing the volume from scan 3 into ImageJ, and translating the volume by the number of pixels specified in the z-direction (10 pixels in theory). The DVC analysis was then repeated using the sub-volumes in Table 6.2, so that the resulting standard deviation and mean values could be compared to those from the static tests.

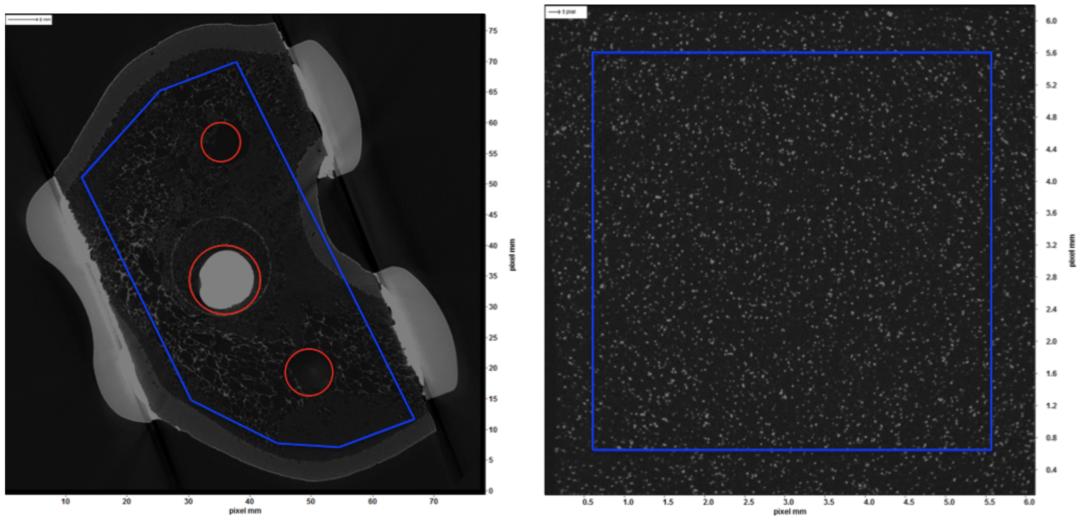

(a) TKR construct mask

(b) Bone cement mask

Figure 6.3: Masks applied to the analysis volumes to exclude the surrounding correlation values and displacement vectors from the analysis (blue line = include internal area, red line = exclude internal area)

Before the correlation values and displacement fields were exported from the DaVis software, permanent masks were applied to the analysed volumes (Figure 6.3), such that the correlation values and displacement vectors surrounding these regions were set to zero and thus excluded from the strain analysis. Matlab software (MathWorks, MA, USA) was used to calculate the strain from the displacement vector fields using the gradient function, with the spacing in the x, y and z direction set as half of the sub-volume size (due to the 50% overlap).

The standard deviation and mean of strain fields (E_{xx}, E_{yy} and E_{zz}) were used to assess the resolution and bias of measurement, respectively, in the static and rigid body translation tests. Comparisons were then made between the DaVis-FFT and DaVis-Direct correlation methods. The experimental error (precision) was taken as the largest standard deviation of the strain measurement in the magnification strain tests, using the chosen sub-volume size. The mean strain values from the magnification strain tests were compared against the theoretical strain value to assess the accuracy of measurements. From the change in resolution between the scans, the strain imposed in the volume can be calculated from Equation 6.1. It is important to remember that a coarser scan resolution value (larger number) in the magnification change scan, corresponds to a decrease in specimen size (compressive strain), and a finer scan resolution value (smaller number) corresponds to an increase in specimen size (tensile strain).

$$\text{Magnification Strain} = \frac{\text{-(Change in resolution)}}{\text{Original resolution}} \tag{6.1}$$

Thus, the magnification-strain imposed in the TKR construct was 0.002513 strain or 2513 $\mu\epsilon$, and the magnification-strain imposed in the bone cement was -0.002654 strain or -2654 $\mu\epsilon$.

6.3 Results

6.3.1 Femur

It was apparent when examining the image slices through the TKR construct that the trabecular foam structure was very sparse in areas (Figure 6.4). In an image slice, the bone cement region appeared white, the PEEK appeared light grey and the bone regions appeared darker grey. There was also beam hardening near the cement regions which caused a variation in grey level values of the voxels in the trabecular foam region. The correlation map in Figure 6.5 shows an example of 2 regions of poor correlation (below 0.9, black) within the trabecular foam region of the static analysis. Even though good correlation values (∼1, white) were obtained in the cement and implant regions, deformation measurements are not possible without a pattern (any pattern in the cement at this resolution is due to partial volume effects and noise).

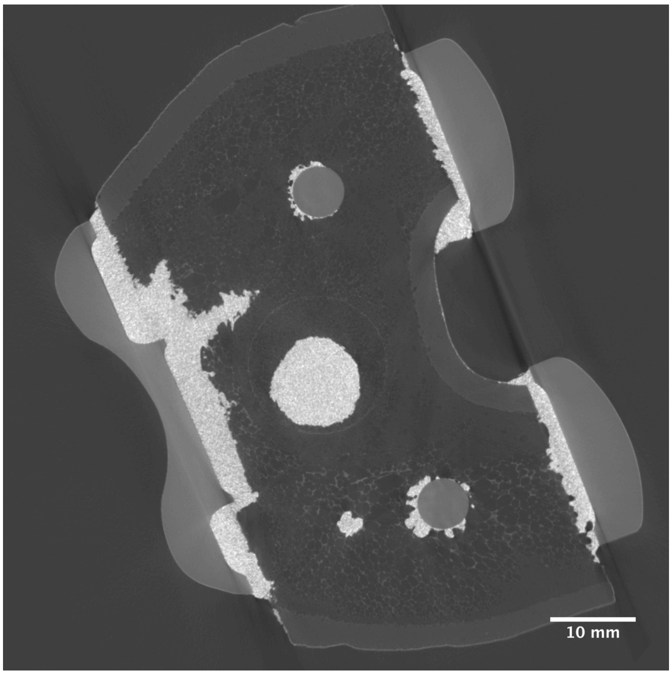

Figure 6.4: Reconstructed CT slice image of the TKR construct specimen, viewed in the transverse plane (with the anterior and posterior flanges of the femoral component are on the left and right sides, respectively)

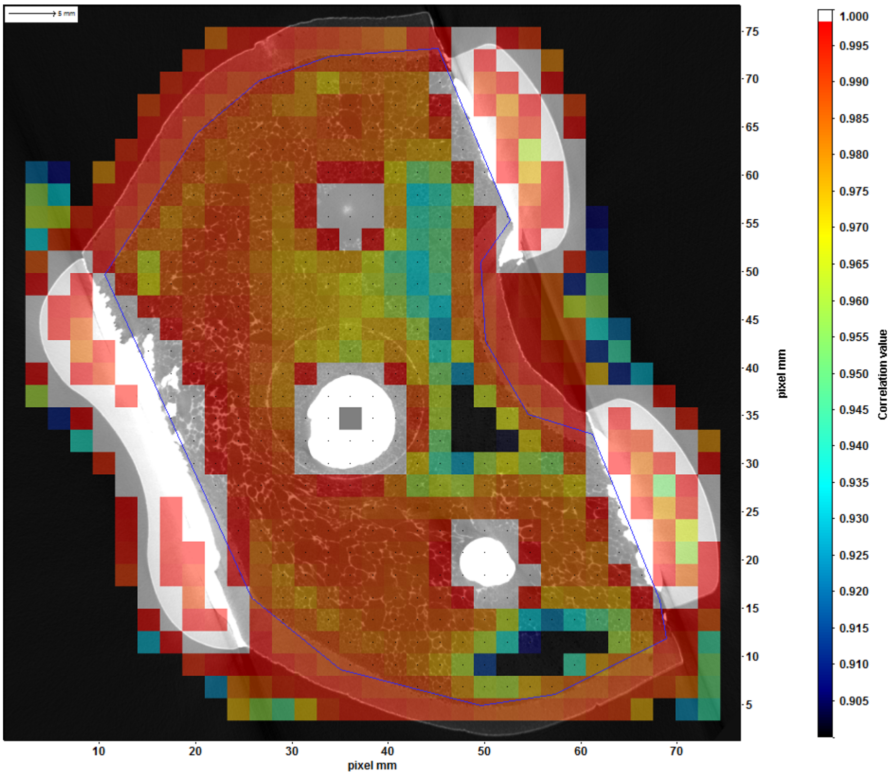

Figure 6.5: Correlation map of the static DVC analysis of the TKR construct using DaVis-FFT

The mean and standard deviation of correlation value with increasing sub-volume size are shown in Table 6.3 for the static tests, using the DaVis-FFT. The corresponding minimum and maximum correlation values are also shown. A large standard deviation was present with every sub-volume size, and the minimum correlation values were below 0.9, giving little confidence in any strain measurements. Due to the complex geometry and sparse foam trabecular structure, the DVC analysis was not taken any further for the TKR construct scans.

Subvolume	**Correlation Value**			
	Mean	**S.D.**	**Min.**	**Max.**
32x32x32	0.7004	0.3658	0.02888	1.0000
48x48x48	0.7642	0.3473	0.02112	0.9999
64x64x64	0.8082	0.3225	0.01661	0.9999
72x72x72	0.8296	0.3097	0.01568	0.9999
96x96x96	0.8678	0.2774	0.02256	0.9999
128x128x128	0.9048	0.2401	0.04574	0.9998

Table 6.3: Femur Correlation Values by sub volume size for static analysis using the DaVis-FFT correlation

6.3.2 Bone Cement

The bone cement scans showed an even spatial distribution of radiopacifier particles, of varying sizes at the μCT scan resolution of 6.32 μm. The particle diameter ranged from 1 - 22 pixels through an image slice (Figure 6.6).

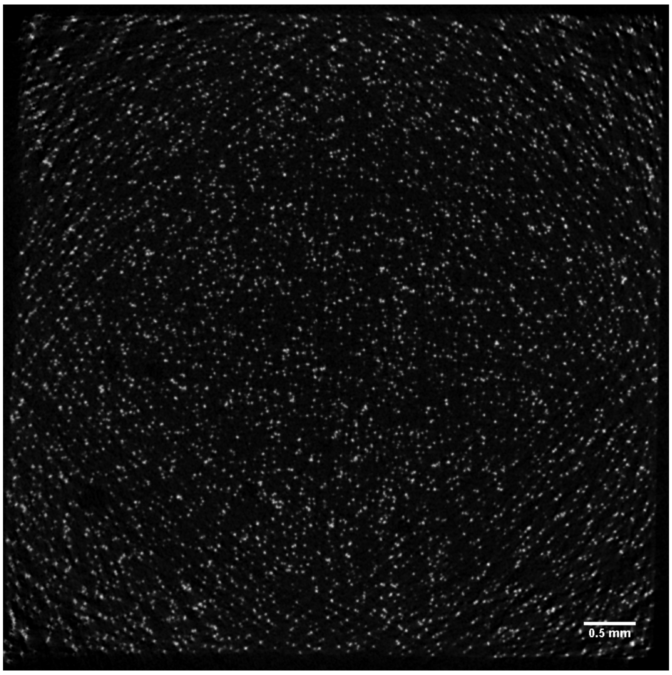

Figure 6.6: Reconstructed CT volume slice image of the bone cement specimen

6.3.2.1 DaVis-FFT Correlation Results

The mean and standard deviations of the correlation values within the region of interest in the bone cement are shown for the static, rigid body translation correction and magnification-strain DVC analyses in Tables 6.4, 6.5 and 6.6, respectively, using the DaVis-FFT correlation algorithm. With increasing sub-volume size, the corresponding minimum and maximum correlation values for each analysis are also shown. Below a sub-volume size of 48x48x48 voxels, the minimum correlation value was below the acceptance criteria of 0.9, even though the standard deviation was small. This reduces the confidence in the validity of the strain measurements with sub-volume sizes in this range.

Subvolume	**Correlation Value**			
	Mean	**S.D.**	**Min.**	**Max.**
24x24x24	0.9893	0.007281	0.3121	0.9995
32x32x32	0.9899	0.005181	0.4958	0.9991
48x48x48	0.9903	0.004524	0.9576	0.9980
64x64x64	0.9903	0.004439	0.9692	0.9971
96x96x96	0.9908	0.003975	0.9732	0.9958

Table 6.4: Cement correlation values with increasing sub-volume size in the static analysis, using the DaVis-FFT

Subvolume	**Correlation Value**			
	Mean	**S.D.**	**Min.**	**Max.**
24x24x24	0.9911	0.006284	0.2428	0.9995
32x32x32	0.9916	0.003144	0.4755	0.9990
48x48x48	0.9919	0.002188	0.9618	0.9977
64x64x64	0.9920	0.002051	0.9806	0.9966
96x96x96	0.9899	0.001854	0.9777	0.9947

Table 6.5: Cement correlation values with increasing sub-volume size in the rigid body translation analysis, using the DaVis-FFT

Subvolume	**Correlation Value**			
	Mean	**S.D.**	**Min.**	**Max.**
24x24x24	0.9892	0.005133	0.3491	0.9971
32x32x32	0.9896	0.002734	0.6858	0.9958
48x48x48	0.9898	0.002027	0.9757	0.9948
64x64x64	0.9898	0.001940	0.9769	0.9942
96x96x96	0.9890	0.002112	0.9764	0.9934

Table 6.6: Cement correlation values with increasing sub-volume size in the magnification strain analysis, using the DaVis-FFT

The mean and standard deviation of E_{xx}, E_{yy} and E_{zz} strain measurements (in the x, y, and z directions, respectively) from the static and rigid body translation analysis, are shown in Tables 6.7 and 6.8, respectively. Under static nominally zero strain conditions, the bias (mean) value did not vary significantly with change in sub-volume size using the DaVis-FFT correlation. The noise decreased with increasing sub-volume size, giving a smaller standard deviation (strain resolution).

Subvolume	$\mathbf{E_{xx}}$ ($\mu\epsilon$)		$\mathbf{E_{yy}}$ ($\mu\epsilon$)		$\mathbf{E_{zz}}$ ($\mu\epsilon$)	
	Mean	**S.D.**	**Mean**	**S.D.**	**Mean**	**S.D.**
24x24x24	84.0	1188.3	76.6	1114.6	73.7	753.5
32x32x32	84.0	566.6	76.8	525.9	77.8	360.5
48x48x48	83.7	200.4	77.0	187.1	74.1	127.2
64x64x64	83.2	102.1	77.3	95.4	74.4	64.4
96x96x96	83.3	42.6	77.3	38.9	74.9	25.2

Table 6.7: Mean and standard deviation of strain in the static analysis volume using DaVis-FFT correlation

In the rigid body translation tests (Table 6.8), the mean of E_{zz}, (the mean strain in the direction that the rigid body translation correction was carried out), varied with increasing sub-volume size. Hence, a correction of a rigid translation can cause variation in the bias within the analysis volume at different sub-volume sizes.

Subvolume	$\mathbf{E_{xx}}$ ($\mu\epsilon$)		$\mathbf{E_{yy}}$ ($\mu\epsilon$)		$\mathbf{E_{zz}}$ ($\mu\epsilon$)	
	Mean	**S.D.**	**Mean**	**S.D.**	**Mean**	**S.D.**
24x24x24	139.3	1021.9	104.7	1002.8	57.5	1016.4
32x32x32	138.9	535.8	104.9	500.0	-31.9	709.1
48x48x48	139.0	178.2	104.2	167.3	102.7	137.4
64x64x64	138.0	95.0	104.1	87.8	89.0	84.1
96x96x96	137.6	43.7	103.7	103.6	103.6	28.6

Table 6.8: Mean and standard deviation of strain in the rigid body translation analysis volume using DaVis-FFT correlation

The strain resolution under nominally zero strain conditions was plotted against sub-volume size (Figure 6.7). 48x48x48 voxels was identified the optimal sub-volume size to give balance between the noise and smoothing of the strain measurement in the static and rigid body translation correction analyses (Figure 6.7a and 6.7b respectively). The size of this sub-volume relative to the distribution of radiopacifier particles in the cement is shown in Figure 6.8.

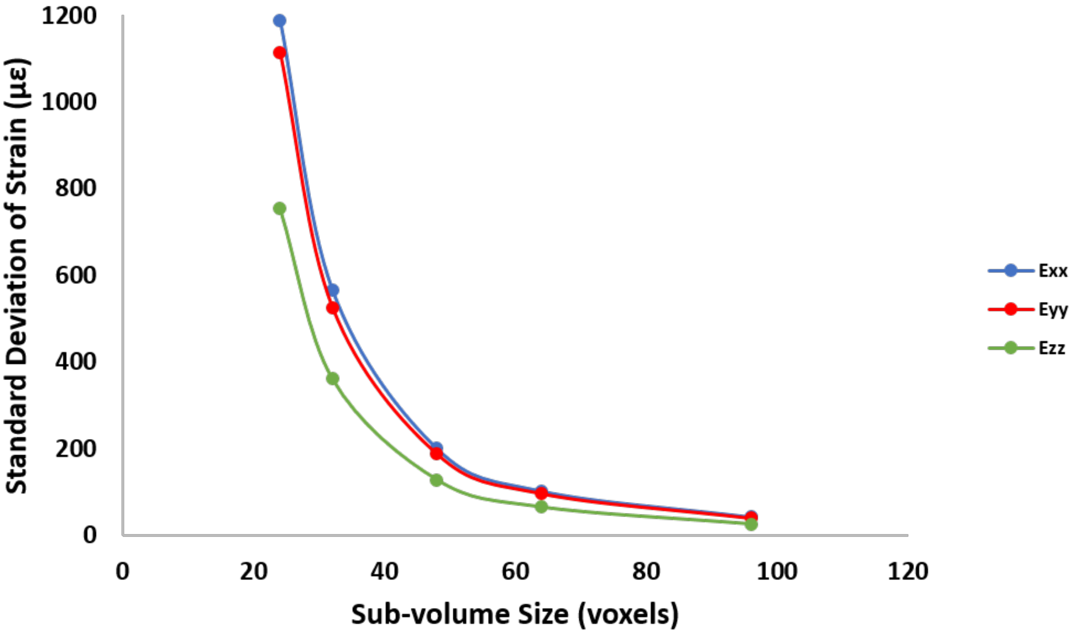

(a) Static

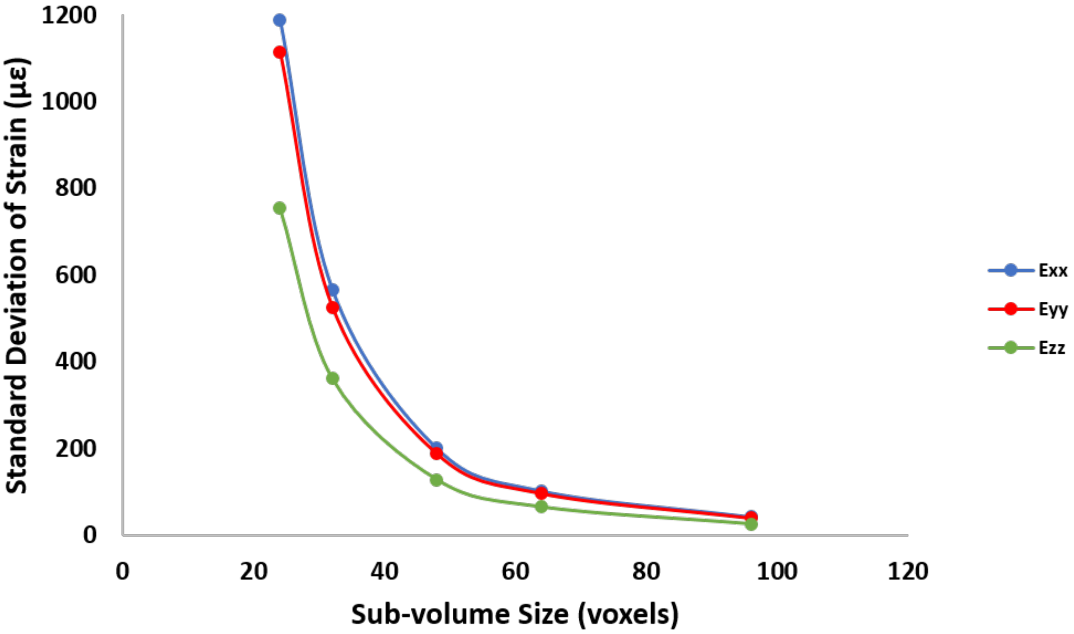

(b) Rigid Body Translation

Figure 6.7: Standard deviation of strain with increasing sub-volume size using the DaVis-FFT correlation, for the static and rigid body translation analyses

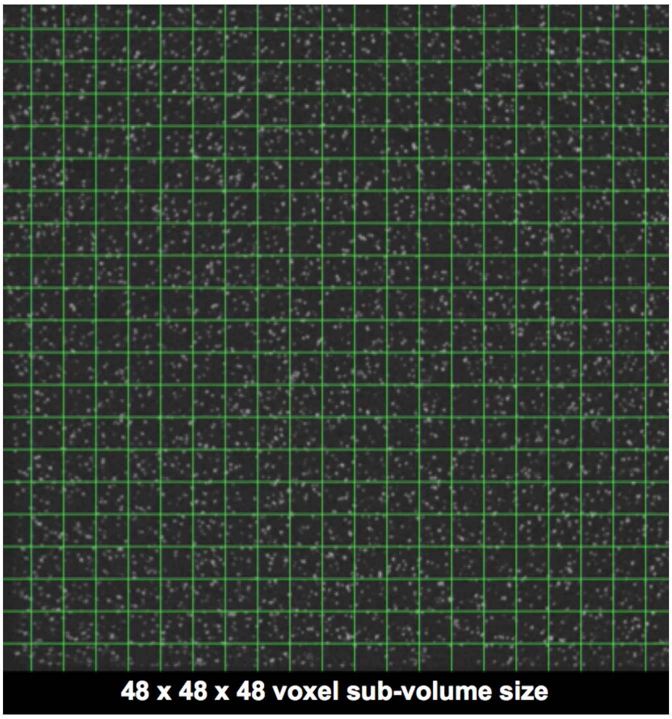

Figure 6.8: 48x48x48 sub-volume size relative to the particle pattern distribution in a cement volume slice

Under strained conditions, the mean and standard deviation of the E_{xx}, E_{yy} and E_{zz} strain measurements in the magnification-strain analysis are shown in Table 6.9 with increasing sub-volume size. At the chosen sub-volume size of 48x48x48 voxels, the mean strain measurement was within 4.5% of the theoretical imposed strain value of -2654 $\mu\epsilon$. The experimental error, taken as the standard deviation of strain, was below 8.7% of the mean strain value, indicating a good signal to noise ratio.

Subvolume	**E_{xx} ($\mu\epsilon$)**		**E_{yy} ($\mu\epsilon$)**		**E_{zz} ($\mu\epsilon$)**	
	Mean	**S.D.**	**Mean**	**S.D.**	**Mean**	**S.D.**
24x24x24	-2546.6	985.1	-2528.0	975.0	-2555.5	700.2
32x32x32	-2548.3	507.4	-2530.5	497.1	-2567.4	353.1
48x48x48	-2550.9	223.4	-2533.6	220.4	-2579.8	133.5
64x64x64	-2550.2	160.4	-2533.4	159.4	-2587.7	80.3
96x96x96	-2529.7	144.8	-2515.0	139.9	-2574.5	95.9

Table 6.9: Mean and standard deviation of strain in the magnification strain analysis volume using DaVis-FFT correlation

The change in mean (bias) and standard deviation (noise) of strain measurement through each slice of the DVC analysis volume of interest is shown in Figure 6.9 and 6.10 for the static and rigid body translation tests, using the DaVis-FFT correlation (48x48x48 voxel sub-volume size). The standard deviation was higher in the x and y directions and whilst the E_{yy} and E_{zz} strain gradually increase, the E_{xx} strain decreases through the volume. There was greater linear deviation in the mean strain for the E_{zz} strain compared to E_{xx} and E_{yy}, and there were large edge effects at high slice numbers in the rigid body translation test, showing increased bias.

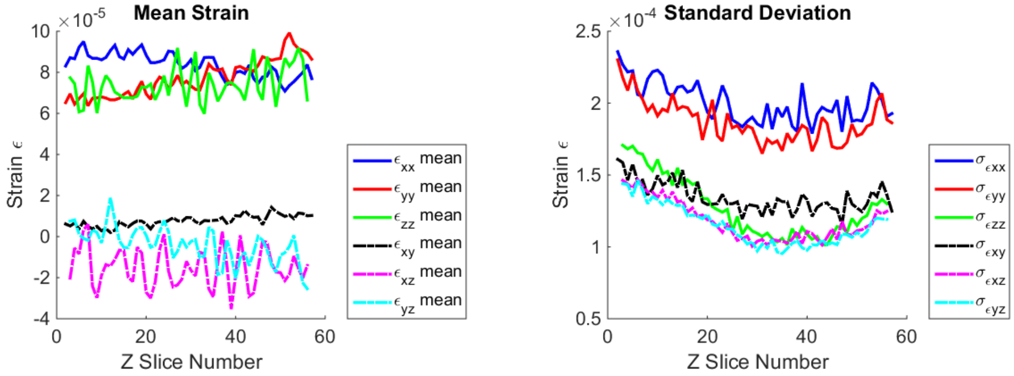

(a) Mean (b) SD

Figure 6.9: Mean and standard deviation of strain in each slice of the static volume test using DaVis-FFT correlation (48x48x48 sub-volume size)

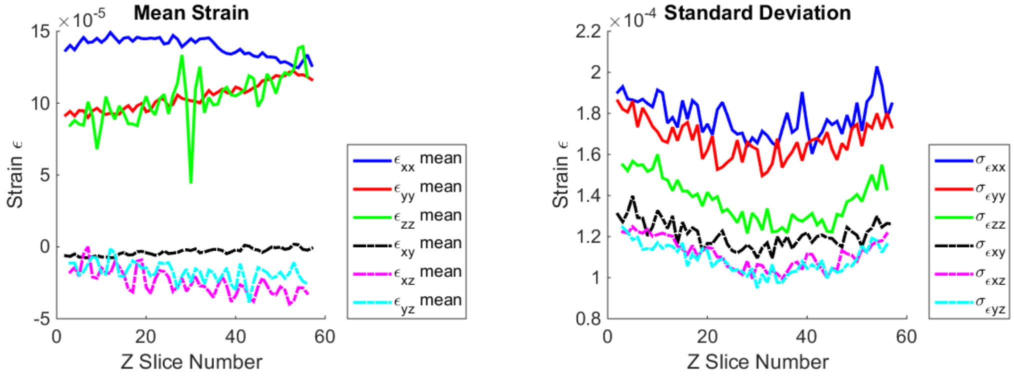

(a) Mean (b) SD

Figure 6.10: Mean and standard deviation of strain in each slice of the rigid body translation volume test using DaVis-FFT correlation (48x48x48 sub-volume size)

Under strained conditions using the DaVis-FFT correlation (48x48x48 voxel sub-volume size), the mean (Figure 6.11a) and standard deviation (Figure 6.11b) for each slice in the DVC analysis volume showed that there was a sinusoidal wave pattern in the E_{zz} strain, whilst the E_{xx} and E_{yy} strain remained linear. A uniform change should be observed for the E_{xx}, E_{yy} and E_{zz} strain measurements by changing the magnification of the μCT scan volume (moving the specimen closer to the detector).

3D strain maps of the E_{xx}, E_{yy} and E_{zz} strain in the magnification-strain test showed that strain distrbution throughout the volume (Figures 6.13a, 6.13b and 6.13c, respectively). The image scale is magnified in Figure 6.12 to show the spatial pattern of strain bands in E_{zz}.

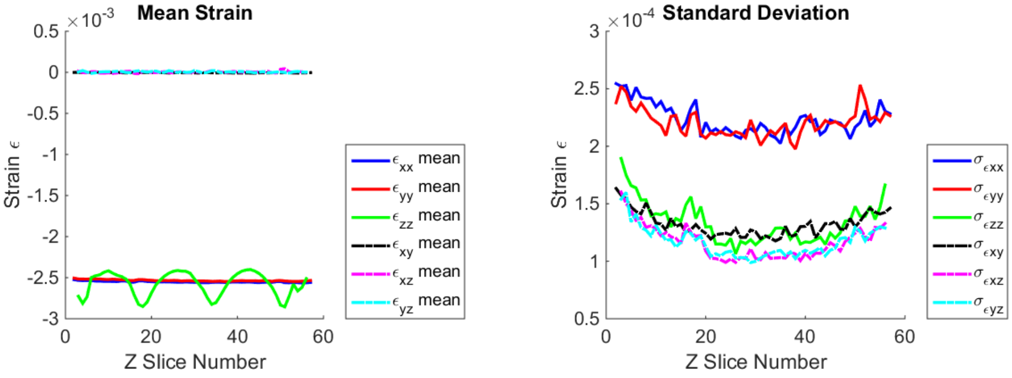

(a) Mean (b) SD

Figure 6.11: Mean and standard deviation of strain in each slice of the magnification-strain volume test using DaVis-FFT correlation (48x48x48 sub-volume size)

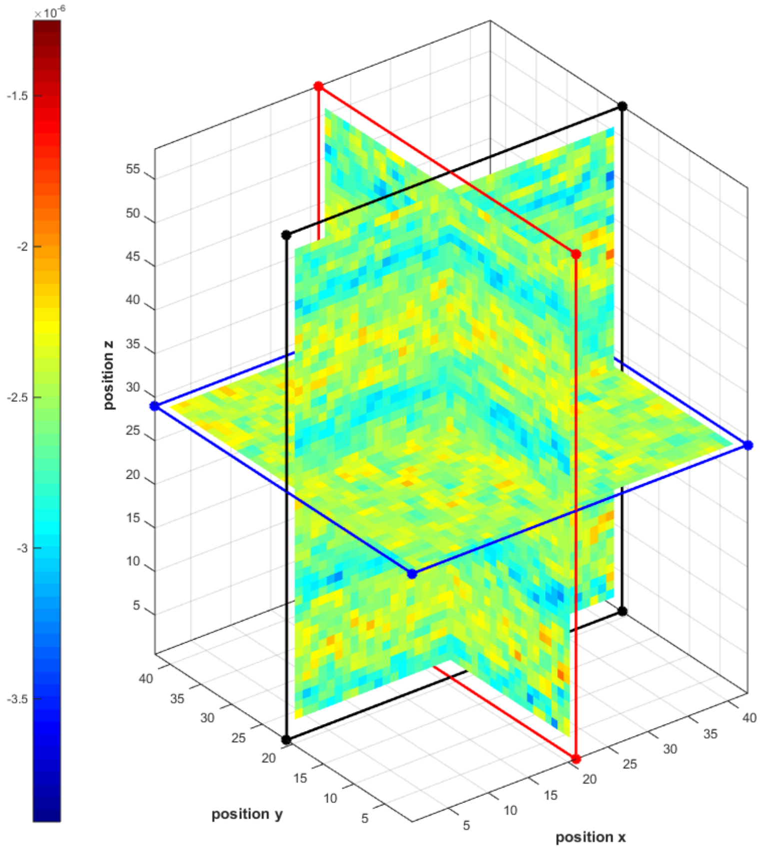

Figure 6.12: Spatial distribution of E_{zz} strain using the DaVis-FFT correlation

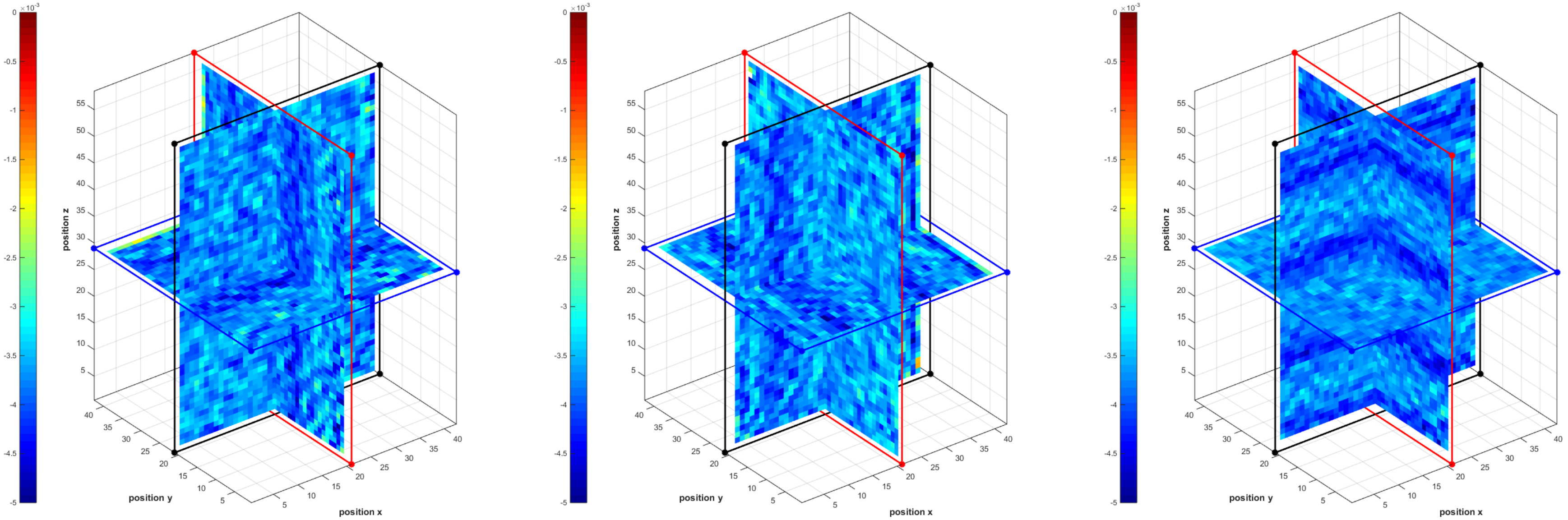

(a) E_{zz} (b) E_{yy} (c) E_{zz}

Figure 6.13: Strain slices through 3D volume of the magnification strain tests using the DaVis-FFT (sub volume size 48x48x48)

6.3.2.2 DaVis-Direct Correlation Results

Using the DaVis-Direct correlation algorithm, the mean and standard deviations of the correlation values within the region of interest in the bone cement are shown for the static, rigid body translation correction and magnification-strain DVC analyses in Tables 6.10, 6.11 and 6.12, respectively. The corresponding minimum and maximum correlation values for each analysis are also shown with increasing sub-volume size. The interpolation method (3^{rd}, 6^{th} or 9^{th} order spline) is also shown for the static tests to determine which would give the greatest correlation between the analysis volumes (Table 6.10). A higher order spline interpolation method gave a lower mean, larger standard deviation and lower minimum correlation value. Therefore a 3^{rd} order interpolation spline was chosen for the rest of the tests. The minimum correlation value was above the acceptance criteria of 0.9 with every sub-volume size tested, with a smaller standard deviation than that achieved with the DaVis-FFT correlation.

Subvolume	**Spline Order**	**Correlation Value**			
		Mean	**S.D.**	**Min.**	**Max.**
24x24x24	3	0.9969	0.001337	0.9905	0.9995
32x32x32	3	0.9969	0.001318	0.9911	0.9992
32x32x32	9	0.9962	0.001762	0.9890	0.9990
40x40x40	3	0.9968	0.001383	0.9910	0.9989
48x48x48	3	0.9970	0.001282	0.9918	0.9989
48x48x48	9	0.9964	0.001674	0.9899	0.9989
64x64x64	3	0.9971	0.001295	0.9918	0.9991
64x64x64	6	0.9971	0.001295	0.9918	0.9991
64x64x64	9	0.9962	0.001549	0.9905	0.9990

Table 6.10: Choice of interpolation spline order based on static correlation values for the DaVis-Direct correlation

Subvolume	**Correlation Value**			
	Mean	**S.D.**	**Min.**	**Max.**
24x24x24	0.9975	0.0006442	0.9939	0.9995
32x32x32	0.9975	0.0006206	0.9942	0.9990
40x40x40	0.9975	0.0006426	0.9944	0.9989
48x48x48	0.9976	0.0005948	0.9946	0.9987
64x64x64	0.9977	0.0005923	0.9947	0.9987

Table 6.11: Correlation values corresponding to the rigid body translation analysis using DaVis-Direct with 3^{rd} order spline interpolation

The correlation values decreased in the magnification-strain analysis (Table 6.12), compared to the tests under nominally zero strain conditions, but the mean values were still above 0.99 and the minimum correlation values were above 0.9 (with the exception of the 24x24x24 sub-volume size).

Subvolume	**Correlation Value**			
	Mean	**S.D.**	**Min.**	**Max.**
24x24x24	0.9914	0.002095	0.8970	0.9973
32x32x32	0.9914	0.001697	0.9480	9961
40x40x40	0.9916	0.001519	0.9715	0.9956
48x48x48	0.9916	0.001457	0.9809	0.9953
64x64x64	0.9916	0.001426	0.9826	0.9949

Table 6.12: Correlation values corresponding to the magnification analysis using DaVis-Direct with 3$^{\text{rd}}$ order spline interpolation

The mean and standard deviation of E_{xx}, E_{yy} and E_{zz} strain measurements (in the x, y, and z directions, respectively) with increasing sub-volume size and change in interpolation method are shown in Table 6.13 for the static tests. At smaller sub-volume sizes, higher order interpolation splines gave larger standard deviations (strain resolution). This confirmed that an interpolation spline of the 3$^{\text{rd}}$ order was most suitable for the DVC analysis of the bone cement volume using the DaVis-Direct correlation.

Subvolume	**Spline Order**	$\mathbf{E_{xx}}$ $(\mu\epsilon)$		$\mathbf{E_{yy}}$ $(\mu\epsilon)$		$\mathbf{E_{zz}}$ $(\mu\epsilon)$	
		Mean	**S.D.**	**Mean**	**S.D.**	**Mean**	**S.D.**
32x32x32	3	85.3	489.6	79.9	458.9	78.3	359.6
32x32x32	9	84.8	651.3	80.6	621.9	78.3	555.2
48x48x48	3	84.5	226.9	80.4	218.0	78.9	193.7
48x48x48	9	84.2	226.1	80.0	217.0	78.6	192.5
64x64x64	3	84.6	297.0	81.0	281.2	78.5	232.4
64x64x64	6	85.6	85.5	81.1	81.0	78.9	64.0
64x64x64	9	85.6	85.5	81.1	81.0	78.9	64.0

Table 6.13: Choice of spline interpolation order based on static noise values

The mean and standard deviation of E_{xx}, E_{yy} and E_{zz} strain measurements (in the x, y, and z directions, respectively) from the static and rigid body translation analysis, are shown in Tables 6.14 and 6.15, respectively, for each sub-volume size tested. Under static and translated nominally zero strain conditions, the bias (mean) value does not vary significantly with a change in sub-volume size using the DaVis-Direct correlation. The noise decreases with increasing sub-volume size, giving a smaller standard deviation (strain resolution). However, there is a maximum increase of 13.2% in noise, compared to the DaVis-FFT. The bias values are also greater than those using the DaVis-FFT, with a maximum increase of 5.7% in the static tests. In the rigid body correction tests, there was a smaller variation in the E_{zz} mean, compared to those achieved using the DaVis-FFT. Hence the DaVis-Direct correlation was more robust to translation correction in the z direction.

Subvolume	$\mathbf{E_{xx}}$ ($\mu\epsilon$)		$\mathbf{E_{yy}}$ ($\mu\epsilon$)		$\mathbf{E_{zz}}$ ($\mu\epsilon$)	
	Mean	**S.D.**	**Mean**	**S.D.**	**Mean**	**S.D.**
24x24x24	85.2	1084.5	80.1	1017.9	77.9	798.1
32x32x32	85.3	489.6	79.9	458.9	78.3	359.6
40x40x40	84.6	297.0	81.0	281.2	78.5	232.4
48x48x48	84.5	226.9	80.4	218.0	78.9	193.7
64x64x64	85.9	85.6	81.5	81.3	79.2	64.3

Table 6.14: Mean and standard deviation of strain in the static analysis volume using DaVis-Direct correlation

Subvolume	$\mathbf{E_{xx}}$ ($\mu\epsilon$)		$\mathbf{E_{yy}}$ ($\mu\epsilon$)		$\mathbf{E_{zz}}$ ($\mu\epsilon$)	
	Mean	**S.D.**	**Mean**	**S.D.**	**Mean**	**S.D.**
24x24x24	146.0	919.9	111.1	875.2	78.9	787.8
32x32x32	145.8	429.5	110.6	405.9	98.4	363.8
40x40x40	145.1	272.9	110.7	257.5	90.2	236.5
48x48x48	145.5	216.0	110.2	207.6	107.5	197.4
64x64x64	146.8	81.7	111.3	76.5	97.1	67.5

Table 6.15: Mean and standard deviation of strain in the rigid body translation analysis volume using DaVis-Direct correlation

The strain resolution under nominally zero strain conditions is plotted against sub-volume size in Figure 6.14. As with the DaVis-FFT correlation method, 48x48x48 voxels was identified as the optimal sub-volume size to give a balance between noise and smoothing of the strain measurement in the static and rigid body translation correction analyses (Figure 6.14a and 6.14b respectively).

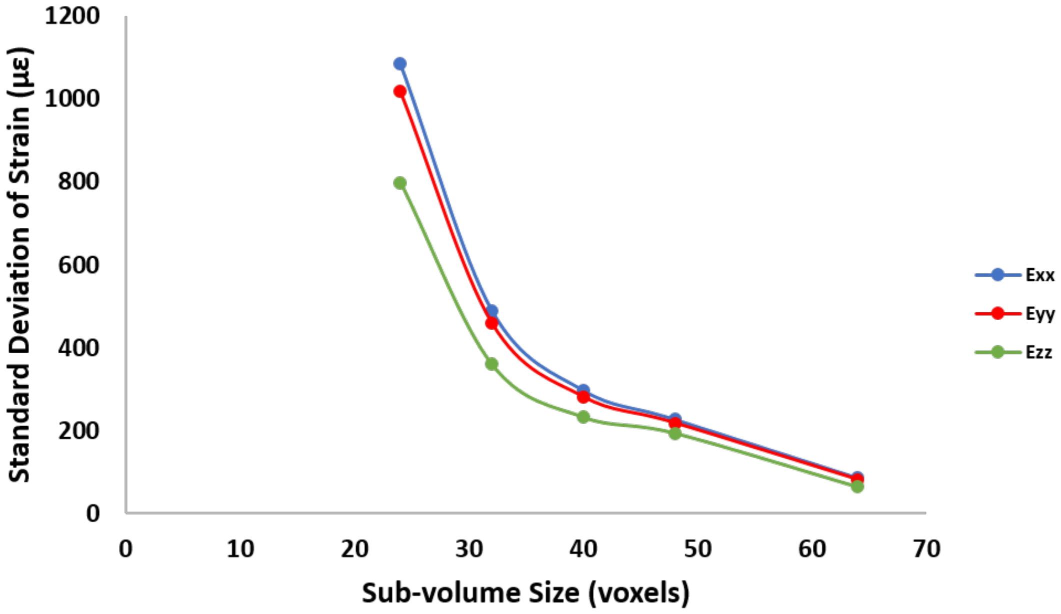

(a) Static

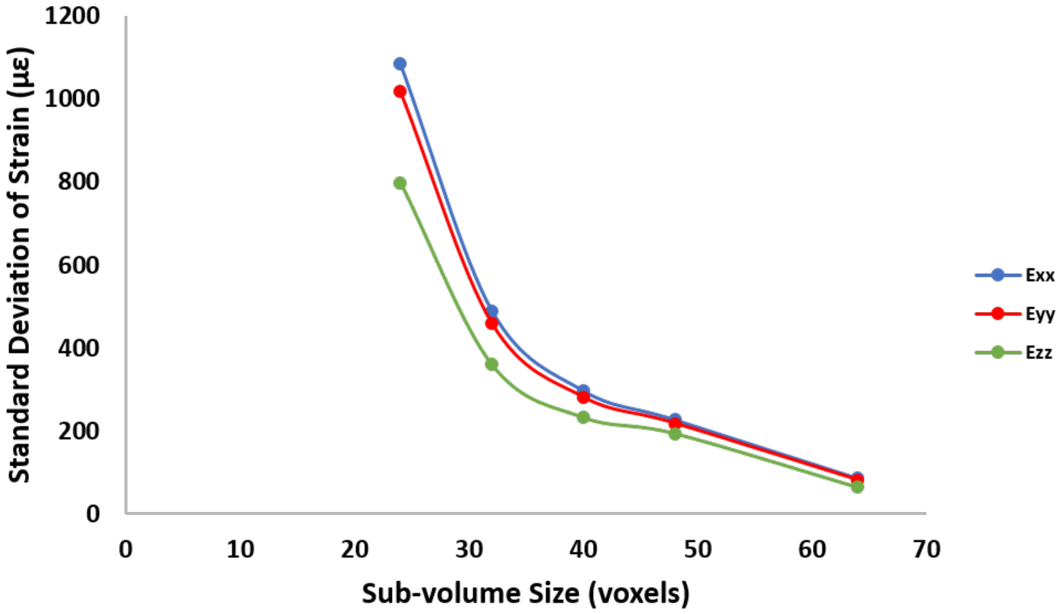

(b) Rigid body translation

Figure 6.14: Standard deviation of strain with increasing sub-volume size using the DaVis-Direct correlation, for the static and rigid body translation analyses

Under strained conditions, the mean and standard deviation of the E_{xx}, E_{yy} and E_{zz} strain measurements in the magnification-strain analysis are shown in Table 6.16 with increasing sub-volume size. At the chosen sub-volume size of 48x48x48 voxels, the mean strain measurement is within 4.6% of the theoretical imposed strain value of -2654 $\mu\epsilon$. The experimental error, taken as the standard deviation of strain, is below 9.3% of the mean strain value, indicating a good signal to noise ratio.

Subvolume	**E_{xx} ($\mu\epsilon$)**		**E_{yy} ($\mu\epsilon$)**		**E_{zz} ($\mu\epsilon$)**	
	Mean	**S.D.**	**Mean**	**S.D.**	**Mean**	**S.D.**
24x24x24	-2553.6	970.5	-2533.3	957.2	-2585.7	817.6
32x32x32	-2556.3	453.7	-2536.5	447.4	-2591.1	366.3
40x40x40	-2550.7	291.9	-2530.8	286.9	-2595.0	244.7
48x48x48	-2550.2	241.1	-2530.5	236.5	-2599.7	213.1
64x64x64	-2567.3	108.1	-2547.5	106.2	-2601.8	74.1

Table 6.16: Mean and standard deviation of strain in the magnification strain analysis volume using DaVis-Direct correlation

The change in mean (bias) and standard deviation (noise) of strain measurement through each slice of the DVC analysis volume of interest is shown in Figure 6.15 and 6.16 for the static and rigid body translation tests, using the DaVis-Direct correlation (48x48x48 voxel sub-volume size). There is greater linear deviation in the mean strain for the E_{zz} strain compared to E_{xx} and E_{yy}, and there are large edge effects at high slice numbers in the rigid body translation test, showing increased bias.

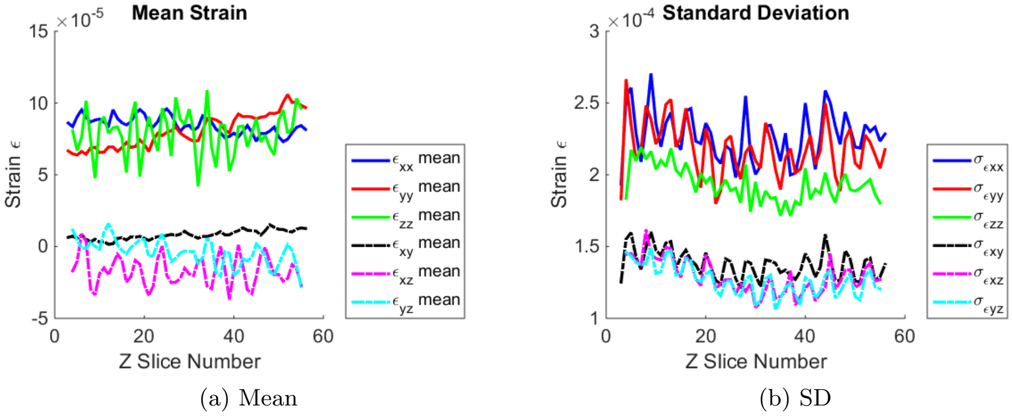

(a) Mean (b) SD

Figure 6.15: Mean and standard deviation of strain in each slice of the static volume test using DaVis-Direct correlation (48x48x48 sub-volume size)

Under strained conditions using the DaVis-Direct correlation (48x48x48 voxel sub-volume size), the mean for each slice in the DVC analysis volume showed that the sinusoidal E_{zz} strain pattern had been eliminated (Figure 6.17a). Edge effects were present at low and high slice numbers in the E_{zz} strain, hence, these regions must be

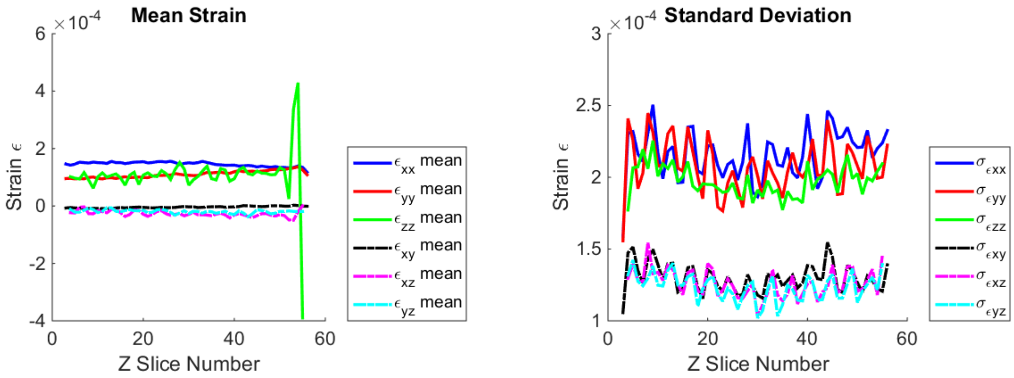

(a) Mean (b) SD

Figure 6.16: Mean and standard deviation of strain in each slice of the rigid body translation volume test using DaVis-FFT correlation (48x48x48 sub-volume size)

masked out for reliable strain measurement. This was reflected in the change in standard deviation throughout the volume (Figure 6.17b).

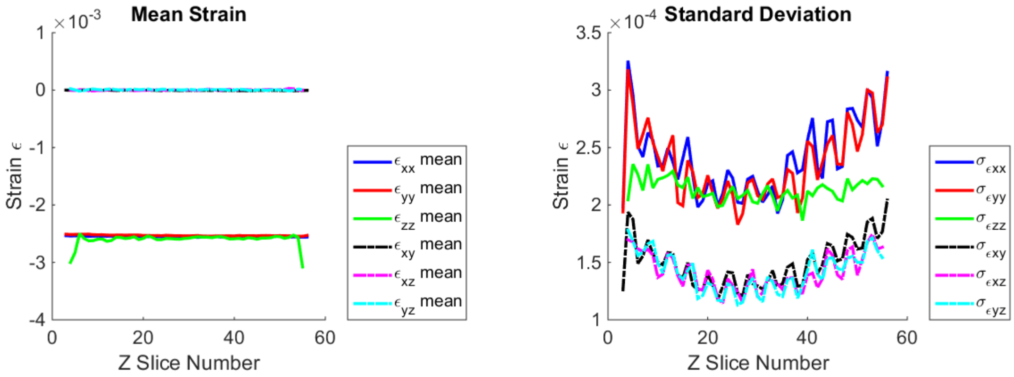

(a) Mean (b) SD

Figure 6.17: Mean and standard deviation of strain in each slice of the magnification-strain volume test using DaVis-FFT correlation (48x48x48 sub-volume size)

3D strain maps of the E_{xx}, E_{yy} and E_{zz} strain in the magnification-strain test are shown in Figures 6.18a, 6.18b and 6.18c, respectively. An even distribution of strain was observed in each direction, without a spatial pattern of strain bands as observed when using the DaVis-FFT correlation.

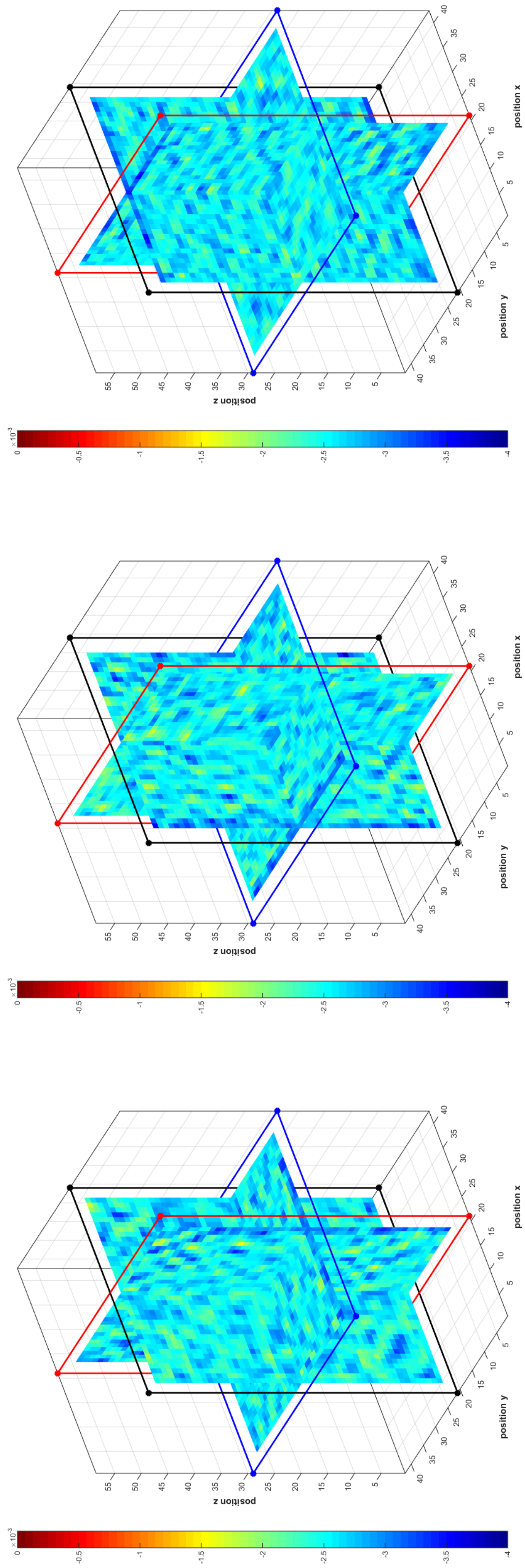

(a) E_{zz}

(b) E_{yy}

(c) E_{zz}

Figure 6.18: Strain slices through 3D volume of the magnification strain tests using the DaVis-Direct correlation (sub volume size 48x48x48)

6.4 Discussion

The purpose of the present study was to present a DVC methodology for *in situ* volumetric strain measurement of the TKR construct, including the strain noise (resolution) and bias values associated with the technique. The quality of strain analysis was assessed using two correlation methods available in the DaVis software, and optimal analysis parameters were determined.

The TKR construct specimen had a sparse foam trabecular structure with thin cell walls, which resulted in poor correlation values throughout the volume (below 0.9) and prevented reliable DVC strain analysis. The correlation relies on sub-volumes with distinct patterns, such that deformation can be tracked from the variation in grey levels (Sutton et al., 2009).

In the bone cement study, the radiopacifier particle pattern was used successfully for deformation tracking using DVC with a scan resolution of 6.32 μm. The particle diameter ranged from 1 to 22 pixels (6.32 to 138.98 μm). Comparing the two correlation methods used, the DaVis-Direct achieved an improved correlation over the DaVis-FFT for every sub-volume size tested, with larger means and minimum correlation values exceeding 0.9. An optimal sub-volume size of 48x48x48 voxels was identified from the balance between noise and smoothing of the signal for both the DaVis-FFT and the DaVis-Direct methods. At this sub-volume size, the noise and bias values were larger in the static analysis using DaVis-Direct compared to DaVis-FFT (maximum increase of 13.2% and 5.7%, respectively). Comparing the strain measurements in the magnification strain analysis to the theoretical strain value (-2654 $\mu\epsilon$), the mean strain measurement was within 4.5% and 4.6% using the DaVis-FFT and DaVis-Direct respectively. However, the DaVis-FFT produced a spatial pattern of strain bands in E_{zz} of the magnification strain analysis volume, which may be attributed to interpolation bias from the trilinear interpolation regime used by the DaVis-FFT (Fu et al., 2013). The DaVis-Direct correlation technique used a 3^{rd} order spline interpolation and produced an even strain distribution throughout the analysis volume in the x, y and z directions (with the exception of edge effects). The experimental error (standard deviation of magnification strain) was below 8.7% and 9.3% of the mean strain value, using DaVis-FFT and DaVis-Direct correlation, respectively, which was comparable to that achieved using the DIC technique in Chapter 4. While the DaVis-Direct correlation technique gave small increases in experimental error and bias, and a reduction in strain resolution, it was able to estimate the strain throughout the volume without sinusoidal bands of strain concentrations as were observed with the DaVis-FFT. Therefore it can be concluded that the DaVis-Direct correlation method is most robust for the analysis of strain within bone cement using the DaVis software.

To the author's knowledge, this is the first study to carry out a full noise analysis study and quantify strain measurement within bone cement, using the radiopacifier particle pattern. Tozzi et al. (2014) measured strain at the bone-cement interface by using the DaVis-FFT with an unloaded reference and a deformed μCT volume, where the specimen was subjected to a global strain of -4%. The study used Simplex P bone cement (Stryker corp., MI, USA) which contains Barium Sulphate radiopacifier particles with an average diameter of 2-5 μm. Although Barium Sulphate can agglomerate into large particles with diameters of up to 200 μm, a dispersion of fine particles ($< 10\mu$m) has previously been shown on μCT scans (Shearwood-Porter, 2013; Sinnett-Jones et al., 2005). Therefore it is likely that partial volume effects would have been present at the 20 μm scan resolution used. The strain within the cement appeared to be between -0.02 and -0.05 strain, but it is likely that this would have a high noise content due to the scan resolution. In addition, a noise study was not carried out and correlation values were not reported (or if they used an acceptance value in their method to discard all data with correlation values below 0.9 for example). Hence the results are not reliable on their own, and cannot be compared with the data from the present study.

There are several limitations with this study. First, the magnification strain analysis used is not entirely representative of the material behaviour under load where uneven strain patterns and crushing may occur, as observed in a study of bone by Gillard et al. (2014). Second, a small sample group and number of reference and deformed μCT scans were used for the DVC analysis due to the cost of the μCT scanning technique and the time required for the DVC analysis of each pair of volumes. The experimental error values were taken from the standard deviation of the magnification strain measurements at the optimal sub-volume size, which may not be a fair representation of a larger population of μCT data. In addition, the strain analysis in a full volume of bone cement may not be entirely representative of that achievable in a full construct analysis, where additional CT artefacts may be present when using the local tomography technique (Boas and Fleischmann, 2012). This is a method of observing a region of interest within a sample that is larger than the size of X-ray beam, at a higher resolution (Faridani et al., 2001). The strain analysis is limited by the resolution of the volume data, which must be sufficient to allow imaging of the zirconium dioxide radiopacifier particles within the cement. The minimum particle size in the image slices was 1 pixel in diameter, which suggests that some partial volume effects may have been present from particles smaller than the resolution. Under-sampling could also have caused localised bias in these regions due to aliasing. The optimal feature size for correlation was recommended by Sutton et al. (2009) to lie between 3-6 pixels.

For evaluation of implanted bone strain with a PEEK femoral component, the DVC methodology needs to be repeated using a biomechanical Sawbone femur model (Sawbones Europe AB, Malmö, Sweden) or a cadaver, with a greater density in the trabecular bone region. The radiolucent PEEK femoral component allows the implant-cement-bone interface to be imaged using μCT, unlike CoCr implants. However, the bone cement region in the TKR construct used in the present study caused beam hardening artefacts within the trabecular bone region due to its zirconium dioxide radiopacifier content. This may lead to a reduction in correlation and higher noise in DVC strain measurements even with an improved foam structure (pattern).

New challenges may arise when imaging the local tomography of the bone cement region within the full construct, as the resolution is limited by how close the specimen can be positioned relative to the gun (including an *in situ* loading rig). The specimen would also have to be scanned off centre to focus on a region of interest with bone cement (underneath either condyle or at the anterior or posterior flanges), making it more difficult to position the specimen accurately. Any displacement of the femur under load could also cause problems for the DVC analysis, if the reference pattern is no longer present in the deformed volume and the rigid body translation cannot be corrected.

In conclusion, the present study has demonstrated the possibility of strain measurement within the bone cement fixation layer of the PEEK TKR construct. With suitable parameter selection, strain measurements can be made at sufficient resolution for measurement of full-field cement strain with adequate accuracy and precision comparable to that of the DIC technique. The methodology presented for the bone cement DVC analysis can now be used for analysis of local strain within the full construct. Although, the main challenge is in obtaining high resolution volumetric data ($\leqslant$6 μm) whilst the specimen is loaded *in situ*.

Chapter 7

Summary and Conclusions

7.1 Summary of Findings

7.1.1 Fixation Strength of the PEEK-Cement Interface

The fixation strength study (Chapter 3) aimed to establish the adhesive properties of the PEEK-cement interface primarily to determine an appropriate surface finish to achieve an interface capable of withstanding the biomechanical environment *in vivo.* This study of the fixation strength of PEEK with PMMA bone cement is without precedent in the literature to the author's knowledge. Shear stress data generated from an FE model was used as an acceptance criterion for the PEEK-cement interface strength (3 MPa). A chart summarising the shear strength results for every sample group tested in the fixation study is shown in Appendix 4 (Figure 2). The key outcomes from the study are summarised:

- The adhesion between untreated PEEK and cement is governed by the mechanical interlock between the two materials, due to the inert nature of the PEEK surface. Adhesion was not achieved between smooth PEEK (as injection moulded) and cement.
- Grit-blasted CFR-PEEK (MOTIS) demonstrated a stronger interface with cement than grit-blasted unfilled PEEK (PEEK-OPTIMA). However, the hard carbon fibre inclusions may cause third body abrasive wear of the PE tibial component, so was excluded from the rest of the fixation study.
- An injection moulded surface topography was chosen due to the risk of third body inclusions from residual grit-blasting material.
- Macro-textured PEEK promoted higher interfacial shear strength than micro-textured PEEK. The highest shear strength was achieved by combining the micro and macro textures to form a hierarchical structure with both the short and long wave components of surface roughness. With a mean apparent interfacial shear strength of 3.62 MPa (S.D. = 0.71 MPa), this surface topography satisfied the shear strength criterion predicted from the FE model of a PEEK TKR construct.

- Plasma treatment of PEEK significantly improved the adhesion strength with cement by increasing the surface energy and promoting physical bonds at the interface. The plasma treated Macro Troughed surface topography achieved the highest interfacial shear strength with cement of 3.39 MPa (S.D. = 0.23 MPa).
- Compared to a metal-cement interface, the increased compliance at the PEEK-cement interface could introduce additive tensile stress components, reducing its failure load. This was evident with the bending of the lap-shear samples.

7.1.2 DIC Evaluation of the Influence of TKR material on Femoral Bone Strain using Analogue Bone

A DIC technique was developed on analogue bone as a comparative tool to test the null hypothesis that a novel compliant PEEK implant has the potential to promote a more physiological bone strain distribution compared to a contemporary metallic implant. Three distal femur models were potted in resin and implanted with a CoCr femoral component, a PEEK-OPTIMA femoral component or left intact for comparison, and a surface speckle pattern was applied. The induced bone strain fields under standing loads were compared in six repeated tests. A detailed methodology for a robust DIC analysis has been presented. The main findings of the study were:

- In the present test setup, and with the speckle pattern applied to the analogue bone surface, a subset size of 41x41 pixels was identified to give the optimum balance between noise and smoothing of the DIC measurements. With a step size of 7 pixels and a strain filter of 15 data points, the maximum strain resolution was a SD of 30 $\mu\epsilon$ with a mean bias value of 38 $\mu\epsilon$.
- The maximum six sigma experimental error (representing 99.7% spread of data error) was ±213 $\mu\epsilon$ or 9.7% of the maximum strain in the virtual gauge region, 2200 $\mu\epsilon$.
- The CoCr implant induced significantly lower bone strain compared to that induced in the intact case ($p = 0.014$). This is indicative of stress shielding, which could be sufficient to cause bone resorption in the central metaphyseal region.
- The strain distribution induced by the metallic implant was corroborated by clinical measurements of bone mineral density change, from the literature, with the majority of the bone loss expected to occur in the central metaphyseal section of the femur.

- The PEEK implant produced a strain distribution closer to that of the intact bone, with no significant difference ($p = 0.231$), suggesting that PEEK could promote the strains necessary for bone maintenance.
- There was a shift in the strain path away from the posterior towards the anterior distal region of the lateral bone surface implanted with PEEK which was attributed to the change in the geometry of the articular surface upon implantation.
- The strain distributions measured for the PEEK and CoCr implanted and the intact femur were similar to the predictions of the FE model.

7.1.3 DIC Analysis of TKR Femoral Bone Strain on Cadaveric Bone

The DIC technique developed on an analogue model was applied to cadaveric bone with the aim to investigate the practicality and accuracy of strain measurements. The reference bone strain distribution was measured on two intact cadaver femurs. Each cadaver was then implanted with a CoCr or PEEK-OPTIMA femoral component and re-tested using the same surface speckle pattern for comparison. The analogue bone strain distribution results were then compared with cadaver bone results to evaluate the technique.

The main findings of the cadaveric bone strain DIC study were:

- A subset size of 31x31 pixels was identified to give the optimal balance between noise and smoothing of the DIC measurements with the speckle pattern applied to the cadaver bone surfaces. With a step size of 7 pixels and a filter size of 15 data points, the maximum strain resolution was a SD of 63 $\mu\epsilon$ and 56 $\mu\epsilon$ on the CoCr and PEEK cadaver bones, respectively. The mean (bias) value was 90 $\mu\epsilon$ and 71 $\mu\epsilon$ on the CoCr and PEEK cadaver bones, respectively.
- The signal to noise ratio was comparably lower on the cadaver bones compared to the analogue bones, with a maximum six sigma experimental error (representing 99.7% spread of data error) of ± 141 $\mu\epsilon$ or 10.6% of the maximum strain within the ROI, 1335 $\mu\epsilon$, at the maximum load of 2.5 kN (4 BW).
- A similar strain distribution was observed on the cadaver bone surface compared to the analogue bone surfaces, although the strain magnitude on the CoCr implanted cadaver femur was greater than on the analogue bone.
- As in the analogue bone study, an anterior shift in strain path was observed for the cadaver implanted with PEEK.

- A quantitative comparison of the intact bone strain against the implanted bone strain for both cadavers showed a large reduction in strain magnitude with both implant materials, indicative of stress shielding. This was unexpected for the PEEK material, which has a stiffness closer to that of bone and showed less of a stress shielding effect with analogue bone.
- The differences in strain magnitude and distribution on the cadaver bones compared to the analogue bone was attributed to the difference in the mediolateral dimension of each bone, in addition to the difference in bone density between the cadavers. The width of the tibial component used for loading, relative to the width of the intact cadaver bone, would also have influenced the surface strain distribution.
- There was poor raw image contrast on the cadaver implanted with PEEK, which was attributed to moisture on the surface causing reflections and saturation of pixels. This could have caused measurement errors and may have contributed towards higher noise values under nominally zero strain conditions.
- DIC had sufficient resolution to measure physiological strain levels, although signal to noise ratio and bias should always be evaluated for each experimental setup.

7.1.4 Volumetric Strain Analysis of the TKR construct

A Digital Volume Correlation analysis method for local *in situ* strain measurement within the PEEK TKR construct was developed using the trabecular foam region of the full PEEK TKR construct specimen and the radiopacifier particles within a bone cement specimen, in grouped μCT volumes. In both cases, the aim was to carry out a DVC noise study using a static and rigid body translation scan setup, to determine the optimal analysis parameters. The accuracy of the technique was assessed by imposing a theoretical isotropic strain on the specimen by changing the scan magnification.

The main findings of the DVC study were:

- The TKR construct analogue bone specimen had a sparse foam trabecular structure with thin cell walls, which resulted in poor correlation values throughout the volume (below 0.9) and prevented reliable DVC strain analysis.
- The zirconium dioxide radiopacifier particle pattern was successfully used for deformation tracking in bone cement using DVC (scan resolution = 6.32 μm). However, the minimum particle size in the image slices was 1 pixel diameter,

which suggests that some partial volume effects may have been present from particles smaller than the resolution.

- The DaVis-Direct correlation technique resulted in an improved correlation over the DaVis-FFT with every sub-volume size tested using the DaVis software for the analysis of the bone cement volumes.
- With a voxel size of 6.32 μm, an optimal sub-volume size of 48x48x48 voxels was identified from the balance between noise and smoothing of the signal for both the DaVis-FFT and the DaVis-Direct methods.
- The DaVis-FFT produced a spatial pattern of strain bands in E_{zz} of the magnification strain analysis volume, which may be attributed to interpolation bias from the trilinear interpolation regime.
- Under the isotropic strain conditions, the experimental error (precision) of the DVC technique was comparable to that of the DIC technique. The accuracy of the strain measurement compared to the theoretical value was within 4.5% and 4.6% using the DaVis-FFT and DaVis-Direct, respectively.

7.1.5 Study Limitations

Throughout these studies, certain limitations have been identified in the experimental methods and materials used. First, the fixation study in Chapter 3 was limited to the investigation of commercially viable PEEK surface topographies, which could be manufactured with injection mould tools at Invibio Ltd. The surface activation study was limited to dry methods, which could be easily isolated to the component backing surface. The overall test specimen geometry was also governed by the injection moulding process, which led to the selection of the lap shear test method. In addition, this was chosen for its simple test setup, which could easily be implemented as an in-house testing technique at Invibio Ltd.

Regarding the experimental techniques, the lap-shear strength test method may have led to bending in the central region of the samples, particularly in the PEEK substrates which have a much higher compliance than metallic substrates. Bending would introduce a tensile or peel stress component, reducing the apparent strength measured. This was evident in particular with very rough specimens, which had a higher failure load and thus a greater bending deformation. This limited the comparison of strength with surface topography. In addition, some of the PEEK plates supplied for testing were warped longitudinally, which could have induced a pre-stress at the PEEK-cement interface when mounted in the test machine. The samples were also not environmentally aged prior to testing, so the effects of the *in vivo* environment on the interface strength remains unknown.

In the DIC study (Chapter 4), only right-side femoral components were available from Invibio Ltd for testing at that time. Therefore, right anatomical foam femur models had to be used rather than biomechanically representative femur models, which are only available from Sawbones as a left-side. This meant that the strain signal was amplified by the lower modulus of the anatomical foam femur model. The Maxx Freedom Knee implant geometry of the CoCr and PEEK femoral components was designed for the Pan-Asian demographic. When implanted on a Sawbone femur model of Caucasian male geometry, a large bone overhang resulted medially and laterally due to the difference in the anterioposterior-mediolateral (AP:ML) aspect ratios. Therefore, the strain distributions mapped on the lateral side of the femurs may be of lower magnitudes than those induced in a femur of the same anterioposterior dimension with a narrower mediolateral dimension, such as an Asian femur. Nevertheless, the bone strain measurements were still valid for a comparative study.

The cadavers used in the DIC study of Chapter 5 originated from different donors with different geometries (including AP:ML ratio) and bone densities, which would have led to variation in the surface strain magnitude and distribution. The small population (due to limited TKR sample supply), also meant that statistical analysis could not be carried out. Again, these bones were of caucasian origin, not Asian, which the size C Maxx Freedom Knee implant was designed for.

In the DVC study of Chapter 6, the technique of imposing isotropic strain by changing the scan magnification (distance from the specimen to the detector) was not representative of the specimen behaviour under load, but it did allow for variation in CT noise artefacts between scans. The DVC experimental error calculations were limited by the number of CT scans of each specimen. The DVC study of bone strain within the TKR construct was limited by poor foam trabecular structure inside the analogue bone specimen used, which resulted in poor correlation and prevented the completion of that part of the study. The DVC study of strain measurement within bone cement was not fully representative of local tomography scans at full construct level which, would be subject to partial volume artefacts.

7.2 Conclusions

PEEK is widely characterised in the literature as a radiolucent, bioinert alternative to metallic implant materials. By facilitating improved load transfer, PEEK has the potential to reduce stress shielding effects, whilst eliminating concerns over metal ion release and improving medical imaging of the implant interface and surrounding tissues. Bone cement is the most realistic fixation choice for a PEEK TKR femoral component, to provide immediate stability and greater variability in implant positioning. However, an implant with greater compliance is likely to experience increased interfacial strains, so the fixation of such a device is likely to be more critical to the overall success *in vivo*.

This was the first study to investigate the interface strength between PEEK and bone cement. It can be concluded that the PEEK-cement interface strength will be governed by the mechanical interlock between the two materials alone, unless the surface chemistry of the PEEK is modified to improve adhesion. A hierarchical surface texture may provide sufficient shear strength at the PEEK-cement interface, to withstand the shear stresses at the knee joint *in vivo*. This surface texture has now been applied to the injection moulded PEEK femoral component design by Invibio Ltd and the proprietary protocol developed for the company shall enable the design and optimisation of all subsequent cemented PEEK knee implants. This was also the first study to show that surface activation of PEEK by oxygen plasma treatment significantly improves the cement adhesion strength and may be used to further enhance the interface strength.

Collectively, the DIC bone strain measurements suggested that PEEK has the potential to improve long term bone preservation following TKR, and to reduce the risk of revision surgery. To underpin the results, paired cadaver bone models would be a robust way to extend the comparative DIC study. This study was the first to highlight that a rigorous DIC protocol must be carried out and reported by the biomechanics community in order to ensure meaningful and reproducible results; the DIC methods presented in this thesis will guide future biomechanical studies for valid comparison of results.

Conclusions should not be drawn from evaluation of strain on the external bone surfaces alone. The strain across the implant-cement-bone interface requires investigation for greater confidence that sufficient interfacial integrity will be achieved with a novel compliant femoral component for long term success *in vivo*. The DVC study has demonstrated the concept of strain measurement within the bone cement fixation region of the PEEK TKR construct. With optimal μCT scan setup and DVC parameter selection, measurements may be obtained which characterise full-field cement strain with sufficient resolution, accuracy and precision, comparable to that of the DIC technique.

7.3 Further Work

Several areas of further investigation have been identified from the work in this project, as shown by the study limitations. A key development to inform further on the fixation properties of the TKR construct would be the investigation of environmental effects on the PEEK-cement interface. If the adhesion at this interface is governed by a mechanical interlock, it is postulated that fluid from the joint cavity may be able to penetrate through capillary action, which could result in degradation of the mechanical integrity of the construct. In addition, cement shrinkage results in residual tensile stresses, which could cause interface cracks if the interfacial strength is exceeded (Orr et al., 2003). The PEEK femoral component could be implanted using radiolucent cement fixation, and then conditioned in a bath of radiopaque dye penetrant (zinc iodide, for example). This would enable non-destructive 3D visualisation of any interface cracks and separation, using μCT scanning (Mavrogordato et al., 2009). As such, the progress of failure at the cement interface could also be monitored using μCT and dynamic loading conditions. The mechanical integrity of the construct could also be compromised by the fatigue of bone cement itself, leading to interfacial debonding and implant loosening. Hence, the fatigue performance of the implant construct under environmental conditions should also be studied (Lewis, 2003; Zelle et al., 2011a).

Considering the strain analysis of the TKR construct, the DIC technique should be repeated using paired cadavers (right and left from the same donor) for a fairer comparative study of the influence of implant material on bone surface strain. This would allow statistical analysis of the results, as well as tests at multiple flexion angles to assess the strain distribution under specific load cases of interest, such as squatting. A more representative contact area could be obtained in the intact case by taking a moulding of the distal femoral articular surface geometry, in the absence of the tibia. If tibias were obtained for a femur pair, then it would be possible to compare the difference in surface strain distribution of the intact femur when loaded using the tibial component or the femoral articular surface moulding, to that obtained with the natural tibia geometry. A positive agreement between the two methods, validating the use of the simpler femur moulding approach, would support a larger population study by conserving the cost of tibias.

To assess further the mechanical integrity of the TKR construct, the DVC analysis technique may now be transferred to local tomography μCT scans of bone cement within the full construct, for measurement of strain across the implant-cement-bone interface. A scan resolution < 6 μm should be used to capture the radiopacifier particle pattern within the volume, and avoid partial volume effects from smaller particles which cannot be resolved. If the space limitations within the μCT scanner prevent this, DVC analysis could be possible with a coarser scan resolution if a radiolucent cement fixation doped with larger diameter (minimum $\sim 50\ \mu$m) ceramic marker beads is used. In any case, the scan protocol in Chapter 6 must be repeated prior to *in situ* loaded scans, to assess the strain resolution and accuracy with a local tomography scan setup. Care must be taken to assess the effect of local tomography CT artefacts, which could degrade the correlation values obtained using DVC, and the resulting noise and bias values in the strain analysis.

Finally, a new investigation of interfacial strain within the PEEK TKR construct is proposed using FBG sensors (see section 2.6.2.2). This technique was outside the remit of this work, but showed great potential for real-time measurement of temperature and strain during cement curing, as well as during loaded construct tests (Ramos et al., 2012; Reikeras et al., 2011). Strain distribution would be mapped through the use of multiple fibres with FBGs across the PEEK and bone fixation surfaces. In addition, there is potential for FBGs to be used with loaded *in situ* μCT scans of a cadaveric or biomechanical Sawbone TKR construct specimen for validation of DVC measurements.

Clinical experience has shown that poor performance in joint replacements is frequently linked to an *in vivo* failure mode that was not predicted or tested, or preclinical testing methods that did not successfully represent the *in vivo* conditions (Steele et al., 2011). The work presented in this thesis, extended according to this suggested further work, should enable pre-clinical test methods to provide a closer representation of the unique response of polymeric orthopaedic implants to the experienced *in vivo* conditions. This would support future polymer orthopaedic implant developments by ensuring more robust pre-clinical analysis.

Bibliography

R. B. Abu-Rajab, W. S. Watson, J. Walker, S. J. Gallacher, and R. M. D. Meek. Peri-prosthetic bone mineral density after total knee arthroplasty. *J Bone Joint Surg (Br)*, 88B:606–613, 2006.

R. D. Adams and R. G. H. Davies. *The Mechanics of Adhesion*, chapter 4, pages 111–144. Elsevier, 2002.

A. Ajovalasit, L. DAcquisto, S. Fragapane, and B. Zuccarello. Stiffness and reinforcement effect of electrical resistance strain gauges. *Strain*, 43:299–305, 2007.

E. Al-Fakir, N. A. A. Osman, and F. R. M. Adikan. The use of fiber Bragg grating sensors in biomechanics and rehabilitation applications: The state-of-the-art and ongoing research topics. *Sensors*, 12:12890–12926, 2012.

B. M. Alice, A. Stephane, S. Jr. Yoshisama, H. Pierre, S. Domizo, M. Hermes, and T. Katia. Evolution of knee kinematics three months after total knee replacement. *Gait and Posture*, 41:624–629, 2015.

Y. H. An and R. A. Draughn, editors. *Mechanical testing of bone and the bone-implant interface.* CRC Press LLC, 2000.

T. L. Anderson. *Fracture Mechanics, Fundamentals and Applications.* Taylor and Francis Group LLC, 2005.

M. J. Archibeck, J. J. Jacobs, K. A. Roebuck, and T. T. Glant. The basic science of periprosthetic osteolysis. *J. Bone Joint Surg Am.*, 82-A:1478–1489, 2000.

C. T. C. Arsene and B. Gabrys. Probabilistic finite element predictions of the human lower limb model in total knee replacement. *Medical Engineering & Physics*, 35:1116 1132, 2013.

Arthritis Research UK Ltd. Registered charity no. 207711, Total Knee Replacement. 2012. URL `http://www.arthritisresearchuk.org/`. date accessed: 11/06/2012.

S. Asada, S. Mori, T. Matsushita, K. Hashimoto, S. Inoue, and M. Akagi. Influence of the sagittal reference axis on the femoral component size. *The Journal of Arthroplasty*, 28:943–949, 2013.

ASTM International Standard E1441. Standard guide for computed tomography (CT) imaging, 2000.

F. Awaja, S. Zhang, N. James, and D. R. McKenzie. Enhanced autohesive bonding of polyetheretherketone (peek) for biomedical applications using a methane/oxygen plasma treatment. *Plasma Processes and Polymers*, 7(12):1010–1021, 2010.

V. Bacova and D. Draganovska. Analyses of the quality of blasted surfaces. *Materials Science*, 40: 125–131, 2004.

M. T. Bah, A. Dickinson, and M. Browne. Finite element analysis of the effects of bone cement Young's modulus and thickness on the performance of a PEEK total knee arthroplasty (TKA) femoral component. Technical report, University of Southampton, 2012. Internal Test Report.

G. Baschek, G. Hartwig, and F. Zahradnik. Effect of water absorption in polymers at low and high temperatures. *Polymer*, 40:3433–3441, 1999.

B. Basgorenay, K. Ulubayram, K. Serbetci, E. Onurhan, and N. Hasirci. Preparation, modification, and characterization of acrylic cements. *Journal of Applied Polymer Science*, 99:3631–3637, 2006.

B. K. Bay, T. S. Smith, D. P. Fyhrie, and M. Saad. Digital volume correlation: Three-dimensional strain mapping using x-ray tomography. *Experimental Mechanics*, 39:217–226, 1999.

J. Beckmann, C. Luring, R. Springorum, F. X. Kock, J. Grifka, and M. Tingart. Fixation of revision TKA: a review of the literature. *Knee Surgery Sports Traumatology Arthroscopy*, 19(6):872–879, 2011. Beckmann, J. Luering, C. Springorum, R. Koeck, F. X. Grifka, J. Tingart, M.

J. Bellemans, H. Vandenneucker, and J. Vanlauwe. Mini symposium: Surgery for knee arthritis (iv) Total knee replacement. *Current Orthopaedics*, 19(6):446–452, 2005.

P. P. Benham, R. J. Crawford, and C. G. Armstrong. *Mechanics of Engineering Materials*, volume Chapter 6. Pearson, 1987.

S. J. Bennett, K. L. Devries, and M. L. Williams. Adhesive fracture mechanics. *International Journal of Fracture*, 10(1):33–43, 1974.

G. Bergmann, A. Bender, F. Graichen, J. Dymke, A. Rohlmann, A. Trepczynski, M. O. Heller, and I. Kutzner. Standardized loads acting in knee implants. *PLoS ONE*, 9(1), 2014a.

G. Bergmann, A. Bender, F. Graichen, J. Dymke, A. Rohlmann, A. Trepczynski, M. O. Heller, and I. Kutzner. Standard loads knee joint, 2014b. URL `http://www.orthoload.com/test-loads/standard-loads-knee-joint/`. date accessed: 31/07/2015.

M. Bessho, I. Ohnishi, J. Matsuyama, T. Matsumoto, K. Imai, and K. Nakamura. Prediction of strength and strain of the proximal femur by a CT-based finite element method. *Journal of Biomechanics*, 40:17451753, 2007.

N. Bhatnagar, S. Jha, S. Bhowmik, G. Gupta, J. B. Moon, and C. G. Kim. Physico chemical characteristics of high performance polymer modified by low and atmospheric pressure plasma. *Surface Engineering and Applied Electrochemistry*, 48(2):117–126, 2012.

B. Bhusan, A. G. Peressadko, and T.-W. Kim. Adhesion analysis of two-level hierarchical morphology in natural attachment systems for 'smart ahesion'. *Journal of Adhesion Science and Technology*, 20: 1475–1491, 2006.

A. Bismarck, M. Hofmeier, and G. Dorner. Effect of hot water immersion on the performance of carbon reinforced unidirectional poly(ether ether ketone) (PEEK) composites: Stress rupture under end-loaded bending. *Composites: Part A*, 38:407–426, 2007.

J. Black and G. Hastings, editors. *Handbook of Biomaterial Properties.* Chapman and Hall, UK, 1998.

F. Blais. Review of 20 years of range sensor development. *Journal of Electronic Imaging*, 13:231–243, 2004.

G. W. Blunn, A. B. Joshi, R. J. Minns, L. Lidgren, P. Lilley, L. Ryd, E. Engelbrecht, and P. S. Walker. Wear in retrieved condylar knee arthroplasties - a comparison of wear in different designs of 280 retrieved condylar knee prostheses. *Journal of Arthroplasty*, 12(3):281–290, 1997.

F. Boas and D. Fleischmann. CT artifacts: Causes and reduction techniques. *Imaging Med.*, 4(2): 229–240, 2012.

E. Boinard, R. A. Pethrick, and C. J. MacFarlane. The influence of thermal history on the dynamic mechanical and dielectric studies of polyetheretherketone exposed to water and brine. *Polymer*, 41: 1063–1076, 2000.

P. J. Boltryk, M. Hill, J. W. McBride, and A. Nasce. A comparison of precision optical displacement sensors for the 3d measurement of complex surface profiles. *Sensors and Actuators A*, 142:2–11, 2008.

R. B. Bourne and J. B. Finlay. The influence of tibial component intramedullary stems and implant-cortex contact on the strain distribution of the proximal tibia following total knee arthroplasty. an in vitro study. *Clinical Orthopaedics and Related Research*, 208:95–99, 1986.

Gary W. Bradley, Michael A. R. Freeman, Michael A. Tuke, and Harry A. McKellop. Evaluation of wear in an all-polymer total knee replacement: Part 2. clinical evaluation of wear in a polyethylene on polyacetal total knee. *Clinical Materials*, 14(2):127–132, 1993.

M. L. Brandi. Microstructure, the key to bone quality. *Rheumatology*, 48:iv3–iv8, 2009.

D. Briem, S. Strametz, K. Schroder, N. M. Meenen, W. Lehmann, W. Linhart, A. Ohl, and J. M. Rueger. Response of primary fibroblasts and osteoblasts to plasma treated polyetheretherketone (PEEK) surfaces. *Journal of Materials Science-Materials in Medicine*, 16(7):671–677, 2005.

A. Briscoe. *Characterisation and computational modelling of acrylic bone cement polymerisation*. PhD thesis, University of Southampton, School of Engineering Sciences, 2006.

J. R. Britton, C. G. Lyons, and P. J. Prendergast. Measurement of the relative motion between an implant and bone under cyclic loading. *Strain*, 40:193–202, 2004.

H. R. Brown. The adhesion between polymers. *Annual Review of Materials Science*, 21:463–489, 1991.

H. R. Brown. The adhesion of polymers: Relations between properties of polymer chains and interface toughness. *Journal of Adhesion*, 82(10):1013–1032, 2006. Times Cited: 7 29th Annual Meeting of the Adhesion-Society Feb 19-22, 2006 Jacksonville, FL Adhes Soc.

T. Brown, Q.-B. Bao, C. M. Agrawal, and N. J. Hallab. An in vitro assessment of wear particulate generated from nubac: A peek-on-peek articulating nucleus replacement device. *Spine*, 36(26): E1675–E1685, 2011.

T. Brynk, A. Laptiev, O. Tolochyn, and Z. Pakiela. The method of fracture toughness measurement of brittle materials by means of high speed camera and dic. *Computational Materials Science*, 64(0): 221–224, 2012. 0927-0256.

BS EN ISO 4288. Geometric product specification (GPS) - surface texture - profile method: Rules and procedures for the assessment of surface texture, 1998.

BS ISO 14243-1. Implants for surgery - wear of total knee-joint prostheses - part 3: loading and displacement parameters for wear-testing machines with displacement control and corresponding environmental conditions for test, 2009.

E. Budyn, J. Jonvaux, and T. Hoc. Digitial image correlation of bone sequential microscopic observations. *International Journal for Numerical Methods in Biomedical Engineering*, 28:815–837, 2012.

A. M. J. Bull, O. Kessler, M. Alam, and A. A. Amis. Changes in knee kinematics reflect the articular geometry after arthroplasty. *Clinical Orthopaedics and Related Research*, 466:2491–2499, 2008.

T. A. Burgers, J. Mason, G. Niebur, and H. L. Ploeg. Compressive properties of trabecular bone in the distal femur. *Journal of Biomechanics*, 41(5):1077–1085, 2008.

W. D. Callister. *Material science and engineering: an introduction.* John Wiley and Sons Inc, 4th edition edition, 1997.

B. C. Carr and T. Goswami. Knee implants - Review of models and biomechanics. *Materials & Design*, 30(2):398–413, 2009.

A. Carriero, A. Abela, A. A. Pitsillides, and S. J. Shefelbine. Ex vivo determination of bone tissue strains for an in vivo mouse tibial loading model. *Journal of Biomechanics*, 47(10):2490–2497, 2014.

C. Chaichankul, A. Tanavalee, and P. Itiravivong. Anthropometric measurements of knee joints in thai population: Correlation to the sizing of current knee prostheses. *Knee*, 18(1):5–10, 2011.

M. Chandler, R. S. Z. Kowalski, N. D. Watkins, A. Briscoe, and A. M. R. New. Cementing techniques in hip resurfacing. *Proc. IMechE Part H: J. Engineering in Medicine*, 220:321–331, 2006.

M. J. Chang, H. Lim, and Y. W. Moon. Diagnosis, causes and treatments of instability following total knee arthroplasty. *Knee Surgery and Related Research*, 26(2):61–67, 2014.

C.-R. Chen and Y.-W. Mai. Comparison of cohesive zone model and linear elastic fracture mechanics for a mode i crack near a compliant/stiff interface. *Engineering Fracture Mechanics*, 77:3408–3417, 2010.

F. Chen, X. Chen, X. Xie, X. Feng, and L. Yang. Full-field 3d measurement using multi-camera digital image correlation system. *Optics and Lasers in Engineering*, 51(9):1044–1052, 2013.

K.-C. Chuang and C.-C. Ma. Pointwise fiber Bragg grating displacement sensor system for dynamic measurements. *Applied Optics*, 47(20):3561–3567, 2008.

L. Claes, S. Fiedler, M. Ohnmacht, and G. N. Duda. Initial stability of fully and partially cemented femoral stems. *Clinical Biomechanics*, 15:750–755, 2000.

B. Clarke. Normal bone anatomy and physiology. *Clinical Journal of the American Society of Nephrology*, 3:S131–S139, 2008.

J. Cognard. Some recent progress in adhesion technology and science. *C. R. Chimie*, 9:13–24, 2006.

A. J. Comer, K. B. Katnam, W. F. Stanley, and T. M. Young. Characterising the behaviour of composite single lap bonded joints using digital image correlation. *International Journal of Adhesion and Adhesives*, 40(0):215–223, 2013. 0143-7496.

A. Completo, J. A. Simoes, and F. Fonseca. Experimental evaluation of strain shielding in distal femur in revision tka. *Experimental Mechanics*, 48:817–824, 2008.

J. Comyn, L. Mascia, and G. Xiao. Plasma-treatment of polyetheretherketone (peek) for adhesive bonding. *Journal of Adhesion and Adhesives*, 16:97–104, 1996.

R. Cowie, A. Briscoe, J. Fisher, and L. Jennings. Influence of lubricant and temperature on the wear of uhmwpe articulating against peek optima. In *International Society for Technology in Arthoplasty Conference, September 24-27th, Kyoto, Japan*, 2014a.

R. M. Cowie, A. Briscoe, J. Fisher, and L. Jennings. The influence of lubricant temperature on the wear of uhmwpe articulating against peek. In *ORS 2014 Annual Meeting, March 15-18th, New Orleans, LA, USA*, 2014b. Poster 0932.

G. Crammond, S. W. Boyd, and J. M. Dulieu-Barton. Speckle pattern quality assessment for digital image correlation. *Optics and Lasers in Engineering*, 51(12):1368–1378, 2013.

L. Cristofolini and M. Viceconti. Comparison of uniaxial and triaxial rosette gages for strain measurement in the femur. *Experimental Mechanics*, 37(3):350–354, 1997.

L. Cristofolini, S. Affatato, P. Erani, W. Leardini, D. Tigani, and M. Viceconti. Long-term implant-bone fixation of the femoral component in total knee replacement. *Proceedings of the Institution of Mechanical Engineers Part H-Journal of Engineering in Medicine*, 222(H3):319–331, 2008.

L. Cyganik, M. Binkowski, G. Kokot, T. Rusin, P. Popik, F. Bolechaa, R. Nowak, Z. Wrbel, and A. John. Prediction of youngs modulus of trabeculae in microscale using macro-scales relationships between bone density and mechanical properties. *Journal of the Mechanical Behavior of Biomedical Materials*, 36(0):120–134, 2014.

E. Dall'Ara, D. Barber, and M. Viceconti. About the inevitable compromise between spatial resolution and accuracy of strain measurement for bone tissue: A 3D zero-strain study. *Journal of Biomechanics*, 47:2956–2963, 2014.

A. D'Amore, A. Pompo, and L. Nicolais. Viscoelastic effects in poly(ether ether ketone) (PEEK) and peek-based composites. *Composites Science and Technology*, 41(3):303–325, 1991.

S. M. Darwish and A. Al-Samhan. The effect of cement stiffness and tibia tray material on the stresses developed in artificial knee. *International Journal of Adhesion and Adhesives*, 28(3):120–125, 2008.

J R Davis, editor. *Handbook of materials for medical devices.* ASM International, 2003.

M. S. DeMers, S. Pal, and S. L. Delp. Changes in tibiofemoral forces due to variations in muscle activity during walking. *Journal of Orthopaedic Research*, 32:769–776, 2014.

C. R. Dennison, P. M. Wild, D. R. Wilson, and M. K. Gilbart. An in-fiber Bragg grating sensor for contact force and stress measurements in articular joints. *Measurement Science and Technology*, 21, 2010.

C. K. Desai, S. Basu, and V. Parameswaran. Determination of complex stress intensity factor for a crack in a bimaterial interface using digital image correlation. *Optics and Lasers in Engineering*, 50 (10):1423–1430, 2012.

K. L. Devries and D. O. Adams. *The Mechanics of Adhesion*, chapter 6, pages 193–234. Elsevier, 2002.

A. S. Dickinson. Activity and loading influence the predicted bone remodeling around cemented hip replacements. *Journal of Biomechanical Engineering*, 136, 2014.

A. S. Dickinson, A. C. Taylor, H. Ozturk, and M. Browne. Experimental validation of a finite element model of the proximal femur using digital image correlation and a composite bone model. *Journal of Biomechanical Engineering*, 133, 2011.

A. S. Dickinson, A. C. Taylor, and M. Browne. The influence of acetabular cup material on pelvis cortex surface strains, measured using digital image correlation. *Journal of Biomechanics*, 45(4): 719–23, 2012.

V.N. Dubey. Photoelastic stress analysis. *Modern Stress and Strain Analysis*, pages 10–11, 2009. Published by Eureka Magazine.

N. J. Dunne and J. F. Orr. Influence of mixing techniques on the physical properties of acrylic bone cement. *Biomaterials*, 22:1819–1826, 2001.

N. J. Dunne and J. F. Orr. Curing characteristics of acrylic bone cement. *Journal of Materials Science: Materials in Medicine*, 13:17–22, 2002.

N. J. Dunne, J. F. Orr, M. T. Mushipe, and R. J. Eveleigh. The relationship between porosity and fatigue characteristics of bone cements. *Biomaterials*, 24:239–245, 2003.

J. Eaton-Evans. Thermoelastic stress analysis. *Modern Stress and Strain Analysis*, pages 18–19, 2009.

O. Ethgen, O. Bruyere, F. Richy, C. Dardennes, and J. Y. Reginster. Health-related quality of life in total hip and total knee arthroplasty - a qualitative and systematic review of the literature. *Journal of Bone and Joint Surgery-American Volume*, 86A(5):963–974, 2004.

A. Faridani, K. A. Buglione, P. Huabsomboon, O. D. Iancu, and J. McGrath. Introduction to local tomography. In *Contemporary Mathematics*, volume 278, pages 29–47. Radon Transforms and Tomography: 2000 AMS-IMS-SIAM Joint Summer Research Conference on Radon Transforms and Tomography, Mount Holyoke College, South Hadley, Massachusetts, USA, June 18-22, 2000, 2001.

R. E. Field. Clinical trials of the mitch cup. In *1st International PEEK Meeting, Philadelphia, PA, USA*, April 2013.

M. A. R. Freeman, G. W. Bradley, and P. A. Revell. Observations upon the interface between bone and polymethylmethacrylate cement. *Journal of Bone and Joint Surgery - British Volume*, 64-B(4): 489–493, 1982.

B. J. Fregly, D. D. D'Lima, and C. W. Colwell Jr. Effective gait patterns for offloading the medial compartment of the knee. *Journal of Orthopaedic Research*, 27:1061–1021, 2009.

H. M. Frost. Bone's mechanostat: A 2003 update. *Anatomical Record Part a-Discoveries in Molecular Cellular and Evolutionary Biology*, 275A(2):1081–1101, 2003.

J. Fu, F. Pierron, and P. D. Ruiz. Elastic stiffness characterization using three-dimensional full-field deformation obtained with optical coherence tomography and digital volume correlation. *Journal of Biomedical Optics*, 18(12):121512, 2013.

M. J. Funk and A. S. Litsky. Effect of cement modulus on the shear properties of the bone-cement interface. *Biomaterials*, 19:1561–1567, 1998.

M. Gates, J. Lambros, and M. T. Heath. Towards high performance digital volume correlation. *Experimental Mechanics*, 51:491–507, 2011.

R. Ghosh, S. Gupta, A. Dickinson, and M. Browne. Experimental validation of finite element models of intact and implant composite hemi-pelvises using digital image correlation. *Journal of Biomechanical Engineering*, 134, 2012a.

R. Ghosh, S. Gupta, A. S. Dickinson, and M. Browne. Verification of the digital image correlation technique for bone surface strain measurements. *Journal of Biomechanics*, 45 supp.1:S277, 2012b.

S. Gilchrist and P. A. Guy, P. annd Cripton. Development of an inertia-driven model of sideways fall for detailed study of femur fracture mechanics. *Journal of Biomechanical Engineering*, 135, 2013.

F. Gillard, Boardman R., M. Mavrogordato, D. Hollis, I. Sinclair, F. Pierron, and M. Browne. The application of digital volume correlation (DVC) to study the microstructural behaviour of trabecular bone during compression. *Journal of the Mechanical Behavior of Biomedical Materials*, 29:480–499, 2014.

T. J. Gioe and A. V. Maheshwari. The all-polyethylene tibial component in primary total knee arthroplasty. *Journal of Bone and Joint Surgery-American Volume*, 92A(2):478–487, 2010.

A. Godara, D. Raabe, and S. Green. The influence of sterilization processes on the micromechanical properties of carbon fiber-reinforced PEEK composites for bone implant applications. *Acta Biomaterialia*, 3:209–220, 2007.

J. Goodfellow and J. O'Connor. Mechanics of knee and prosthesis design. *Journal of Bone and Joint Surgery-British Volume*, 60(3):358–369, 1978.

S. B. Goodman, E. Gibon, and Z. Yao. The basic science of periprosthetic osteolysis. *Instr Course Lect.*, 62:201–206, 2013.

P. Grant and C. Q. Rousseau. *Composite Structures: Theory and Practice, Issue 1383.* ASTM International, 2001.

L. Grassi, S. P. Vaananen, S. A. Yavari, H. Weinans, J. S. Jurvelin, A. A. Zadpoor, and H. Isaksson. Experimental validation of finite element model for proximal composite femur using optical measurements. *Journal of the Mechanical Behavior of Biomedical Materials*, 21:86–94, 2013.

L. Grassi, S. P. Vaananen, S. A. Yavari, J. S. Jurvelin, H. Weinans, M. Ristinmaa, A. A. Zadpoor, and H. Isaksson. Full-field strain measurement during mechanical testing of the human femur at physiologically relevant strain rates. *Journal of Biomechanical Engineering-Transactions of the Asme*, 136(11), 2014.

W Grellmann and S Seidler. *Deformation and Fracture Behaviour of Polymers.* Springer, 2001.

T. M. Grupp, S. Utzschneider, C. Schroeder, J. Schwiesau, B. Fritz, A. Maas, W. Bloemer, and V. Jansson. Biotribology of alternative bearing materials for unicompartmental knee arthroplasty. *Acta Biomaterialia*, 6(9):3601–3610, 2010.

S. Gungor. Moire interferometry. *Modern Stress and Strain Analysis*, pages 8–9, 2009. Published by Eureka Magazine.

S. P. Guy, M. A. Farndon, S. Sidhom, M. Al-Lami, C. Bennett, and N. J. London. Gender differences in distal femoral morphology and the role of gender specific implants in total knee replacement: A prospective clinical study. *The Knee*, 19(1):28–31, 2012.

S. W. Ha, A. Gisep, J. Mayer, E. Wintermantel, H. Gruner, and M. Wieland. Topographical characterization and microstructural interface analysis of vacuum-plasma-sprayed titanium and hydroxyapatite coatings on carbon fibre-reinforced poly(etheretherketone). *Journal of Materials Science-Materials in Medicine*, 8(12):891–896, 1997.

N. J. Hallab, K. McAllister, M. Brady, and M. Jarman-Smith. Macrophage reactivity to different polymers demonstrates particle size- and material-specific reactivity: PEEK-OPTIMA (R) particles versus UHMWPE particles in the submicron, micron, and 10 micron size ranges. *Journal of Biomedical Materials Research Part B-Applied Biomaterials*, 100B(2):480–492, 2012. 1552-4973.

L. Hallmann, A. Mehl, N. Sereno, and H.F. Hammerlem. The improvement of adhesive properties of peek through different pre-treatments. *Applied Surface Science*, 258:7213–7218, 2012.

C.-M. Han, E.-J. Lee, H.-E. Kim, Y.-H. Koh, K. N. Kim, Y. Ha, and S.-U. Kuh. The electron beam deposition of titanium on polyetheretherketone (PEEK) and the resulting enhanced biological properties. *Biomaterials*, 31(13):3465–3470, 2010.

M. R. Hardisty and C. M. Whyne. Whole bone strain quantification by image registration: A validation study. *Journal of Biomechanical Engineering*, 131, 2009.

A. P. Harsha, U. S. Tewari, and B. Venkatraman. Three-body abrasive wear behaviour of polyaryletherketone composites. *Wear*, 254:680–692, 2003.

C. M. Haydon, R. Mehin, S. Burnett, C. H. Rorabeck, R. B. Bourne, R. W. McCalden, and S. J. MacDonald. Revision total hip arthroplasty with use of a cemented femoral component. results at a mean of ten years. *J Bone Joint Surg Am.*, 86:1179–1185, 2004.

B. Helgason, S. Gilchrist, O. Ariza, J. D. Chak, G. Zheng, R. P. Widmer, S. J. Ferguson, P. Guy, and P. A. Cripton. Development of a balanced experimental-computational approach to understaunder the mechanics of proximal femur fractures. *Medical Engineering & Physics*, 36:793–799, 2014.

P. R. Hinton, C. Brownlow, I. McMurray, and B. Cozens. *SPSS Explained*. London : Routledge, 2004.

K. Hitt, J. R. Shurman, K. Greene, J. McCarthy, J. Moskal, T. Hoeman, and M. A. Mont. Anthropometric measurements of the human knee: Correlation to the sizing of current knee arthroplasty systems. *Journal of Bone and Joint Surgery-American Volume*, 85A:115–122, 2003. 4 70th Annual Meeting of the American-Academy-of-Orthopaedic-Surgeons Feb 05-09, 2003 New orleans, louisiana Amer Acad Orthopaedic Surg.

W. P. Ho, C. K. Cheng, and H. J. Liau. Morphometrical measurements of resected surface of femurs in chinese knees: Correlation to the sizing of current femoral implants. *Knee*, 13(1):12–14, 2006. 0968-0160.

D. Hoey and D. Taylor. Quantitive analysis of the effect of porosity on the fatigue strength of bone cement. *Acta Biomaterialia*, 5:719–726, 2009.

J. Horta, W. Brostow, G. Martinez, and V. M. Castano. Characterisation of bones by speckle interferometry. *Journal of Medical Engineering and Technology*, 27:49–53, 2003.

C. H. Huang, H. M. Ma, J. J. Liau, F. Y. Ho, C. K. Cheng, Kevin Lee, and Stuart B. Goodman. Current state and future of joint replacements in the hip and knee. *Journal of Bone and Joint Surgery-American Volume*, 5(3):383–393, 2008.

R. Huiskes, H. Weinans, H. J. Grootenboer, M. Dalstra, B. Fudla, and T. J. Slooff. Adaptive bone-remodeling theory applied to prosthetic-design analysis. *Journal of Biomechanics*, 20: 1135–1150, 1987.

R. Huiskes, H. Weinans, and M. Dalstra. Adaptive bone remodeling and biomechanical design considerations. *Orthopedics*, 12(9):1255–1267, 1989.

J.-P. Hung and F.-C. Chang. Computational modeling of debonding behavior at the bone/cement interface with experimental validation. *Materials Science & Engineering C-Materials for Biological Applications*, 30(3):445–453, 2010.

D. E. Hurwitz, D. R. Sumner, T. P. Andriacchi, and D. A. Sugar. Dynamic knee loads during gait predict proximal tibial bone distribution. *Journal of Biomechanics*, 31:423–430, 1998.

A. I. Hussein, P. E. Barbone, and E. F. Morgan. Digital volume correlation for study of the mechanics of whole bones. *Procedia IUTAM.*, 4:116–125, 2012.

S. J. Incavo, K. M. Coughlin, and B. D. Beynnon. Femoral component sizing in total knee arthroplasty. *The Journal of Arthroplasty*, 19(4):493–497, 2004.

M. Iodice, V. Striano, G. Cappuccino, and G. Cocorullo. Fiber Bragg grating sensors-based system for strain measurements. In *Proceedings of 2005 IEEE/LEOS Workshop on Fibres and Optical Passive Components*, June 2005.

H. M. S. Iqbal, S. Bhowmik, and R. Benedictus. Surface modification of high performance polymers by atmospheric pressure plasma and failure mechanism of adhesive bonded joint. *International Journal of Adhesion and Adhesives*, 30:418424, 2010.

Istituto Ortopedico Rizzoli. *Bonemat*. Via Di Barbiano, 1/10 - 40136 Bologna, Italy, 2007. URL `http://www.bonemat.org`. date accessed: 14/07/2015.

V. Janarthanan, P. D. Garrett, R. S. Stein, and M. Srinivasarao. Adhesion enhancement in immiscible polymer bilayer using oriented macroscopic roughness. *Polymer*, 38(1):105–111, 1997.

J. Jarvenpaa, T. Soininvaara, J. Kettunen, H. Miettinen, and H. Kroger. Changes in bone mineral density of the distal femur after total knee arthroplasty: A 7-year dexa follow-up comparing results between obese and nonobese patients. *The Knee*, 21:232235, 2014.

S. Jha, S. Bhowmik, N. Bhatnagar, N. K. Bhattacharya, U. Deka, H. M. S. Iqbal, and R. Benedictus. Experimental investigation into the effect of adhesion properties of peek modified by atmospheric pressure plasma and low pressure plasma. *Journal of Applied Polymer Science*, 118:173–179, 2010.

L.-H. Kang, D.-K. Kim, and J.-H. Han. Estimation of dynamic structural displacements using fiber Bragg grating strain sensors. *Journal of Sound and Vibration*, 305:534–542, 2007.

S. L. Kaplan and P. W. Rose. Plasma surface treatment of plastics to enhance adhesion. *International Journal of Adhesion and Adhesives*, 11:109–113, 1991.

A. Karbowski, M. Schwitalle, A. Eckardt, and J. Heine. Periprosthetic bone remodelling after total knee arthroplasty: early assessment by dual energy x-ray absorptiometry. *Arch Orthop Trauma Surg*, 119:324326, 1999.

A. Katzer, H. Marquardt, J. Westendorf, J. V. Wening, and G. von Foerster. Polyetheretherketone - cytotoxicity and mutagenicity in vitro. *Biomaterials*, 23(8):1749–1759, 2002.

S. Kawahara, S. Matsuda, S. Fukagawa, H. Mitsuyasu, H. Nakahara, H. Higaki, T. Shimoto, and Y. Iwamoto. Upsizing the femoral component increases patellofemoral contact force in total knee replacement. *Journal of Bone and Joint Surgery - British Volume*, 94B:56–61, 2012.

D. J. Kemmish, S. Schubert, and K. Schlufter. *Practical Guide to High Performance Engineering Plastics*. Smithers Rapra, 2011.

W. S. Kim, I. H. Yun, J. J. Lee, and H. T. Jung. Evaluation of mechanical interlock effect on adhesion strength of polymer-metal interfaces using micro-patterned surface topography. *International Journal of Adhesion and Adhesives*, 30(6):408–417, 2010. English.

T. V. King and R. D. Scott. Femoral component loosening in total knee arthroplasty. *Clinical Orthopaedics and Related Research*, 194:285–290, 1985.

A. J. Kinloch. Review: The science of adhesion. *Journal of Materials Science*, 15:2141–2166, 1980.

L. A. Knight, S. Pal, J. C. Coleman, F. Bronson, H. Haider, D. Levine, M. Taylor, and P. J. Rullkoetter. Comparison of long-term numerical and experimental total knee replacement wear during simulated gait loading. *Journal of Biomechanics*, 40:1550–1558, 2007.

S. S. Kohles and R. Vanderby. Thermographic strain analysis of the proximal canine femur. *Medical Engineering and Physics*, 19:262–266, 1997.

M. Kopec, J. C. Milbrandt, T. Duellman, D. Mangan, and D. G. Allan. Effect of hand packing versus cement gun pressurization on cement mantle in total knee arthroplasty. *Canadian Journal of Surgery*, 52(6):490–494, 2009.

A. Krishnan and L. R. Xu. Systematic evaluation of bonding strengths and fracture toughnesses of adhesive joints. *Journal of Adhesion*, 87(1):53–71, 2011.

S. M. Kurtz. *PEEK Biomaterials Handbook*. William Andrew, 2011.

S. M. Kurtz and J. N. Devine. PEEK biomaterials in trauma, orthopedic, and spinal implants. *Biomaterials*, 28(32):4845–4869, 2007.

S. M. Kurtz, L. Pruitt, C. W. Jewett, R. P. Crawford, D. J. Crane, and A. A. Edidin. The yielding, plastic flow, and fracture behavior of ultra-high molecular weight polyethylene used in total joint replacements. *Biomaterials*, 19:1989–2003, 1998.

S. M. Kurtz, T. H. Lanman, G. Higgs, D. W. MacDonald, S. H. Berwen, J. E. Isaza, E. Phillips, and M. J. Steinbeck. Retrieval analysis of PEEK rods for posterior fusion and motion preservation. *Eur Spine J*, 22:2752–2759, 2013.

M. S. Kuster, G. A. Wood, G. W. Stachowiak, and A. Gachter. Joint load considerations in total knee replacement. *J Bone Joint Surg (Br)*, 79-B:109–113, 1997.

R. S. LaButti, M. Bayers-Thering, and K. A. Krackow. Enhancing femoral cement fixation in total knee arthroplasty. *The Journal of Arthroplasty*, 18(8):973–983, 2003.

E. N. Landis and D. T. Keane. X-ray microtomography. *Materials Characterization*, 61:1305–1316, 2010.

M. Lane. Interface fracture. *Annual Review of Materials Research*, 33:29–54, 2003.

R. A. Latour. *Encyclopedic Handbook of Biomaterials and Bioengineering: v.1-2 Applications*, chapter 12. Fibre Reinforced Composite Biomaterials, pages 359–382. CRC Press, 1995.

F. Laurin, J. S. Charrier, D. Lvque, J. F. Maire, A. Mavel, and P. Nuez. Determination of the properties of composite materials thanks to digital image correlation measurements. *Procedia IUTAM*, 4(0):106–115, 2012. 2210-9838.

P. J. Laz, S. Pal, A. Fields, A. J. Petrella, and P. J. Rullkoetter. Effects of knee simulator loading and alignment variability on predicted implant mechanics: A probabilistic study. *Journal of Orthopaedic Research*, 24:2212–2221, 2006.

D. Lecompte, A. Smits, Sven Bossuyt, H. Sol, J. Vantomme, D. Van Hemelrijck, and A. M. Habraken. Quality assessment of speckle patterns for digital image correlation. *Optics and Lasers in Engineering*, 44(11):1132–1145, 2006.

P. Lecomte-Grosbras, B. Paluch, M. Brieu, G. De Saxcé, and Laurent Sabatier. Interlaminar shear strain measurement on angle-ply laminate free edge using digital image correlation. *Composites Part*

A: Applied Science and Manufacturing, 40(12):1911–1920, 2009. Interlaminar shear strain measurement on angle-ply laminate free edge using digital image correlation.

K. Lee and S. B. Goodman. Current state and future of joint replacements in the hip and knee. *Expert Review of Medical Devices*, 5(3):383–393, 2008.

G. Lewis. Properties of acrylic bone cement: state of the art review. *Journal of Biomedical Materials Research Part B: Applied Biomaterials*, 38:155–182, 1997.

G. Lewis. Fatigue testing and performance of acrylic bone-cement materials: State-of-the-art review. *Journal of Biomedical Materials Research Part B-Applied Biomaterials*, 66B(1):457–486, 2003.

G. Lewis. Alternative acrylic bone cement formulations for cemented arthroplasties: present status, key issues, and future prospects. *Journal of Biomedical Materials Research Part B: Applied Biomaterials*, 84:301–319, 2008.

G. Lewis, J. Xu, S. Madigan, and M. R. Towler. Influence of two changes in the composition of an acrylic bone cement on its handling, thermal, physical, and mechanical properties. *J Mater Sci: Mater Med*, 18:1649–1658, 2007.

B.-W. Li, H.-P. Zhao, Q.-H. Qin, X.-Q. Feng, and S.-W. Yu. Numerical study on the effects of hierarchical wavy interface morphology on fracture toughness. *Computational Materials Science*, 57: 14–22, 2012.

J. J. Liau, C. K. Cheng, C. H. Huang, and W. H. Lo. The effect of malalignment on stresses in polyethylene component of total knee prostheses a finite element analysis. *Clinical Biomechanics*, pages 140–146, 2002.

N. Limodin, J. Rethore, J. Adrien, J. Y. Buffiere, F. Hild, and S. Roux. Analysis and artifact correction for volume correlation measurements using tomographic images from a laboratory x-ray source. *Experimental Mechanics*, 51:959–970, 2011.

E. M. Liston, L. Martinu, and L. R. Wertheimer. Plasma surface modification of polymers for improved adhesion: a critical review. *Journal of adhesion science and technology*, 7(10):1091–1127, 1993.

L. Liu and E. F. Morgan. Accuracy and precision of digital volume correlation in quantifying displacements and strains in trabecular bone. *Journal of Biomechanics*, 40:3516–3520, 2007.

Q. Liu, T. Y. Wang, X. P. Yang, K. Li, L. L. Gao, C. Q. Zhang, and Y. H. Guo. Strain distribution in the intervertebral disc under unconfined compression and tension load by the optimized digital image correlation technique. *Proc. IMechE Part H: J. Engineering in Medicine*, 228(5):486–493, 2014.

C. S. Lo, S. J. Wang, and S. S. Wu. Knee stiffness on extension caused by an oversized femoral component after total knee arthroplasty. *Journal of Arthroplasty*, 18(6):804–808, 2003.

A. V. Lombardi, K. R. Berend, and J. B. Adams. Management of bone loss in revision TKA: it's a changing world. *Orthopedics*, 33(9):662–662, 2010. ¡Go to ISI¿://MEDLINE:20839684.

J. H. Lonner, J. G. Jasko, and B. S. Thomas. Anthropomorphic differences between the distal femora of men and women. *Clinical Orthopaedics and Related Research*, 466(11):2724–2729, 2008. Open Scientific Meeting of the Knee-Society Mar, 2007 San Francisco, CA Knee Soc.

W. Lowe. Knee anatomy. 2012. URL `http://www.drwaltlowe.com/knee-anatomy/`. date accessed: 01/06/12.

J. Lundskog. Heat and bone tissue. an experimental investigation of the thermal properties of bone and threshold levels for thermal injury. *Scandinavian Journal of Plastic and Reconstructive Surgery*, 9:1–80, 1972.

K. Madi, G. Tozzi, Q. H. Zhang, J. Tong, A. Cossey, A. Au, D. Hollis, and F. Hild. Computation of full-field displacements in a scaffold implant using digital volume correlation and finite element analysis. *Medical Engineering & Physics*, 35:1298–1312, 2013.

M. Mahfouz, E. E. A. Fatah, L. S. Bowers, and G. Scuderi. Three-dimensional morphology of the knee reveals ethnic differences. *Clinical Orthopaedics and Related Research*, 470(1):172–185, 2012. Three-dimensional Morphology of the Knee Reveals Ethnic Differences.

R. A. Malinzak, S. R. Small, R. D. Rogge, D. B. Archer, J. W. Oja, M. E. Berend, and M. A. Ritter. The effect of rotating platform tka on strain distribution and torque transmission on the proximal tibia. *The Journal of Arthroplasty*, 29(3):541–547, 2014.

K. A. Mann, D. C. Ayers, F. W. Werner, R. J. Nicoletta, and M. D. Fortino. Tensile strength of the cement-bone interface depends on the amount of bone interdigitated with pmma cement. *Journal of Biomechanics*, 30(4):339–346, 1997.

K. A. Mann, F. W. Werner, and D. C. Ayers. Mechanical strength of the cement-bone interface is greater in shear than in tension. *Journal of Biomechanics*, 32(11):1251–1254, 1999.

K. A. Mann, M. A. Miller, J. R. Goodheart, T. H. Izant, and R. J. Cleary. Peri-implant bone strains and micro-motion following in vivo service: A postmortem retrieval study of 22 tibial components from total knee replacements. *Journal of Orthopaedic Research*, 32(3):355–361, 2014.

S. J. Marshall, S. C. Bayne, R. Baier, A. P. Tomsia, and G. W. Marshall. A review of adhesion science. *Dental Materials*, 26:e11–116, 2010.

R. B. Martin. Toward a unifying theory of bone remodeling. *Bone*, 26(1):1–6, 2000.

K. Marya, J. S. Dua, S. Chawla, P. R. Sonoo, A. Aggarwal, and V. Singh. Polyetheretherketone (peek) dental implants: A case for immediate loading. *International Journal of Oral Implantology and Clinical Research*, 2(2):97–103, 2011.

M. Mavrogordato, M. Taylor, A. Taylor, and M. Browne. Acoutic emission monitoring and 3d visualisation of polymerisation-induced damage of acrylic polymer materials. *Journall of Biomedical Materials Research*, 90B:223–228, 2009.

Maxx Medical Pvt Ltd. Freedom knee fact sheet. online, September 2013. URL `http://www.maxxmed.com/row/pdf/fact-sheet.pdf`.

N. McCormick and J. Lord. Digital image correlation. *Materials Today*, 13(12):52–54, 2010. 1369-7021.

H. A. McKellop, T. Rostlund, and G. Bradley. Evaluation of wear in an all-polymer total knee replacement: Part 1. laboratory testing of polyethylene on polyacetal bearing surfaces. *Clinical Materials*, 14(2):117–126, 1993.

F. C. McLean and M. R. Urist. *Bone.* The University of Chicago Press, Chicago 60637, 3rd edition, 1968.

S. Moaveni. *Finite Element Analysis: Theory and Application with ANSYS.* Pearson Education Inc, New Jersey, USA, 3rd edition, 2008.

K. M. Moerman, C. A. Holt, S. L. Evans, and C. K. Simms. Digital image correlation and finite element modelling as a method to determine mechanical properties of human soft tissue in vivo. *Journal of Biomechanics*, 42(8):1150–1153, 2009.

L. Mohanty, S. C. Tijin, D. T. T. Lie, S. E. C. Panganiban, and P. K. H. Chow. Fiber grating sensor for pressure mapping during total knee arthroplasty. *Sensors and Actuators, A*, 7:323–328, 2007.

D. C. Montgomery and G. C. Runger. *Applied statistics and probability for engineers.* John Wiley and Sons Inc, 4th edition edition, 2007.

D. J. Moore, M. A. R. Freeman, P. A. Revell, G. W. Bradley, and M. Tuke. Can a total knee replacement prosthesis be made entirely of polymers? *Journal of Arthroplasty*, 13(4):388–395, 1998.

G. Mordan. Electrical resistance strain gauges. *Modern Stress and Strain Analysis*, pages 4–5, 2009. Published by Eureka Magazine.

E. F. Morgan and T. M. Keaveny. Dependence of yield strain of human trabecular bone on anatomic site. *Journal of Biomechanics*, 34:569–577, 2001.

C. Morrison, R. Macnair, C. Macdonald, A. Wykman, I. Goldie, and M. H. Grant. In-vitro biocompatibility testing of polymers for orthopedic implants using cultured fibroblasts and osteoblasts. *Biomaterials*, 16(13):987–992, 1995.

C. Morrison, R. Macnair, C. Macdonald, A. Wykman, I. Goldie, M. H. Grant, J. Y. Rho, L. Kuhn-Spearing, and P. Zioupos. Mechanical properties and the hierarchical structure of bone. *Biomaterials*, 20(2):92–102, 1998.

V. C. Mow and R. Huiskes, editors. *Basic Orthopaedic Biomechanics and Mechanio-Biology.* Lippincott Williams and Wilkins, PA, USA, 2005.

M. Murphy, S. Journeaux, and T. Russell. High-flexion total knee arthroplasty: a systematic review. *International Orthopaedics (SICOT)*, 33:887–893, 2009.

T. Nagura, C. O. Dyrby, E. J. Alexander, and T. P. Andriacchi. Mechanical loads at the knee joint during deep flexion. *Journal of Orthopaedic Research*, 20:881–886, 2002.

K. Narayan, G. Thomas, and R. Kumar. Is extreme flexion of the knee after total knee replacement a prerequisite for patient satisfaction? *International Orthopaedics (SICOT)*, 33:671–674, 2009.

National Joint Registry for England and Wales. 8th Annual Report. Technical report, NJR Centre, 2011.

National Joint Registry for England, Wales and Northern Ireland. 10th Annual Report. Technical report, NJR Centre, 2013.

M. Navarro, A. Michiardi, O. Castano, and J. A. Planell. Biomaterials in orthopaedics. *J. R. Soc. Interface*, 5:1137–1158, 2008.

D Neut, O S Kluin, J Thompson, H C van der Mei, and H J Busscher. Gentamicin release from commercially-available gentamicin-loaded pmma bone cements in a prosthesis-related interfacial gap model and their antibacterial efficacy. *BMC Muscoskeletal Disorders*, 11, 2010.

T. L. Nguyen, S. A. Hall, P. Vacher, and G. Viggiani. Fracture mechanisms in soft rock: Identification and quantification of evolving displacement discontinuities by extended digital image correlation. *Tectonophysics*, 503:117–128, 2011.

T. Nieminen, I. Kallela, E. Wuolijoki, H. Kainulainen, I. Hiidenheimo, and I. Rantala. Amorphous and crystalline polyetheretherketone: mechanical properties and tissue reactions during a 3-year follow-up. *Journal of Biomedical Materials Research Part A*, 84A(2):377–383, 2008.

J. F. Orr, N. J. Dunne, and J. C. Quinn. Shrinkage stresses in bone cement. *Biomaterials*, 24(17): 2933–2940, 2003.

D. E. Packham. *Surfaces, Chemistry and Applications*, chapter 7, pages 317–349. Elsevier, 2002.

D. E. Packham. Surface energy, surface topography and adhesion. *International Journal of Adhesion and Adhesives*, 23(6):437–448, 2003.

M. Palanca, G. Tozzi, L. Cristofolini, M. Viceconti, and E. Dall'Ara. Three-dimensional local measurements of bone strain and displacement: Comparison of three digital volume correlation approaches. *Journal of Biome*, 137, 2015.

G. Panegrossi, M. Ceretti, and M. and Papalia. Bone loss management in total knee revision surgery. *International Orthopaedics (SICOT)*, 38:419–427, 2014.

J. W. Park and Y. H. Kim. Simultaneous cemented and cementless total knee replacement in the same patients a prospective comparison of long-term outcomes using an identical design of nexgen prosthesis. *Journal of Bone and Joint Surgery-British Volume*, 93B(11):1479–1486, 2011.

S. Pickering and D. Armstrong. Alignment in total knee replacement. *The Bone and Joint Journal*, 2013. URL `www.boneandjoint.org.uk/content/focus/alignment-total-knee-replacement`.

F. Pierron. Digital speckle pattern interferometry. *Modern Stress and Strain Analysis*, 2009.

G. T. Pittman, C. L. Peters, J. L. Hines, and K. N. Bachus. Mechanical bond strength of the cement-tibial component interface in total knee arthroplasty. *Journal of Arthroplasty*, 21(6): 883–888, 2006.

X. Poulain, L. W. Kohlman, W. Binienda, G. D. Roberts, R. K. Goldberg, and A. A. Benzerga. Determination of the intrinsic behavior of polymers using digital image correlation combined with video-monitored testing. *International Journal of Solids and Structures*, 50:1869–1878, 2013.

A. H. C. Poulsson, D. Eglin, C. Kamenisch, C. Sprecher, Y. Agrawal, D. Nehrbass, S. Zeiter, and R. G. Richards. Investigation into the osseointegration of oxygen plasma modified and unmodified PEEK in a sheep model. In *1st International PEEK Meeting, Philadelphia, April 25-26th, PA, USA*, 2013.

P. J. Prendergast and S. A. Maher. Issues in pre-clinical testing of implants. *Journal of Materials Processing Technology*, 118(1-3):337–342, 2001.

S. G. Prolongo, G. Rosario, and A. Urena. Study of the effect of substrate roughness on adhesive joints by sem image analysis. *Journal of Adhesion Science and Technology*, 20(5):457–470, 2006.

G. Qi, B. Zhang, K. A. Mann, and J. Li. On evaluating the implant interface bonding strength. In *2007 SEM Annual Conference & Exposition on Experimental and Applied Mechanics*, 2007.

P. J. Rae, E. N. Brown, and E. B. Orler. The mechanical properties of poly(ether-ether-ketone) (peek) with emphasis on the large compressive strain response. *Polymer*, 48(2):598–615, 2007.

N. A. Ramaniraka, L. R. Rakotomanana, and P. F. Leyvraz. The fixation of the cemented femoral component - effects of stem stiffness, cement thickness and roughness of the cement-bone surface. *Journal of Bone and Joint Surgery-British Volume*, 82B(2):297–303, 2000.

A. Ramos, M. W. Schiller, I. Abes, and P. A. Lopes. Experimental measurement and numerical validation of bone cement mantle strains of an in vitro hip replacement using optical FBG sensors. *Experimental Mechanics*, 52:1267–1274, 2012.

A. S. Ranawat, S. S. Mohanty, S. E. Goldsmith, V. J. Rasquinha, J. A. Rodriguez, and C. S. Ranawat. Experience with an all-polyethylene total knee arthroplasty in younger, active patients with follow-up from 2 to 11 years. *Journal of Arthroplasty*, 20(7):7–11, 2005. 15th Annual Meeting of the American-Association-of-Hip-and-Knee-Surgeons, Nov 04-06, Dallas, TX.

K. Rankin. Moisture absorption of peek. Technical report, University of Southampton, 2011. Summer Internship Report, Supervised by M. Browne. August.

K. Rankin, M. T. Bah, A. S. Dickinson, I. Sinclair, A. Briscoe, and M. Browne. Characterisation of the fixation of a novel polyetheretherketone implant for total knee replacement. In *1st International PEEK Meeting, Philadelphia, April 25-26th, PA, USA*, 2013.

F. W. Reckling and W. L. Dillon. Bone-cement interface temperature during total joint replacement. *Journal of Bone and Joint Surgery-American Volume*, 59(1):80–82, 1977.

O. Reikeras, G. T. Aarnes, H. Steen, P. Ludvigsen, and G. Sagvolden. Differences in external and internal cortical strain with prosthesis in the femur. *The Open Orthopaedics Journal*, 5:379–384, 2011.

L. Ren, G. Song, M. Conditt, P. C. Noble, and H. Li. Fiber Bragg grating displacement sensor for movement measurement of tendons and ligaments. *Applied Optics*, 46(28):6867–6871, 2007.

M. D. Ries, E. Young, L. Al-Marashi, P. Goldstein, A. Hetherington, T. Petrie, and L. Pruitt. In vivo behavior of acrylic bone cement in total hip arthroplasty. *Biomaterials*, 26:256–261, 2006.

E. L. Ritman. Current status of developments and applications of micro-ct. *Annu. Rev. Biomed. Eng.*, 13:531–552, 2011.

C. H. Rivard, S. Rhalmi, and C. Coillard. In vivo biocompatibility testing of peek polymer for a spinal implant system: A study in rabbits. *Journal of Biomedical Materials Research*, 62(4):488–498, 2002.

B. C. Roberts, E. Perilli, and K. J. Reynolds. Application of the digital volume correlation technique for the measurement of displacement and strain fields in bone: A literature review. *Journal of Biomechanics*, 47:923–934, 2014.

S. Roux, F. Hild, and H. Leclerc. Mechanical assistance to dic. *Procedia IUTAM*, 4(0):159–168, 2012. 2210-9838.

L. Ruiter, D. Janssen, A. Briscoe, and N. Verdonschot. Biomechanical compatibility of a peek-optima femoral total knee arthroplasty implant design during gait. In *International Society for Technology in Arthoplasty Conference, September 24-27th, Kyoto, Japan*, 2014.

F. Scarano. Tomographic PIV: Principles and practice. *Measurement Science and Technology*, 24(1), 2013.

T. Scheerlinck, P. Vandenbussche, and P. C. Noble. Quantification of stem-cement interfacial gaps - in vitro ct analysis of charnley-kerboul and lubinus spii femoral hip implants. *Journal of Bone and Joint Surgery-British Volume*, 90B(1):107–113, 2008.

P. R. Schmidlin, B. Stawarczyk, M. Wieland, T. Attin, C. H. F. Haemmerle, and J. Fischer. Effect of different surface pre-treatments and luting materials on shear bond strength to peek. *Dental Materials*, 26(6):553–559, 2010.

S. C. Scholes and A. Unsworth. The wear properties of CFR-PEEK-OPTIMA articulating against ceramic assessed on a multidirectional pin-on-plate machine. *Proc. Inst. Mech. Eng. Part H J. Eng. Med.*, 221(3):281–289, 2007.

S. C. Scholes and A. Unsworth. Pitch-based carbon-fibre-reinforced poly(ether-ether-ketone) OPTIMA assessed as a bearin material in a mobile bearing unicondylar knee joint. *Proc. IMechE Part H: J. Engineering in Medicine*, 223:13–24, 2009.

S. C. Scholes and A. Unsworth. The wear performance of PEEK-OPTIMA based self-mating couples. *Wear*, 268(3-4):380–387, 2010.

S. C. Scholes, I. A. Inman, A. Unsworth, and E. Jones. Tribological assessment of a flexible carbon-fibre-reinforced poly(ether-ether-ketone) acetabular cup articulating against an alumina femoral head. *Proceedings of the Institution of Mechanical Engineers Part H-Journal of Engineering in Medicine*, 222(H3):273–283, 2008.

M. S. Scholz, J. P. Blanchfield, L. D. Bloom, B. H. Coburn, M. Elkington, J. D. Fuller, M. E. Gilbert, S. A. Muflahi, M. F. Pernice, S. I. Rae, J. A. Trevarthen, S. C. White, P. M. Weaver, and I. P. Bond. The use of composite materials in modern orthopaedic medicine and prosthetic devices: A review. *Composites Science and Technology*, 71(16):1791–1803, 2011.

C. E. H. Scott, M. J. Eaton, R. W. Nutton, F. A. Wade, P. Pankaj, and S. L. Evans. Proximal tibial strain in medial unicompartmental knee replacements: A biomechanical study of implant design. *Bone & Joint Journal*, 96B(10):1339–1347, 2013.

J. K. Seon, J. K. Park, Y. J. Shin, H. Y. Seo, K. B. Lee, and E. K. Song. Comparisons of kinematics and range of motion in high-flexion total knee arthroplasty: cruciate retaining vs. substituting designs. *Knee Surgery Sports Traumatology Arthroscopy*, 19:2016–2022, 2011.

S. Shah, H. Bougherara, E. H. Schemitsch, and R. Zdero. Biomechanical stress maps of an artificial femur obtained using a new infrared thermography technique validated by strain gages. *Medical Engineering & Physics*, 34(10):14961502, 2012.

N. Shearwood-Porter. *Micromechanical Characterisation of Fatigue Failure in Acrylic Bone Cement.* PhD thesis, Faculty of Engineering and the Environment, University of Southampton, 2013.

K. B. Shelburne, M. R. Torry, and M. G. Pandy. Contributions of muscles, ligaments, and the ground-reaction force to tibiofemoral joint loading during normal gait. *Journal of Orthopaedic Research*, 24:1983–1990, 2006.

H. W. Shreier, J. R. Braasch, and M. A. Sutton. Systematic errors in digital image correlation caused by intensity interpolation. *Optical Engineering*, 39(11), 2000.

L. Silvestri, H. R. Brown, and S. Carra. Chain entanglements and fracture energy in interfaces between immiscible polymers. *Journal of Chemical Physics*, 119(15):8140–8149, 2003.

M Simonsen. Strain tensors in Vic-3D. 2011. URL `http://www.correlatedsolutions.com/support/index.php?/Knowledgebase/Article/View/2/1/strain-tensors-in-vic`. Correlated Solutions Knowledgebase: Application Notes, Date accessed: 13/07/2015.

P. Sinnett-Jones. *Micromechanical aspects of fatigue failure in conventional and carbon nanotube-reinforced acrylic bone cement.* PhD thesis, Faculty of engineering, science and mathematics, School of engineering sciences, University of Southampton, 2007.

P. E. Sinnett-Jones, M. Browne, W. Ludwig, J. Y. Buffiere, and I. Sinclair. Microtomography assessment of failure in acrylic bone cement. *Biomaterials*, 26(33):6460–6466, 2005.

Smart Fibres Ltd. Smart FBG Fibre Bragg Grating Sensor. URL `http://smartfibres.com/docs/SmartFBG.pdf`. data sheet, date accessed: 16/07/2015.

M. C. Sobieraj, J. M. Murphy, J. G. Brinkman, S. M. Kurtz, and C. M. Rimnac. Notched fatigue behaviour of PEEK. *Biomaterials*, 31:9156–9162, 2010.

T. A. Soininvaara, H. J. A. Miettinen, J. S. Jurvelin, O. T. Suomalainen, E. M. Alhava, and H. P. J. Kroger. Periprosthetic femoral bone loss after total knee arthroplasty: 1-year follow-up study of 69 patients. *Knee*, 11(4):297–302, 2004.

T. A. Soininvaara, K. A. L. Harju, H. J. A. Miettinen, and H. P. J. Kroger. Periprosthetic bone mineral density changes after unicondylar knee arthroplasty. *The Knee*, 20:120–127, 2013.

A. J. Spittlehouse, C. J. Getty, and R. Eastell. Measurement of bone mineral density by dual-energy x-ray absorptiometry around an uncemented knee prosthesis. *The Journal of Arthroplasty*, 14(8): 957–963, 1999.

M Stanczyk and B. van Rietbergen. Thermal analysis of bone cement polymerisation at the cement-bone interface. *Journal of Biomechanics*, 37:1803–1810, 2004.

B. Stawarczyk, F. Beuer, T. Wimmer, D. Jahn, B. Sener, M. Roos, and P. R. Schmidlin. Polyetheretherketone - a suitable material for fixed dental prostheses? *Journal of Biomedical Materials Research B: Applied Biomaterials*, 00B, 2013.

G. D. Steele, T. K. Fehring, S. M. Odum, A. C. Dennos, and M. C. Nadaud. Early failure of articular surface replacement xl total hip arthroplasty. *The Journal of Arthroplasty*, 26(6):14–18, 2011.

T. A. Stolarski. Tribology of polyetheretherketone. *Wear*, 158(1-2):71–78, 1992.

M. Su, P. R. Samala, H. H. Jiang, S. Liu, L. Yang, and H. Yokota. Measurement of bone strain using electronic speckle pattern interferometry. *Journal of Holography and Speckle*, 2:34–39, 2005.

C. Sukjamsri, D. Geraldes, T. Gregory, F. Ahmed, D. Hollis, S. Schenk, A. Amis, R. Emery, and U. Hansen. Digital volume correlation and micro-ct: an in-vitro technique for measuring full-field interface micromotion around polyethylene implants. *Journal of Biomechanics*, 2015.

M. A. Sutton, J. J. Orteu, and H. Schreier. *Image correlation for shape, motion and deformation measurements: Basic concepts, theory and applications.* Springer, New York, 2009.

P. Sztefek, M. Vanleene, R. Olsson, R. Collinson, A. A. Pitsillides, and S. Shefelbine. Using digital image correlation to determine bone surface strains during loading and after adaptation of the mouse tibia. *Journal of Biomechanics*, 43(4):599–605, 2010.

P. M. Talaia, A. Ramos, I. Abe, M. W. Schiller, P. Lopes, R. N. Nogueira, L. R. Pinto, R. Claramunt, and J. A. Simoes. Plated and intact femur strains in fracture fixation using fiber Bragg gratings and strain gauges. *Experimental Mechanics*, 47:355–363, 2007.

K. H. Tan, C. K. Chua, K. F. Leong, C. M. Cheah, P. Cheang, M. S. Abu Bakar, and S. W. Cha. Scaffold development using selective laser sintering of polyetheretherketone-hydroxyapatite biocomposite blends. *Biomaterials*, 24(18):3115–3123, 2003.

T. Tang, V. Ebacher, P. Cripton, P. Guy, H. McKay, and R. Wang. Shear deformation and fracture of human cortical bone. *Bone*, 71:25–35, 2015.

M. Taylor. Finite element analysis of the resurfaced femoral head. *Proc. IMechE Part H: J. Engineering in Medicine*, 220(2):289–297, 2006.

S. J. G. Taylor, P. S. Walker, S. J. Perry, and S. R. Cannon. The forces in the distal femur and the knee during walking and other activities measured by telemetry. *The Journal of Arthroplasty*, 13(4): 428–437, 1998.

W. R. Taylor, M. O. Heller, G. Bergmann, and G. N. Duda. Tibio-femoral loading during human gait and stair climbing. *Journal of Orthopaedic Research*, 22(3):625–632, 2004.

Taylor-Hobson. Surface profilometers. 2011. URL `http://www.taylor-hobson.com/surface-profilers.html`. date accessed: 01/06/12.

S. H. Teoh. Fatigue of biomaterials: a review. *International Journal of Fatigue*, 22:825–837, 2000.

A. Terrier, X. Larrea, J. Guerdat, and X. Crevoisier. Development and experimental validation of a finite element model of total ankle replacement. *Journal of Biomechanics*, 47(3):742–745, 2014.

A. Thambyah and J. Fernandez. Squatting-related tibiofemoral shear reaction forces and a biomechanical rationale for femoral component loosening. *The Scientific World Journal*, 2014:1–7, 2014.

M. S. Thompson, H. Schell, J. Lienau, and G. N. Duda. Digital image correlation: A technique for determining local mechanical conditions within early bone callus. *Medical Engineering & Physics*, 29:820–823, 2007.

B. Tietjens. Right sizing of the femoral component in total knee replacement. *J Bone Joint Surg Br.*, 91-B:Supp II 339, 2009.

R. Tiossi, L. Lin, R. C. S. Rodrigues, Y. C. Heo, H. J. Conrad, M. da Gloria Chiarello de Mattos, R. F. Ribeiro, and A. S. L. Fok. Digital image correlation analysis of the load transfer by implant-supported restorations. *Journal of Biomechanics*, 44(6):1008–1013, 2011.

R. Tiossi, L. Lin, H. J. Conrad, R. C. S. Rodrigues, Y. C. Heo, M. da Gloria Chiarello de Mattos, A. S.-L. Fok, and R. F. Ribeiro. A digital image correlation analysis on the influence of crown material in implant-supported prostheses on bone strain distribution. *Journal of Prosthodontic Research*, 56(1):25–31, 2012.

R. Tiossi, M. A. A. Vasco, H. J. Lin, L.and Conrad, O. L. Bezzon, R. F. Ribeiro, and A. S. L. Fok. Validation of finite element models for strain analysis of implant-supported prostheses using digital image correlation. *Dental Materials*, 29(7):788–796, 2013.

M. Tissakht, A. M. Ahmed, and K. C. Chan. Calculated stress-shielding in the distal femur after total knee replacement corresponds to the reported location of bone loss. *Journal of Orthopaedic Research*, 14(5):778–785, 1996.

G. Tozzi, Q. H. Zhang, and J. Tong. Microdamage assessment of bone-cement interfaces under monotonic and cyclic compression. *Journal of Biomechanics*, 47:3466–3474, 2014.

A. Trepczynski, I. Kutzner, E. Kornaropoulos, W. R. Taylor, G. N. Duda, G. Bergmann, and M. O. Heller. Patellofemoral joint contact forces during activities with high knee flexion. *Journal of Orthopaedic Research*, 30(3):408–415, 2012.

M. Tuncer, J. P. Cobb, U. N. Hansen, and A. A. Amis. Validation of multiple subject-specific finite element unicompartmental knee replacement. *Medical Engineering & Physics*, 35:1457–1464, 2013.

S. Utzschneider, F. Becker, T. M. Grupp, B. Sievers, A. Paulus, O. Gottschalk, and V. Jansson. Inflammatory response against different carbon fiber-reinforced peek wear particles compared with uhmwpe in vivo. *Acta Biomaterialia*, 6(11):4296–4304, 2010.

S. P. Vaananen, S. A. Yavari, H. Weinans, A. A. Zadpoor, J. S. Jurvelin, and H. Isaksson. Repeatability of digital image correlation for measurement of surface strains in composite long bones. *Journal of Biomechanics*, 46(11):19281932, 2013.

S. V. Vaidya, C. S. Ranawat, A. Aroojis, and N. S. Laud. Anthropometric measurements to design total knee prostheses for the indian population. *Journal of Arthroplasty*, 15(1):79–85, 2000.

G. H. van Lenthe, M. C. D. Malefijt, and R. Huiskes. Stress shielding after total knee replacement may cause bone resorption in the distal femur. *Journal of Bone and Joint Surgery-British Volume*, 79B (1):117–122, 1997.

G. H. van Lenthe, M. M. M. Willems, N. Verdonschot, M. C. D. Malefijt, and R. Huiskes. Stemmed femoral knee prostheses - effects of prosthetic design and fixation on bone loss. *Acta Orthopaedica Scandinavica*, 73(6):630–637, 2002.

D. Van Wynsberghe, C. R. Noback, and R. Carola. *Human anatomy and Physiology.* McGraw-Hill, 1995.

M. Vaninbroukx, L. Labey, B. Innocenti, and J. Bellemans. Cementing the femoral component in total knee arthroplasty: Which technique is the best? *The Knee*, 16:265–268, 2009.

N. Verdonschot and R. Huiskes. Surface roughness of debonded straight-tapered stems in cemented tha reduces subsidence but not cement damage. *Biomaterials*, 19(19):1773–1779, 1998.

N. Verdonschot, E. Tanck, and R. Huiskes. Effects of prosthesis surface roughness on the failure process of cemented hip implants after stem-cement debonding. *Journal of Biomedical Materials Research*, 42:554–559, 1998.

E. Verhulp, B. van Rietbergen, and R. Huiskes. A three-dimensional digital image correlation technique for strain measurements in microstructures. *Journal of Biomechanics*, 37:1313–1320, 2004.

K. D. Vernon-Parry. Scanning electron microscopy: An introduction. *III-Vs Review*, 13(4):40–44, 2000.

J. Victor. Rotational alignment of the distal femur: A literature review. *Orthopaedics & Traumatology: Surgery & Research*, 95:365–372, 2009.

P. S. Walker and S. Sathasivam. Design forms of total knee replacement. *Proceedings of the Institution of Mechanical Engineers Part H-Journal of Engineering in Medicine*, 214(H1):101–119, 2000.

S. C. Walpole, D. Prieto-Marino, P. Edwards, J. Cleland, G. Stevens, and I. Roberts. The weight of nations: an estimation of adult human biomass. *BMC Public Health*, 12:439, 2012.

D. E. Walrath and D. F. Adams. The iosipescu shear test as applied to composite materials. *Experimental M*, pages 105–110, 1983.

W. R. Walsh, M. J. Svehla, J. Russell, M. Salto, T. Nakashima, R. M. Gillies, and W. Bruce. Cemented fixation with pmma or bis-gma resin hydroxyapatite cement: effect of implant surface roughness. *Biomaterials*, 25(20):4929–4934, 2004.

D. J. Walton and J. P. Lorimer. *Polymers*. Oxford University Press, 2000.

A. Wang, R. Lin, V. K. Polineni, A. Essner, C. Stark, and J. H. Dumbleton. Carbon fiber reinforced polyether ether ketone composite as a bearing surface for total hip replacement. *Tribology International*, 31(11):661–667, 1998.

A. Wang, R. Lin, C. Stark, and J. H. Dumbleton. Suitability and limitations of carbon fiber reinforced peek composites as bearing surfaces for total joint replacements. *Wear*, 225:724–727, 1999. 12th International Conference on Wear of Materials, Apr 25-29, Atlanta, GA, USA.

A. Wang, D. Lawrynowicz, L. A. Korduba, and L. Herrera. Polyether ether ketone as an orthopaedic bearing surface against uhmwpe. In *5th UHMWPE International Meeting, Philadelphia, PA, USA*, September 2011.

J. S. Wang, M. Taylor, G. Flivik, and L. Lidgren. Factors affecting the static shear strength of the prosthetic stem-bone cement interface. *Journal of Materials Science-Materials in Medicine*, 14(1): 55–61, 2003.

S. Wang. The science and engineering electron microscopy centre. *University of Southampton*, 2002. URL `www.micro.soton.ac.uk`. date accessed: 01/03/10.

Y. Q. Wang, M. A. Sutton, H. A. Bruck, and H. W. Schreier. Quantitative error assessment in pattern matching: effects of intensity pattern noise, interpolation, strain and image contrast on motion measurements. *Strain*, 45(2):160–178, 2009.

J. F. Watts, J. Comyn, K. B. Armstrong, R. J. Ashley, D. E. Packham, J. M. Martin Martinez, J. F. Padday, G. W. Critchlow, D. Briggs, A. D. Crocombe, and J. Guthrie. *Handbook of Adhesion*. John Wiley & Sons, Ltd, 2005.

J. C. J. Webb and R. F. Spencer. The role of polymethylmethacrylate bone cement in modern orthopaedic surgery. *Journal of Joint and Bone Surgery (Br)*, 89-B:851–857, 2007.

D. F. Williams, A. McNamara, and R. M. Turner. Potential of polyetheretherketone (peek) and carbon-fiber-reinforced peek in medical applications. *Journal of Materials Science Letters*, 6(2): 188–190, 1987.

C. R. Winby, D. G. Lloyd, T. F. Besier, and T. B. Kirk. Muscle and external load contribution to knee joint contact loads during normal gait. *Journal of Biomechanics*, 42:22942300, 2009.

X-P Xu and A Needleman. Numerical simulations of dynamic crack growth along an interface. *International Journal of Fracture*, 74:289–324, 1996.

S. Yaofeng and J. H. L. Pang. Study of optimal subset size in digital image correlation of speckle pattern images. *Optics and Lasers in Engineering*, 45(9):967–974, 2007.

D. N. Yetkinler and A. S. Litsky. Viscoelastic behaviour of acrylic bone cements. *Biomaterials*, 19(17): 1551–1559, 1998.

B. Yue, K. M. Varadarajan, S. Ai, T. Tang, H. E. Rubash, and G. Li. Differences of knee anthropometry between chinese and white men and women. *Journal of Arthroplasty*, 26(1):124–130, 2011.

J. Zelle, D. Janssen, S. Peeters, C. Brouwer, and N. Verdonschot. Mixed-mode failure strength of implant-cement interface specimens with varying surface roughness. *Journal of Biomechanics*, 44(4): 780–783, 2011a.

J. Zelle, D. Janssen, J. Van Eijden, M. De Waal Malefijt, and N. Verdonschot. Does high-flexion total knee arthroplasty promote early loosening of the femoral component? *Journal of Orthopaedic Research*, 29:976–983, 2011b.

D. Zhang and D. D. Arola. Applications of digital image correlation to biological tissues. *Journal of Biomedical Optics*, 9(4):691–699, 2004.

G. G. Zhang, R. A. Latour, J. M. Kennedy, H. DelSchutte, and R. J. Friedman. Long-term compressive property durability of carbon fibre-reinforced polyetheretherketone composite in physiological saline. *Biomaterials*, 17(8):781–789, 1996.

H. Zhang, L. T. Brown, L. A. Blunt, and S. M. Barrans. Influence of femoral stem surface finish on the apparent static shear strength at the stem-cement interface. *Journal of the Mechanical Behavior of Biomedical Materials*, 1(1):96–104, 2008.

L. Zhang. Hygrothermal resistance of the interface in high performance polymer composites. Master's thesis, Department of Chemical Engineering and Applied Chemistry, University of Toronto, 1998.

D. Zhao, S. A. Banks, D. D. D'Lima, C. W. Colwell Jr., and B. J. Fregly. In vivo medial and lateral tibial loads during dynamic and high flexion activities. *Journal of Orthopaedic Research*, 25: 593–602, 2007.

Fixation Study - Shear Strength Results

A box plot has been used to show the distribution in shear strength data for every textured sample group tested (Figure 1).

Table 1 shows the analysis of variance of the textured PEEK-cement lap shear strength results (section 3.3.2.2), obtained using the method in section 3.3.1.5. An asterisk (*) indicated that the mean difference is significant at the 0.05 level. A negative value indicates the sample shear strength is significantly weaker, and a positive value indicates the sample interfacial strength is significantly stronger, than the (I) sample.

(I) Sample	**(J) Comparate**	**Mean Difference (I-J)**	**Std. Error**	**Sig.**	**95% Confidence Interval**	
					Lower Bound	**Upper Bound**
Grit Blasted	Waffle	-4.92800E+03	2.04812E+05	1.000	-7.3873E+05	7.2887E+05
	Conical Frustums	1.69504E+05	2.04812E+05	1.000	-5.6430E+05	9.0331E+05
	Inverted Conical Frustums	4.66507E+05	2.34936E+05	.869	-3.7522E+05	1.3082E+06
	Micro-roughened 1	3.18840E+05	2.34936E+05	.996	-5.2289E+05	1.1606E+06
	Scaled effect	4.93400E+04	2.34936E+05	1.000	-7.9239E+05	8.9107E+05
	Micro-roughened 2	7.10340E+05	2.34936E+05	.210	-1.3139E+05	1.5521E+06
	Micro-roughened 3	7.24173E+05	2.34936E+05	.184	-1.1756E+05	1.5659E+06
	Micro-roughened 4	-1.13160E+05	2.34936E+05	1.000	-9.5489E+05	7.2857E+05
	Random Protuberances	2.96507E+05	2.34936E+05	.998	-5.4522E+05	1.1382E+06
	Macro Ribbed	-8.34827E+05	2.34936E+05	.054	-1.6766E+06	6.9030E+03
	Macro Troughed	-1.41316E+006*	2.34936E+05	.000	-2.2549E+06	-5.7143E+05
	Sawtooth	7.14707E+05	2.34936E+05	.201	-1.2702E+05	1.5564E+06
	CoCr	-6.84316E+006*	2.16600E+05	.000	-7.6192E+06	-6.0671E+06
	Micro-rough + Macro Ribbed (1mm)	-2.38816E+006*	2.48633E+05	.000	-3.2790E+06	-1.4974E+06
	Micro-rough + Macro Ribbed (2mm)	-2.19216E+006*	2.48633E+05	.000	-3.0830E+06	-1.3014E+06
Waffle	Grit Blasted	4.92800E+03	2.04812E+05	1.000	-7.2887E+05	7.3873E+05
	Conical Frustums	1.74432E+05	1.99350E+05	1.000	-5.3980E+05	8.8866E+05
	Inverted Conical Frustums	4.71435E+05	2.30189E+05	.838	-3.5329E+05	1.2962E+06
	Micro-roughened 1	3.23768E+05	2.30189E+05	.994	-5.0096E+05	1.1485E+06
	Scaled effect	5.42680E+04	2.30189E+05	1.000	-7.7046E+05	8.7899E+05
	Micro-roughened 2	7.15268E+05	2.30189E+05	.174	-1.0946E+05	1.5400E+06
	Micro-roughened 3	7.29101E+05	2.30189E+05	.151	-9.5622E+04	1.5538E+06
	Micro-roughened 4	-1.08232E+05	2.30189E+05	1.000	-9.3296E+05	7.1649E+05
	Random Protuberances	3.01435E+05	2.30189E+05	.997	-5.2329E+05	1.1262E+06
	Macro Ribbed	-8.29899E+005*	2.30189E+05	.047	-1.6546E+06	-5.1754E+03
	Macro Troughed	-1.40823E+006*	2.30189E+05	.000	-2.2330E+06	-5.8351E+05
	Sawtooth	7.19635E+05	2.30189E+05	.166	-1.0509E+05	1.5444E+06
	CoCr	-6.83823E+006*	2.11442E+05	.000	-7.5958E+06	-6.0807E+06
	Micro-rough + Macro Ribbed (1mm)	-2.38323E+006*	2.44152E+05	.000	-3.2580E+06	-1.5085E+06
	Micro-rough + Macro Ribbed (2mm)	-2.18723E+006*	2.44152E+05	.000	-3.0620E+06	-1.3125E+06
Conical Frustums	Grit Blasted	-1.69504E+05	2.04812E+05	1.000	-9.0331E+05	5.6430E+05
	Waffle	-1.74432E+05	1.99350E+05	1.000	-8.8866E+05	5.3980E+05

	Inverted Conical Frustums	2.97003E+05	2.30189E+05	.998	-5.2772E+05	1.1217E+06
	Micro-roughened 1	1.49336E+05	2.30189E+05	1.000	-6.7539E+05	9.7406E+05
	Scaled effect	-1.20164E+05	2.30189E+05	1.000	-9.4489E+05	7.0456E+05
	Micro-roughened 2	5.40836E+05	2.30189E+05	.646	-2.8389E+05	1.3656E+06
	Micro-roughened 3	5.54669E+05	2.30189E+05	.602	-2.7005E+05	1.3794E+06
	Micro-roughened 4	-2.82664E+05	2.30189E+05	.999	-1.1074E+06	5.4206E+05
	Random Protuberances	1.27003E+05	2.30189E+05	1.000	-6.9772E+05	9.5173E+05
	Macro Ribbed	-1.00433E+006*	2.30189E+05	.004	-1.8291E+06	-1.7961E+05
	Macro Troughed	-1.58266E+006*	2.30189E+05	.000	-2.4074E+06	-7.5794E+05
	Sawtooth	5.45203E+05	2.30189E+05	.632	-2.7952E+05	1.3699E+06
	CoCr	-7.01266E+006*	2.11442E+05	.000	-7.7702E+06	-6.2551E+06
	Micro-rough + Macro Ribbed (1mm)	-2.55766E+006*	2.44152E+05	.000	-3.4324E+06	-1.6829E+06
	Micro-rough + Macro Ribbed (2mm)	-2.36166E+006*	2.44152E+05	.000	-3.2364E+06	-1.4869E+06
Inverted Conical Frustums	Grit Blasted	-4.66507E+05	2.34936E+05	.869	-1.3082E+06	3.7522E+05
	Waffle	-4.71435E+05	2.30189E+05	.838	-1.2962E+06	3.5329E+05
	Conical Frustums	-2.97003E+05	2.30189E+05	.998	-1.1217E+06	5.2772E+05
	Micro-roughened 1	-1.47667E+05	2.57359E+05	1.000	-1.0697E+06	7.7440E+05
	Scaled effect	-4.17167E+05	2.57359E+05	.976	-1.3392E+06	5.0490E+05
	Micro-roughened 2	2.43833E+05	2.57359E+05	1.000	-6.7824E+05	1.1659E+06
	Micro-roughened 3	2.57667E+05	2.57359E+05	1.000	-6.6440E+05	1.1797E+06
	Micro-roughened 4	-5.79667E+05	2.57359E+05	.714	-1.5017E+06	3.4240E+05
	Random Protuberances	-1.70000E+05	2.57359E+05	1.000	-1.0921E+06	7.5207E+05
	Macro Ribbed	-1.30133E+006*	2.57359E+05	.000	-2.2234E+06	-3.7926E+05
	Macro Troughed	-1.87967E+006*	2.57359E+05	.000	-2.8017E+06	-9.5760E+05
	Sawtooth	2.48200E+05	2.57359E+05	1.000	-6.7387E+05	1.1703E+06
	CoCr	-7.30967E+006*	2.40737E+05	.000	-8.1722E+06	-6.4472E+06
	Micro-rough + Macro Ribbed (1mm)	-2.85467E+006*	2.69921E+05	.000	-3.8217E+06	-1.8876E+06
	Micro-rough + Macro Ribbed (2mm)	-2.65867E+006*	2.69921E+05	.000	-3.6257E+06	-1.6916E+06
Micro-roughened 1	Grit Blasted	-3.18840E+05	2.34936E+05	.996	-1.1606E+06	5.2289E+05
	Waffle	-3.23768E+05	2.30189E+05	.994	-1.1485E+06	5.0096E+05
	Conical Frustums	-1.49336E+05	2.30189E+05	1.000	-9.7406E+05	6.7539E+05
	Inverted Conical Frustums	1.47667E+05	2.57359E+05	1.000	-7.7440E+05	1.0697E+06
	Scaled effect	-2.69500E+05	2.57359E+05	1.000	-1.1916E+06	6.5257E+05
	Micro-roughened 2	3.91500E+05	2.57359E+05	.987	-5.3057E+05	1.3136E+06
	Micro-roughened 3	4.05333E+05	2.57359E+05	.982	-5.1674E+05	1.3274E+06
	Micro-roughened 4	-4.32000E+05	2.57359E+05	.966	-1.3541E+06	4.9007E+05
	Random Protuberances	-2.23333E+04	2.57359E+05	1.000	-9.4440E+05	8.9974E+05
	Macro Ribbed	-1.15367E+006*	2.57359E+05	.003	-2.0757E+06	-2.3160E+05
	Macro Troughed	-1.73200E+006*	2.57359E+05	.000	-2.6541E+06	-8.0993E+05
	Sawtooth	3.95867E+05	2.57359E+05	.985	-5.2620E+05	1.3179E+06
	CoCr	-7.16200E+006*	2.40737E+05	.000	-8.0245E+06	-6.2995E+06
	Micro-rough + Macro Ribbed (1mm)	-2.70700E+006*	2.69921E+05	.000	-3.6741E+06	-1.7399E+06
	Micro-rough + Macro Ribbed (2mm)	-2.51100E+006*	2.69921E+05	.000	-3.4781E+06	-1.5439E+06
Scaled effect	Grit Blasted	-4.93400E+04	2.34936E+05	1.000	-8.9107E+05	7.9239E+05
	Waffle	-5.42680E+04	2.30189E+05	1.000	-8.7899E+05	7.7046E+05
	Conical Frustums	1.20164E+05	2.30189E+05	1.000	-7.0456E+05	9.4489E+05
	Inverted Conical Frustums	4.17167E+05	2.57359E+05	.976	-5.0490E+05	1.3392E+06
	Micro-roughened 1	2.69500E+05	2.57359E+05	1.000	-6.5257E+05	1.1916E+06
	Micro-roughened 2	6.61000E+05	2.57359E+05	.486	-2.6107E+05	1.5831E+06
	Micro-roughened 3	6.74833E+05	2.57359E+05	.448	-2.4724E+05	1.5969E+06
	Micro-roughened 4	-1.62500E+05	2.57359E+05	1.000	-1.0846E+06	7.5957E+05
	Random Protuberances	2.47167E+05	2.57359E+05	1.000	-6.7490E+05	1.1692E+06
	Macro Ribbed	-8.84167E+05	2.57359E+05	.076	-1.8062E+06	3.7902E+04
	Macro Troughed	-1.46250E+006*	2.57359E+05	.000	-2.3846E+06	-5.4043E+05

	Sawtooth	6.65367E+05	2.57359E+05	.474	-2.5670E+05	1.5874E+06
	CoCr	-6.89250E+006*	2.40737E+05	.000	-7.7550E+06	-6.0300E+06
	Micro-rough + Macro Ribbed (1mm)	-2.43750E+006*	2.69921E+05	.000	-3.4046E+06	-1.4704E+06
	Micro-rough + Macro Ribbed (2mm)	-2.24150E+006*	2.69921E+05	.000	-3.2086E+06	-1.2744E+06
Micro-roughened 2	Grit Blasted	-7.10340E+05	2.34936E+05	.210	-1.5521E+06	1.3139E+05
	Waffle	-7.15268E+05	2.30189E+05	.174	-1.5400E+06	1.0946E+05
	Conical Frustums	-5.40836E+05	2.30189E+05	.646	-1.3656E+06	2.8389E+05
	Inverted Conical Frustums	-2.43833E+05	2.57359E+05	1.000	-1.1659E+06	6.7824E+05
	Micro-roughened 1	-3.91500E+05	2.57359E+05	.987	-1.3136E+06	5.3057E+05
	Scaled effect	-6.61000E+05	2.57359E+05	.486	-1.5831E+06	2.6107E+05
	Micro-roughened 3	1.38333E+04	2.57359E+05	1.000	-9.0824E+05	9.3590E+05
	Micro-roughened 4	-8.23500E+05	2.57359E+05	.139	-1.7456E+06	9.8569E+04
	Random Protuberances	-4.13833E+05	2.57359E+05	.977	-1.3359E+06	5.0824E+05
	Macro Ribbed	-1.54517E+006*	2.57359E+05	.000	-2.4672E+06	-6.2310E+05
	Macro Troughed	-2.12350E+006*	2.57359E+05	.000	-3.0456E+06	-1.2014E+06
	Sawtooth	4.36667E+03	2.57359E+05	1.000	-9.1770E+05	9.2644E+05
	CoCr	-7.55350E+006*	2.40737E+05	.000	-8.4160E+06	-6.6910E+06
	Micro-rough + Macro Ribbed (1mm)	-3.09850E+006*	2.69921E+05	.000	-4.0656E+06	-2.1314E+06
	Micro-rough + Macro Ribbed (2mm)	-2.90250E+006*	2.69921E+05	.000	-3.8696E+06	-1.9354E+06
E_MT1055	Grit Blasted	-7.24173E+05	2.34936E+05	.184	-1.5659E+06	1.1756E+05
	Waffle	-7.29101E+05	2.30189E+05	.151	-1.5538E+06	9.5622E+04
	Conical Frustums	-5.54669E+05	2.30189E+05	.602	-1.3794E+06	2.7005E+05
	Inverted Conical Frustums	-2.57667E+05	2.57359E+05	1.000	-1.1797E+06	6.6440E+05
	Micro-roughened 1	-4.05333E+05	2.57359E+05	.982	-1.3274E+06	5.1674E+05
	Scaled effect	-6.74833E+05	2.57359E+05	.448	-1.5969E+06	2.4724E+05
	Micro-roughened 2	-1.38333E+04	2.57359E+05	1.000	-9.3590E+05	9.0824E+05
	Micro-roughened 4	-8.37333E+05	2.57359E+05	.122	-1.7594E+06	8.4735E+04
	Random Protuberances	-4.27667E+05	2.57359E+05	.969	-1.3497E+06	4.9440E+05
	Macro Ribbed	-1.55900E+006*	2.57359E+05	.000	-2.4811E+06	-6.3693E+05
	Macro Troughed	-2.13733E+006*	2.57359E+05	.000	-3.0594E+06	-1.2153E+06
	Sawtooth	-9.46667E+03	2.57359E+05	1.000	-9.3154E+05	9.1260E+05
	CoCr	-7.56733E+006*	2.40737E+05	.000	-8.4298E+06	-6.7048E+06
	Micro-rough + Macro Ribbed (1mm)	-3.11233E+006*	2.69921E+05	.000	-4.0794E+06	-2.1453E+06
	Micro-rough + Macro Ribbed (2mm)	-2.91633E+006*	2.69921E+05	.000	-3.8834E+06	-1.9493E+06
Micro-roughened 4	Grit Blasted	1.13160E+05	2.34936E+05	1.000	-7.2857E+05	9.5489E+05
	Waffle	1.08232E+05	2.30189E+05	1.000	-7.1649E+05	9.3296E+05
	Conical Frustums	2.82664E+05	2.30189E+05	.999	-5.4206E+05	1.1074E+06
	Inverted Conical Frustums	5.79667E+05	2.57359E+05	.714	-3.4240E+05	1.5017E+06
	Micro-roughened 1	4.32000E+05	2.57359E+05	.966	-4.9007E+05	1.3541E+06
	Scaled effect	1.62500E+05	2.57359E+05	1.000	-7.5957E+05	1.0846E+06
	Micro-roughened 2	8.23500E+05	2.57359E+05	.139	-9.8569E+04	1.7456E+06
	Micro-roughened 3	8.37333E+05	2.57359E+05	.122	-8.4735E+04	1.7594E+06
	Random Protuberances	4.09667E+05	2.57359E+05	.980	-5.1240E+05	1.3317E+06
	Macro Ribbed	-7.21667E+05	2.57359E+05	.328	-1.6437E+06	2.0040E+05
	Macro Troughed	-1.30000E+006*	2.57359E+05	.000	-2.2221E+06	-3.7793E+05
	Sawtooth	8.27867E+05	2.57359E+05	.134	-9.4202E+04	1.7499E+06
	CoCr	-6.73000E+006*	2.40737E+05	.000	-7.5925E+06	-5.8675E+06
	Micro-rough + Macro Ribbed (1mm)	-2.27500E+006*	2.69921E+05	.000	-3.2421E+06	-1.3079E+06
	Micro-rough + Macro Ribbed (2mm)	-2.07900E+006*	2.69921E+05	.000	-3.0461E+06	-1.1119E+06
Random Protuberances	Grit Blasted	-2.96507E+05	2.34936E+05	.998	-1.1382E+06	5.4522E+05
	Waffle	-3.01435E+05	2.30189E+05	.997	-1.1262E+06	5.2329E+05

	Conical Frustums	-1.27003E+05	2.30189E+05	1.000	-9.5173E+05	6.9772E+05
	Inverted Conical Frustums	1.70000E+05	2.57359E+05	1.000	-7.5207E+05	1.0921E+06
	Micro-roughened 1	2.23333E+04	2.57359E+05	1.000	-8.9974E+05	9.4440E+05
	Scaled effect	-2.47167E+05	2.57359E+05	1.000	-1.1692E+06	6.7490E+05
	Micro-roughened 2	4.13833E+05	2.57359E+05	.977	-5.0824E+05	1.3359E+06
	Micro-roughened 3	4.27667E+05	2.57359E+05	.969	-4.9440E+05	1.3497E+06
	Micro-roughened 4	-4.09667E+05	2.57359E+05	.980	-1.3317E+06	5.1240E+05
	Macro Ribbed	-1.13133E+006*	2.57359E+05	.003	-2.0534E+06	-2.0926E+05
	Macro Troughed	-1.70967E+006*	2.57359E+05	.000	-2.6317E+06	-7.8760E+05
	Sawtooth	4.18200E+05	2.57359E+05	.975	-5.0387E+05	1.3403E+06
	CoCr	-7.13967E+006*	2.40737E+05	.000	-8.0022E+06	-6.2772E+06
	Micro-rough + Macro Ribbed (1mm)	-2.68467E+006*	2.69921E+05	.000	-3.6517E+06	-1.7176E+06
	Micro-rough + Macro Ribbed (2mm)	-2.48867E+006*	2.69921E+05	.000	-3.4557E+06	-1.5216E+06
Macro Ribbed	Grit Blasted	8.34827E+05	2.34936E+05	.054	-6.9030E+03	1.6766E+06
	Waffle	8.29899E+005*	2.30189E+05	.047	5.1754E+03	1.6546E+06
	Conical Frustums	1.00433E+006*	2.30189E+05	.004	1.7961E+05	1.8291E+06
	Inverted Conical Frustums	1.30133E+006*	2.57359E+05	.000	3.7926E+05	2.2234E+06
	Micro-roughened 1	1.15367E+006*	2.57359E+05	.003	2.3160E+05	2.0757E+06
	Scaled effect	8.84167E+05	2.57359E+05	.076	-3.7902E+04	1.8062E+06
	Micro-roughened 2	1.54517E+006*	2.57359E+05	.000	6.2310E+05	2.4672E+06
	Micro-roughened 3	1.55900E+006*	2.57359E+05	.000	6.3693E+05	2.4811E+06
	Micro-roughened 4	7.21667E+05	2.57359E+05	.328	-2.0040E+05	1.6437E+06
	Random Protuberances	1.13133E+006*	2.57359E+05	.003	2.0926E+05	2.0534E+06
	Macro Troughed	-5.78333E+05	2.57359E+05	.718	-1.5004E+06	3.4374E+05
	Sawtooth	1.54953E+006*	2.57359E+05	.000	6.2746E+05	2.4716E+06
	CoCr	-6.00833E+006*	2.40737E+05	.000	-6.8708E+06	-5.1458E+06
	Micro-rough + Macro Ribbed (1mm)	-1.55333E+006*	2.69921E+05	.000	-2.5204E+06	-5.8626E+05
	Micro-rough + Macro Ribbed (2mm)	-1.35733E+006*	2.69921E+05	.000	-2.3244E+06	-3.9026E+05
Macro Troughed	Grit Blasted	1.41316E+006*	2.34936E+05	.000	5.7143E+05	2.2549E+06
	Waffle	1.40823E+006*	2.30189E+05	.000	5.8351E+05	2.2330E+06
	Conical Frustums	1.58266E+006*	2.30189E+05	.000	7.5794E+05	2.4074E+06
	Inverted Conical Frustums	1.87967E+006*	2.57359E+05	.000	9.5760E+05	2.8017E+06
	Micro-roughened 1	1.73200E+006*	2.57359E+05	.000	8.0993E+05	2.6541E+06
	Scaled effect	1.46250E+006*	2.57359E+05	.000	5.4043E+05	2.3846E+06
	Micro-roughened 2	2.12350E+006*	2.57359E+05	.000	1.2014E+06	3.0456E+06
	Micro-roughened 3	2.13733E+006*	2.57359E+05	.000	1.2153E+06	3.0594E+06
	Micro-roughened 4	1.30000E+006*	2.57359E+05	.000	3.7793E+05	2.2221E+06
	Random Protuberances	1.70967E+006*	2.57359E+05	.000	7.8760E+05	2.6317E+06
	Macro Ribbed	5.78333E+05	2.57359E+05	.718	-3.4374E+05	1.5004E+06
	Sawtooth	2.12787E+006*	2.57359E+05	.000	1.2058E+06	3.0499E+06
	CoCr	-5.43000E+006*	2.40737E+05	.000	-6.2925E+06	-4.5675E+06
	Micro-rough + Macro Ribbed (1mm)	-9.75000E+005*	2.69921E+05	.046	-1.9421E+06	-7.9263E+03
	Micro-rough + Macro Ribbed (2mm)	-7.79000E+05	2.69921E+05	.280	-1.7461E+06	1.8807E+05
Sawtooth	Grit Blasted	-7.14707E+05	2.34936E+05	.201	-1.5564E+06	1.2702E+05
	Waffle	-7.19635E+05	2.30189E+05	.166	-1.5444E+06	1.0509E+05
	Conical Frustums	-5.45203E+05	2.30189E+05	.632	-1.3699E+06	2.7952E+05
	Inverted Conical Frustums	-2.48200E+05	2.57359E+05	1.000	-1.1703E+06	6.7387E+05
	Micro-roughened 1	-3.95867E+05	2.57359E+05	.985	-1.3179E+06	5.2620E+05
	Scaled effect	-6.65367E+05	2.57359E+05	.474	-1.5874E+06	2.5670E+05
	Micro-roughened 2	-4.36667E+03	2.57359E+05	1.000	-9.2644E+05	9.1770E+05
	Micro-roughened 3	9.46667E+03	2.57359E+05	1.000	-9.1260E+05	9.3154E+05
	Micro-roughened 4	-8.27867E+05	2.57359E+05	.134	-1.7499E+06	9.4202E+04
	Random Protuberances	-4.18200E+05	2.57359E+05	.975	-1.3403E+06	5.0387E+05
	Macro Ribbed	-1.54953E+006*	2.57359E+05	.000	-2.4716E+06	-6.2746E+05
	Macro Troughed	-2.12787E+006*	2.57359E+05	.000	-3.0499E+06	-1.2058E+06

	CoCr	-7.55787E+006*	2.40737E+05	.000	-8.4204E+06	-6.6954E+06
	Micro-rough + Macro Ribbed (1mm)	-3.10287E+006*	2.69921E+05	.000	-4.0699E+06	-2.1358E+06
	Micro-rough + Macro Ribbed (2mm)	-2.90687E+006*	2.69921E+05	.000	-3.8739E+06	-1.9398E+06
CoCr	Grit Blasted	6.84316E+006*	2.16600E+05	.000	6.0671E+06	7.6192E+06
	Waffle	6.83823E+006*	2.11442E+05	.000	6.0807E+06	7.5958E+06
	Conical Frustums	7.01266E+006*	2.11442E+05	.000	6.2551E+06	7.7702E+06
	Inverted Conical Frustums	7.30967E+006*	2.40737E+05	.000	6.4472E+06	8.1722E+06
	Micro-roughened 1	7.16200E+006*	2.40737E+05	.000	6.2995E+06	8.0245E+06
	Scaled effect	6.89250E+006*	2.40737E+05	.000	6.0300E+06	7.7550E+06
	Micro-roughened 2	7.55350E+006*	2.40737E+05	.000	6.6910E+06	8.4160E+06
	Micro-roughened 3	7.56733E+006*	2.40737E+05	.000	6.7048E+06	8.4298E+06
	Micro-roughened 4	6.73000E+006*	2.40737E+05	.000	5.8675E+06	7.5925E+06
	Random Protuberances	7.13967E+006*	2.40737E+05	.000	6.2772E+06	8.0022E+06
	Macro Ribbed	6.00833E+006*	2.40737E+05	.000	5.1458E+06	6.8708E+06
	Macro Troughed	5.43000E+006*	2.40737E+05	.000	4.5675E+06	6.2925E+06
	Sawtooth	7.55787E+006*	2.40737E+05	.000	6.6954E+06	8.4204E+06
	Micro-rough + Macro Ribbed (1mm)	4.45500E+006*	2.54122E+05	.000	3.5445E+06	5.3655E+06
	Micro-rough + Macro Ribbed (2mm)	4.65100E+006*	2.54122E+05	.000	3.7405E+06	5.5615E+06
Micro-rough + Macro Ribbed (1mm)	Grit Blasted	2.38816E+006*	2.48633E+05	.000	1.4974E+06	3.2790E+06
	Waffle	2.38323E+006*	2.44152E+05	.000	1.5085E+06	3.2580E+06
	Conical Frustums	2.55766E+006*	2.44152E+05	.000	1.6829E+06	3.4324E+06
	Inverted Conical Frustums	2.85467E+006*	2.69921E+05	.000	1.8876E+06	3.8217E+06
	Micro-roughened 1	2.70700E+006*	2.69921E+05	.000	1.7399E+06	3.6741E+06
	Scaled effect	2.43750E+006*	2.69921E+05	.000	1.4704E+06	3.4046E+06
	Micro-roughened 2	3.09850E+006*	2.69921E+05	.000	2.1314E+06	4.0656E+06
	Micro-roughened 3	3.11233E+006*	2.69921E+05	.000	2.1453E+06	4.0794E+06
	Micro-roughened 4	2.27500E+006*	2.69921E+05	.000	1.3079E+06	3.2421E+06
	Random Protuberances	2.68467E+006*	2.69921E+05	.000	1.7176E+06	3.6517E+06
	Macro Ribbed	1.55333E+006*	2.69921E+05	.000	5.8626E+05	2.5204E+06
	Macro Troughed	9.75000E+005*	2.69921E+05	.046	7.9263E+03	1.9421E+06
	Sawtooth	3.10287E+006*	2.69921E+05	.000	2.1358E+06	4.0699E+06
	CoCr	-4.45500E+006*	2.54122E+05	.000	-5.3655E+06	-3.5445E+06
	Micro-rough + Macro Ribbed (2mm)	1.96000E+05	2.81923E+05	1.000	-8.1408E+05	1.2061E+06
Micro-rough + Macro Ribbed (2mm)	Grit Blasted	2.19216E+006*	2.48633E+05	.000	1.3014E+06	3.0830E+06
	Waffle	2.18723E+006*	2.44152E+05	.000	1.3125E+06	3.0620E+06
	Conical Frustums	2.36166E+006*	2.44152E+05	.000	1.4869E+06	3.2364E+06
	Inverted Conical Frustums	2.65867E+006*	2.69921E+05	.000	1.6916E+06	3.6257E+06
	Micro-roughened 1	2.51100E+006*	2.69921E+05	.000	1.5439E+06	3.4781E+06
	Scaled effect	2.24150E+006*	2.69921E+05	.000	1.2744E+06	3.2086E+06
	Micro-roughened 2	2.90250E+006*	2.69921E+05	.000	1.9354E+06	3.8696E+06
	Micro-roughened 3	2.91633E+006*	2.69921E+05	.000	1.9493E+06	3.8834E+06
	Micro-roughened 4	2.07900E+006*	2.69921E+05	.000	1.1119E+06	3.0461E+06
	Random Protuberances	2.48867E+006*	2.69921E+05	.000	1.5216E+06	3.4557E+06
	Macro Ribbed	1.35733E+006*	2.69921E+05	.000	3.9026E+05	2.3244E+06
	Macro Troughed	7.79000E+05	2.69921E+05	.280	-1.8807E+05	1.7461E+06
	Sawtooth	2.90687E+006*	2.69921E+05	.000	1.9398E+06	3.8739E+06
	CoCr	-4.65100E+006*	2.54122E+05	.000	-5.5615E+06	-3.7405E+06
	Micro-rough + Macro Ribbed (1mm)	-1.96000E+05	2.81923E+05	1.000	-1.2061E+06	8.1408E+05

Table 1: ANOVA multiple comparison test of PEEK-cement interfacial mean shear strength with surface textures: * = The mean difference is significant at the 0.05 level. A negative value indicates the sample shear strength is significantly weaker and a positive value indicates the sample interfacial strength is significantly stronger than the (I) sample.

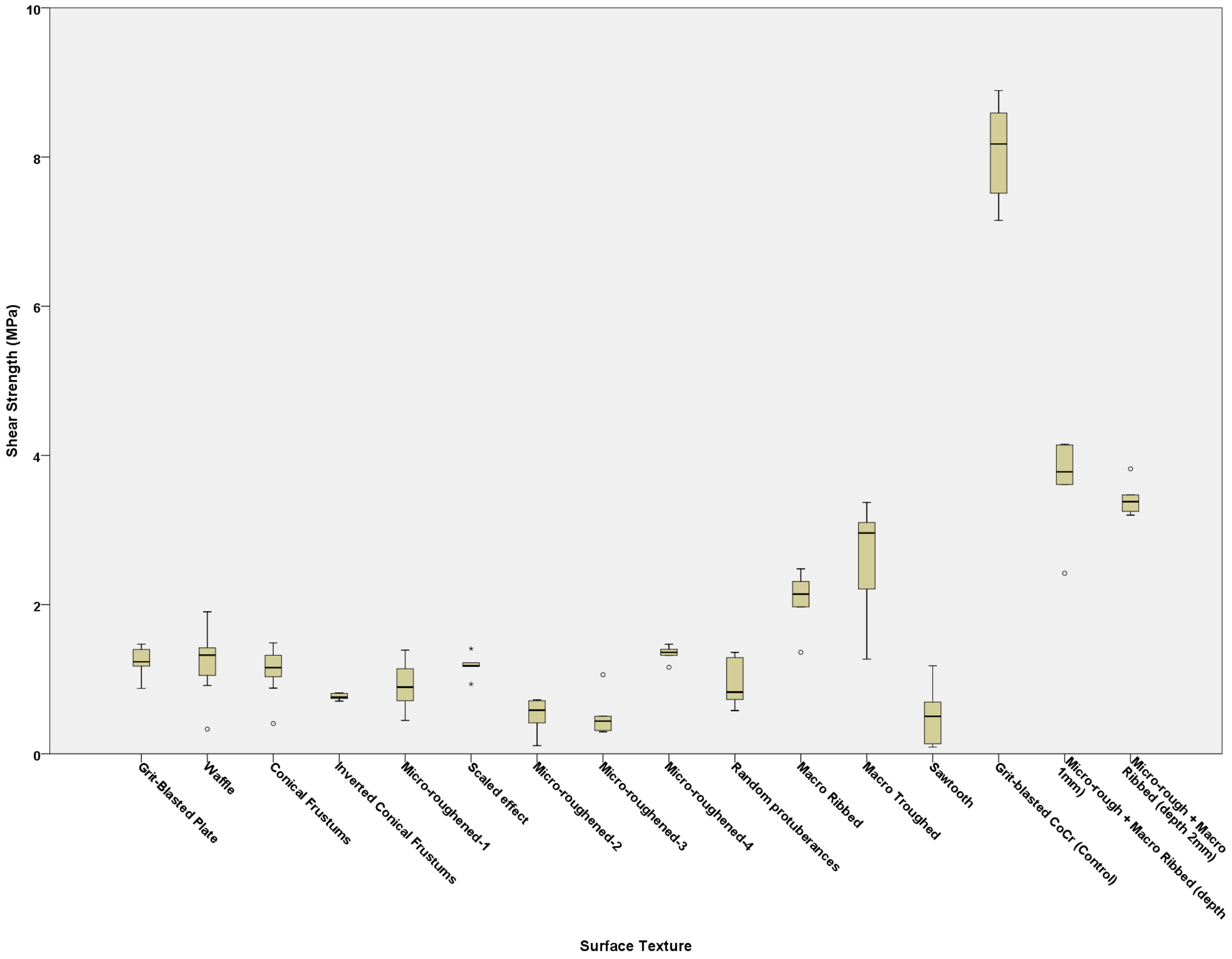

Figure 1: Box plot showing the shear strength data distribution for each sample group (○ = outlier, ∗ = extreme value)

Table 2 shows the analysis of variance of the plasma treated PEEK-cement lap shear strength results compared to the untreated samples (section 3.4.2.2), obtained using the method in section 3.3.1.5. An asterisk (*) indicated that the mean difference is significant at the 0.05 level. A negative value indicates the sample shear strength is significantly weaker, and a positive value indicates the sample interfacial strength is significantly stronger, than the (I) sample. 'UoS' denotes that the sample was plasma treated at the University of Southampton and 'Invibio' denotes that the samples were supplied as plasma treated by Invibio Ltd (Thornton Cleveleys, UK).

(I) Sample	**(J) Comparate**	**Mean Difference (I-J)**	**Std. Error**	**Sig.**	**95% Confidence Interval**	
					Lower Bound	**Upper Bound**
Grit Blasted	Waffle	-4.92800E+03	1.90337E+05	1.000	-7.3890E+05	7.2905E+05
	Conical Frustums	1.14496E+05	1.90337E+05	1.000	-6.1948E+05	8.4847E+05
	PT Plate (UoS)	8.57173E+05	2.76170E+05	.350	-2.0779E+05	1.9221E+06
	PT Waffle (Invibio)	-1.92483E+006*	2.76170E+05	.000	-2.9898E+06	-8.5987E+05
	PT Conical Frustums (Invibio)	-1.15483E+006*	2.76170E+05	.017	-2.2198E+06	-8.9865E+04
	Micro-roughened 1	3.18840E+05	2.18331E+05	1.000	-5.2309E+05	1.1608E+06
	Macro Ribbed	-8.34827E+05	2.18331E+05	.055	-1.6768E+06	7.0992E+03
	Macro Troughed	-1.41316E+006*	2.18331E+05	.000	-2.2551E+06	-5.7123E+05
	PT Macro Troughed (UoS)	-2.15316E+006*	2.48936E+05	.000	-3.1131E+06	-1.1932E+06
	PT Micro-roughened 1 (UoS)	-3.10660E+05	2.48936E+05	1.000	-1.2706E+06	6.4928E+05
	PT Macro Ribbed (UoS)	-2.02816E+006*	2.48936E+05	.000	-2.9881E+06	-1.0682E+06
	PT Conical Frustums (UoS)	-8.45660E+05	2.48936E+05	.183	-1.8056E+06	1.1428E+05
	PT Waffle (UoS)	-1.51816E+006*	2.48936E+05	.000	-2.4781E+06	-5.5822E+05
Waffle	Grit Blasted	4.92800E+03	1.90337E+05	1.000	-7.2905E+05	7.3890E+05
	Conical Frustums	1.19424E+05	1.85260E+05	1.000	-5.9497E+05	8.3382E+05
	PT Plate (UoS)	8.62101E+05	2.72696E+05	.312	-1.8946E+05	1.9137E+06
	PT Waffle (Invibio)	-1.91990E+006*	2.72696E+05	.000	-2.9715E+06	-8.6833E+05
	PT Conical Frustums (Invibio)	-1.14990E+006*	2.72696E+05	.015	-2.2015E+06	-9.8334E+04
	Micro-roughened 1	3.23768E+05	2.13920E+05	1.000	-5.0115E+05	1.1487E+06
	Macro Ribbed	-8.29899E+005*	2.13920E+05	.046	-1.6548E+06	-4.9832E+03
	Macro Troughed	-1.40823E+006*	2.13920E+05	.000	-2.2331E+06	-5.8332E+05
	PT Macro Troughed (UoS)	-2.14823E+006*	2.45076E+05	.000	-3.0933E+06	-1.2032E+06
	PT Micro-roughened 1 (UoS)	–3.05732E+05	2.45076E+05	1.000	-1.2508E+06	6.3933E+05
	PT Macro Ribbed (UoS)	-2.02323E+006*	2.45076E+05	.000	-2.9683E+06	-1.0782E+06
	PT Conical Frustums (UoS)	-8.45660E+05	2.48936E+05	.183	-1.8056E+06	1.1428E+05
	PT Waffle (UoS)	-1.51816E+006*	2.48936E+05	.000	-2.4781E+06	-5.5822E+05
Conical Frustums	Grit Blasted	-1.14496E+05	1.90337E+05	1.000	-8.4847E+05	6.1948E+05
	Waffle	-1.19424E+05	1.85260E+05	1.000	-8.3382E+05	5.9497E+05
	PT Plate (UoS)	7.42677E+05	2.72696E+05	.641	-3.0889E+05	1.7942E+06
	PT Waffle (Invibio) 1	-2.03932E+006*	2.72696E+05	.000	-3.0909E+06	-9.8776E+05
	PT Conical Frustums (Invibio)	-1.26932E+006*	2.72696E+05	.003	-2.3209E+06	-2.1776E+05
	Micro-roughened 1	2.04344E+05	2.13920E+05	1.000	-6.2057E+05	1.0293E+06
	Macro Ribbed	-9.49323E+005*	2.13920E+05	.007	-1.7742E+06	-1.2441E+05
	Macro Troughed	-1.52766E+006*	2.13920E+05	.000	-2.3526E+06	-7.0274E+05
	PT Macro Troughed (UoS)	-2.26766E+006*	2.45076E+05	.000	-3.2127E+06	-1.3226E+06
	PT Micro-roughened 1	-4.25156E+05	2.45076E+05	.998	-1.3702E+06	5.1990E+05
	PT Macro Ribbed (UoS)	2.14266E+006*	2.45076E+05	.000	-3.0877E+06	-1.1976E+06
	PT Conical Frustums (UoS)	-9.60156E+005*	2.45076E+05	.041	-1.9052E+06	-1.5097E+04
	PT Waffle (UoS)	-1.63266E+006*	2.45076E+05	.000	-2.5777E+06	-6.8760E+05

PT Plate (UoS)	Grit Blasted	-8.57173E+05	2.76170E+05	.350	-1.9221E+06	2.0779E+05
	Waffle	-8.62101E+05	2.72696E+05	.312	-1.9137E+06	1.8946E+05
	Conical Frustums	-7.42677E+05	2.72696E+05	.641	-1.7942E+06	3.0889E+05
	PT Waffle (Invibio)	-2.78200E+006*	3.38237E+05	.000	-4.0863E+06	-1.4777E+06
	PT Conical Frustums (Invibio)	-2.01200E+006*	3.38237E+05	.000	-3.3163E+06	-7.0769E+05
	Micro-roughened 1	-5.38333E+05	2.92922E+05	.994	-1.6679E+06	5.9123E+05
	Macro Ribbed	-1.69200E+006*	2.92922E+05	.000	-2.8216E+06	-5.6244E+05
	Macro Troughed	-2.27033E+006*	2.92922E+05	.000	-3.3999E+06	-1.1408E+06
	PT Macro Troughed (UoS)	-3.01033E+006*	3.16392E+05	.000	-4.2304E+06	-1.7903E+06
	PT Micro-roughened 1	-1.16783E+06	3.16392E+05	.082	-2.3879E+06	5.2233E+04
	PT Macro Ribbed (UoS)	-2.88533E+006*	3.16392E+05	.000	-4.1054E+06	-1.6653E+06
	PT Conical Frustums (UoS)	-1.70283E+006*	3.16392E+05	.000	-2.9229E+06	-4.8277E+05
	PT Waffle (UoS)	-2.37533E+006*	3.16392E+05	.000	-3.5954E+06	-1.1553E+06
PT Waffle (Invibio)	Grit Blasted	1.92483E+006*	2.76170E+05	.000	8.5987E+05	2.9898E+06
	Waffle	1.91990E+006*	2.72696E+05	.000	8.6833E+05	2.9715E+06
	Conical Frustums	2.03932E+006*	2.72696E+05	.000	9.8776E+05	3.0909E+06
	PT Plate (UoS)	2.78200E+006*	3.38237E+05	.000	1.4777E+06	4.0863E+06
	PT Conical Frustums (Invibio)	7.70000E+05	3.38237E+05	.914	-5.3431E+05	2.0743E+06
	Micro-roughened 1	2.24367E+006*	2.92922E+05	.000	1.1141E+06	3.3732E+06
	Macro Ribbed	1.09000E+06	2.92922E+05	.076	-3.9562E+04	2.2196E+06
	Macro Troughed	5.11667E+05	2.92922E+05	.997	-6.1790E+05	1.6412E+06
	PT Macro Troughed (UoS)	-2.28333E+05	3.16392E+05	1.000	-1.4484E+06	9.9173E+05
	PT Micro-roughened 1	1.61417E+006*	3.16392E+05	.000	3.9410E+05	2.8342E+06
	PT Macro Ribbed (UoS)	–1.03333E+05	3.16392E+05	1.000	-1.3234E+06	1.1167E+06
	PT Conical Frustums (UoS)	1.07917E+06	3.16392E+05	.176	-1.4090E+05	2.2992E+06
	PT Waffle (UoS)	4.06667E+05	3.16392E+05	1.000	-8.1340E+05	1.6267E+06
PT Conical Frustums (Invibio)	Grit Blasted	1.15483E+006*	2.76170E+05	.017	8.9865E+04	2.2198E+06
	Waffle	1.14990E+006*	2.72696E+05	.015	9.8334E+04	2.2015E+06
	Conical Frustums	1.26932E+006*	2.72696E+05	.003	2.1776E+05	2.3209E+06
	PT Plate (UoS)	2.01200E+006*	3.38237E+05	.000	7.0769E+05	3.3163E+06
	PT Waffle (Invibio)	-7.70000E+05	3.38237E+05	.914	-2.0743E+06	5.3431E+05
	Micro-roughened 1	1.47367E+006*	2.92922E+05	.001	3.4410E+05	2.6032E+06
	Macro Ribbed	3.20000E+05	2.92922E+05	1.000	-8.0956E+05	1.4496E+06
	Macro Troughed	-2.58333E+05	2.92922E+05	1.000	-1.3879E+06	8.7123E+05
	PT Macro Troughed (UoS)	-9.98333E+05	3.16392E+05	.316	-2.2184E+06	2.2173E+05
	PT Micro-roughened 1	8.44167E+05	3.16392E+05	.683	-3.7590E+05	2.0642E+06
	PT Macro Ribbed (UoS)	-8.73333E+05	3.16392E+05	.612	-2.0934E+06	3.4673E+05
	PT Conical Frustums (UoS)	3.09167E+05	3.16392E+05	1.000	-9.1090E+05	1.5292E+06
	PT Waffle (UoS)	-3.63333E+05	3.16392E+05	1.000	-1.5834E+06	8.5673E+05
Micro-roughened 1	Grit Blasted	-3.18840E+05	2.18331E+05	1.000	-1.1608E+06	5.2309E+05
	Waffle	-3.23768E+05	2.13920E+05	1.000	-1.1487E+06	5.0115E+05
	Conical Frustums	-2.04344E+05	2.13920E+05	1.000	-1.0293E+06	6.2057E+05
	PT Plate (UoS)	5.38333E+05	2.92922E+05	.994	-5.9123E+05	1.6679E+06
	PT Waffle (Invibio)	-2.24367E+006*	2.92922E+05	.000	-3.3732E+06	-1.1141E+06
	PT Conical Frustums (Invibio)	-1.47367E+006*	2.92922E+05	.001	-2.6032E+06	-3.4410E+05
	Macro Ribbed	-1.15367E+006*	2.39170E+05	.001	-2.0760E+06	-2.3138E+05
	Macro Troughed	-1.73200E+006*	2.39170E+05	.000	-2.6543E+06	-8.0972E+05
	PT Macro Troughed (UoS)	-2.47200E+006*	2.67400E+05	.000	-3.5031E+06	-1.4409E+06
	PT Micro-roughened 1	-6.29500E+05	2.67400E+05	.881	-1.6606E+06	4.0164E+05
	PT Macro Ribbed (UoS)	-2.34700E+006*	2.67400E+05	.000	-3.3781E+06	-1.3159E+06
	PT Conical Frustums (UoS)	-1.16450E+006*	2.67400E+05	.009	-2.1956E+06	-1.3336E+05
	PT Waffle (UoS)	-1.83700E+006*	2.67400E+05	.000	-2.8681E+06	-8.0586E+05
Macro Ribbed	Grit Blasted	8.34827E+05	2.18331E+05	.055	-7.0992E+03	1.6768E+06
	Waffle	8.29899E+005*	2.13920E+05	.046	4.9832E+03	1.6548E+06

	Conical Frustums	9.49323E+005*	2.13920E+05	.007	1.2441E+05	1.7742E+06
	PT Plate (UoS)	1.69200E+006*	2.92922E+05	.000	5.6244E+05	2.8216E+06
	PT Waffle (Invibio)	-1.09000E+06	2.92922E+05	.076	-2.2196E+06	3.9562E+04
	PT Conical Frustums (Invibio)	-3.20000E+05	2.92922E+05	1.000	-1.4496E+06	8.0956E+05
	Micro-roughened 1	1.15367E+006*	2.39170E+05	.001	2.3138E+05	2.0760E+06
	Macro Troughed	-5.78333E+05	2.39170E+05	.848	-1.5006E+06	3.4395E+05
	PT Macro Troughed (UoS)	-1.31833E+006*	2.67400E+05	.001	-2.3495E+06	-2.8719E+05
	PT Micro-roughened 1	5.24167E+05	2.67400E+05	.985	-5.0698E+05	1.5553E+06
	PT Macro Ribbed (UoS)	-1.19333E+006*	2.67400E+05	.006	-2.2245E+06	-1.6219E+05
	PT Conical Frustums (UoS)	-1.08333E+04	2.67400E+05	1.000	-1.0420E+06	1.0203E+06
	PT Waffle (UoS)	-6.83333E+05	2.67400E+05	.764	-1.7145E+06	3.4781E+05
Macro Troughed	Grit Blasted	1.41316E+006*	2.18331E+05	.000	5.7123E+05	2.2551E+06
	Waffle	1.40823E+006*	2.13920E+05	.000	5.8332E+05	2.2331E+06
	Conical Frustums	1.52766E+006*	2.13920E+05	.000	7.0274E+05	2.3526E+06
	PT Plate (UoS)	2.27033E+006*	2.92922E+05	.000	1.1408E+06	3.3999E+06
	PT Waffle (Invibio)	-5.11667E+05	2.92922E+05	.997	-1.6412E+06	6.1790E+05
	PT Conical Frustums (Invibio)	2.58333E+05	2.92922E+05	1.000	-8.7123E+05	1.3879E+06
	Micro-roughened 1	1.73200E+006*	2.39170E+05	.000	8.0972E+05	2.6543E+06
	Macro Ribbed	5.78333E+05	2.39170E+05	.848	-3.4395E+05	1.5006E+06
	PT Macro Troughed (UoS)	-7.40000E+05	2.67400E+05	.606	-1.7711E+06	2.9114E+05
	PT Micro-roughened 1	1.10250E+006*	2.67400E+05	.021	7.1356E+04	2.1336E+06
	PT Macro Ribbed (UoS)	-6.15000E+05	2.67400E+05	.904	-1.6461E+06	4.1614E+05
	PT Conical Frustums (UoS)	-1.56037E+006*	2.67400E+05	.000	-2.5915E+06	-5.2922E+05
	PT Waffle (UoS)	-1.05000E+05	2.67400E+05	1.000	-1.1361E+06	9.2614E+05
PT Macro Troughed (UoS)	Grit Blasted	2.15316E+006*	2.48936E+05	.000	1.1932E+06	3.1131E+06
	Waffle	2.14823E+006*	2.45076E+05	.000	1.2032E+06	3.0933E+06
	Conical Frustums	2.26766E+006*	2.45076E+05	.000	1.3226E+06	3.2127E+06
	PT Plate (UoS)	3.01033E+006*	3.16392E+05	.000	1.7903E+06	4.2304E+06
	PT Waffle (Invibio)	2.28333E+05	3.16392E+05	1.000	-9.9173E+05	1.4484E+06
	PT Conical Frustums (Invibio)	9.98333E+05	3.16392E+05	.316	-2.2173E+05	2.2184E+06
	Micro-roughened 1	2.47200E+006*	2.67400E+05	.000	1.4409E+06	3.5031E+06
	Macro Ribbed	1.31833E+006*	2.67400E+05	.001	2.8719E+05	2.3495E+06
	PT Macro Troughed (UoS)	7.40000E+05	2.67400E+05	.606	-2.9114E+05	1.7711E+06
	PT Micro-roughened 1	1.84250E+006*	2.92922E+05	.000	7.1294E+05	2.9721E+06
	PT Macro Ribbed (UoS)	1.25000E+05	2.92922E+05	1.000	-1.0046E+06	1.2546E+06
	PT Conical Frustums (UoS)	1.30750E+006*	2.92922E+05	.006	1.7794E+05	2.4371E+06
	PT Waffle (UoS)	6.35000E+05	2.92922E+05	.949	-4.9456E+05	1.7646E+06
PT Micro-roughened 1 (UoS)	Grit Blasted	3.10660E+05	2.48936E+05	1.000	-6.4928E+05	1.2706E+06
	Waffle	3.05732E+05	2.45076E+05	1.000	-6.3933E+05	1.2508E+06
	Conical Frustums	4.25156E+05	2.45076E+05	.998	-5.1990E+05	1.3702E+06
	PT Plate (UoS)	1.16783E+06	3.16392E+05	.082	-5.2233E+04	2.3879E+06
	PT Waffle (Invibio)	-1.61417E+006*	3.16392E+05	.000	-2.8342E+06	-3.9410E+05
	PT Conical Frustums (Invibio)	-8.44167E+05	3.16392E+05	.683	-2.0642E+06	3.7590E+05
	Micro-roughened 1	6.29500E+05	2.67400E+05	.881	-4.0164E+05	1.6606E+06
	Macro Ribbed	-5.24167E+05	2.67400E+05	.985	-1.5553E+06	5.0698E+05
	PT Macro Troughed (UoS)	-1.10250E+006*	2.67400E+05	.021	-2.1336E+06	-7.1356E+04
	PT Micro-roughened 1	-1.84250E+006*	2.92922E+05	.000	-2.9721E+06	-7.1294E+05
	PT Macro Ribbed (UoS)	-1.71750E+006*	2.92922E+05	.000	-2.8471E+06	-5.8794E+05
	PT Conical Frustums (UoS)	-5.35000E+05	2.92922E+05	.995	-1.6646E+06	5.9456E+05
	PT Waffle (UoS)	-1.20750E+006*	2.92922E+05	.021	-2.3371E+06	-7.7938E+04
PT Macro Ribbed (UoS)	Grit Blasted	2.02816E+006*	2.48936E+05	.000	1.0682E+06	2.9881E+06

	Waffle	2.02323E+006*	2.45076E+05	.000	1.0782E+06	2.9683E+06
	Conical Frustums	2.14266E+006*	2.45076E+05	.000	1.1976E+06	3.0877E+06
	PT Plate (UoS)	2.88533E+006*	3.16392E+05	.000	1.6653E+06	4.1054E+06
	PT Waffle (Invibio)	1.03333E+05	3.16392E+05	1.000	-1.1167E+06	1.3234E+06
	PT Conical Frustums (Invibio)	8.73333E+05	3.16392E+05	.612	-3.4673E+05	2.0934E+06
	Micro-roughened 1	2.34700E+006*	2.67400E+05	.000	1.3159E+06	3.3781E+06
	Macro Ribbed	1.19333E+006*	2.67400E+05	.006	1.6219E+05	2.2245E+06
	Macro Troughed	6.15000E+05	2.67400E+05	.904	-4.1614E+05	1.6461E+06
	PT Macro Troughed	-1.25000E+05	2.92922E+05	1.000	-1.2546E+06	1.0046E+06
	PT Micro-roughened 1	1.71750E+006*	2.92922E+05	.000	5.8794E+05	2.8471E+06
	PT Conical Frustums (UoS)	1.18250E+006*	2.92922E+05	.028	5.2938E+04	2.3121E+06
	PT Waffle (UoS)	5.10000E+05	2.92922E+05	.998	-6.1956E+05	1.6396E+06
PT Conical Frustums (UoS)	Grit Blasted	8.45660E+05	2.48936E+05	.183	-1.1428E+05	1.8056E+06
	Waffle	8.40732E+05	2.45076E+05	.168	-1.0433E+05	1.7858E+06
	Conical Frustums	9.60156E+005*	2.45076E+05	.041	1.5097E+04	1.9052E+06
	PT Plate (UoS)	1.70283E+006*	3.16392E+05	.000	4.8277E+05	2.9229E+06
	PT Waffle (Invibio)	-1.07917E+06	3.16392E+05	.176	-2.2992E+06	1.4090E+05
	PT Conical Frustums (Invibio)	-3.09167E+05	3.16392E+05	1.000	-1.5292E+06	9.1090E+05
	Micro-roughened 1	1.16450E+006*	2.67400E+05	.009	1.3336E+05	2.1956E+06
	Macro Ribbed	1.08333E+04	2.67400E+05	1.000	-1.0203E+06	1.0420E+06
	Macro Troughed	-5.67500E+05	2.67400E+05	.960	-1.5986E+06	4.6364E+05
	PT Macro Troughed	-1.30750E+006*	2.92922E+05	.006	-2.4371E+06	-1.7794E+05
	PT Micro-roughened 1	5.35000E+05	2.92922E+05	.995	-5.9456E+05	1.6646E+06
	PT Macro Ribbed (UoS)	-1.18250E+006*	2.92922E+05	.028	-2.3121E+06	-5.2938E+04
	PT Waffle (UoS)	-6.72500E+05	2.92922E+05	.906	-1.8021E+06	4.5706E+05
PT Waffle (UoS)	Grit Blasted	1.51816E+006*	2.48936E+05	.000	5.5822E+05	2.4781E+06
	Waffle	1.51323E+006*	2.45076E+05	.000	5.6817E+05	2.4583E+06
	Conical Frustums	1.63266E+006*	2.45076E+05	.000	6.8760E+05	2.5777E+06
	PT Plate (UoS)	2.37533E+006*	3.16392E+05	.000	1.1553E+06	3.5954E+06
	PT Waffle (Invibio)	-4.06667E+05	3.16392E+05	1.000	-1.6267E+06	8.1340E+05
	PT Conical Frustums (Invibio)	3.63333E+05	3.16392E+05	1.000	-8.5673E+05	1.5834E+06
	Micro-roughened 1	1.83700E+006*	2.67400E+05	.000	8.0586E+05	2.8681E+06
	Macro Ribbed	6.83333E+05	2.67400E+05	.764	-3.4781E+05	1.7145E+06
	Macro Troughed	1.05000E+05	2.67400E+05	1.000	-9.2614E+05	1.1361E+06
	PT Macro Troughed	-6.35000E+05	2.92922E+05	.949	-1.7646E+06	4.9456E+05
	PT Micro-roughened 1	1.20750E+006*	2.92922E+05	.021	7.7938E+04	2.3371E+06
	PT Macro Ribbed (UoS)	-5.10000E+05	2.92922E+05	.998	-1.6396E+06	6.1956E+05
	PT Conical Frustums (UoS)	6.72500E+05	2.92922E+05	.906	-4.5706E+05	1.8021E+06

Table 2: ANOVA multiple comparison test of PEEK-cement interfacial mean shear strength with surface activation through plasma treatment: * = The mean difference is significant at the 0.05 level. A negative value indicates the sample shear strength is significantly weaker and a positive value indicates the sample interfacial strength is significantly stronger than the (I) sample.

The error bar chart shown in Figure 2 gives the 95% confidence intervals of shear strength for every sample group tested in the fixation study. No overlap in the error bars suggests that there is significant difference in the results.

Figure 2: Error bar chart showing the 95% confidence intervals of shear strength for each sample group (PT = plasma treated)